AWARD NUMBER: W81XWH-19-1-0045

TITLE: A Targeted Alpha-Particle Radiopharmaceutical for Bone Metastatic Breast Cancer

PRINCIPAL INVESTIGATOR: Yusuke Shiozawa, M.D., Ph.D.

CONTRACTING ORGANIZATIONS: Wake Forest University Health Sciences
University of Iowa

REPORT DATE: MAY 2022

TYPE OF REPORT: Annual report

PREPARED FOR: U.S. Army Medical Research and Development Command
Fort Detrick, Maryland 21702-5012

DISTRIBUTION STATEMENT: Approved for Public Release;
Distribution Unlimited

REPORT DOCUMENTATION PAGE

Form Approved
OMB No. 0704-0188

1. REPORT DATE MAY 2022	**2. REPORT TYPE** Annual	**3. DATES COVERED** 04/01/2021 – 03/31/2022

4. TITLE AND SUBTITLE

A Targeted Alpha-Particle Radiopharmaceutical for Bone Metastatic Breast Cancer

5a. CONTRACT NUMBER

5b. GRANT NUMBER
W81XWH-19-1-0045

5c. PROGRAM ELEMENT NUMBER

6. AUTHOR(S)

Yusuke Shiozawa, MD, PhD; Thaddeus Wadas, PhD

E-Mail: yshiozaw@wakehealth.edu, thaddeus-wadas@uiowa.edu

5d. PROJECT NUMBER

5e. TASK NUMBER

5f. WORK UNIT NUMBER

7. PERFORMING ORGANIZATION NAME(S) AND ADDRESS(ES)

Wake Forest University Health Sciences
Medical Center Blvd.,
Winston-Salem NC 27157

University of Iowa
Iowa City, IA 52242

8. PERFORMING ORGANIZATION REPORT NUMBER

9. SPONSORING / MONITORING AGENCY S) AND ADDRESS(ES)

U.S. Army Medical Research and Development Command
Fort Detrick, Maryland 21702-5012

10. SPONSOR/MONITOR'S ACRONYM(S)

11. SPONSOR/MONITOR'S REPORT NUMBER(S)

12. DISTRIBUTION / AVAILABILITY STATEMENT

Approved for Public Release; Distribution Unlimited

13. SUPPLEMENTARY NOTES

14. ABSTRACT

The proposed studies will develop and evaluate a new therapeutic strategy for treating breast cancer bone metastasis by disrupting the interactions between breast cancer cells and sensory neurons within bone using alpha particle-emitting radiopharmaceuticals that target the CGRP-CRLR axis. The successful completion of this project will establish a new therapeutic target for cancer-induced bone pain and bone metastatic breast cancer; while providing the foundation required to develop new therapies that will decrease suffering and improve survival of breast cancer patients with bone metastases.

During this period, we encountered COVID-19-related issues which have negatively impacted our productivity. However, after conducting online training with Dr. Wadas, Dr. Shiozawa obtained institutional radiation safety approval to perform proposed work in November 2021 so that Dr. Shiozawa is able to perform radioactive work at Wake Forest School of Medicine. Additionally, we have created the CRLC-over-expressing breast cancer cells which will be used to evaluate the ^{225}Ac-PTCA-CGRP$_{27\text{-}37}$ peptides *in vitro* and *in vivo* during the next year. The team also completed the first radiochemistry experiments with the PCTA-CGRP$_{27\text{-}37}$ peptides and developed strategies to overcome the severe lipophilicity of the agents under investigation.

15. SUBJECT TERMS

Breast Cancer; Bone metastasis; Cancer-induced bone pain; Radiopharmaceuticals; Calcitonin receptor-like receptor; Actinium-225

16. SECURITY CLASSIFICATION OF:			**17. LIMITATION OF ABSTRACT**	**18. NUMBER OF PAGES**	**19a. NAME OF RESPONSIBLE PERSON** USAMRDC
a. REPORT Unclassified	**b. ABSTRACT** Unclassified	**c. THIS PAGE** Unclassified	Unclassified	91	**19b. TELEPHONE NUMBER** *(include area code)*

Table of Contents

Page

1. INTRODUCTION:

When breast cancer (BCa) patients develop bone metastases, their 5-year survival rate declines by more than 70%. External beam radiation is used primarily for palliative treatment for patients with bone metastases. Bisphosphonate and anti-receptor activator of nuclear factor κB ligand (RANKL) antibody to decrease bone resorption can reduce the onset of pain, but they ultimately fail to improve overall survival. Radium-223 ($^{223}RaCl_2$) can extend overall survival of prostate cancer patients with bone metastases, but only to a limited extent. Since these treatments mainly target bone remodeling, **new approaches that target factors other than bone remodeling are needed.**

Cancer-induced bone pain is the most common and intractable symptom of bone metastases, and it substantially impairs quality of life. Eighty percent of patients with bone metastasis have cancer-induced bone pain, and its management is a tremendous challenge for patients and caregivers. It has also been suggested that cancer-induced bone pain may be a negative indicator of survival. The ALSYMPCA trial, which investigated the role of $^{223}RaCl_2$ in prostate cancer patients with bone metastases, revealed that decreased pain levels corelated with increased overall survival. Thus, treating bone metastases by targeting pain signals are a promising approach to improve mortality.

Calcitonin gene-related peptide (CGRP), a 37-amino acid neuropeptide widely distributed in the peripheral and central nervous systems, is closely associated with pain behavior. Sensory nerves that express CGRP were enriched in the periosteum and bone marrow of a murine model of BCa bone metastasis. Patients with bone metastatic prostate cancer have elevated serum levels of CGRP. Sensory nerve-derived CGRP stimulated lung cancer growth. We have also found that: (i) bone metastatic prostate cancer directly affects sensory nerves to induce bone pain; (ii) sensory nerves that express CGRP are enriched in the marrow of those with bone metastatic prostate cancer; (iii) prostate cancer patients with bone metastatic disease have elevated serum levels of CGRP; (iv) samples from patients with bone metastatic BCa expressed higher levels of a CGRP receptor, calcitonin receptor-like receptor (CRLR); and (v) CGRP induces proliferation of BCa cells through CRLR. These data suggest that the CGRP/CRLR axis influences bone metastatic progression and could be a valuable therapeutic target.

The recent therapeutic efficacy of $^{223}RaCl_2$ ($t_{1/2}$ = 11.4 d; $E\alpha_{max}$ = 6-7 MeV) for treatment of prostate cancer patients with bone metastases has renewed interest in the development of alpha particle-based therapies. The effectiveness of $^{223}RaCl_2$ results from its ability to form complexes with hydroxylapatite in remodeling bone. $^{223}RaCl_2$ emits alpha particles and deposits substantial ionizing energy via high linear energy transfer (LET) over < 100 µm within bone tissue. When DNA is exposed to high LET, irreparable double-stranded breaks occur, resulting in cell death. $^{223}RaCl_2$ is more potent than low LET β-emitting bone-seeking agents, and its cytotoxicity is not affected by hypoxia or mechanisms of radio- or chemoresistance. However, its chemical properties make it difficult to conjugate to molecular delivery systems, such as antibodies that target solid tumors.

There is growing consensus that actinium-225 (^{225}Ac) ($t_{1/2}$ = 10 d; $E\alpha_{max}$ = 6-8 MeV) could be a superior alternative for targeted alpha particle therapy of bone metastases. Unlike other alpha particles, ^{225}Ac of high specific activity and radionuclide purity is available. It has a long half-life, which synergizes well with the biological half-life of a circulating antibody. At the target site, it releases a large amount of kinetic energy per nuclear decay, making it highly cytotoxic when properly targeted. **Unlike $^{223}RaCl_2$,^{225}Ac's chemistry is amenable to chelation and conjugation to targeting molecules such as antibodies and peptides**. Recent *in vivo* preclinical evaluation of ^{225}Ac radiotherapeutics demonstrates that ^{225}Ac may provide new strategies for targeted alpha particle therapy development. Although the recent clinical success of ^{225}Ac radiotherapeutics that target prostate-specific membrane antigen (PSMA) demonstrate that targeted alpha particle therapy approaches could have a significant and positive impact on the management of prostate cancer, targeting PSMA is not applicable for other cancer types including breast cancer.

Hypothesis:

The delivery of alpha particle radiation to bone metastatic foci using CRLR-targeting ligands will reduce BCa tumor burden and cancer-induced bone pain.

Specific Aims:

Aim 1: Determine the best alpha particle radiopharmaceuticals targeted to the CRLR.

We will develop CRLR-targeted peptide (CGRP$_{27-37}$) conjugated with actinium-225 (^{225}Ac, ^{225}Ac-CGRP$_{27-37}$). Then, the binding affinity of ^{225}Ac-CGRP$_{27-37}$ to CRLR will be determined *in vitro*. The biodistribution of ^{225}Ac-CGRP$_{27-37}$ and organ dosimetry will be determined *in vivo*.

Aim 2: Determine the impact of CRLR-targeted alpha particle therapy on BCa bone metastases and cancer-induced bone pain.

Using an *in vivo* bone metastatic model that allows us to measure tumor growth, bone remodeling, skeletal innervation, and pain behaviors within each mouse, we will determine the safety and efficacy of ^{225}Ac-CGRP$_{27-37}$ in the treatment of bone metastatic progression and its resultant pain.

Our proposal would be the first to rigorously investigate the use of ^{225}Ac-based targeted alpha particle therapy to target the CRLR, a receptor for the pain-related neuropeptide CGRP, in breast cancer bone metastases. If successful, the proposed studies will yield a paradigm-shifting treatment strategy for BCa patients with bone metastases.

The **immediate benefits** of this research will provide essential preliminary data for the design of subsequent clinical translational studies. Our results could be quickly translated into novel treatment strategies to reduce breast cancer-associated morbidity and mortality.

The potential for **long-term and positive impact** of our work is substantial. This work will inform new treatment strategies to address both bone metastatic progression and cancer-induced bone pain of BCa.

2. KEYWORDS:

Breast Cancer; Bone metastasis; Cancer-induced bone pain; Radiopharmaceuticals; Calcitonin receptor-like receptor; Actinium-225

3. ACCOMPLISHMENTS:

What were the major goals and objectives of the project?

This application will test a new and innovative approach for ^{225}Ac-based targeted alpha particle therapy of breast cancer bone metastases by exploiting CRLR as a potential therapeutic target for breast cancer bone metastases, with the goal of improving both patients' quality of life and overall survival.

Task 1: *In vitro* selection of CRLR-targeted alpha particle radiopharmaceuticals.

Months 1-12.

- Synthesize the $CGRP_{27-37}$ (**Months 1-2; Dr. Shiozawa**).
- Conjugate $CGRP_{27-37}$ to ^{225}Ac-PCTA (**Months 3-5; Dr. Wadas**).
- Test the serum stability of ^{225}Ac-$CGRP_{27-37}$ (**Months 6-8; Dr. Wadas**).
- Establish CRLR-down-regulated, CRLR-overexpressed breast cancer cells (**Months 6-8; Dr. Shiozawa**).
- Perform receptor binding assays and internalization assays (**Months 9-12; Dr. Wadas**).

Task 2: *In vivo* selection of CRLR-targeted alpha particle radiopharmaceuticals.

Months 1-18.

- Submit documents for local IACUC review. (**Months 1-2; Dr. Shiozawa**).
- Submit IACUC approval and necessary documents for review by the Animal Care and Use Review Office (ACURO). (**Months 3-4; Dr. Shiozawa**).
- Perform biodistribution and dosimetry assays (**Months 13-18; Drs. Shiozawa and Wadas**).

Task 3: Determine the maximum tolerated dose of CRLR-based targeted alpha particle therapy.

Months 18-24.

- Perform maximum tolerated dose studies (**Months 18-24; Drs. Shiozawa and Wadas**).
- Co-author comprehensive review of radiopharmaceutical treatment and bone metastasis. (**Months 20-14; Drs. Shiozawa and Wadas**).

Task 4: Determine treatment efficacy of CRLR-based targeted alpha particle therapy.

Months 25-34.

- Test the effects of ^{225}Ac-CGRP$_{27\text{-}37}$ on tumor growth in the marrow, bone remodeling, and pain-related behavior within the same animal (**Months 25-34; Drs. Shiozawa and Wadas**).
- Co-authored manuscript summarizing all the results. (**Months 33-36; Drs. Shiozawa and Wadas**).

<u>What was accomplished under these goals?</u>

(2019-2020)

The Award Transfer (Drs. Wadas and Shiozawa).

^{225}Ac-PCTA-CGRP$_{27\text{-}37}$ was stable in human serum (Dr. Wadas): Task 1.

The CALCRL in breast cancer cells were down-regulated using shRNA (Dr. Shiozawa): Task 1.

(2020-2021)

The plan for training Dr. Shiozawa in the safe use of radioactive materials (Drs. Wadas and Shiozawa).

The joint publication (Drs. Shiozawa and Wadas): Task 3.

The synthesis of CGRP$_{27-37}$ analogs (Dr. Wadas): Task 1.

The development of the over-expression virus vector for CRLR (Dr. Shiozawa): Task 1.

(2021-2022)

No cost extension on this award (Drs. Shiozawa and Wadas).

One-year no cost extension on this award was approved due to the COVID-19 pandemic.

Institutional radiation safety approval by Wake Forest School of Medicine (Dr. Shiozawa).

Due to the relocation of Dr. Wadas from Wake Forest School of Medicine to University of Iowa, Dr. Shiozawa must have obtained institutional approval for the radioactive work to perform the proposed experiments and receive the appropriate training. However, we experienced delays in obtaining institutional approval to perform the proposed radio isotope experiments due to the COVID-19 pandemic as well as the relocation and lab renovations of Dr. Wadas. After conducting online training with Dr. Wadas, Dr. Shiozawa obtained institutional radiation safety approval to perform proposed work in November 2021.

The CALCRL over-expression in breast cancer cells (Dr. Shiozawa): Task 1.

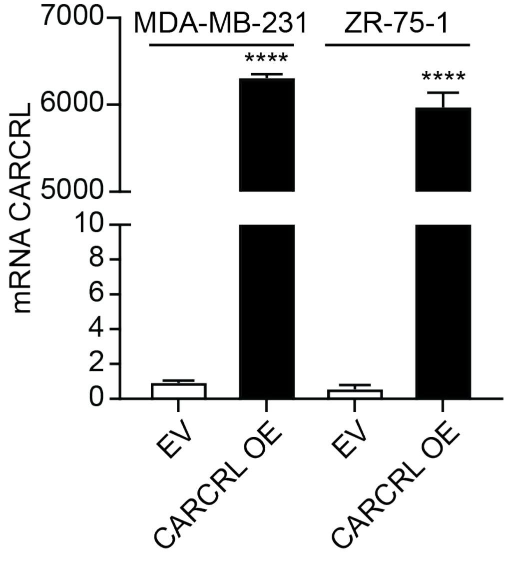

Fig. 1: The over-expression of CALCRL in breast cancer cells.
CALCRL over-expression in MDA-MB-231 and ZR-75-1 cells. $^{****}p \leq 0.0001$ vs. empty vector control (Student's *t*-test). Presented as mean ± SEM.

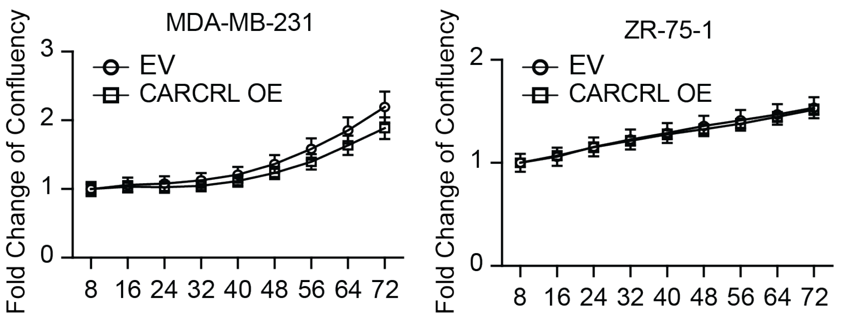

Fig. 2: CALCRL over-expression did not affect proliferation in breast cancer cells.
CALCLR-over-expressed and empty vector-transfected control breast cancer cells (MDA-MB-231 and ZR-75-1) were seeded in a 96 well plate (1000 cells/well) and proliferation was monitored by Incucyte Live-Cell Analysis Systems for 72 hours. Presented as mean fold change ± SEM.

To test the binding affinity of ^{225}Ac-PCTA-CGRP$_{27-37}$ to CRLR on breast cancer cells, we needed to manipulate the levels of CRLR in breast cancer cells. To do so, during the previous period, we developed (i) the CALCRL (gene name of CRLR)-downregulated breast cancer cells and CALCRL-over-expression lentiviral vector. During the current funding period, we successfully over-expressed CALCRL in both MDA-MB-231 and ZR-

75-1 cells with CALCRL-over-expression lentiviral vector (**Fig. 1**). Upon successful cell line establishment, CALCRL-over-expressed and control breast cancer cells lines were evaluated for proliferation, and CALCRL-over-expression did not affect cell proliferation (**Fig. 2**).

What opportunities for training and professional development did the project provide?

(2019-2020)

Dr. Shiozawa was invited to give a talk at The U.S. Bone and Joint Initiative (USBJI) and Bone and Joint Canada (BJC) Young Investigator Initiative Workshop Spring 2019 (Rosemont, IL) on April 27, 2019.

Dr. Shiozawa was invited to give a seminar at University of North Carolina at Chapel hill, Adams School of Dentistry (Chapel hill, NC) on December 03, 2019.

Dr. Wadas gave a lecture at the University of Iowa's Free Radical and Radiation Biology Program. This lecture dealt with the use of alpha particle therapy in cancer care. University of Iowa, Iowa City, IA (February 25, 2020).

Dr. Wadas accepted the role as Guest Editor of a Special Issue of *Molecules* that focuses on the use of radiotherapy of disease. The Issue description and call for papers can be found at https://www.mdpi.com/journal/molecules/special_issues/radiopharmaceutical_chemistry_radiotherapy.

(2020-2021)

Dr. Wadas gave a lecture at the University of Iowa's Cancer Biology Program. This lecture dealt with the development of targeted alpha particle-based radiotherapy and its use in oncology. University of Iowa, Iowa City, IA (November 26, 2020).

Dr. Wadas gave a lecture at the University of Iowa's Human Toxicology Program. This lecture dealt with the use of PET imaging in the precision medicine era. University of Iowa, Iowa City, IA (December 20, 2020).

(2021-2022)

As of July 1st, 2021, Dr. Shiozawa was promoted to an Associate Professor with Tenure.

Dr. Shiozawa was chosen to participate in the 2022 cohort of the Wake Forest Clinical and Translational Science Institute's Mentor Academy (February 2022-June 2022).

Dr. Shiozawa was chosen to participate in the 2022 cohort of the Wake Forest Clinical and Translational Science Institute's Leadership Academy (February 2022-June 2022).

Dr. Shiozawa became the Cancer Biology representative to the Molecular and Cellular Biosciences (MCB) (PhD) track admission committee (2021-Present).

Dr. Shiozawa became a member of Biomedical Science (BMSC)-Research Pathway (Master of Science) program recruitment committee (2022-Present).

Dr. Wadas received a secondary appointment as an Associate Professor of Radiation Oncology. Department of Radiation Oncology, University of Iowa, Iowa City. IA.

Dr. Wadas served on NIH Special Emphasis Panel/Scientific Review Group **ZCA1 RPRB-H (M1) S.** February 2022.

How were the results disseminated to communities of interest?

There is nothing to report.

What do you plan to do during the next reporting period to accomplish the goals and objectives?

1) Determine the binding affinity of radiopharmaceuticals to breast cancer cells *in vitro* (Aim 1).
2) Determine the biodistribution and dosimetry of radiopharmaceuticals *in vivo* (Aim 1).
3) Determine the impact of radiopharmaceuticals on BCa bone metastases and cancer-induced bone pain *in vivo* (Aim 2).
4) Dr. Shiozawa will complete his radioactive material handling training with Dr. Wadas in person.

4. IMPACT:

What was the impact on the development of the principal discipline(s) of the project?

(2019-2020)

1. We found that ^{225}Ac-PTCA-CGRP$_{27-37}$ were stable in human serum.
2. We were able to down-regulate CRLC expression levels in BCa using shRNA.

(2020-2021)

1. Drs. Shiozawa and Wadas published together a review manuscript relevant to this study.
2. We were able to synthesize several different analogs of CGRP$_{27-37}$.
3. We are currently developing the over-expression virus vector for CRLR.

(2021-2022)

1. Drs. Shiozawa and Wadas obtained the one-year no cost extension on this award due to the COVID-19 pandemic.
2. Dr. Shiozawa obtained the institutional radiation safety approval from Wake Forest School of Medicine to perform the proposed experiments.
3. We were able to over-express CRLR in breast cancer cells.
4. The Wadas research group developed methods to overcome the solubility issues with the bioconjugates under investigation.
5. The Wadas group synthesized several new analogs for evaluation that are in addition to the molecules proposed in the original application.

What was the impact on other disciplines?

We were able to develop new methods of radiopharmaceutical production. While specific to this project, they may have broad applicability to radiopharmaceutical development in general.

What was the impact on technology transfer?

There is nothing to report at this time.

What was the impact on society beyond science and technology?

There is nothing to report at this time.

5. CHANGES/PROBLEMS:

Changes in approach and reasons for change

Nothing to report.

Actual or anticipated problems or delays and actions or plans to resolve them

(2019-2020)

Nothing to report.

(2020-2021)

There has been some non-key personnel turnover (Technician) and maternity leave (Postdoc) in Dr. Shiozawa's lab as well as the recent COVID-19 pandemic which have impacted the timeliness of conducting the proposed studies. Due to COVID-19, Wake Forest University Health Sciences (WFUHS) issued an institutional stop work order from the middle of March to the end of May 2020. The personnel have been replaced and the lab has resumed normal operations.

In the original application, all of the experimental work involving radioactivity was to be conducted by Dr. Wadas' laboratory and under his radiation safety protocol. Shortly after this application was funded however, Dr. Wadas accepted a position in the Department of Radiology at the University of Iowa and moved his laboratory there. Unfortunately, his move to the University of Iowa coincided with the COVID-19 pandemic. At that time the University of Iowa enacted an institutional stop work order from the middle of March to the end of July 2020. This stop work order hindered Dr. Wadas' productivity on two levels. Foremost, he was unable to work on the aims as currently outlined in the SOW after the award was successfully transferred to the University of Iowa. Secondly, this stop work order prevented the renovation of Dr. Wadas' laboratories to accommodate radioactive materials. The expected completion date of renovations is July 1, 2021. The renovation schedule also affected the timeline of the hands-on radiation safety training, which we are planning to conduct so that Dr. Shiozawa may receive approval to use radioactive materials at WFUHS. Although Dr. Shiozawa has completed the appropriate radiation safety training required by WFUHS and additional didactic training with Dr. Wadas via videoconference, the WFUHS Radiation Committee is still requiring that Dr. Shiozawa receive hands-on training in the proper handling, use, storage and disposal of alpha particle-emitting radioisotopes from Dr. Wadas at the University of Iowa. Once the WFUHS' COVID-19 travel restriction order, which prevents work-related travel, is rescinded on June 30, 2021 Drs. Wadas and Shiozawa will schedule a week-long radiation safety training session at the University of Iowa.

In the next year term, we will try to catch up the speed of project productivity and continue to (i) determine the binding affinity of radiopharmaceuticals to breast cancer cells *in vitro* (Aim 1) and (ii) determine the biodistribution and dosimetry of radiopharmaceuticals *in vivo* (Aim 1).

(2021-2022)

Nothing to report.

<u>Changes that have a significant impact on expenditures</u>

Nothing to report.

<u>Significant changes in use or care of human subjects, vertebrate animals, biohazards, and/or select agents</u>

Nothing to report.

6. PRODUCTS:

Publications, conference papers, and presentations

Journal Publications

Peer reviewed journal

(2019-2020)

1. Lycan TW, Hsu F, Ahn CS, Thomas A, Walker FO, Sangueza OP, **Shiozawa Y**, Park SH, Peters CM, Romero-Sandoval EA, Melin SA, Sorscher S, Ansley K, Lesser GJ, Cartwright MS, Strowd RE. Neuromuscular ultrasound for taxane peripheral neuropathy in breast cancer. **Muscle and Nerve**. 2020; 61(5):587-594. PMID: 32052458. PMCID: In Progress.

   Status of Publication: Published

   Acknowledgement of federal support: Yes

2. Tafreshi NK, Tichacek CJ, Pandya DN, Doligalski ML, Budzevich M, Kil H-J, Bhatt NB, Kock ND, Messina J, Ruiz EE. Delva NC, Weaver A, Gibbons WR, Boulware DC, Khushalani NL, El-Haddad G, Triozzi PL, Moros EG, McLaughlin ML, **Wadas TJ**, Morse DL. Melanocortin 1 Receptor–Targeted α-Particle Therapy for Metastatic Uveal Melanoma. **J. Nucl. Med.** 2019; 60(8): 1124-1133. PMID: 30733316. PMCID: PMC6681690.

   Status of Publication: Published

   Acknowledgement of federal support: No

3. Tichacek CJ, Budzevich MM, **Wadas TJ**, Morse DL, Moros EG. A Monte Carlo Method for Determining the Response Relationship between Two Commonly Used Detectors to Indirectly Measure Alpha Particle Radiation Activity. **Molecules.** 2019; 24(18): 3397-3402. PMID: 31546752. PMCID: PMC6767018.

   Status of Publication: Published

   Acknowledgement of federal support: No

4. Tafreshi NK, Doligalski ML, Tichacek CJ, Pandya DN, Budzevich MM, El-Haddad G, Khushalani NI, Moros EG, McLaughlin ML, **Wadas TJ**, Morse DL. Development of Targeted Alpha Particle Therapy for Solid Tumors. **Molecules.** 2019; 24(23): 4314-4362. PMID: 31779154. PMCID: PMC6930656.

   Status of Publication: Published

   Acknowledgement of federal support: No

(2020-2021)

1. Wu S-Y, Xing F, Sharma S, Wu K, Tyagi A, Liu Y, Zhao D, Deshpande RP, **Shiozawa Y**, Ahmed T, Zhang W, Chan M, Ruiz J, Lycan TW, Dothard A, Watabe K. Nicotine promotes brain metastasis by polarizing microglia and suppressing innate immune function. ***JEM***. 2020;217:e20191131. PMID: 32496556. PMCID: PMC7398164.

   Status of Publication: Published

   Acknowledgement of federal support: No

2. Eber MR, Park SH, Contino KF, Patel CM, Hsu F-C, **Shiozawa Y**. Osteoblasts derived from mouse mandible enhance tumor growth of prostate cancer more than osteoblasts derived from long bone. ***J Bone Oncology***. 2021;26:100346. PMID: 33425674. PMCID: PMC7779864.

   Status of Publication: Published

   Acknowledgement of federal support: Yes

3. Park SH, Eber MR, M. Fonseca M, Patel CM, Cunnane KA, Ding H, Hsu F-C, Peters CM, Ko M-C, Strowd RE, Wilson JA, Hsu W, Romero-Sandoval EA, **Shiozawa Y**. Usefulness of the measurement of neurite outgrowth of primary sensory neurons to study cancer-related painful complications. ***Biochem Pharmacol***. 2021;188:114520. PMID: **33741328.** PMCID: In Progress.

   Status of Publication: Published

   Acknowledgement of federal support: Yes

4. Widner DB, Liu C, Qingxia Z, Sharp S, Eber MR, Park SH, Files DC, **Shiozawa Y**. Activated Mast Cells in Skeletal Muscle Can be a Potential Mediator for Cancer-Associated Cachexia. ***J. Cachexia Sarcopenia Muscle***. 2021; In Press. PMID: In Progress. PMCID: In Progress.

   Status of Publication: In Press

   Acknowledgement of federal support: Yes

(2021-2022)

1. Wu K, Feng J, Lyu F, Xing F, Sharma S, Liu Y, Wu S-Y, Zhao D, Tyagi A, Deshpande RP, Pei X, Ruiz MG, Takahashi H, Tsuzuki S, Kimura T, Mo Y-Y, **Shiozawa Y**, Singh R, Watabe K. Exosomal miR-19a and IBSP cooperate to induce osteolytic bone metastasis of estrogen receptor-positive breast cancer. ***Nat Commun***. 2021;12:5196 PMID: 34465793. PMCID: PMC8408156.

   Status of Publication: Published

   Acknowledgement of federal support: No

2. Kiguchi N, Ding H, Park SH, Mabry KM, Kishioka S, **Shiozawa Y**, Romero-Sandoval EA, Peters CM, Ko M-C. Functional roles of neuromedin B and gastrin-releasing peptide in regulating itch and

pain in the spinal cord of non-human primates. ***Biochem Pharmacol***. 2022;198:1144972. PMID: 35189108. PMCID: In Progress.

Status of Publication: Published

Acknowledgement of federal support: No

3. Tafreshi NK, Pandya DN, Tichacek CJ, Budzevich MM, Wang Z, Reff JN, Engelman RW, Boulware DC, Chiappori AA, Strosberg JR, Ji H, **Wadas TJ,** El-Haddad G, Morse DL. Preclinical evaluation of [^{225}Ac]Ac-DOTA-TATE for treatment of lung neuroendocrine neoplasms. Eur J Nucl Med Mol Imaging. 2021 Oct;48(11):3408-3421. doi: 10.1007/s00259-021-05315-1. PMID: 33772332.

   Status of Publication: Published

   Acknowledgement of federal support: No

4. Tafreshi NK, Kil H, Pandya DN, Tichacek CJ, Doligalski ML, Budzevich MM, Delva NC, Langsen ML, Vallas JA, Boulware DC, Engelman RW, Gage KL, Moros EG, **Wadas TJ**, McLaughlin ML, Morse DL. Lipophilicity Determines Routes of Uptake and Clearance, and Toxicity of an Alpha-Particle-Emitting Peptide Receptor Radiotherapy. ACS Pharmacol Transl Sci. 2021;4(2):953-965. doi: 10.1021/acsptsci.1c00035. PMID: 33860213; PMCID: PMC8033749.

   Status of Publication: Published

   Acknowledgement of federal support: No

Invited reviews

(2019-2020)

Nothing to report.

(2020-2021)

1. Patel CM, **Wadas TJ**, **Shiozawa Y**. Progress in Targeted Alpha-Particle-Emitting Radiopharmaceuticals as Treatments for Prostate Cancer Patients with Bone Metastases. ***Molecules***. 2021; In Press. PMID: In Progress. PMCID: In Progress.

   Status of Publication: In Press

   Acknowledgement of federal support: Yes

(2021-2022)

1. Contino KF, Yadav H, **Shiozawa Y**. The gut microbiota can be a potential regulator and treatment target of bone metastasis. ***Biochem Pharmacol***. 2022;197:114916. PMID: 35041811. PMCID: PMC8858876.

   Status of Publication: Published

   Acknowledgement of federal support: Yes

Book

(2019-2020)

1. Park SH, **Shiozawa Y**. (2019) Genomic mutation as a potential driver of the development of bone-related cancers. In Zaidi M (Ed.), *Encyclopedia of Bone Biology*. In Press. Elsevier.

   Status of Publication: In Press

   Acknowledgement of federal support: Yes

2. **Shiozawa Y**. (2019) The roles of bone marrow-resident cells as a microenvironment for bone metastasis. In Birbrair A (Ed.), *Tumor Microenvironments in Different Organs – Part A*. In Press. Switzerland: Springer Nature.

   Status of Publication: Published

   Acknowledgement of federal support: Yes

(2020-2021)

1. Eber MR, Jimenez-Andrade JM, Peters CM, **Shiozawa Y**. (2020) A method of bone-metastatic tumor progression assessment in mice using longitudinal radiography. In Deep G (Ed.), *Cancer Biomarkers: Methods and Protocols*, Methods in Molecular Biology, In Press. New York: Humana Press. Methods Mol Biol. In Press. PMID: In Progress. PMCID: N/A.

   Status of Publication: In Press

   Acknowledgement of federal support: Yes

(2021-2022)

Nothing to report.

Presentation

(2019-2020)

1. Strowd RE, Lycan T, Thomas A, Hsu FC, Ahn C, Sangueza O, **Shiozawa Y**, Park SH, **Peters CM**, EA Romero-Sandoval, Melin SA, Sorscher S, Lesser GJ, Walker FO, Cartwright MS. Neuromuscular ultrasound for the non-invasive assessment of breast cancer patients with peripheral neuropathy from taxanes. The American Academy of Neurology 71st Annual Meeting, Philadelphia, PA, USA, May 4-10, 2019. Poster.

2. Tsuzuki S, Park S, Eber M, Widner B, Kamata Y, Kimura T, Bianchi-Frias D, Coleman I, Nelson P, Hsu F-C, **Peters C**, **Shiozawa Y**. A pain-related neuropeptide calcitonin gene-related peptide promotes bone metastatic progression of prostate cancer through p38. American Society for Bone and Mineral Research (ASBMR) 2019 Annual Meeting, Orland, FL, USA, September 20-23, 2019. Poster.

3. Park S, Eber M, Tsuzuki S, Cain R, Widner B, Kamata Y, Kimura T, Bianchi-Frias D, Coleman I, Nelson P, Hsu F-C, **Peters C**, **Shiozawa Y**. The role of the SCF/c-kit pathway in cancer-induced bone pain. American Society for Bone and Mineral Research (ASBMR) 2019 Annual Meeting, Orland, FL, USA, September 20-23, 2019. Poster.
    - **Selected as a Plenary Poster**

4. Cain R, Park SH, Eber M, Martin TJ, Parker R, Jimenez-Andrade JM, **Shiozawa Y**, **Peters C**. Characterization of a syngeneic mouse model of prostate cancer induced bone pain. Neuroscience 2019, Chicago, IL, USA, October 19-23, 2019. Poster.

(2020-2021)

1. Ding H, Kiguchi N, Park SH, Kishioka S, **Shiozawa Y**, Peters C, Ko M-C. Functional roles of neuromedin B and gastrin-releasing peptide in regulating itch and pain in the spinal cord of primates. **FASEB J**. 2030;34 (S1):03569. Experimental Biology 2020 (Cancelled, but abstract was published).

2. Eber M, Park S, Hsu F-C, **Shiozawa Y**. Osteoblasts Derived from Mouse Mandible Enhance Tumor Growth of Prostate Cancer More Than Osteoblasts Derived from Long Bone. The Cancer and Bone Society (CABS) / American Society for Bone and Mineral Research (ASBMR) Pre- Meeting, The Seed and Soil: Therapeutic Targets for Cancer in Bone, Virtual, September 9-10, 2020. e-Poster.

3. Eber M, Park S, Hsu F-C, **Shiozawa Y**. Osteoblasts Derived from Mouse Mandible Enhance Tumor Growth of Prostate Cancer More Than Osteoblasts Derived from Long Bone. American Society for

Bone and Mineral Research (ASBMR) 2020 Annual Meeting, Virtual, September 11-14, 2020. e-Poster.

4. Widner DB, Eber M, Park S, **Shiozawa Y**. Skeletal Muscle Resident Mast Cells as a Potential Novel Biomarker for Cancer-Associated Cachexia. Cancer Cachexia 2020, Virtual, September 10-11, 2020. e-Poster.

(2021-2022)

1. Li J, Hilimire T, Cheng C, Broude EV, Liu Y, Lilly M, **Shiozawa Y**, Wilding G, Roninson IB, Chen M. Inhibition of CDK8/19 Mediator kinase suppresses primary and metastatic growth of castration-resistant prostate cancer. 28th Annual PCF Scientific Retreat, Virtual, October 28-29, November 4-5, 2021. e-Poster.
2. Park S, Eber M, Widner B, Tsuzuki S, Kimura T, Cain RM, Parker R, Jimenez-Andrade JM, Ramirez-Rosas M, Husu F-C, Peters C, **Shiozawa Y**. The role of the SCF/c-Kit pathway in cancer-induced bone pain. The Cancer and Bone Society (CABS) Young Investigator Symposium, Virtual, February 15-16, 2022. Oral.
3. Wadas, TJ. Improving the kidney toxicity profile of actinium-225 radiopharmaceuticals American Chemical Society Meeting, San Diego, CA. Virtual. March 22, 2022
4. Wadas, TJ. Using polyazamacrocycle ligands to improve the zirconium-89 immuno-PET paradigm. Department of Chemistry Colloquium Series. University of Iowa, Iowa City, IA. October 15, 2021.
5. Wadas, TJ. The therapeutic potential of actinium-225 radiopharmaceuticals. College of Pharmacy Seminar Series. University of Iowa, Iowa City, IA. November 2, 2021.

Website(s) or other Internet site(s)

Nothing to report.

Technologies or techniques

Nothing to report.

Inventions, patent applications, and/or licenses

Nothing to report.

Other products

Nothing to report.

7. PARTICIPANTS & OTHER COLLABORATING ORGANIZATIONS

What individuals have worked on the project?

Name: Yusuke Shiozawa

Project Role: PI, W81XWH-19-1-0045

Researcher Identifier (e.g. ORCID ID): orcid.org/0000-0001-9814-9230

Nearest person month worked: 1.2

Contribution to Project: Dr. Shiozawa is an Assistant Professor in the Department of Cancer Biology. He has extensive experience in the study of prostate cancer bone metastasis, and will provide oversight of the entire program including development and implementation of all policies, procedures, and processes. In this role, Dr. Shiozawa will be responsible for the completion of the project and for ensuring that systems are in place to guarantee institutional compliance with US laws, including biosafety and animal research guidelines, data collection and analyses, and facilities. Dr. Shiozawa will supervise other personnel on the project to ensure timely and effective studies.

Funding Support: Department of Defense, National Cancer Institute, Matavivor, TEVA Pharmaceuticals

Name: Thaddeus Wadas

Project Role: Partnering PI, W81XWH-19-1-0046

Researcher Identifier (e.g. ORCID ID):

Nearest person month worked: 1.2

Contribution to Project: Dr. Wadas is an Associate Professor in the Department of Radiology at University of Iowa. Dr. Wadas will share oversight of the entire program with Dr. Shiozawa, including development and implementation of all policies, procedures, and processes. Dr. Wadas has a Ph.D. in Chemistry and has extensive experience in peptide chemistry, radiochemistry and developing *in vivo* studies in various tumor models as well as microPET imaging to evaluate radiopharmaceuticals. Dr. Wadas will assist Dr. Shiozawa's laboratory in radiochemistry, radiopharmaceutical-related *in vitro* experiments and all imaging data analysis. Dr. Wadas has access to all the resources and facilities needed to execute this research successfully, and his lab has successfully collaborated with the Dr. Shiozawa. Dr. Wadas will meet with Dr. Shiozawa remotely on a monthly basis to discuss progress on projects related to this Award.

Funding Support: Department of Defense, National Cancer Institute, Matavivor

Name: Christopher Peters

Project Role: Co-Investigator, W81XWH-19-1-0045

Researcher Identifier (e.g. ORCID ID):

Nearest person month worked: 0.6

Contribution to Project: Dr. Peters is an Assistant Professor in the Department of Anesthesiology. Dr. Peters' research interests are in central and peripheral mechanisms of pain chronicity including postsurgical, bone cancer and chemotherapy induced pain and neuropathy. Dr. Peters will be responsible for supervising and training personnel in evoked and non-evoked bone cancer pain behavioral assays. Dr. Peters will also assist with histological and immunohistochemical analysis of skeletal tissue as part of Aims 2. He has extensive experience with the behavioral analysis, immunohistochemistry, biochemical analysis and fluorescent, brightfield, and confocal microscopic imaging required for this project.

Funding Support: National Institutes of Health, Department of Defense

Name: Fang-Chi Hsu

Project Role: Co-Investigator, W81XWH-19-1-0045

Researcher Identifier (e.g. ORCID ID):

Nearest person month worked: 0.36

Contribution to Project: Dr. Hsu is a Professor in the Department of Biostatistical Sciences. She will work closely with Dr. Shiozawa and the team to analyze the results of the project.

Funding Support: National Institutes of Health, Department of Defense

Has there been a change in the other active support of the PD/PI(s) or senior/key personnel since the last reporting period?

Nothing to report.

What other organizations have been involved as partners?

Nothing to report.

8. SPECIAL REPORTING REQUIREMENTS:

QUAD CHARTS.

9. APPENDICES:

The original copies of manuscript are attached.

A targeted alpha particle radiopharmaceutical for bone metastatic breast cancer

BC180720

W81XWH-19-1-0045, W81XWH-19-1-0046

PI: Yusuke Shiozawa
Thaddeus Wadas

Org: Wake Forest University Health Sciences
University of Iowa

Award Amount: $299,999 (Shiozawa)
$299,999 (Wadas)

Study/Product Aim(s)

- **Aim 1: Determine the best alpha particle radiopharmaceuticals targeted to the CRLR.**
- **Aim 2: Determine the impact of CRLR-targeted alpha particle therapy on breast cancer bone metastases and cancer-induced bone pain.**

Approach

The proposed studies will develop a new therapeutic strategy for treating bone metastatic breast cancer using an alpha-particle radiopharmaceutical. This work will lay the needed foundation to develop new therapeutic targets for both cancer-induced bone pain and bone metastatic breast cancer, to decrease suffering and improve survival of breast cancer patients with bone metastases.

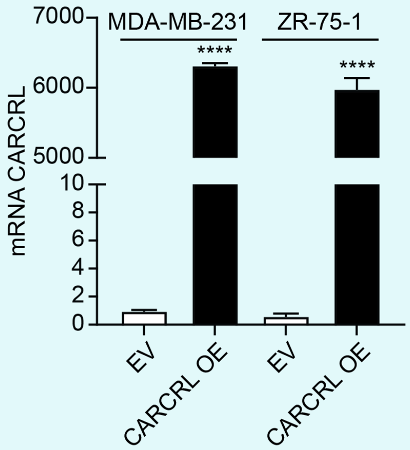

Fig. 1: The over-expression of CALCRL in breast cancer cells. CALCRL over-expression in MDA-MB-231 and ZR-75-1 cells. $^{*}p \le 0.05$, $^{****}p \le 0.0001$ vs. empty vector control (One-way ANOVA, Dunnett's multiple comparisons). Mean fold change ± SEM.

- **We created CRLR over-expressing breast cancer cells.**

Timeline and Cost

Activities	**CY**	**19**	**20**	**21**	**22**
Aim 1 (In vitro studies)		🟩	🟩		
Aim 1 (Animal studies)			🟩	🟩	
Aim 2 (Animal studies)				🟩	🟩
Estimated Budget ($K)		**$100**	**$100**	**$200**	**$200**

Updated: 03/31/2022

Goals/Milestones (Example)

CY19 Goal – Team development

✓ Set up and organize the monthly meeting

CY20 Goals – In vitro studies

☐ *In vitro* selection of ^{225}Ac-CGRP$_{27\text{-}37}$

☐ *In vivo* selection of ^{225}Ac-CGRP$_{27\text{-}37}$

CY21 Goal – Animal studies

☐ *In vivo* selection of ^{225}Ac-CGRP$_{27\text{-}37}$

☐ Determine the maximum tolerated dose of ^{225}Ac-CGRP$_{27\text{-}37}$

CY22 Goal – Animal studies

☐ Determine the maximum tolerated dose of ^{225}Ac-CGRP$_{27\text{-}37}$

☐ Determine treatment efficacy of ^{225}Ac-CGRP$_{27\text{-}37}$

Comments/Challenges/Issues/Concerns

- Personnel changes and COVID-19-related issues have negatively affected our productivity.

Budget Expenditure to Date

Projected Expenditure: $400K

Actual Expenditure: $100K (Shiozawa) + $125K (Wadas)

nature COMMUNICATIONS

ARTICLE

https://doi.org/10.1038/s41467-021-25473-y OPEN

Check for updates

Exosomal miR-19a and IBSP cooperate to induce osteolytic bone metastasis of estrogen receptor-positive breast cancer

Kerui Wu[1], Jiamei Feng[1,2], Feng Lyu[1,3], Fei Xing[1], Sambad Sharma[1], Yin Liu[1], Shih-Ying Wu[1], Dan Zhao[1], Abhishek Tyagi[1], Ravindra Pramod Deshpande[1], Xinhong Pei[1,4], Marco Gabril Ruiz[1], Hiroyuki Takahashi[5], Shunsuke Tsuzuki[5], Takahiro Kimura[5], Yin-yuan Mo[6], Yusuke Shiozawa[1], Ravi Singh[1] & Kounosuke Watabe[1]✉

Bone metastasis is an incurable complication of breast cancer. In advanced stages, patients with estrogen-positive tumors experience a significantly higher incidence of bone metastasis (>87%) compared to estrogen-negative patients (<56%). To understand the mechanism of this bone-tropism of ER$^+$ tumor, and to identify liquid biopsy biomarkers for patients with high risk of bone metastasis, the secreted extracellular vesicles and cytokines from bone-tropic breast cancer cells are examined in this study. Both exosomal miR-19a and Integrin-Binding Sialoprotein (IBSP) are found to be significantly upregulated and secreted from bone-tropic ER$^+$ breast cancer cells, increasing their levels in the circulation of patients. IBSP is found to attract osteoclast cells and create an osteoclast-enriched environment in the bone, assisting the delivery of exosomal miR-19a to osteoclast to induce osteoclastogenesis. Our findings reveal a mechanism by which ER$^+$ breast cancer cells create a microenvironment favorable for colonization in the bone. These two secreted factors can also serve as effective biomarkers for ER$^+$ breast cancer to predict their risks of bone metastasis. Furthermore, our screening of a natural compound library identifies chlorogenic acid as a potent inhibitor for IBSP-receptor binding to suppress bone metastasis of ER$^+$ tumor, suggesting its preventive use for bone recurrence in ER$^+$ patients.

---

[1] Department of Cancer Biology, Wake Forest University School of Medicine, Winston-Salem, NC, USA. [2] Mammary Department, Shuguang Hospital Affiliated to Shanghai University of Traditional Chinese Medicine, Shanghai, China. [3] Department of Breast Surgery, Henan Provincial People's Hospital, People's Hospital of Zhengzhou University, People's Hospital of Henan University, Zhengzhou, Henan, China. [4] Department of Breast Surgery, The First Affiliated Hospital of Zhengzhou University, Zhengzhou, Henan, China. [5] Department of Pathology, Jikei University School of Medicine, Minato City, Tokyo, Japan. [6] Cancer Institute, University of Mississippi Medical Center, Jackson, MS, USA. ✉email: kwatabe@wakehealth.edu

Bone metastasis is the most predominant complication of breast cancer. More than 50% of patients have bone as the first site of distant metastases, followed by lung (17%), brain (16%), and liver (6%)[1]. Ultimately, 70% of metastatic breast cancer patients experience a distant bone relapse during the course of disease[2,3]. Bone metastasis leads to a worse prognosis in breast cancer patients, with a 16-month median survival[4], and it causes many other complications. Patients develop skeletal-related events (SREs) such as severe bone pain, pathological fracture, hypercalcemia, and infiltration of the bone marrow[5]. Crosstalk between cancer cells and bone stroma cells, including mesenchymal stem cells, osteoblast cells, and osteoclast (OC) cells, play critical roles in bone metastasis[6]. Most breast cancer patients develop osteolytic lesions, which are mainly resulted from OC-mediated bone resorption rather than physical destruction by the cancer cells[7,8]. The interaction with breast cancer cells activates OC cells, induces the bone resorption[9,10], and liberates the growth factors embedded in the bone matrix, which in turn stimulate the growth of cancer cells[11]. This process is termed “the vicious cycle of bone metastases”[12]. To impede this pathway, bisphosphonate (Zoledronic Acid) and RANKL inhibitor (Denosumab) were developed as bone-targeted therapies[13,14]. However, the use of these drugs in breast cancer patients has several limitations. As to the preventive use of bone-targeted therapies for bone metastasis, while bisphosphonate showed a moderate preventive effect in postmenopausal breast cancer patients, it did not decrease the rate of bone recurrence in premenopausal patients[15]. The significant side effects, including osteonecrosis of the jaws[16], make it an unfavorable preventive regimen. Moreover, RANKL inhibitor (Denosumab) failed to prevent bone recurrence among both premenopausal and postmenopausal patients[17]. For therapeutic use, these drugs have been proven to reduce the symptoms, but not to extend the patients’ survival[18,19]. Thus, there is an urgent need for effective treatments for preventive and curative management of breast cancer bone metastasis (BCBM).

Among different subtypes of breast cancer, patients with estrogen receptors$^+$ (ER$^+$) tumors experience the most frequent bone metastases. Bone metastases account for as high as 87% of metastatic diseases among ER$^+$ breast cancer patients, while the incidence of bone metastasis is <56% among ER$^-$ breast cancer patients[20] with metastatic diseases. ER positivity is also associated with a higher rate of bone recurrence[21,22], and ER$^+$ breast cancer relapses more frequently in the bone than in other organs[23]. Although ER$^+$ breast cancer patients are regularly treated with adjuvant endocrine therapy for a long-term after surgery, cancer cells frequently develop late-onset recurrence in bone[22]. This suggests drug resistance to endocrine therapy developed in the bone-metastatic cells. The long-dormant period also deprioritizes current preventive bone-targeted therapy due to their significant side effects. Thus, it is important to identify biomarkers that can be used for predicting the risk of bone recurrence among ER$^+$ breast cancer patients. Despite the strong association between ER positivity and bone metastasis, how ER$^+$ cancer cells acquire the bone tropism remains unclear. Understanding the mechanism of such organotropism warrants major opportunities to identify specific biomarkers and preventive/therapeutic targets for ER$^+$ breast cancer bone metastasis. To survive in the bone microenvironment, breast cancer cells need to interact with bone microenvironment cells. Cell-secreted free proteins, including PTHrP, IL-1, and IL-6 were known to facilitate the communication between cancer cells and bone cells[24]. In addition to the cytokines, cancer cells are also able to interact with microenvironment cells through extracellular vesicles (EVs)[25]. These vesicles, including apoptotic bodies (ABs), microvesicles (MVs), and exosomes, encapsulate tumor-specific content, and transmit them into environmental cells and circulation. They promote tumor growth by directly transducing tumor cells[26], or affecting surrounding cells to generate metastatic niche[27–29]. As yet, no secretory factors specific to ER$^+$ breast cancer have been identified to elucidate the association between ER positivity and bone metastasis.

In the current study, to decipher the molecular mechanism by which ER$^+$ cancer preferentially metastasizes to the bone, we examined both the EVs and the free proteins secreted by ER$^+$ bone-tropic breast cancer. We found that the expression of exosomal miR-19a and IBSP is significantly upregulated in the secretion of ER$^+$ bone-tropic breast cancer cell lines, as well as in ER$^+$ breast cancer patients with bone metastases. While the miR-19a was found to be upregulated in breast cancer, its exact role in tumor progression has been poorly understood[30,31]. IBSP is a major structural protein of the bone matrix and is mainly expressed by bone cells[32]. We found that ectopic expression of both factors promoted bone metastasis in our in vivo models, suggesting both factors cooperate for ER$^+$ breast cancer bone metastasis. We also screened a natural compound library and identified chlorogenic acid (CGA) that is capable of blocking this pathway. These findings illustrate a unique pathway of how ER$^+$ breast cancer interacts with the bone microenvironment and establishes bone colonization. Furthermore, these two secretory factors would serve as prognostic markers for predicting the risk of bone metastasis in ER$^+$ breast cancer patients.

Results

Bone-metastatic ER$^+$ breast cancer cells secrete miR-19a and IBSP. Considering the importance of cell–cell communication in bone metastasis, ER$^+$ cells may shed secretory factors in the bone microenvironment to exert strong bone tropism. To test this hypothesis, we examined both EVs and proteins secreted from bone-tropic breast cancer cells. Small non-coding RNA is known to be selectively transported and enriched in EVs[33,34], suggesting its importance as a disease regulator and feasible biomarker. Thus, we compared the transcriptome profiles of miRNA in EVs isolated from MCF7BoM2, a previously reported organotropic ER$^+$ breast cancer cell line that prefers bone colonization[35], with the EVs from its parental cell line MCF7 (Fig. 1a). We made sure that the increased bone metastasis rate of the MCF7BoM2 line was not due to an alteration in the cell growth ability, as implantation of MCF7 and MCF7BoM2 into the mammary fat pads generated primary tumors with similar sizes and weights (Supplementary Fig. 1a–d). We found 157 miRNAs that were significantly upregulated in the EVs from MCF7BoM2. To validate the clinical relevance of these exosomal miRNAs, we examined whether they are secreted into the blood of ER$^+$ patients using the cohort data set of the circulating miRNA profiles from 23 ER$^+$ breast cancer patients and 22 healthy donors (Fig. 1a). Among the 157 miRNAs, three of them (miR-19a, miR-133b, and miR-576-5p) were found to be significantly upregulated in the blood of ER$^+$ breast cancer patients. Kaplan–Meier survival analyses were performed to investigate the association between these three miRNAs with metastatic events, and only miR-19a was found to be positively correlated with metastatic disease in ER$^+$ breast cancer patients (Fig. 1b). There is no difference in metastatic incidence between ER$^-$ breast cancer patients with or without elevated miR-19a expression (Fig. 1b), and both miR-133b and miR-576-5p are not significantly associated with metastasis in either ER$^+$ or ER$^-$ patients (Supplementary Fig. 2a). We also compared the ER$^+$ breast cancer tissue from bone-metastatic lesions with ER$^+$ primary breast cancer tissue from breast cancer patients without recurrence for 10 years, and with brain and lung metastatic lesions from ER$^+$ breast cancer patients with visceral metastases

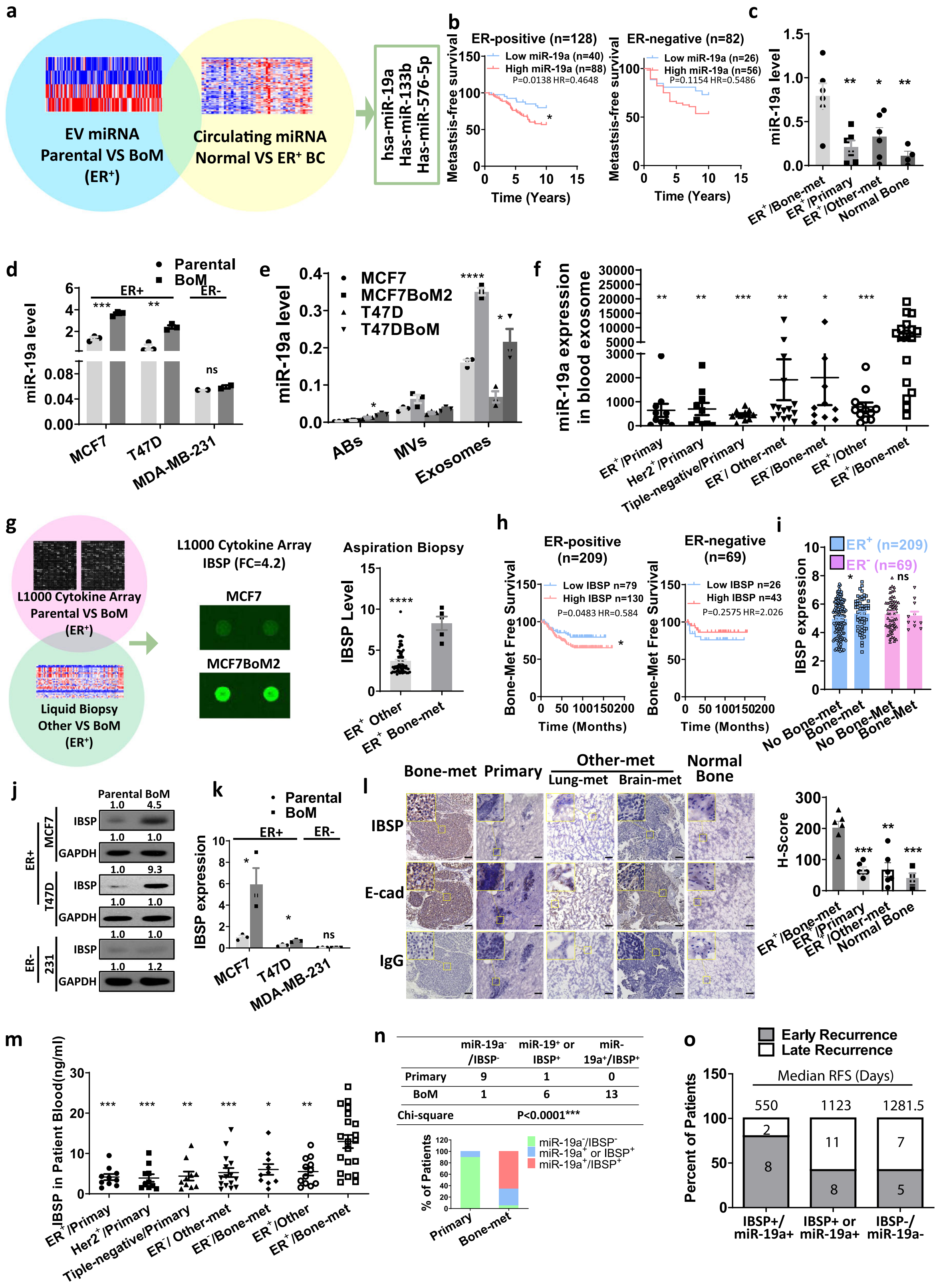

only, as well as with normal bone tissue. It was found that miR-19a is indeed only increased in bone-metastatic tissues (Fig. 1c). To validate the specificity of miR-19a associated with ER$^+$ tumor, we established another ER$^+$ bone-tropic cell line, T47DBoM. Similar to MCF7BoM2, T47DBoM generated comparable size and weight of primary tumors when implanted in the mammary fat pads. On the other hand, T47DBoM caused more aggressive bone metastases when it was implanted intravenously (Supplementary Fig. 1e–h). We examined the expression of miR-19a in ER$^+$ and ER$^-$ cancer cell lines and found that the ER$^+$ bone-tropic breast cancer cells, MCF7BoM2 and T47DBoM, have a higher endogenous expression of miR-19a compared to the parental cell lines, MCF7 and T47D (Fig. 1d). On the other hand, the expression of miR-19a did not show any difference in the bone-

Fig. 1 Bone-metastatic ER^{+} breast cancer cells secrete miR-19a and IBSP. a EVs were prepared from the conditioned medium of bone-metastatic cell line MCF7BoM2 and the parental cell line MCF7, followed by extraction of RNA. They were then subjected to miRNA profiling by GeneAtlas miRNA Array. Using the criteria of FDR < 0.05 and Fold change > 1.3, 156 miRNAs were selected for further study. These miRNAs were then examined whether they are secreted in the blood of ER^{+} patients using the cohort data set (GSE41922) of the circulating microRNA profiles between 23 ER^{+} breast cancer (BC) patients and 22 healthy donors (Normal). Three miRNAs (miR-19a. miR-133b, miR-576-5p), were found to be significantly upregulated (FDR < 0.05 and logFC > 0.5) in the blood of breast cancer patients. BoM, bone metastatic. **b** Kaplan–Meier analysis of miR-19a was performed between breast cancer patients with low miR-19a and high miR-19a expression using GSE22220. **c** RNA from bone-met(metastatic) lesions ($n = 6$), primary tumors ($n = 6$), lung and brain lesions ($n = 6$) of ER^{+} breast cancer patients, and normal bones ($n = 4$) was extracted and miR-19a expression was examined by Taqman-PCR. A two-sided student's t-test was performed (Primary vs Bone-met, $p = 0.0047$; Other-met vs Bone-met, $p = 0.0249$; Normal Bone vs Bone-met, $p = 0.0059$). Data are presented as mean values ± SEM. **d** The expression of miR-19a in parental cell lines (MCF7, T47D, and MDA-MB-231) and bone-tropic cell lines (MCF7BoM2, T47DBoM, and 231BoM-1833) were assayed by Taqman PCR. Two-sided student's t-tests were performed between parental groups and bone-metastatic (BoM) groups. $p = 0.0003$ (MCF7 vs MCF7BoM2, $n = 3$), $p = 0.0028$ (T47D vs T47DBoM, $n = 3$), $p = 0.1996$ (MDA-MB-231 vs 231BoM-1833, $n = 2$). Data are presented as mean values ± SEM. **e** The expressions of miR-19a in ABs, MVs, and exosomes from the parental cell lines (MCF7 and T47D) as well as their bone-tropic variants (MCF7BoM2 and T47DBoM) were examined by Taqman PCR. Two-sided student's t-tests were performed between parental groups and bone-metastatic (BoM) groups, $n = 3$ in each group. $p = 0.0408$ (ABs, T47D vs T47DBoM), $p < 0.0001$ (Exosomes, MCF7 vs MCF7BoM2), $p = 0.0167$ 0001 (Exosomes, T47D vs T47DBoM). Data are presented as mean values ± SEM. **f** Exosomes were isolated from the serum of breast cancer patients and the expression of miR-19a was compared among seven groups: (i) ER^{+} ($n = 10$), (ii) Her2^{+} ($n = 10$), and (iii) triple-negative ($n = 10$) breast cancer patients who were recurrence-free for 10 years, and (iv) ER^{-} breast cancer patients with visceral metastases ($n = 15$), (v) ER^{-} breast cancer patients with bone metastasis ($n = 10$), (vi) ER^{+} breast cancer patients with visceral metastases ($n = 12$) and ER^{+} breast cancer patients with bone metastasis ($n = 20$). Two-sided student's t-tests were performed to compare the miR-19a expression between the ER^{+}/Bone-met group with each of the other groups. $p = 0.0012$, 0.003, 0.0008, 0.0036, 0.016, and 0.0005 from left to right. Data are presented as mean values ± SEM. **g** Cytokine/growth factor profiling was performed on conditioned media from MCF7 and MCF7BoM2 using L1000 array (Raybiotech), and 49 upregulated cytokines (fold change > 3) were selected. This list was cross-examined with gene profiles of the ER^{+} breast cancer biopsy database (GSE56493). Genes upregulated (FDR < 0.05 and fold change > 1.2) in biopsy of bone metastasis ($n = 5$) compared to other sites ($n = 75$) were selected. IBSP in conditioned media, as well as in ER^{+} breast cancer biopsy from the bone lesion and other sites (GSE56493, $p < 0.0001$, presented as mean values ± SEM) were presented. **h** Kaplan–Meier analyses were performed for the association between IBSP expression and bone metastasis-free survival among 209 ER^{+} breast cancer patients and 69 ER^{-} breast cancer patients using GSE2034. **i** The IBSP expression was compared between ER^{+} breast cancer patients with ($n = 57$) or without ($n = 152$) bone metastasis ($p = 0.04625$, two-sided student's t-test), as well as between ER^{-} breast cancer patients with ($n = 11$) or without ($n = 58$) bone metastases ($p = 0.6944$, two-sided student's t-test). Data are presented as mean values ± SEM. **j** Western blot analysis for IBSP expression in MCF7 and MCF7BoM2, T47D and T47DBoM, MDA-MB-231 and 231BoM-1833. Quantification of the bands was performed using the ImageJ program and the value was normalized to that of control (left panel). **k** PCR analysis for IBSP expression was performed in MCF7 and MCF7BoM2 ($p = 0.0341$), T47D and T47DBoM ($p = 0.0120$), MDA-MB-231 and 231BoM-1833 ($p = 0.3494$), $n = 3$ in all groups. Two-sided student's t-tests were used in each pair of comparisons. Data are presented as mean values ± SEM. **l** IBSP was examined by IHC on bone lesions ($n = 6$), primary breast cancer tissue without recurrence for 10 years ($n = 6$), brain and lung lesions ($n = 6$) and normal bones ($n = 4$). The staining was quantified by H-score assessment and compared by the two-sided student's t-test. $p = 0.0002$ (Primary vs Bone-met); $p = 0.0014$ (Other-met vs Bone-met); $p = 0.0006$ (Normal Bone vs Bone-met). Data are presented as mean values ± SEM. E-cad (E-cadherin) was stained as the marker of breast cancer cells. Rabbit IgG was used as isotype control. Scale bar, 100 μm. **m** ELISA was performed to quantify the IBSP level in the serum of ER^{+} ($n = 10$), Her2^{+} ($n = 10$) and triple-negative ($n = 10$) breast cancer patients without recurrence for 10 years, and ER^{-} breast cancer patients with visceral metastases ($n = 15$), ER^{-} breast cancer patients with bone metastasis ($n = 10$), ER^{+} breast cancer patients with visceral metastases ($n = 12$) and ER^{+} breast cancer patients with bone metastasis ($n = 20$). Two-sided student's t-tests were performed to compare the miR-19a expression between the ER^{+}/Bone-met group with each of the other groups. $p = 0.0009$, 0.0009, 0.0016, 0.0010, 0.0101, and 0.0024 from left to right. Data are presented as mean values ± SEM. **n** ER^{+} breast cancer patients with or without bone metastases were separated into three groups according to the serum levels of IBSP and exosomal miR-19a, including miR-19a low/IBSP low group (miR-19a^{-}/IBSP^{-}), miR-19a low/IBSP high or miR-19a high/IBSP low group (miR-19^{+} or IBSP^{+}) and miR-19a high/IBSP high group (miR-19a^{+}/IBSP^{+}). The percentage in each group was calculated and plotted as the bar graph. The chi-square test was performed. **o** ER^{+} breast cancer patients with recurrent disease were selected from TCGA. Patients with early recurrence (<1000 days) and late recurrence (≥1000 days) were separated into three groups: miR-19a low/IBSP low group (miR-19a^{-}/IBSP^{-}), miR-19a low/IBSP high or miR-19a high/IBSP low group (miR-19^{+} or IBSP^{+}) and miR-19a high/IBSP high group (miR-19a^{+}/IBSP^{+}). The percentage of patients and the median RFS (recurrence-free survival) days in each group were calculated.

tropic triple-negative cell line derived from MDA-MB-231[36] (Fig. 1d). To examine whether free or vesicle-encapsulated miRNAs are the major source of secreted miR-19a, we treated the conditioned medium from MCF7BoM2 with RNase. The RNase treatment did not degrade the secreted miR-19a from breast cancer cells, suggesting that they are protected in the membrane vesicles (Supplementary Fig. 2b). This finding is consistent with the previous report that the majority of miRNA in serum is encapsulated by EVs[37,38]. EVs include ABs, MVs and exosomes. To further clarify the source of EV-derived miR-19a, we examined the miR-19a expression in these three components of EVs from MCF7 and T47D as well as their bone-tropic variants. After confirming the purity of the isolated vesicles by nanoparticle tracking analysis (NTA), electron microscope (EM), as well as a western blot (Supplementary Fig. 2c, d), the expression of miR-19a in these vesicles, were examined by Taqman PCR. We found that miR-19a is most highly expressed in exosomes compared to other EVs (Fig. 1e). Importantly, there is a strong upregulation of miR-19a in the exosomes from ER^{+} bone-metastatic variants, MCF7BoM2 and T47DBoM (Fig. 1e), compared to their parental cell lines. However, ER^{-} 231BoM showed only a negligible increase of miR-19a in the exosomes (Supplementary Fig. 2e). Next, we examined whether the increase of exosomal miR-19a can be detected in the serum of ER^{+} breast cancer patients with bone metastases. Strikingly, ER^{+} breast cancer patients with bone metastasis are significantly associated with higher expression of exosomal miR-19a in serum (Fig. 1f). It should be noted that the expression of exosomal miR-19a remained low in the patients with primary breast cancer with no recurrence within 10 years. We also did not observe any increase in exosomal miR-19a in the serum of ER$^-$ breast cancer patients at advanced stages nor in ER$^+$ patients with visceral metastases but with no bone involvement (Fig. 1f). These data suggest that miR-19a is specifically upregulated in both endogenous and exosomal levels of ER$^+$ bone-tropic breast cancer cells.

We also examined secreted proteins and cytokines from ER$^+$ bone-tropic breast cancer cells. By performing L1000 cytokine array analysis, 1000 secreted proteins were examined in the conditioned medium from MCF7 and MCF7BoM2, and 49 proteins were found to be upregulated in the cell culture media from MCF7BoM2. Among these 49 proteins, IBSP was the only significantly upregulated gene in the aspiration biopsy from bone-metastatic lesions of ER$^+$ breast cancer patients, compared to the biopsy samples from other sites (Fig. 1g). IBSP is a major structural protein of the bone matrix. It is synthesized by skeletal-associated cell types as a secreted protein, and is able to bind to calcium and hydroxyapatite via its acidic amino acid clusters[39]. In breast cancer, we observed cancer cell-specific upregulation of IBSP, while the paired normal breast epithelial cells did not express IBSP (Supplementary Fig. 2f). This finding suggests a possible role of IBSP in breast cancer progression. Since many cytokines were previously reported to bind to the surface of EVs, we also looked at the membrane fractions of EVs by western blot (Supplementary Fig. 2g), but IBSP was not detected. We also performed immunostaining of IBSP and CD63 for the exosomes isolated from MCF7BoM2, and found that only CD63 but not IBSP was detected on the surface of exosomes (Supplementary Fig. 2h). Thus, we concluded that IBSP in the extracellular region is mainly in the form of free secreted protein. To further clarify the connection between IBSP and bone metastasis of ER$^+$ breast cancer, we performed Kaplan–Meier analyses among 278 breast cancer patients. IBSP was found to be positively correlated with bone metastasis only in ER$^+$ breast cancer patients, but not in ER$^-$ breast cancer patients (Fig. 1h). There is an increase in IBSP expression in the bone-metastatic group compared to the non-bone-metastatic group among ER$^+$ breast cancer patients, but not among ER$^-$ breast cancer patients (Fig. 1i). We also verified that ER$^+$ bone-metastatic cell lines have higher expression of IBSP compared to the parental cell lines. The PCR and western blot analyses confirmed the upregulation of IBSP in MCF7BoM2 and T47DBoM, but not in ER$^-$ bone-metastatic cell line 231BoM (Fig. 1j, k). When ER$^+$ breast cancer tissue from bone lesions was compared with ER$^+$ primary breast cancer tissue from patients with no recurrence within 10 years, and with brain and lung metastatic lesions from ER$^+$ breast cancer patients with visceral metastases only, as well as with normal bone tissue, IBSP was found to be significantly increased in bone-metastatic tissues (Fig. 1l). Next, we examined whether the increase of IBSP can be detected in the serum of ER$^+$ breast cancer patients with bone metastases. A significant upregulation of IBSP protein in the serum of ER$^+$ breast cancer patients with bone metastasis was detected (Fig. 1m), but not in the serum of patients with only primary breast cancer, advanced ER$^-$ breast cancer patients, or ER$^+$ breast cancer patients with visceral metastases other than bone.

Our data (Fig. 1a–m) suggest both miR-19a and IBSP are positively related to bone metastasis of ER$^+$ cancer cells. However, how they are associated with bone metastasis remains unknown. We further investigated whether miR-19a and IBSP are mutually related to bone metastasis of ER$^+$ breast cancer cells. We combined the results from Fig. 1f with Fig. 1m, and stratified the patients into three groups: both miR-19a and IBSP low, miR-19a or IBSP high, both miR-19a and IBSP high. Strikingly, ER$^+$ breast cancer patients with bone metastasis are significantly associated with higher expression of both IBSP and miR-19a. Upregulation of sole factor led to a negligible, but not significant increase of the bone-metastatic incidence, suggesting a possible cooperative role of these two factors in bone metastasis of ER$^+$ breast cancer cells (Fig. 1n). Next, we examined the expression of miR-19a and IBSP in breast cancer patients using the TCGA database. Among 41 ER$^+$ breast cancer patients with recurrence, IBSP and miR-19a could predict the recurrence risk as the majority of patients with high levels of both factors experienced earlier recurrence within 1000 days (Fig. 1o). The median recurrence-free survival (RFS) time of patients with high levels of both miR-19a and IBSP is only 550 days, while the median RFS time of patients with high expression of either miR-19a or IBSP and patients with low levels of both miR-19a/IBSP are 1123 days and 1281.5 days, respectively. These results indicate that miR-19a and IBSP are positively associated with bone metastasis, and they serve as biomarkers for a higher risk of bone metastasis when they are both upregulated in ER$^+$ breast cancers.

Both IBSP and miR-19a are essential for bone metastasis of ER$^+$ breast cancer. To test whether both miR-19a and IBSP are required for bone metastasis of ER$^+$ breast cancer cells, we ectopically expressed IBSP and miR-19a in MCF7, and established stable overexpression cell lines (Supplementary Fig. 3a–d). Ectopic expression of miR-19a did not alter the level of IBSP, and vice versa, indicating there is no regulatory network involved between IBSP and miR-19a. Neither miR-19a nor IBSP could induce any change of exosome production (Supplementary Fig. 3e), proliferation, or migration of the cells in vitro (Supplementary Fig. 3f, g). Intra-mammary fat pad injection of MCF7 with miR-19a and/or IBSP forced-expression did not induce any difference in tumor growth in vivo (Fig. 2a, b). Strikingly, ectopic expression of both miR-19a and IBSP together in MCF7 led to a significant increase in bone metastasis in the xenograft model with the intracardiac injection of cancer cells (Fig. 2c). Nonetheless, miR-19a or IBSP alone did not increase the incidence of bone metastasis. These data suggest miR-19a and IBSP promote bone metastasis through the tumor microenvironment instead of affect cancer cells directly. Since IBSP is known to regulate bone turnover by binding to integrin αVβ3 receptor on the surface of OC cells[40], we examined the bone densities of mice implanted with the breast cancer cells. We found that ectopic expression of both IBSP/miR-19a resulted in a significant decrease in bone density in the tumor lesions (Fig. 2d). We also quantified the total area of TRAP$^+$ OC surface and its percentage of total bone surface area (OC.S/BS%) in the tumor-bearing bones and found that synchronous overexpression of miR-19a and IBSP significantly increased the osteoclastogenesis (Fig. 2e). We then repeated this experiment in another ER$^+$ cell line, T47D. Both IBSP and miR-19a were ectopically introduced into T47D (Supplementary Fig. 3h, i), and stable overexpression cell lines had been established (Supplementary Fig. 3j, k) before the cells were inoculated into mouse tibia. Similar to MCF7, ectopic expression of both miR-19a and IBSP resulted in increased tumor burden in the bones (Fig. 2f), while discrete expression of miR-19a or IBSP alone did not affect the tumor growth. Bone lesions of T47D/IBSP/miR-19a presented decreased bone densities (Fig. 2g) and increased OC activities (Fig. 2h). These results indicate that miR-19a and IBSP work together to induce osteolytic bone metastasis in ER$^+$ breast cancer patients, though not directly affecting cancer cell growth or motility.

miR-19a promotes osteolytic bone metastasis. Because both miR-19a and IBSP are necessary to promote the bone metastasis of ER$^+$ breast cancer cells, we investigated how each of them contributes to the bone-tropic metastasis of cancer cells. MiR-19a,

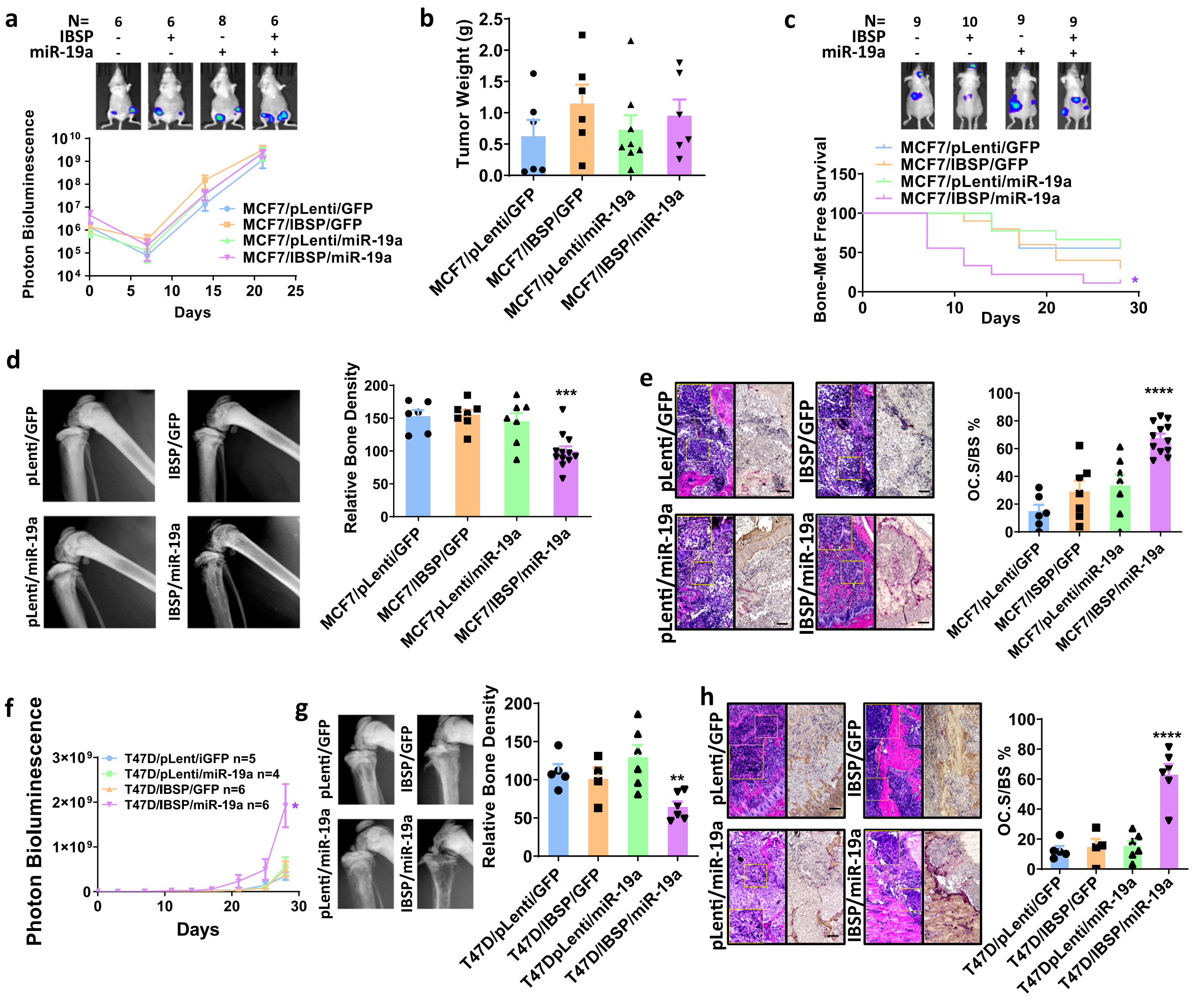

Fig. 2 Both IBSP and miR-19a are essential for bone metastasis of ER$^+$ breast cancer. **a** miR-19a and/or IBSP were ectopically expressed in MCF7, and they were transplanted into mammary fat pads of female nude mice. The growth of the tumor was monitored by measuring the luciferase activity by IVIS Bioimager. $p = 0.3110$ (MCF7/pLenti/GFP vs MCF7/IBSP/miR-19a; $n = 6$ vs 6), $p = 0.2649$ (MCF7/pLenti/GFP vs MCF7/IBSP/GFP; $n = 6$ vs 6), $p = 0.4739$ (MCF7/pLenti/GFP vs MCF7/pLenti/miR-19a; $n = 6$ vs 8). Data are presented as mean values ± SEM. **b** At day 21, tumors were removed from the mammary fat pad and their weights were measured. $p = 0.3971$ (MCF7/pLenti/GFP vs MCF7/IBSP/miR-19a; $n = 6$ vs 6), $p = 0.2178$ (MCF7/pLenti/GFP vs MCF7/IBSP/GFP; $n = 6$ vs 6), $p = 0.7632$ (MCF7/pLenti/GFP vs MCF7/pLenti/miR-19a; $n = 6$ vs 8). Data are presented as mean values ± SEM. **c** miR-19a and/or IBSP were ectopically expressed, and they were transplanted into female nude mice via intracardiac injection. The incidence of bone metastasis was monitored by measuring the luciferase activity by IVIS Bioimager. Log-rank (Mantel–Cox) test was performed to calculate the *p*-value. $p = 0.0105$ (MCF7/pLenti/GFP vs MCF7/IBSP/miR-19a), $p = 0.3982$ (MCF7/pLenti/GFP vs MCF7/IBSP/GFP), $p = 0.9230$ (MCF7/pLenti/GFP vs MCF7/pLenti/miR-19a). **d** The legs of mice were imaged by X-ray and the bone density was measured by ImageJ. $p = 0.0007$ (MCF7/pLenti/GFP vs MCF7/IBSP/miR-19a; $n = 6$ vs 12), $p = 0.8621$ (MCF7/pLenti/GFP vs MCF7/IBSP/GFP, $n = 6$ vs 7), $p = 0.6397$ (MCF7/pLenti/GFP vs MCF7/pLenti/miR-19a, $n = 6$ vs 7). Two-sided student's *t*-tests were performed. Data are presented as mean values ± SEM. **e** TRAP staining was performed in tumor-bearing bones from mice. The total OC surface area relative to the bone surface area was measured by ImageJ, then calculated and compared among different groups. H&E staining of the same field was shown together with the TRAP staining. Scale bar, 100 μm. $p < 0.0001$ (MCF7/pLenti/GFP vs MCF7/IBSP/miR-19a, $n = 6$ vs 12), $p = 0.1598$ (MCF7/pLenti/GFP vs MCF7/IBSP/GFP, $n = 6$ vs 7), $p = 0.0867$(MCF7/pLenti/GFP vs MCF7/pLenti/miR-19a, $n = 6$ vs 7). Two-sided student's *t*-tests were performed. Data are presented as mean values ± SEM. **f** miR-19a and/or IBSP were ectopically expressed, and they were transplanted into female nude mice via intra-tibia injection. The growth of tumor in bone was monitored by measuring the luciferase activity by IVIS Bioimager. $p = 0.0175$ (T47D/pLenti/GFP vs T47D/IBSP/miR-19a), $p = 0.4877$ (T47D/pLenti/GFP vs T47D/IBSP/GFP), $p = 0.3305$ (T47D/pLenti/GFP vs T47D/pLenti/miR-19a). Data are presented as mean values ± SEM. **g** The legs of mice were imaged by X-ray and the bone density was measured by ImageJ. $p = 0.0034$ (T47D/pLenti/GFP vs T47D/IBSP/miR-19a $n = 5$ vs 6), $p = 0.5750$ (T47D/pLenti/GFP vs T47D/IBSP/GFP, $n = 5$ vs 4), $p = 0.3809$ (T47D/pLenti/GFP vs T47D/pLenti/miR-19a, $n = 5$ vs 6). Two-sided student's *t*-tests were performed. Data are presented as mean values ± SEM. **h** TRAP staining was performed in tumor-bearing bones from the mice. The OC surface relative to the bone surface was calculated and compared among different groups. H&E staining of the same field was shown together with the TRAP staining. Scale bar, 100 μm. $p = 0.0001$ (T47D/pLenti/GFP vs T47D/IBSP/miR-19a, $n = 5$ vs 6), $p = 0.7711$ (T47D/pLenti/GFP vs T47D/IBSP/GFP, $n = 5$ vs 4), $p = 0.5701$ (T47D/pLenti/GFP vs T47D/pLenti/miR-19a, n = 5 vs 6). Two-sided student's *t*-tests were performed. Data are presented as mean values ± SEM.

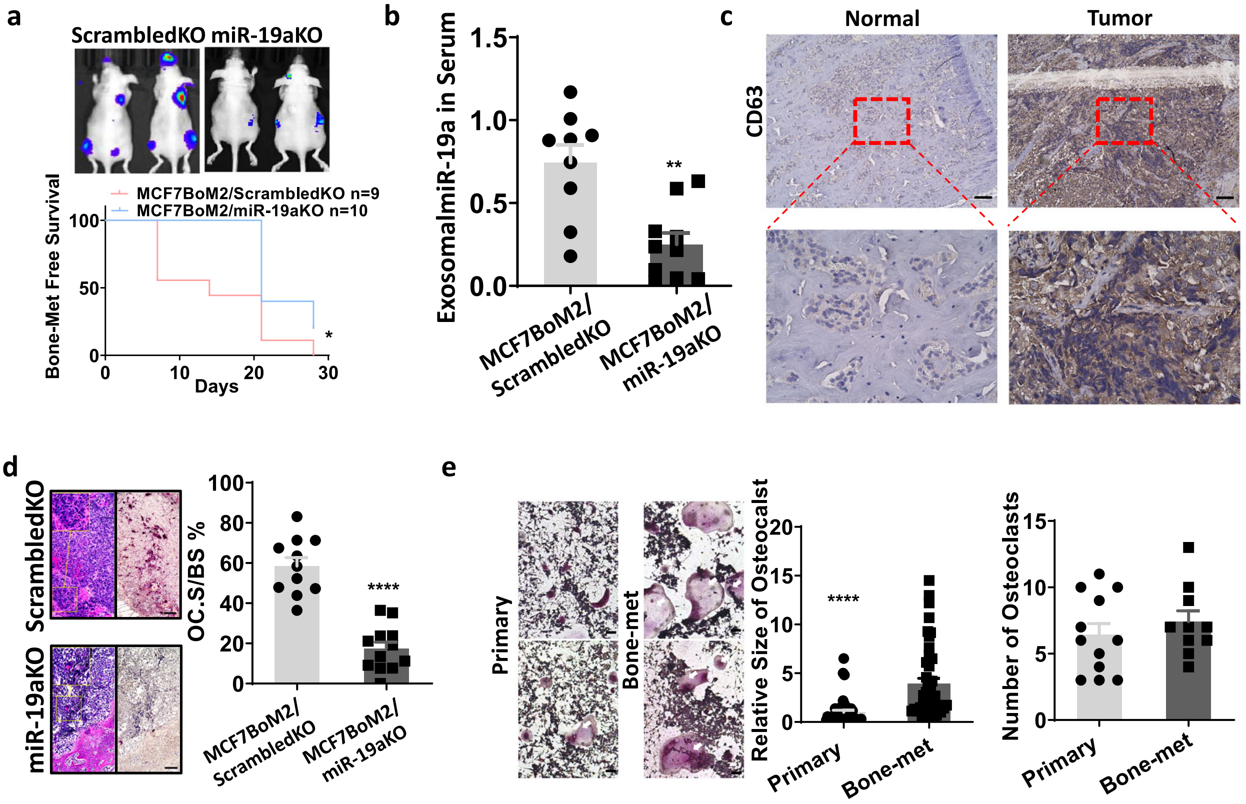

Fig. 3 miR-19a promotes osteolytic bone metastasis. a MCF7BoM2/ScrambledKO and MCF7BoM2/miR-19aKO were transplanted into female nude mice via intracardiac injection. The growth of bone metastasis was monitored by measuring the luciferase activity by IVIS Bioimager. Log-rank (Mantel–Cox) test was performed to calculate the *p*-value ($p = 0.0109$). **b** At the endpoint (day 28), mice were sacrificed and the expression of exosomal miR-19a from serum was examined by Taqman. A two-sided student's *t*-test was performed ($p = 0.0011$, $n = 9$ vs 10). Data are presented as mean values ± SEM. **c** Representative figures of the expression of exosomal marker CD63 in normal bone and tumor-bearing bone from the mice. Scale bar, 100 µm. **d** TRAP staining for osteoclast cells in tumor-bearing bones from the mice transplanted with MCF7BoM2/ScrambledKO or MCF7BoM2/miR-19aKO. OC surface relative to the bone surface was calculated and compared. H&E staining of the same field was shown together with the TRAP staining. Scale bar, 100 µm. A two-sided student's *t*-test was performed ($p = 0.00000014$, $n = 11$ vs 12). Data are presented as mean values ± SEM. **e** Exosomes from the serum of ER^+ breast cancer patients with ($n = 10$) or without ($n = 12$) bone metastasis were isolated. The harvested exosomes were incubated with mouse bone marrow-derived monocytes. After 1 week, the cells were fixed and TRAP staining was performed. The size ($p = 0.0000039$) and number ($p = 0.4254$) of differentiated OC were quantified and compared. Scale bar, 100 µm. Two-sided student's *t*-tests were performed. Data are presented as mean values ± SEM.

as a member of the OncomiR-1 family, was previously found to be upregulated in multiple malignancies[41–43]. It was also found to be expressed in breast cancer cells, although its role remains unclear[30,44]. We found both endogenous and secreted levels of miR-19a were higher in the bone-metastatic cell lines compared to the parental cell lines. However, endogenous expression of miR-19a did not affect breast cancer cells per se because the ectopic expression of miR-19a did not alter the growth or motility of cells in vitro (Supplementary Fig. 3f, g). To further clarify the role of miR-19a in bone metastasis of ER^+ breast cancer cells, we applied the CRISPR/Cas9 technology to knock out the miR-19a in MCF7BoM cells. A specific gRNA (guide RNA) was designed to target the stem-loop of miR-19a precursor so that the biogenesis of mature miR-19a was hindered. The genomic DNA cleaving ability of our gRNA targeting miR-19a was verified by the T7E1 enzyme (Supplementary Fig. 4a). Four independent clones with minimal miR-19a expression and unaltered proliferation were selected and combined to establish the stable knockout cell line (Supplementary Fig. 4b–d). When tested in vitro, we found that knockout of miR-19a did not alter the cell migration or invasion abilities (Supplementary Fig. 4e–f). However, when miR-19a knockout cells were implanted into nude mice by intracardiac injection, loss of miR-19a significantly decreased bone metastasis (Fig. 3a). These data are consistent with our previous finding that miR-19a is needed for bone-tropic metastasis of MCF7BoM2. MCF7BoM2 has a high expression of both miR-19a and IBSP. Knockout of miR-19a, but leaving IBSP alone, compromised the bone-metastatic ability of MCF7BoM2. Interestingly, when we examined the serum exosomes in the mice, we found that the knockout of miR-19a significantly decreased exosomal miR-19a in the serum (Fig. 3b). This finding suggests that serum exosome could represent the dynamic changes of breast cancer cells. These results are also in agreement with the previous finding that miR-19a could not induce the intrinsic change of cancer motility. Accordingly, we investigated whether exosomal miR-19a could promote bone metastasis by remodeling environmental cells in a paracrine manner instead of directly affecting cancer cells. The tumor lesion in the bone exhibited abundant expression of exosomal marker CD63 (Fig. 3c), implying exosome activity in the microenvironment. Since we found an aberrant osteolytic change in our previous data, we examined the OC in the bone lesions. There was a decrease of osteoclastogenesis in the tumor-bearing bones when miR-19a was knocked out from the cancer cells (Fig. 3d), indicating a possible role of exosomal miR-19a in promoting OC cells. To verify this hypothesis, exosomes from serum of ER$^+$ breast cancer patients with or without bone metastases were isolated and incubated with primary OC precursors. Exosomes prepared from the patients with bone metastases significantly promoted OC maturation and differentiation (Fig. 3e). These results indicate that miR-19a is involved in the osteolytic bone metastasis and exosomal miR-19a could directly promote OC activity in the bone microenvironment.

Exosomal miR-19a targets PTEN/AKT pathway to promote osteoclastogenesis. To validate our hypothesis that exosomal miR-19a promotes the activity of OC cells, we first examined whether exosomes can be directly up-taken by OC cells. OC precursor RAW264.7 cells were treated with PalmGFP-labeled exosomes derived from bone-metastatic breast cancer cells. The result indicates that exosomes from MCF7BoM2 were indeed incorporated into RAW264.7 cells 24 h after the treatment (Fig. 4a). It was reported that miR-19a targeted PTEN 3′UTR[45] and that OC differentiation and their activity were regulated by NF-κB and AKT pathways[46,47], both of which were known to be inhibited by PTEN[48,49]. Thus, it is plausible that cancer cells secrete miR-19a and suppress PTEN expression in OC cells when exosomes are internalized. The decrease of PTEN leads to activation of NF-κB and AKT pathways that promote OC cells. To test this notion, we examined whether exosomal miR-19a modulates OC activity by suppressing PTEN expression, using the 3′ UTR reporter assay. We confirmed that the miR-19a-targeted sequence on PTEN is conserved between human and mouse (Supplementary Fig. 5a, b), and found that ectopic expression of miR-19a indeed targeted PTEN, while mutation of the miR-19a binding site on PTEN 3′UTR rescued the reporter activity (Fig. 4b). Furthermore, ectopic expression of miR-19a in OC precursor cells, RAW264.7, suppressed PTEN expression and induced NF-κB and AKT pathway with increased phosphorylated P65 and AKT (Fig. 4c, d). We also examined whether increased miR-19a could promote OC differentiation of RAW264.7 by performing TRAP staining. The ectopic expression of miR-19a significantly increased the number of mature OC cells and their size (Fig. 4e). Next, we tested whether direct treatment of OC precursor cells with exosomal miR-19a, instead of lentiviral overexpression, could also induce the activation of P65 and AKT pathways. Although there was no difference in the efficiency of exosome uptake (Supplementary Fig. 5c), compared to exosomes from the parental cell line, exosomes from bone-metastatic MCF7BoM2 increased miR-19a, decreased PTEN and induced AKT, and P65 activation in mouse bone marrow monocyte (mBMM), which is the primary precursor of OC (Fig. 4f, g). In addition, exosomes from MCF7BoM2 promoted the differentiation of mBMM into OC (Fig. 4h). In a bone resorption assay, mBMMs were seeded on the bone chips and incubated with exosomes from MCF7 and MCF7BoM2. Exosomes from MCF7BoM2 exhibited significantly higher competence to induce the osteolytic activities of OC cells as shown by the increased area of resorption pit (Fig. 4i). Consistent with our finding of enriched miR-19a in exosomes, only exosomes, but not MV or AB, could induce the differentiation of OC cells (Supplementary Fig. 5d). To further investigate whether miR-19a is responsible for the OC-promoting effect of the exosomes, OC cells were incubated with exosomes isolated from MCF7BoM2/ScrabmbleKO cells or MCF7BoM2/miR-19aKO cells (Fig. 4j–m and Supplementary Fig. 6a–c). When miR-19a was knockout, exosomes were unable to deliver miR-19a into OC cells and suppress PTEN expression (Fig. 4j and Supplementary Fig. 6b). We also found that exosomes prepared from bone-metastatic breast cells with miR-19a knockout could not induce P65 and AKT activation (Fig. 4k and Supplementary Fig. 6c) and reversed the OC-promoting effect (Fig. 4l, m and Supplementary Fig. 6a). Collectively, we demonstrated that bone-metastatic cells delivered miR-19a-containing exosomes to OC precursor cells and suppressed PTEN expression. Decreased PTEN induced the activation of NF-κB and AKT signaling pathways, promoting the differentiation and osteolytic activity of OC cells. This notion was also verified by examining the effect of exosomes from MCF7 and MCF7/miR-19a cell lines on OC cells. Compared to exosomes from parental MCF7 cells, exosomes from MCF7 with ectopic expression of miR-19a significantly increased the miR-19a expression and decreased PTEN expression in both recipient RAW264.7 and mBMM cells, increased OC number, and promoted the differentiation of OC in vitro (Supplementary Fig. 6d–i).

ER$^+$ breast cancer cells secrete IBSP to recruit osteoclast precursors. Next, we examined the role of IBSP in osteolytic bone metastasis induced by miR-19a. IBSP is known to act as a ligand of integrin αVβ3 receptor that is highly expressed on the surface of OC[40]. A previous study found that IBSP knockout in mice resulted in decreased OC number in bones[40]. Integrin αVβ3 is known to be associated with OC migration and adhesion[50,51], and IBSP was previously found to be a cell-secreted protein with bone matrix binding ability[52]. Therefore, we hypothesize that IBSP secreted from the bone lodging cancer cells can recruit the OC precursors to the micro-metastatic site followed by creating an OC precursor-enriched niche. Such an environment enhances the uptake of miR-19a-containing exosomes by the OC precursors in a concentration-dependent manner. In a trans-well migration assay, we found that both MCF7BoM2 and MCF7/IBSP recruited more OC precursors to abluminal chambers compared to MCF7 (Fig. 5a), which supports our hypothesis that IBSP attracts OC precursors. We then performed the knockout of IBSP using the CRISPR-Cas9 system in MCF7BoM2. To rule out the clonal effect, three clones that showed no IBSP expression and no alteration of growth ability were selected and mixed into one heterogeneous line, MCF7BoM2/IBSPKO (Fig. 5b, c and Supplementary Fig. 7a). The knockout of IBSP expression did not alter the cell migration ability of MCF7BoM2/IBSPKO (Fig. 5d). However, the bone-metastatic ability was significantly compromised by IBSP knockout in MCF7BoM2/IBSPKO cells in the xenograft mouse model (Fig. 5e). Loss of IBSP also preserved the density of tumor-bearing bones (Fig.5f). Results from TRAP staining of the tumor-bearing tibias also suggested that the IBSP knockout led to decreased osteoclastogenesis (Fig. 5g). These results strongly support our hypothesis that IBSP recruits OC cells to the tumor lesions in the bone, which is essential for the uptake of exosomes and establishment of bone metastasis of ER$^+$ breast cancer cells.

CGA blocks cooperative function of miR-19a and IBSP in ER$^+$ BCBM. We hypothesized that cooperation between exosomal miR-19a and IBSP generates the osteolytic bone microenvironment, enabling the ER$^+$ tumor growth in the bone. Therefore, we examined the changes in bone microenvironment induced by directly injecting IBSP and exosomal miR-19a prepared from MCF7BoM2 into the tibial bone of mice every two days without tumor cell injection. This treatment resulted in a significant increase in the number of OC at the treatment site (Supplementary Fig. 7b). We also found that the DiD-labeled exosomes from MCF7BoM2 were incorporated into OC cells when they were injected into the tibial bone (Supplementary Fig. 7c). These results suggest that exosomal miR-19a and IBSP cooperatively create an osteolytic bone microenvironment. We then tested whether such change could enhance the growth of primary MCF7

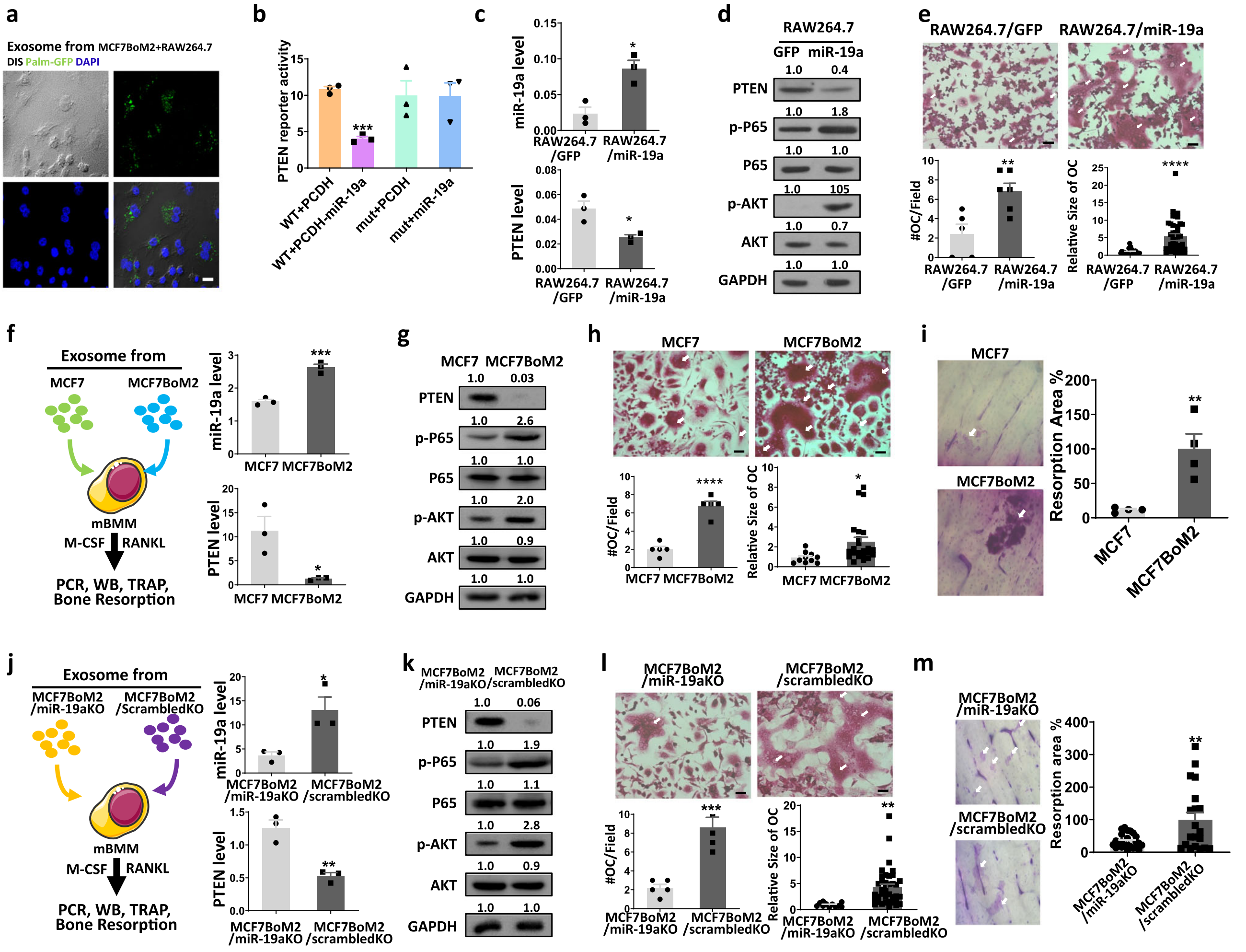

Fig. 4 Exosomal miR-19a targets PTEN/AKT pathway to promote osteoclastogenesis. **a** Exosomes were labeled with GFP by ectopic expression of PalmGFP in MCF7BoM2 cells. OC cells were then treated with the labeled exosomes. After 24 h, uptake of exosome by osteoclast cells was monitored by confocal microscope. Scale bar, 10 μm. **b** Luciferase reporter assay for the constructs containing wild-type PTEN 3′UTR or mutant PTEN 3′UTR was performed after transfecting the cells with the miR-19a expression vector. $p = 0.0001$ (WT + PCDH vs WT + PCDH-miR-19a, two-sided student's *t*-test). Data are presented as mean values ± SEM. **c** Taqman PCR for miR-19a expression ($p = 0.0131$, $n = 3$), and SYBR Green qPCR for PTEN expression ($p = 0.0232$, $n = 3$) in RAW264.7/GFP and RAW264.7/miR-19a were performed. Two-sided student's *t*-tests were performed. Data are presented as mean values ± SEM. **d** Western blot analysis for PTEN, phospho-NF-κB P65, total NF-κB P65, phospho-AKT and total AKT expression in RAW264.7/GFP and RAW264.7/miR-19a cell lines. The band intensity was quantified and normalized to that of control (left panels). **e** TRAP staining of RAW264.7/GFP and RAW264.7/miR-19a cells. On day 4, the number of differentiated osteoclasts ($p = 0.0080$, $n = 5$ vs 6) and the size of these cells ($p < 0.0001$, $n = 30$ vs 40) were measured. Two-sided student's *t*-tests were performed. Data are presented as mean values ± SEM. Scale bar, 100 μm. **f** Mouse BMMs were induced into OC cells with the treatment of exosomes and cytokines. Taqman PCR for miR-19a expression ($p = 0.0008$, $n = 3$) and SYBR Green qPCR for PTEN ($p = 0.0271$, $n = 3$) expression were performed for OC cells treated with exosomes from MCF7 and MCF7BoM2. Two-sided student's *t*-tests were performed. Data are presented as mean values ± SEM. **g** Western blot analysis for PTEN, phospho-NF-κB P65, total NF-κB P65, phospho-AKT and total AKT expression in mouse BMMs treated with exosomes from MCF7 and MCF7BoM2. The band intensity was quantified and normalized to that of control (left panels). **h** TRAP staining was performed for mouse BMMs treated with exosomes from MCF7 and MCF7BoM2. On day 4, the number of differentiated osteoclast ($p = 0.000036$, $n = 5$ vs 5) and their sizes ($p = 0.0323$, $n = 10$ vs 23) were measured. Two-sided student's *t*-tests were performed. Data are presented as mean values ± SEM. Scale bar, 100 μm. **i** Bone-resorbing activities of OC treated with exosomes from MCF7 and MCF7BoM2 were measured by the bone-resorption assay. BMMs were seeded on a bone chip and treated with exosomes and cytokines. Resorption pits were measured and compared ($p = 0.0070$, $n = 4$). Two-sided student's *t*-tests were performed. Data are presented as mean values ± SEM. **j** Taqman PCR for miR-19a expression ($p = 0.0291$, $n = 3$) and SYBR Green qPCR for PTEN expression ($p = 0.0047$, $n = 3$) were performed for mouse BMMs treated with exosomes from MCF7BoM2/miR-19aKO and MCF7BoM2/ScrambledKO. Two-sided student's *t*-tests were performed. Data are presented as mean values ± SEM. **k** Western blot analysis was performed for PTEN, phospho-NF-κB P65, total NF-κB P65, phospho-AKT, and total AKT expression in mouse BMMs treated with exosomes from MCF7BoM2/miR-19aKO and MCF7BoM2/ScrambledKO. The band intensity was quantified and normalized to that of control (left panels). **l** TRAP staining was performed for mouse BMMs that were treated with exosomes from MCF7BoM2/miR-19aKO and MCF7BoM2 /ScrambledKO. On day 4, the number of differentiated osteoclast cells ($p = 0.0005$, $n = 5$ vs 5) and their sizes were measured ($p = 0.0029$, $n = 11$ vs 38). Scale bar, 100 μm. Two-sided student's *t*-tests were performed. Data are presented as mean values ± SEM. **m** The bone-resorbing activity of OC was measured by the bone-resorption assay using BMMs that were treated with exosomes from MCF7BoM2/miR-19aKO and MCF7BoM2/ScrambledKO ($p = 0.0025$, $n = 24$ vs 20). Two-sided student's *t*-tests were performed. Data are presented as mean values ± SEM.

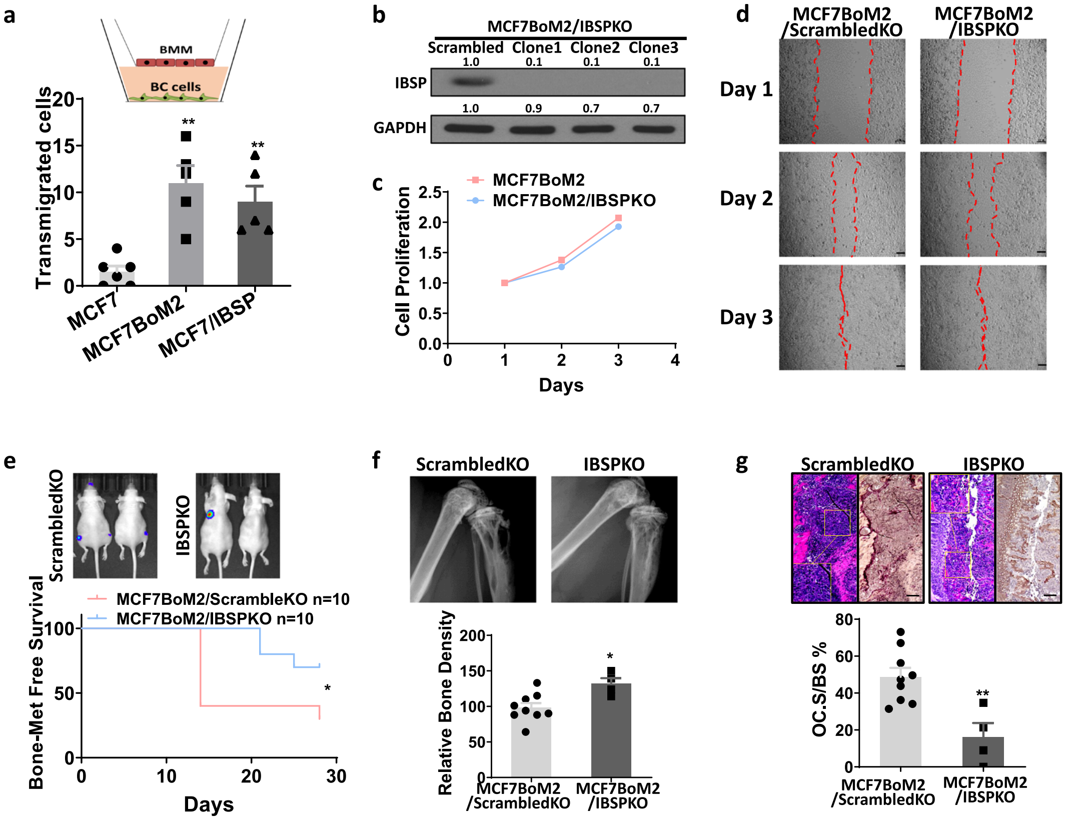

Fig. 5 ER$^+$ breast cancer cells secrete IBSP to recruit osteoclast precursors. a Trans-well migration assays were performed to measure the migration ability of BMMs towards breast cancer cells. BMMs were seeded on the luminal side and breast cancer cells (MCF7, MCF7BoM2, and MCF7/IBSP) were seeded on the abluminal chamber. Data are presented as mean values ± SEM. **b** CRISPR-Cas9 mediated knockout of IBSP in MCF7BoM2. Three knockout clones were confirmed by western blot. The band intensity was quantified and normalized to that of control (left panels). **c** The selected clones were mixed and designated as MCF7BoM2IBSPKO. Cell proliferation was measured for MCF7BoM2 and MCF7BoM2/IBSPKO by MTS assay. A two-sided student's *t*-test was performed on day 3 and $p = 0.0496$ ($n = 3$ vs 3). Data are presented as mean values ± SEM. **d** Cell migration ability of MCF7BoM2 and MCF7BoM2/IBSPKO was measured by wound-healing assay. Scale bar, 100 µm. **e** MCF7BoM2/ScrambledKO and MCF7BoM2/IBSPKO (500,000/0.1 ml PBS) were transplanted into female nude mice via intracardiac injection. The growth of bone metastasis was monitored by measuring the luciferase activity by IVIS Bioimager, and the Kaplan–Meier analysis was done for bone metastasis-free survival ($p = 0.0496$, HR = 4.101). **f** The tumor-bearing bones were imaged by X-ray, and the relative bone densities were quantified by ImageJ ($p = 0.0124$, $n = 9$ vs 4). Two-sided student's *t*-tests were performed. Data are presented as mean values ± SEM. **g** OC surface relative to the bone surface was calculated and compared after TRAP staining. H&E staining of the same field was shown together with the TRAP staining ($p = 0.0036$, $n = 9$ vs 4). Two-sided student's *t*-tests were performed. Data are presented as mean values ± SEM. Scale bar, 100 µm.

cells in the mice's tibias (Fig. 6a). MCF7 cells were transplanted into the tibial bone. At the same time, both IBSP and exosomes from MCF7BoM2 were given every two days into the tumor site. To evaluate the roles of exosomal miR-19a, exosomes from MCF7BoM2/miR-19aKO were used as a control. We found that the injection of miR-19a-containing exosomes and IBSP significantly promoted tumor growth (Fig. 6a) in the bones, which resulted in a decrease in bone density (Fig. 6b) and an increase in OC activity (Fig. 6c). These results suggest the indispensable roles of exosomal miR-19a and IBSP in bone metastasis of ER$^+$ breast cancer cells. Consistent with these results, knockout of miR-19a or IBSP from MCF7BoM2 significantly decreased the bone-metastatic ability of cancer cells, while ectopic expression of each factor alone did not rescue the effect. (Supplementary Fig. 7d, e).

Because IBSP plays a critical role in recruiting OC precursor cells and enabling the delivery of exosomal miR-19a to promote bone metastasis, targeting IBSP could be an effective preventive strategy to block the IBSP/exosome pathway, and decrease the risks of bone metastasis/recurrence. Therefore, we used a competitive binding assay to screen a natural compounds library aiming at identifying compound(s) that block the binding of IBSP with its receptor integrin αVβ3. In this assay, we layered integrin αVβ3 on the bottom of wells, followed by adding IBSP in the presence or absence of 176 natural compounds. The binding of IBSP protein to integrin αVβ3 was quantified using an enzyme-tagged antibody to measure the inhibitory effect of natural compounds. We found that Chlorogenic acid (CGA) most significantly inhibited the binding of IBSP to integrin αVβ3 (Fig. 6d). To ensure that the inhibitory ability is not a result of direct interaction between the natural compound and the enzyme tag, we repeated our screening with a different enzyme-tagged antibody (Supplementary Fig. 8a). In a chemotaxis assay, we found that CGA significantly blocked the recruitment of OC precursors (mBMM) by IBSP (Fig. 6e). On the other hand, CGA did not directly suppress the growth or migration of cancer cells (Supplementary Fig. 8b, c). These data indicate CGA is a competent inhibitor of the recruitment of OC by IBSP. Importantly, in the xenograft model, both CGA and exosome inhibitor GW4869 effectively suppressed ER$^+$ breast cancer bone metastasis (Fig. 7a), while no notable side effects were observed with the mice received CGA treatment (Supplementary Fig. 8d, e). It should be noted that the inhibitory effect of CGA on bone metastasis is not a result of its effect on tumor cell growth, because CGA did not affect the primary tumor growth

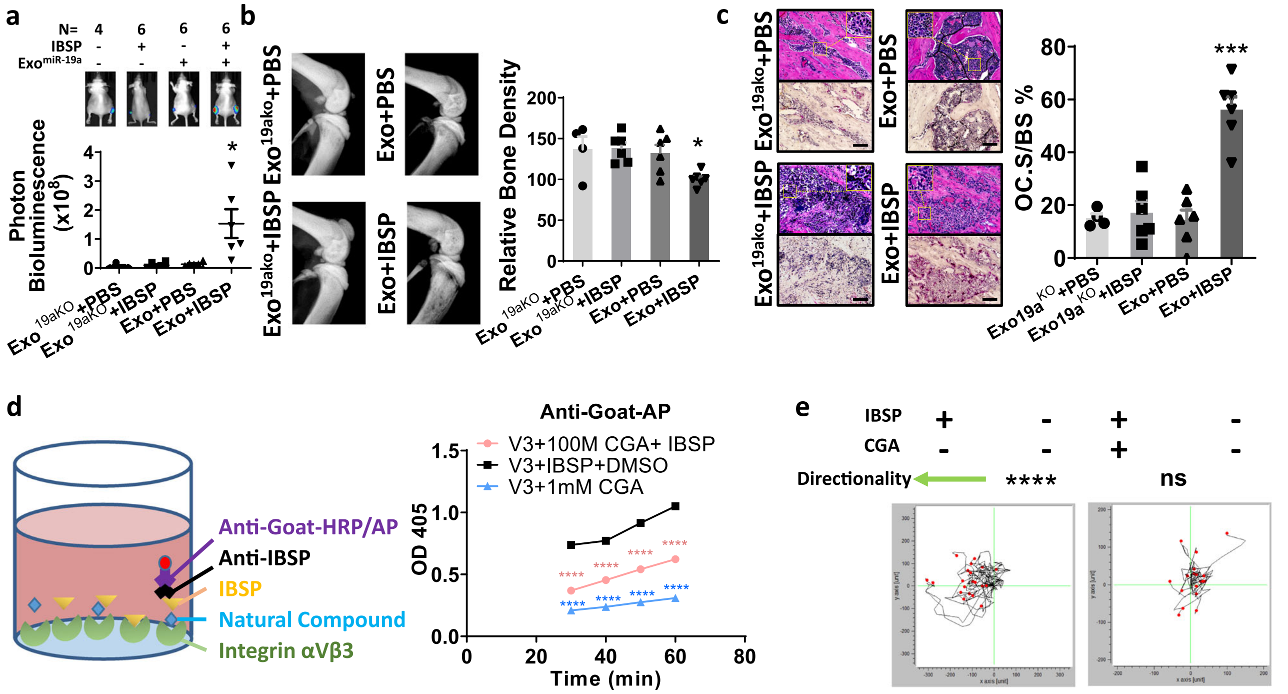

Fig. 6 IBSP and miR-19a cooperatively induce osteoclastogenesis and promote cancer cell growth in the bone. a, **b** MCF7 cells were injected into the tibias of mice. These mice also received 2 μg exosomes prepared from MCF7BoM2 and 0.5 μg recombinant IBSP injected into the tibias every 2 days. The exosomes prepared from MCF7BoM2/miR-19aKO and PBS were used as controls. After three weeks, the bioluminescence signals of tibial bones were measured. Two-sided student's t-tests were performed. $p = 0.4670$ (Exo^{19aKO} + PBS vs Exo^{19aKO} + IBSP, $n = 4$ vs 6), $p = 0.1949$ (Exo^{19aKO} + PBS vs Exo + PBS, $n = 4$ vs 6), $p = 0.0446$ (Exo^{19aKO} + PBS vs Exo + IBSP, $n = 4$ vs 6). Data are presented as mean values ± SEM (**a**). The bones were then removed and bone densities were measured by X-ray. Two-sided student's *t*-tests were performed; $p = 0.9280$ (Exo^{19aKO} + PBS vs Exo^{19aKO} + IBSP, $n = 4$ vs 6), $p = 0.9143$ (Exo^{19aKO} + PBS vs Exo + PBS, $n = 4$ vs 6), $p = 0.0257$ (Exo^{19aKO} + PBS vs Exo + IBSP, $n = 4$ vs 6) Data are presented as mean values ± SEM (**b**). **c** The removed bones were decalcified, sectioned, and examined for the amount of OC surface by TRAP staining followed by quantification using the ImageJ. Two-sided student's *t*-tests were performed; $p = 0.7224$ (Exo^{19aKO} + PBS vs Exo^{19aKO} + IBSP, $n = 4$ vs 6), $p = 0.8773$ (Exo^{19aKO} + PBS vs Exo + PBS, $n = 4$ vs 6), $p = 0.0002$ (Exo^{19aKO} + PBS vs Exo + IBSP, $n = 4$ vs 6). Data are presented as mean values ± SEM. **d** Integrin αVβ3 was seeded on the bottoms of 96-well plates. IBSP was then added to the well in the presence or absence of the library of natural compounds. The bound IBSP was measured by colorimetric substrates of alkaline phosphatase (AP). The OD 405 was compared between CGA-treated groups and the DMSO-treated group. Two-sided student's *t*-tests were performed; $p < 0.0001$ ($n = 3$) in all groups. CGA was found to most significantly inhibit the binding of IBSP to integrin αVβ3. Data are presented as mean values ± SEM. **e** The role of IBSP as a chemoattractant of osteoclast cells, and the inhibitory effect of CGA on this chemoattraction were examined by the μ-Slide Chemotaxis assay. The movement of 20 OC cells with the highest mobility was tracked and the directionality was calculated by Chemotaxis and Migration Tool. *p*-value was calculated with the Rayleigh test (left: $p = 0.0000002$, right: $p = 0.194763$).

(Supplementary Fig. 8f, h). On the other hand, CGA did not suppress the bone metastasis of 231BoM cells in our ER$^-$ breast cancer xenograft model (Supplementary Fig. 8i). These results demonstrate that CGA is a promising preventive reagent for bone metastasis of ER$^+$ breast cancer. With either CGA treatment or exosome blockade, the bone-metastatic lesions showed significantly decreased osteoclastogenesis (Fig. 7b) and increased bone density (Fig. 7c). We also confirm our findings in the T47D xenograft mouse model. When the T47D cells were implanted into mice by intracardiac injection, ectopic expression of miR-19a and IBSP significantly increased the rate of bone metastasis (Fig. 7d), decreased the bone density of the metastatic lesions (Fig. 7e), and increased the OC activities (Fig. 7f). The CGA treatment significantly decreased the rate of bone metastasis, and rescue the osteolytic changes in the bone lesions (Fig. 7d–f). Interestingly, when we generated organ culture of tumor tissues from various distant metastatic lesions in the T47D inoculated mice, we found significantly more exosomal miR-19a in the culture media of bone-metastatic lesions compared to other metastatic sites (Supplementary Fig. 8j). We also examined whether CGA was able to suppress the established bone metastasis. We first transplanted MCF7BoM2 into the tibial bone of mice. After confirming the tumor growth by measuring the bioluminescent signals, CGA or bisphosphonate-DMDP (Dichloromethylenediphosphonic acid disodium salt) was given to the mice. We found that CGA was able to suppress the cancer cell growth of established tumors in the bone more effectively compared to the control group or the bisphosphonate treatment group (Fig. 7g, h).

Discussion

ER$^+$ breast cancer patients have a considerably higher risk of bone metastasis[20,22,53–55] compared to other subtypes. In this study, we identified exosomal miR-19a and IBSP as key secreted factors from ER$^+$ bone-metastatic cells. Ectopic expression of one factor alone did not increase bone lesions in our animal models. However, upregulation of both factors together significantly promoted the tumor growth in the bone and osteoclastogenesis, indicating the cooperative roles of exosomal mIR-19a and IBSP in promoting osteolytic bone metastasis. We found that ER$^+$ cancer cells secrete IBSP as a chemoattractant for precursors of OC cells, while exosomal miR-19a enhances the osteoclastogenesis in the early metastatic site, which promotes the bone colonization of ER$^+$ breast cancer cells (Fig. 8). Importantly, in both serum and transcriptome profiles of breast cancer patients, we verified that miR-19a and IBSP are correlated with bone metastasis and recurrence

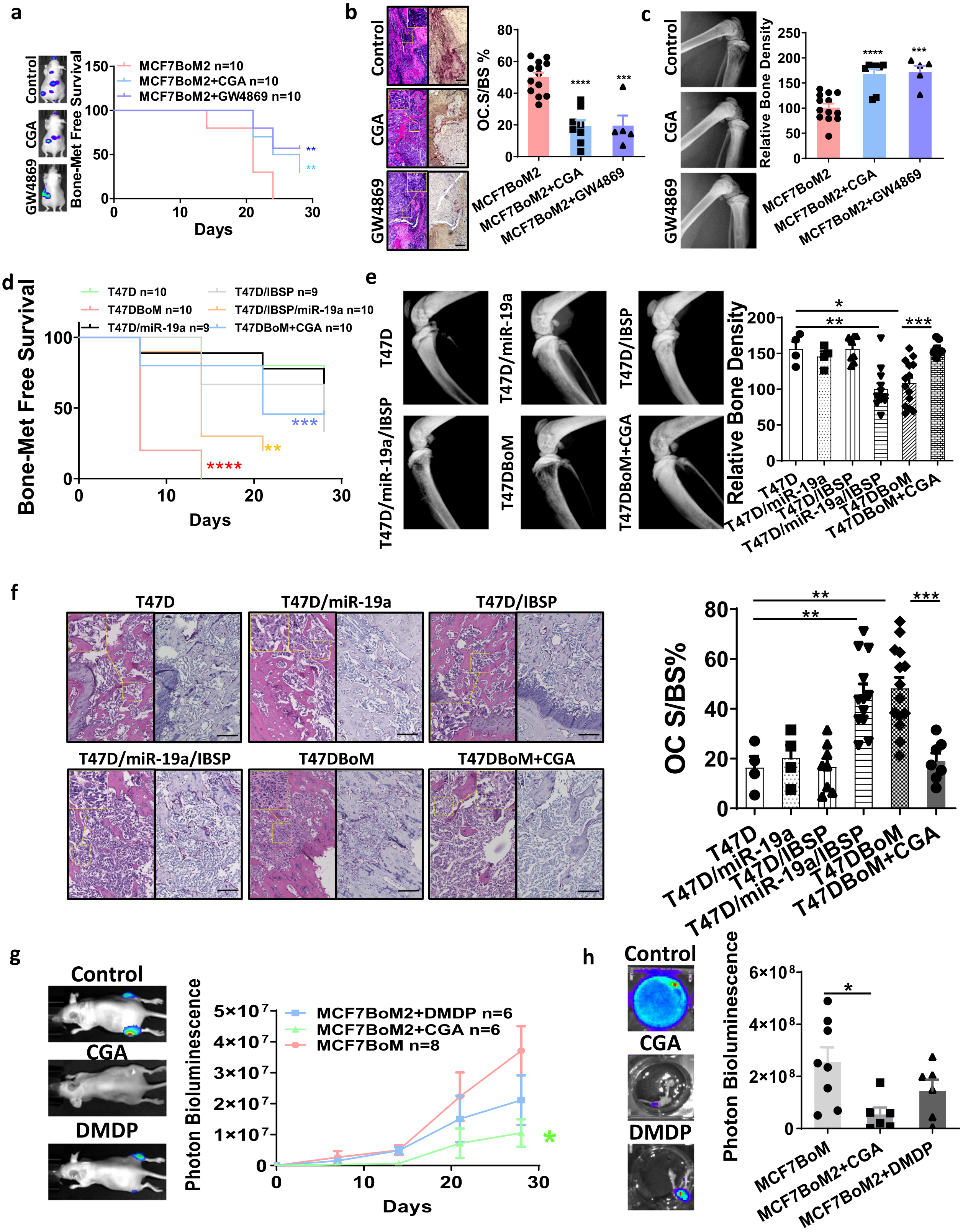

status. While the serum of advanced breast cancer patients in this study was collected during the course of treatment with tumor burden, we did not see a significant difference in the expression of exosomal miR-19a and IBSP between groups with different treatment histories (Supplementary Data 5). These data suggest the potential use of exosomal miR-19a and IBSP of serum as liquid biomarkers to stratify ER^+ breast cancer patients with a high risk of bone recurrence.

MiR-19a is located in the miR-17-92 cluster (oncomiR-1), which is characterized as a set of mammalian microRNA oncogenes[56]. The tumor-promoting role of miR-19a has been reported in multiple types of cancers[57–61], and it is known to

Fig. 7 CGA blocks cooperative function of miR-19a and IBSP in ER$^+$ BCBM. a The mice were treated with 2 μg exosomes prepared from MCF7BoM2 and 0.5 μg recombinant IBSP by injecting them into the tibias every two days. The exosomes from MCF7BoM2/miR-19aKO and PBS were used as controls. After two weeks, the bones were removed, and the TRAP staining of the bones was performed. The OC surface of the bone surface was quantified by ImageJ and compared by the two-sided student's t-test. $p = 0.0181$ (PBS + Exo^{19aKO} vs IBSP + Exo), $p = 0.2436$ (PBS + Exo^{19aKO} vs PBS + Exo), $p = 0.4594$ (PBS + Exo^{19aKO} vs IBSP + Exo^{19aKO}). $n = 5$ in all groups. **b** The ratio of OC surface relative to the bone surface was calculated after TRAP staining. $p < 0.0001$ (MCF7BoM2 vs MCF7BoM2 + CGA, $n = 13$ vs 8), $p = 0.0001$ (MCF7BoM2 vs MCF7BoM2 + GW4869, $n = 13$ vs 5). Representative H&E staining of the same field was shown (left panel) together with the TRAP staining (right panel). Scale bar, 100 μm. Two-sided student's t-tests were performed. Data are presented as mean values ± SEM. **c** The legs of tumor-bearing mice were imaged by X-ray, and the bone density was measured by ImageJ. Two-sided student's t-tests were performed. $p < 0.0001$ (MCF7BoM2 vs MCF7BoM2 + CGA, $n = 13$ vs 8), $p = 0.0002$ (MCF7BoM2 vs MCF7BoM2 + GW4869, $n = 13$ vs 5). Data are presented as mean values ± SEM. **d** T47D, T47DBoM, and T47D with ectopic expression of miR-19a or/and IBSP were intra-cardially injected into mice. One group of mice injected with T47DBoM also received CGA treatment. The growth of bone metastasis was monitored by IVIS Bioimager, and the Kaplan–Meier analysis and log-rank tests were performed for bone metastasis-free survival. $p = 0.000036$ (T47D vs T47DBoM); $p = 0.0078$ (T47D vs T47D/IBSP/miR-19a); $p = 0.0003$ (T47DBoM vs T47DBoM + CGA). **e** The legs of tumor-bearing mice were imaged by X-ray, and the bone density was measured by ImageJ. $p = 0.0027$ (T47D vs T47D/IBSP/miR-19a, $n = 4$ vs 12); $p = 0.0111$ (T47D vs T47DBoM, $n = 4$ vs 14); $p = 0.0009$ (T47DBoM vs T47DBoM + CGA, $n = 14$ vs 7). Two-sided student's t-tests were performed. Data are presented as mean values ± SEM. **f** The ratio of OC surface relative to the bone surface was calculated and compared after TRAP staining. H&E staining of the same field was shown (left panels) together with the TRAP staining (right panels). Scale bar, 100 μm. $p = 0.0028$ (T47D vs T47D/IBSP/miR-19a, $n = 4$ vs12); $p = 0.0023$ (T47D vs T47DBoM, $n = 4$ vs 14); $p = 0.0003$ (T47DBoM vs T47DBoM + CGA, $n = 14$ vs 7). Two-sided student's t-tests were performed. Data are presented as mean values ± SEM. **g** One week after intra-tibia injection of MCF7BoM2, mice were treated with CGA or DMDP. The growth of bone tumors was monitored by measuring the luciferase activity by IVIS Bioimager. Two-sided student's t-tests were performed. $p = 0.0215$ (MCF7BoM2 vs MCF7BoM2 + CGA, $n = 8$ vs 6), $p = 0.1920$ (MCF7BoM2 vs MCF7BoM2 + DMDP $n = 8$ vs 6). Data are presented as mean values ± SEM. **h** After 24 days, the legs were removed and the bioluminescence of each leg was quantified. Two-sided student's t-tests were performed. $p = 0.0144$ (MCF7BoM2 vs MCF7BoM2 + CGA, $n = 8$ vs 6), $p = 0.1747$ (MCF7BoM2 vs MCF7BoM2 + DMDP $n = 8$ vs 6). Data are presented as mean values ± SEM.

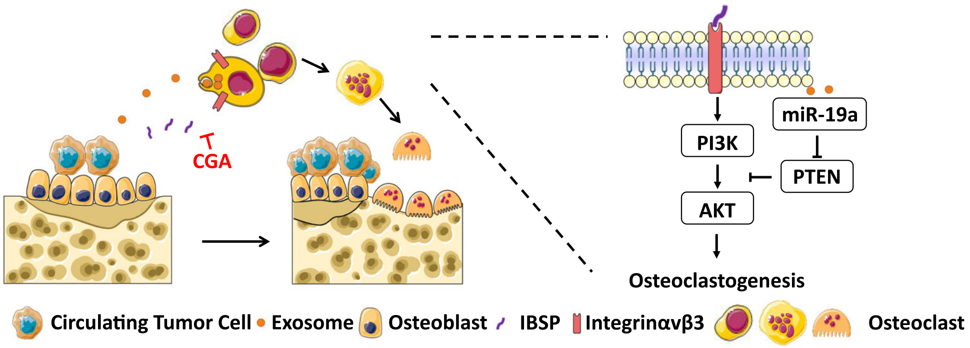

Fig. 8 Proposed mechanism of exosomal miR-19a and IBSP mediated bone metastasis in ER$^+$ breast cancer. In the early metastatic niche, ER$^+$ breast cancer cells secrete IBSP as a chemoattractant to recruit precursors of OC cells, creating an OC precursor-enriched microenvironment. OC precursors incorporate exosomes from breast cancer cells, and miR-19a is transported into OC precursors. Inside the OC precursors, miR-19a suppresses PTEN expression, activates NF-κB and AKT pathways, and promotes osteoclastogenesis. Mature OC cells induce bone resorption, liberating growth factors from the bone matrix, which further promote the growth of cancer cells.

directly target tumor suppressor PTEN[42,62,63]. It is also predicted to target ER. However, overexpression of miR-19a did not alter the level of ER in breast cancer cells[64], and the exact role of miR-19a in breast cancer is yet poorly understood. The previous study has characterized miR-19a targets in breast cancer by quantitative proteomic approach[30]. No growth-suppressive effect was found when those targets were ectopically expressed, suggesting that endogenous miR-19a does not directly alter the growth of cancer cells per se. Consistent with their finding, the results of our study revealed that modulation of miR-19a expression in breast cancer cells did not alter the growth or migration abilities in vitro. Interestingly, ectopic expression of miR-19a did not affect the expression of PTEN in the cancer cells (data not shown). A possible explanation is that miR-19a is actively sorted out of cancer cells by exosomes. Accordingly, miR-19a expression is positively correlated with osteolytic bone metastasis in vivo, strongly suggesting a role of miR-19a as a key modulator of tumor microenvironment in the process of bone metastasis of breast cancer. In the “vicious cycle of bone metastasis”[65], breast cancer cells are known to interact with host cells to generate a favorable microenvironment for cancer cell growth in the bone through direct cell–cell contact or via secreted proteins[66–68]. We found that the oncogenic role of miR-19a in ER$^+$ breast cancer is dependent on its secretory nature as exosomes. Exosomal miR-19a secreted from tumor cells are internalized into the OC precursor and induces the differentiation of OC into mature OC. OC osteoclastogenesis is one of the key steps related to the establishment of bone metastasis, and miR-19a augments this process by activating the p-AKT pathway. Therefore, this study revealed a specific role of miR-19a in ER$^+$ breast cancer bone metastasis. The nature of miR-19a encapsulated inside exosomes also makes it a promising candidate as a circulating biomarker for diagnostic and prognostic purposes[69–72].

IBSP constitutes around 12% of the non-collagenous proteins in human bone and it is synthesized by bone resident cells. Several types of cancers, including colon, breast, prostate, and lung cancers were reported to have upregulated IBSP expression[73]. In breast cancer, IBSP was also detected in cancer cells[74], and we found that IBSP is only expressed in breast cancer cells but not in normal breast tissue, making it a good candidate as a tumor-specific biomarker. Indeed, IBSP was previously reported to be associated with poor survival of breast cancer patients[75]. Interestingly, it was also found to be positively associated with bone metastasis, but negatively associated with lung metastasis in breast cancer[75]. These observations can be well explained by our results, as we found IBSP regulates bone metastasis in ER$^+$ breast cancer. ER$^+$ breast cancer is known to have a higher incidence of bone metastasis compared to other subtypes, while they have a lower incidence of lung metastasis[55]. By classifying subtypes of breast cancer patients, we have shown the feasibility of using IBSP, together with exosomal miR-19a to predict the risk of bone metastasis in ER$^+$ patients. More importantly, we clarified a cooperative pathway between IBSP and miR-19a, that mobilizes the bone microenvironment to guide the ER$^+$ breast cancer cells to the bone and support their cell growth. However, in this study, we did not observe a regulatory effect in gene expression between miR-19a and IBSP (Supplementary Fig. 2a, b). Therefore, the increased bone metastasis is likely to be a result of the colonial selection of high miR-19a/IBSP cells that adapt well to the early metastatic niche due to the interaction with OC cells.

Currently, there is no effective and safe regimen to prevent bone recurrence in breast cancer. The present bone-targeted therapy does not improve the survival of breast cancer patients, and patients with bone metastases still rely on systemic treatment. However, patients with bone recurrence develop resistance to systemic treatment as the cancer cells acquired resistance to these drugs at an early stage. In this study, we found that CGA blocks the interaction between IBSP and OCs, inhibiting the pro-osteoclastogenesis effect of cancer-derived exosomes. CGA is abundant in the extract from plants, and it has minimum side effects for long-term preventive treatment. By using exosomal miR-19a and IBSP to predict the risk of bone metastasis, ER$^+$ breast cancer patients could benefit from this agent in preventing late-onset recurrence in the bone. CGA could also be used as a combination therapy to treat ER$^+$ breast cancer patients with bone metastasis.

Collectively, our study identified exosomal miR-19a and IBSP as mediators of cell–cell communication between breast cancer cells and OC cells, which promotes the vicious cycle of bone metastasis in ER$^+$ breast cancer. Importantly, the natural compound CGA can block this process. This study sheds light on the molecular mechanism of bone metastasis in ER$^+$ breast cancer, which warrants further investigation on the miR19a-IBSP axis for the development of an effective therapeutic strategy.

Methods

Cells and cell culture. Human breast carcinoma cell lines, MDA-MB-231, MCF7, T47D, and mouse monocyte/macrophage cell line RAW 264.7 were purchased from American Type Tissue Culture Collection (ATCC, Manassas, VA, USA). MCF7BoM2 and 231BoM-1833, the bone-metastatic derivative of breast cancer cell lines were kindly provided by Dr. Joan Massagué (Memorial Sloan-Kettering Cancer Center)[76,35]. To select bone-tropic T47DBoM, 100,000 T47D cells were injected into the left cardiac ventricle of athymic-nu/nu mice. Subsequently, bone-metastatic tumor cells were isolated from the tibias. Three rounds of selection were performed to establish the T47DBoM cell line. Luciferase-labeled cells were generated by infecting the lentivirus carrying the firefly luciferase gene. MDA-MB-231, MCF7 cells and their variants, as well as RAW264.7, were cultured in DMEM medium supplemented with 10% FBS and antibiotics. Murine bone marrow-derived monocytes and macrophages (BMMs) were generated as previously described[77]. Briefly, bone marrow cells were harvested by flushing the femurs and tibias of six to eight-week-old C57BL/6 mice (The Jackson Laboratory, Bar Harbor, ME, USA) with minimum essential medium-α (α-MEM; Invitrogen, Carlsbad, CA, USA). The cells were then washed, centrifuged, and incubated in complete α-MEM containing 10% heat-inactivated fetal bovine serum and penicillin/streptomycin for 18 h to separate the floating and adherent cells. The floating cells were collected and cultured in complete α-MEM supplemented with 50 ng/ml murine recombinant Macrophage Colony Stimulating Factor (M-CSF; Peprotech, Rocky Hill, NJ, USA). After 3 days, non-adherent cells were washed out and the adherent cells were used as BMMs.

Animal experiments. For experimental metastasis assay, cancer cells in 100 μl of PBS were injected into the left cardiac ventricle of the athymic-nu/nu mice (7–8 weeks). For intratibial implantation of cancer cells, cells with or without ectopic expression of miR-19a and IBSP were injected into the tibia at a final concentration of 100,000 cells/10 μl. To investigate the effect of miR-19a and IBSP on the primary tumor, cancer cells (1×10^6) in 50 μl PBS were mixed with Matrigel matrix (Corning, Corning, NY, USA) at 1:1 ration, and implanted into mammary fat pads of athymic-nu/nu mice. All mice received implantation of 1.7 mg estradiol continuous release pellets (Innovative Research of America). To confirm a successful injection, we immediately monitored photon flux from the whole body of the mice after injection. The growth of tumors in the bones was monitored and quantified by measuring luminescence using IVIS Xenogen bioimager (Caliper Life Science), and the images were analyzed using Living Image (Caliper Life Science) version 4.7.3 software and Aura software (Spectral Instruments Imaging, LLC) version 3.2. For CGA (Sigma-Aldrich, St. Louis, MO, USA) treatment, the compound dissolved in deionized water was administered orally at doses of 200 mg/kg body weight per day. For GW4869 (Cayman Chemical, Ann Arbor, MI, USA) treatment, the drug was intraperitoneally (i.p.) injected at the dose of 2.5 μg/g every three days. For DMDP (Dichloromethylenediphosphonic acid disodium salt) treatment, the drug was intraperitoneally (i.p.) injected at the dose of 10 mg/kg twice a week. For in vivo exosome uptake assay, the mice were treated with 2 μg Vybrant DiD-labeled exosomes with or without 0.5 μg recombinant IBSP by injecting them into the tibias every two days. After two weeks, the bones were extracted and sectioned with a diamond knife. The sectioned bone was then stained with FITC-CTSK (Cathepsin K) and DAPI. The co-localization of OC and exosome was examined by Keyence All-in-one Fluorescence Microscope (BZ-X700). For measurement of the percentage of OC surface per bone surface (OC.S/BS%), bioluminescence and H&E staining were performed to identify the metastatic sites. For each of the mice, all the bone-metastatic sites were TRAP stained and cumulative osteoclast surface and bone surface were measured by ImageJ (FIJI, 1.52n)[78].

X-ray imaging. On days 28 before euthanization, X-ray images of the mice were captured with Faxitron Multifocus 10 × 15 Digital Radiography System. Mice were anesthetized and placed dorsal side up in the X-ray chamber with legs in the capture region. X-ray images of the tibias were analyzed using ImageJ (ImageJ 1.8.0_112; 64-bit; National Institute of Health) according to previous publications[79,80] and relative bone density was quantified. The image was calibrated to a standard aluminum wedge. The average mean grayscale value of the area of interest was recorded after the value of background soft-tissue was subtracted.

Human L1000 array. The cell culture supernatants were dialyzed and biotinylated according to the manual of L-Series Human Antibody Array 1000 (RayBiotech, Peachtree Corners, GA, USA). The glass slide arrays were then locked and incubated with biotin-labeled samples to allow the binding of target proteins to the preprinted capture antibodies. Streptavidin-conjugated fluorescent dye is then used to interact with the bound proteins. Finally, when the slide is dried, laser fluorescence scanning was performed with GenePix® 4000B Microarray Scanner to visualize signals. To compare the expression of each protein target, Protein Array Analyzer was used to quantify the signals.

Gene knockout and overexpression. IBSP and miR-19a knockout was carried out with CRISPR/Cas9 system. lentiCRISPR v2 was a gift from Feng Zhang (Addgene plasmid # 52961; http://n2t.net/addgene:52961; RRID:Addgene_52961) Guide RNAs for IBSP (AGAACTTACTGAGAAAGCAC) and miR-19a (AATCTATGCAAAACTGATGG) were cloned into vectors according to the provided protocol. Lentivirus was prepared by transfection of plasmids into HEK 293T cells. MCF7BoM2 was infected with lentivirus and screened with puromycin. The success of knockout was confirmed by the T7E1 assay (NEB). Single-cell clones were picked by limit dilution. Four miR-19a knockout clones and three IBSP knockout clones were selected. The knockout clones of each gene were mixed to generate the heterogeneous knockout cell lines and they were used for functional assays. The stabilities of the knockout were verified every five passages by PCR and western blot analysis. The plasmid for overexpression of IBSP (LV185867) was purchased from ABM (Applied Biological Materials, Richmond, BC, Canada) and the plasmid for overexpression of miR-19a (PCDH-miR-19a) was a kind gift from Dr. Yin-yuan Mo.

Osteoclastogenesis assay and tartrate-resistant acid phosphatase (TRAP) staining. Murine BMMs at a density of 1×10^6 cells/ml or RAW264.7 cells at a density of 1×10^5 cells/ml were plated in a chamber slide (Thermofisher, Waltham, MA, USA) and cultured in complete α-MEM supplemented with 50 ng/ml murine recombinant M-CSF, 25 ng/ml murine recombinant RANKL (Peprotech, Rocky Hill, NJ, USA) in the presence or absence of 20 μg/ml exosomes, a concentration used previously in multiple studies[27,66,81,82]. On day 4, TRAP staining was performed using a leukocyte acid phosphatase kit (Sigma-Aldrich, St. Louis, MO, USA) according to the manufacturer's instructions. The multinucleated TRAP-positive cells from five biological replicates were considered mature OC cells and monitored by Zeiss Axioplan2 microscope. The size of OC cells was measured by ImageJ as reported[83].

Bone-resorption assay. To determine the role of exosomal miR-19a in the bone resorption activity of OC cells, pit assay was performed on bone slices (Immunodiagnostic Systems). 50,000 bone marrow-derived OC precursor BMMs were seeded on sterilized bone slices placed in a 96-well plate. The BMMs were cultured with complete α-MEM supplemented with 50 ng/ml murine recombinant M-CSF, 25 ng/ml murine recombinant RANKL (Peprotech, Rocky Hill, NJ, USA) in the presence or absence of 20 μg/ml exosomes. The media was changed every 2–3 days. After two weeks of cell culture, cells were washed, and resorption pits were stained with 1% toluidine blue. The resorption area was photographed under microscopy and the image was analyzed by ImageJ.

Extracellular vesicles purification and tracking analysis. Extracellular vesicles (EVs) from cells were isolated by ultracentrifugation. Cells were grown in EVs-depleted media for 48 h before CM was collected for EVs purification. To isolate total EVs, CM was centrifuged at 300 × *g* for 10 min to remove cells. EVs were collected by ultracentrifugation at 120,000 × *g* for 70 min. Apoptotic bodies (ABs), microvesicles (MVs), and exosomes were isolated by differential centrifugation as published before[84,85]. Briefly, the harvested CM was centrifuged at 300 × *g* for 10 min to remove cells. ABs were collected by centrifugation at 2000 × *g* for 20 min. The supernatant was centrifuged at 16,500 × *g* for 20 min to collect MVs. After that, the Supernatant was passed through a 0.2 μm filter (Sarstedt, Nümbrecht, GERMANY) to remove the particles larger than 200 nm. Exosomes were then pelleted by ultracentrifugation at 120,000 × *g* for 70 min. The isolated EVs were analyzed and quantified by nanoparticle tracking analysis (NTA) and electron microscope with negative staining.

Imaging of exosomes by transmission electron microscopy. For negative staining, Purified exosomes were incubated onto discharged 200 mesh copper EM grids and fixed with 2% Paraformaldehyde (PFA). 1% uranyl acetate (UA) solution was used to stain the exosomes on the surface of the EM grids. The exosomes were imaged by FEI Tecnai BioTwin Transmission Electron Microscope. For immunostaining of IBSP and CD63 on the surface of exosomes, Anti-CD63 (1:100) (Santa Cruz Biotechnology, Dallas, Texas, USA) and anti-IBSP (1:100) (Thermofisher, Waltham, MA, USA) were used to incubate the fixed exosomes on the grids. The 10 nm colloidal gold-labeled protein A (1:50)(BOSTER BIOLOGICAL TECHNOLOGY, Pleasanton, CA, USA) was then used to label the primary antibodies. After that, negative staining was performed with 2% uranyl acetate and the grid was imaged by transmission electron microscopy.

Exosome uptaking assay. Breast cancer cell lines were labeled with lentivirus expressing PalmGFP (a kind gift from Dr. Xandra O. Breakefield). Cells with intense fluorescence were selected by BD FACSAria Cell Sorter. Exosomes labeled with PalmGFP were isolated by differential ultracentrifuge. To monitor the uptake of exosomes in OC cells, RAW264.7 cells were seeded in chamber slides overnight and 20 μg/ml exosomes were added into the media. After 24 h of incubation, the cells were washed and fixed. Cell nuclei were stained with DAPI followed by sealing the slides with coverslips. The uptake of exosomes was confirmed by examining the GFP signal under Olympus FV1200 SPECTRAL laser scanning confocal microscope.

ExoELISA. To compare the exosome production from cells after ectopic expression of miR-19a and IBSP, exosome concentration in the cell culture media was determined using ExoElisa from System Biosciences (SBI, Mountain View, CA, USA). According to the manufacturer's instruction, exosomes from a comparable amount of different cell lines were purified by ExoQuick-TC precipitation solution (SBI, Mountain View, CA, USA). Diluted exosomes, together with protein standards, were incubated with a provided microtiter plate. The detection antibody was added to the wells, followed by a horseradish peroxidase enzyme-linked secondary antibody. Finally, TMB ELISA substrate was added to develop the signal, and a stop buffer was used to stop the reaction. OD value was recorded with a spectrophotometric plate reader at 450 nm. The data were normalized to the cell count.

Immunohistochemistry. Immunohistochemical analysis was carried out for paraffin-embedded, surgically resected specimens of breast cancer bone metastases. Briefly, the sections were de-paraffinized, rehydrated, and heated at 100 °C for 20 min in Tris-buffered saline (pH 9.0) for antigen exposure. They were treated with 3% H_2O_2 to block endogenous peroxidase activity, followed by treatment with 5% BSA solution for 30 min. The slides were then incubated with primary antibodies targeting IBSP (Invitrogen, PA5-50633, 1:100) and E-cadherin (Cell Signaling Technology, clone 24E10, #3195, 1:200) for 16 h at 4 °C. After washing in PBS/0.1% Tween-20, the sections were treated with the secondary antibody anti-rabbit (Bio-Rad, #1706515, 1:500). The sections were washed extensively, and DAB substrate chromogen solution was applied followed by counterstaining with hematoxylin. For negative control, we added the rabbit IgG isotype control (Invitrogen, 02-6102, 1:250) instead of primary antibodies during the primary antibody incubation. The expression of the protein of interest was evaluated by H scoring as the sum of the frequency and the intensity (0: none; 1: weak; 2: moderate; 3: strong). The final score = 1 × (% of 1 + cells) + 2 × (% of 2 + cells) + 3 × (% of 3 + cells). IHC scores were determined by concordance among the scores of two independent reviewers.

MTS assay. Viability of cell lines was quantified by using the CellTiter 96 Aqueous One solution cell proliferation assay kit (Promega, Madison, WI, USA). Cells were plated in 96-well tissue culture plates at a density of 5000 cells per well. At the time of measurement, 20 μl of CellTiter 96 AQueous One solution reagent was added into each well of the 96-well assay plate containing the samples in 100 μl of culture medium. The plate was incubated at 37 °C for 1 h in a humidified, 5% CO_2 atmosphere. The absorbance at 490 nm was measured and recorded.

Wound-healing migration assay. The cell migration was estimated by a wound-healing migration assay and monitored by the Olympus IX-70 microscope. Cells were seeded in 12 well cell culture dish and a scratch was made on the monolayer using a sterile tip when cells reach 100% confluence. The distance of migration by cancer cells was measured every 24 h.

Real-time PCR and western blotting. Total RNA was isolated by using Direct-zol RNA MiniPrep Plus (Zymo Research Corp, Irvine, CA, USA) and miRNeasy Mini Kit (Qiagen, Germantown, MD, USA) for mRNA and microRNA, respectively. We used iScript Reverse Transcription Supermix (Life Science Research, Hercules, CA, USA) and TaqMan MicroRNA Reverse Transcription kit (ThermoFisher Scientific, Waltham, MA, USA) for mRNA and miRNA reverse transcription, respectively. Quantitative PCR (qPCR) for miRNA was conducted by using TaqMan Universal Master Mix II and TaqMan microRNA assays (ThermoFisher Scientific, Waltham, MA, USA). All miRNA assays were purchased from ThermoFisher Scientific. U6 snRNA and RNU48 TaqMan probes were used as endogenous controls for human and mouse cells, respectively. For coding genes, qPCR was conducted by using iTaq Universal SYBR Green Supermix (Life Science Research, Hercules, CA, USA). Primers used in this study were listed in Supplementary Data 1. Western blotting was carried out using general methods. Briefly, the protein was extracted from the cells using RIPA buffer, quantified by Protein Assay (Bio-Rad, Hercules, California, USA), resolved by 10% SDS-polyacrylamide gel, and then electrotransferred to nitrocellulose membrane. Primary antibodies against IBSP (Invitrogen, PA5-50633, 1:500), Phospho-NF-κB p65 (Ser536) (Cell Signaling Technology, clone 93H1, #3033, 1:1000), NF-κB p65 (Cell Signaling Technology, #8242, 1:1000), Phospho-Akt (Ser473) (Cell Signaling Technology, clone D9E, #4060, 1:3000), Akt (Cell Signaling Technology, #9272, 1:2000), HSP70 (Invitrogen, Clone 5A5, #MA3-007, 1:1000), PTEN (Santa Cruz Biotechnology, clone A2B1, sc-7974, 1:1000), CD63 (Santa Cruz Biotechnology, clone MX-49.129.5, sc-5275, 1:500), TSG101 (Santa Cruz Biotechnology, clone C-2, sc-7964, 1:1000), GRP94 (Santa Cruz Biotechnology, clone H-10, sc-393402, 1:500), α-actinin-4 (Santa Cruz Biotechnology, clone G-4, sc-390205, 1:500), Calregulin (Santa Cruz Biotechnology, clone A-9, sc-166837, 1:500), GAPDH (Cell Signaling Technology, clone D16H11, #5174, 1:15,000), α-tubulin (Cell Signaling Technology, #2144, 1:2000) were used. HRP-conjugated anti-mouse IgG (Cell Signaling Technology, #7076) or anti-rabbit IgG (Bio-Rad, #1706515) and mouse IgG kappa binding protein m-IgGκ BP-HRP (Santa Cruz Biotechnology, sc-516102) were used as secondary antibodies. Immunoblotting images were captured by Amersham Imager 600 or the X-ray film processor. Images were quantified with ImageJ software.

Receptor–ligand in vitro binding assay. The receptor–ligand in vitro binding assay was developed according to previous publications[86,87]. Briefly, a high-binding 96-well plate was coated with integrin αVβ3 in the carbonate-bicarbonate buffer. The plate was sealed and incubated at 4 °C overnight. The plate was then washed and blocked with PBS (0.1% Tween and 1% BSA). IBSP with or without the natural compound library was incubated with coated integrin αVβ3 at room temperature for 2 h. The plate was then washed and further incubated with primary antibody Goat anti-IBSP (R&D SYSTEMS, AF4014, 1:100) or Goat IgG Control (R&D SYSTEMS, AB-108-C, 1:100). Anti-goat IgG tagged with either HRP (horseradish peroxidase) (Invitrogen, A15999, 1:5000) or AP (alkaline phosphatase) (Invitrogen, A16002, 1:2500) was used as the secondary antibody. After washing the plates, the substrate was added, and the plates were incubated for 30 min followed by adding the stop solution. The binding of integrin αVβ3 and IBSP was quantified by measuring the absorbance value with a plate reader.

μ-Slide chemotaxis assay. The μ-Slide chemotaxis assay was carried out according to the manufacturer's instructions. Briefly, OC precursors BMMs at 3×10^6 cells/ml were mixed with collagen type I gels and other ingredients before being seeded into the middle channel. Left and right chambers were filled with FBS media with or without IBSP. The movement of cells was tracked according to a previous publication[88]. Time-lapse video microscopy was performed using an inverted Nikon microscope. Cell tracking was performed using the ImageJ software (National Institutes of Health, Bethesda, USA) plugin "Manual Tracking" (Fabrice

Cordelières, Institut Curie, Orsay, France), then analyzed with Chemotaxis and Migration Tool (Version 2.0, IBIDI).

Clinical samples. Clinical samples from breast cancer patients and healthy individuals were obtained from Tumor Tissue and Pathology Shared Resource of Wake Forest Baptist Comprehensive Cancer Center and Cooperative Human Tissue Network. The serum samples from early-stage breast cancer patients were collected before surgery and the serum samples from advanced breast cancer patients were collected during the course of treatment. Population characteristics including patient age, race, diagnosis, metastasis, receptor status, and treatment history were retrieved from medical records, and summarized in Supplementary Data 2 and 3. The patient information of tumor tissue and healthy bone tissue was summarized in Supplementary Data 4.

MiRNA array, bioinformatics, statistical tests, and reproducibility. EVs from MCF7 and MCF7BoM2 were collected and miRNA was extracted using miRNeasy Micro Kit (Qiagen, Hilden, North Rhine-Westphalia, Germany). Expression profiling of miRNA was performed by using the Affymetrix GeneChip miRNA Array. For calculation of FDR and fold change in differential expression analyses, the ComparativeMarkerSelection module from GenePattern[89] (Broad Institute, Cambridge, MA, USA) was used. For clustering and visualization, the HierarchicalClustering and HierarchicalClusteringViewer modules from GenePattern were used. For metastasis-free survivals, Kaplan–Meier curves were plotted using the time to event as the outcome. Statistical differences in survival across groups were assessed using the log-rank test. For other analyses, student's *t*-tests (two-sided) were used unless otherwise noted. All other statistical analyses were performed using the GraphPad Prism 8 Program (GraphPad Software, San Diego, CA, USA). Asterisk: $^{*}p < 0.05$, $^{**}p < 0.01$, $^{***}p < 0.001$, $^{****}p < 0.001$, $^{ns}p \geq 0.05$. Representative experiments were repeated independently three times with similar results.

Reporting summary. Further information on research design is available in the Nature Research Reporting Summary linked to this article.

Data availability

CEL and expression files associated with the GeneChip miRNA array in this study are deposited at GEO (https://www.ncbi.nlm.nih.gov/geo/) with the accession number GSE176105. The GEO data set (GSE41922, GSE22220, GSE56493, GSE2034), TCGA referenced during the study are available in a public repository from https://www.ncbi.nlm.nih.gov/geo/ and https://portal.gdc.cancer.gov/ websites. The source data underlying Figs. 1–7 and Supplementary Figs. 1–8 are provided as a Source Data file. All the other data supporting the findings of this study are available within the article and its supplementary information files and from the corresponding author upon reasonable request. A reporting summary for this article is available as a Supplementary Information file. Source data are provided with this paper.

Received: 30 October 2019; Accepted: 10 August 2021;
Published online: 31 August 2021

References

1. Patanaphan, V., Salazar, O. M. & Risco, R. Breast cancer: metastatic patterns and their prognosis. *South. Med. J.* **81**, 1109–1112 (1988).
2. Manders, K. et al. Clinical management of women with metastatic breast cancer: a descriptive study according to age group. *BMC Cancer* **6**, 179 (2006).
3. Coleman, R. E. Clinical features of metastatic bone disease and risk of skeletal morbidity. *Clin. Cancer Res.* **12**, 6243s–6249s (2006).
4. Coleman, R. et al. Bone health in cancer patients: ESMO Clinical Practice Guidelines. *Ann. Oncol.* **25**, iii124–iii137 (2014).
5. Coleman, R. E. Metastatic bone disease: clinical features, pathophysiology and treatment strategies. *Cancer Treat. Rev.* **27**, 165–176 (2001).
6. Esposito, M., Guise, T. & Kang, Y. The biology of bone metastasis. *Cold Spring Harb. Perspect. Med.* **8**, a031252 (2018).
7. Roodman, G. D. Mechanisms of bone metastasis. *N. Engl. J. Med.* **350**, 1655–1664 (2004).
8. Kang, Y. et al. A multigenic program mediating breast cancer metastasis to bone. *Cancer Cell* **3**, 537–549 (2003).
9. Rucci, N., Sanita, P., Delle Monache, S., Alesse, E. & Angelucci, A. Molecular pathogenesis of bone metastases in breast cancer: proven and emerging therapeutic targets. *World J. Clin. Oncol.* **5**, 335–347 (2014).
10. Azim, H. A., Kamal, N. S. & Azim, H. A. Jr Bone metastasis in breast cancer: the story of RANK-ligand. *J. Egypt. Natl Cancer Inst.* **24**, 107–114 (2012).
11. Kang, Y. Dissecting tumor-stromal interactions in breast cancer bone metastasis. *Endocrinol. Metab.* **31**, 206–212 (2016).
12. Guise, T. A. The vicious cycle of bone metastases. *J. Musculoskelet. Neuronal Interact.* **2**, 570–572 (2002).
13. Coleman, R. et al. Adjuvant zoledronic acid in patients with early breast cancer: final efficacy analysis of the AZURE (BIG 01/04) randomised open-label phase 3 trial. *Lancet Oncol.* **15**, 997–1006 (2014).
14. Stopeck, A. T. et al. Denosumab compared with zoledronic acid for the treatment of bone metastases in patients with advanced breast cancer: a randomized, double-blind study. *J. Clin. Oncol.* **28**, 5132–5139 (2010).
15. Early Breast Cancer Trialists' Collaborative Group (EBCTCG). Adjuvant bisphosphonate treatment in early breast cancer: meta-analyses of individual patient data from randomised trials. *Lancet* **386**, 1353–1361 (2015).
16. Rodriguez-Lozano, F. & Oñate-Sanchez, R. Treatment of osteonecrosis of the jaw related to bisphosphonates and other antiresorptive agents. *Med. Oral Patol. Oral Cir. Bucal.* **21**, e595–600 (2016).
17. Ottewell, P. & Wilson, C. Bone-targeted agents in breast cancer: do we now have all the answers? *Breast Cancer* **13**, 117822341984350 (2019).
18. Coleman, R. et al. Safety of zoledronic acid and incidence of osteonecrosis of the jaw (ONJ) during adjuvant therapy in a randomised phase III trial (AZURE: BIG 01-04) for women with stage II/III breast cancer. *Breast Cancer Res. Treat.* **127**, 429–438 (2011).
19. Rosen, L. S. et al. Long-term efficacy and safety of zoledronic acid compared with pamidronate disodium in the treatment of skeletal complications in patients with advanced multiple myeloma or breast carcinoma: a randomized, double-blind, multicenter, comparative trial. *Cancer* **98**, 1735–1744 (2003).
20. Savci-Heijink, C. D. et al. Retrospective analysis of metastatic behaviour of breast cancer subtypes. *Breast Cancer Res. Treat.* **150**, 547–557 (2015).
21. Hess, K. R., Pusztai, L., Buzdar, A. U. & Hortobagyi, G. N. Estrogen receptors and distinct patterns of breast cancer relapse. *Breast Cancer Res. Treat.* **78**, 105–118 (2003).
22. Han, H. H. et al. Estrogen receptor status predicts late-onset skeletal recurrence in breast cancer patients. *Medicine* **95**, e2909 (2016).
23. Rueda, O. M. et al. Dynamics of breast-cancer relapse reveal late-recurring ER-positive genomic subgroups. *Nature* **567**, 399–404 (2019).
24. Mundy, G. R. Metastasis to bone: causes, consequences and therapeutic opportunities. *Nat. Rev. Cancer* **2**, 584–593 (2002).
25. Wu, K., Xing, F., Wu, S.-Y. & Watabe, K. Extracellular vesicles as emerging targets in cancer: Recent development from bench to bedside. *Biochim. Biophys. Acta* **1868**, 538–563 (2017).
26. Rossi, M., Battafarano, G., D'Agostini, M. & Del Fattore, A. The role of extracellular vesicles in bone metastasis. *Int. J. Mol. Sci.* **19**, 1136 (2018).
27. Peinado, H. et al. Melanoma exosomes educate bone marrow progenitor cells toward a pro-metastatic phenotype through MET. *Nat. Med.* **18**, 883–891 (2012).
28. Valencia, K. et al. miRNA cargo within exosome-like vesicle transfer influences metastatic bone colonization. *Mol. Oncol.* **8**, 689–703 (2014).
29. Tiedemann, K. et al. Exosomal release of L-plastin by breast cancer cells facilitates metastatic bone osteolysis. *Transl. Oncol.* **12**, 462–474 (2019).
30. Ouchida, M. et al. Novel direct targets of miR-19a identified in breast cancer cells by a quantitative proteomic approach. *PLoS ONE* **7**, e44095 (2012).
31. Peng, Y., Huang, D., Ma, K., Deng, X. & Shao, Z. MiR-19a as a prognostic indicator for cancer patients: a meta-analysis. *Biosci. Rep.* **39**, BSR20182370 (2019).
32. Bianco, P., Fisher, L. W., Young, M. F., Termine, J. D. & Robey, P. G. Expression of bone sialoprotein (BSP) in developing human tissues. *Calcif. Tissue Int.* **49**, 421–426 (1991).
33. Ferguson, S. W. & Nguyen, J. Exosomes as therapeutics: the implications of molecular composition and exosomal heterogeneity. *J. Control. Release* **228**, 179–190 (2016).
34. Goldie, B. J. et al. Activity-associated miRNA are packaged in Map1b-enriched exosomes released from depolarized neurons. *Nucleic Acids Res.* **42**, 9195–9208 (2014).
35. Kim, M. Y. et al. Tumor self-seeding by circulating cancer cells. *Cell* **139**, 1315–1326 (2009).
36. Zhang, X. H. et al. Latent bone metastasis in breast cancer tied to Src-dependent survival signals. *Cancer Cell* **16**, 67–78 (2009).
37. Gallo, A., Tandon, M., Alevizos, I. & Illei, G. G. The majority of microRNAs detectable in serum and saliva is concentrated in exosomes. *PLoS ONE* **7**, e30679 (2012).
38. Tanaka, Y. et al. Clinical impact of serum exosomal microRNA-21 as a clinical biomarker in human esophageal squamous cell carcinoma. *Cancer* **119**, 1159–1167 (2013).
39. Kawasaki, K., Suzuki, T. & Weiss, K. M. Genetic basis for the evolution of vertebrate mineralized tissue. *Proc. Natl Acad. Sci. USA* **101**, 11356–11361 (2004).
40. Malaval, L. et al. Bone sialoprotein plays a functional role in bone formation and osteoclastogenesis. *J. Exp. Med.* **205**, 1145–1153 (2008).

41. Ye, H. et al. MicroRNA and transcription factor co-regulatory network analysis reveals miR-19 inhibits CYLD in T-cell acute lymphoblastic leukemia. *Nucleic Acids Res.* **40**, 5201–5214 (2012).
42. Feng, Y. et al. miR-19a acts as an oncogenic microRNA and is up-regulated in bladder cancer. *J. Exp. Clin. Cancer Res.* **33**, 67 (2014).
43. Mogilyansky, E. & Rigoutsos, I. The miR-17/92 cluster: a comprehensive update on its genomics, genetics, functions and increasingly important and numerous roles in health and disease. *Cell Death Differ.* **20**, 1603–1614 (2013).
44. Zhang, X. et al. MicroRNA-19 (miR-19) regulates tissue factor expression in breast cancer cells. *J. Biol. Chem.* **286**, 1429–1435 (2011).
45. Wang, Y., Zhao, S., Zhu, L., Zhang, Q. & Ren, Y. MiR-19a negatively regulated the expression of PTEN and promoted the growth of ovarian cancer cells. *Gene* **670**, 166–173 (2018).
46. Boyce, B. F., Xiu, Y., Li, J., Xing, L. & Yao, Z. NF-κB-mediated regulation of osteoclastogenesis. *Endocrinol. Metab.* **30**, 35 (2015).
47. Moon, J. B. et al. Akt induces osteoclast differentiation through regulating the GSK3β/NFATc1 signaling cascade. *J. Immunol.* **188**, 163–169 (2012).
48. Georgescu, M. M. PTEN tumor suppressor network in PI3K-Akt pathway control. *Genes Cancer* **1**, 1170–1177 (2010).
49. Zhang, L.-L. et al. Phosphatase and Tensin Homolog (PTEN) represses colon cancer progression through inhibiting paxillin transcription via PI3K/AKT/NF-κB pathway. *J. Biol. Chem.* **290**, 15018–15029 (2015).
50. Kim, J.-M., Lee, K. & Jeong, D. Selective regulation of osteoclast adhesion and spreading by PLCγ/PKCα-PKCδ/RhoA-Rac1 signaling. *BMB Rep.* **51**, 230–235 (2018).
51. Nakamura, I. et al. Role of alpha(v)beta(3) integrin in osteoclast migration and formation of the sealing zone. *J. Cell Sci.* **112**, 3985–3993 (1999).
52. Hunter, G. K. & Goldberg, H. A. Nucleation of hydroxyapatite by bone sialoprotein. *Proc. Natl Acad. Sci. USA* **90**, 8562–8565 (1993).
53. Xiong, Z. et al. Bone metastasis pattern in initial metastatic breast cancer: a population-based study. *Cancer Manag. Res.* **10**, 287–295 (2018).
54. Lee, S. J. et al. Implications of bone-only metastases in breast cancer: favorable preference with excellent outcomes of hormone receptor positive breast cancer. *Cancer Res. Treat.* **43**, 89–95 (2011).
55. Kennecke, H. et al. Metastatic behavior of breast cancer subtypes. *J. Clin. Oncol.* **28**, 3271–3277 (2010).
56. Kort, E. J. et al. The E2F3-Oncomir-1 axis is activated in Wilms' tumor. *Cancer Res.* **68**, 4034–4038 (2008).
57. Liu, Y. et al. miR-19a promotes colorectal cancer proliferation and migration by targeting TIA1. *Mol. Cancer* **16**, 53 (2017).
58. Chen, Q., Guo, W., Zhang, Y., Wu, Y. & Xiang, J. MiR-19a promotes cell proliferation and invasion by targeting RhoB in human glioma cells. *Neurosci. Lett.* **628**, 161–166 (2016).
59. Ma, Q. et al. miR-19a correlates with poor prognosis of clear cell renal cell carcinoma patients via promoting cell proliferation and suppressing PTEN/SMAD4 expression. *Int. J. Oncol.* **49**, 2589–2599 (2016).
60. Wang, T. et al. miR-19a promotes colitis-associated colorectal cancer by regulating tumor necrosis factor alpha-induced protein 3-NF-kappaB feedback loops. *Oncogene* **36**, 3240–3251 (2016).
61. Hu, W., Jin, P., Ding, C. & Liu, W. miR-19a/b modulates lung cancer cells metastasis through suppression of MXD1 expression. *Oncol. Lett.* **12**, 1901–1905 (2016).
62. Pezzolesi, M. G., Platzer, P., Waite, K. A. & Eng, C. Differential expression of PTEN-targeting microRNAs miR-19a and miR-21 in Cowden syndrome. *Am. J. Hum. Genet.* **82**, 1141–1149 (2008).
63. Wang, F. et al. MicroRNA-19a/b regulates multidrug resistance in human gastric cancer cells by targeting PTEN. *Biochem. Biophys. Res. Commun.* **434**, 688–694 (2013).
64. Pandey, D. P. & Picard, D. miR-22 inhibits estrogen signaling by directly targeting the estrogen receptor mRNA. *Mol. Cell. Biol.* **29**, 3783–3790 (2009).
65. Kozlow, W. & Guise, T. A. Breast cancer metastasis to bone: mechanisms of osteolysis and implications for therapy. *J. Mammary Gland Biol. Neoplasia* **10**, 169–180 (2005).
66. Wang, H. et al. The osteogenic niche promotes early-stage bone colonization of disseminated breast cancer cells. *Cancer Cell* **27**, 193–210 (2015).
67. Sethi, N., Dai, X., Winter, C. G. & Kang, Y. Tumor-derived JAGGED1 promotes osteolytic bone metastasis of breast cancer by engaging notch signaling in bone cells. *Cancer Cell* **19**, 192–205 (2011).
68. Chen, Y. C., Sosnoski, D. M. & Mastro, A. M. Breast cancer metastasis to the bone: mechanisms of bone loss. *Breast Cancer Res.* **12**, 215 (2010).
69. Cortez, M. A., Welsh, J. W. & Calin, G. A. Circulating microRNAs as noninvasive biomarkers in breast cancer. *Recent Results Cancer Res.* **195**, 151–161 (2012).
70. Endzelins, E. et al. Diagnostic, prognostic and predictive value of cell-free miRNAs in prostate cancer: a systematic review. *Mol. Cancer* **15**, 41 (2016).
71. Izzotti, A. et al. Extracellular MicroRNA in liquid biopsy: applicability in cancer diagnosis and prevention. *Am. J. Cancer Res.* **6**, 1461–1493 (2016).
72. Kosaka, N., Iguchi, H. & Ochiya, T. Circulating microRNA in body fluid: a new potential biomarker for cancer diagnosis and prognosis. *Cancer Sci.* **101**, 2087–2092 (2010).
73. Fedarko, N. S., Jain, A., Karadag, A., Van Eman, M. R. & Fisher, L. W. Elevated serum bone sialoprotein and osteopontin in colon, breast, prostate, and lung cancer. *Clin. Cancer Res.* **7**, 4060–4066 (2001).
74. Sharp, J. A., Sung, V., Slavin, J., Thompson, E. W. & Henderson, M. A. Tumor cells are the source of osteopontin and bone sialoprotein expression in human breast cancer. *Lab. Investig.* **79**, 869–877 (1999).
75. Bellahcene, A., Menard, S., Bufalino, R., Moreau, L. & Castronovo, V. Expression of bone sialoprotein in primary human breast cancer is associated with poor survival. *Int. J. Cancer* **69**, 350–353 (1996).
76. Bos, P. D. et al. Genes that mediate breast cancer metastasis to the brain. *Nature* **459**, 1005–1009 (2009).
77. Yu, H. et al. FTY720 inhibited proinflammatory cytokine release and osteoclastogenesis induced by *Aggregatibacter actinomycetemcomitans*. *Lipids Health Dis.* **14**, 66 (2015).
78. Choi, S. W. et al. Osteoporotic bone of miR-150-deficient mice: Possibly due to low serum OPG-mediated osteoclast activation. *Bone Rep.* **3**, 5–10 (2015).
79. Falk, S., Al-Dihaissy, T., Mezzanotte, L. & Heegaard, A.-M. Sex-difference affects disease progression in the MRMT-1 model of cancer-induced bone pain. *F1000Res.* **4**, 445 (2015).
80. Sliepen, S. H. J. et al. Cancer-induced bone pain impairs burrowing behaviour in mouse and rat. *In Vivo* **33**, 1125–1132 (2019).
81. Nakase, I. & Futaki, S. Combined treatment with a pH-sensitive fusogenic peptide and cationic lipids achieves enhanced cytosolic delivery of exosomes. *Sci. Rep.* **5**, 10112 (2015).
82. Lv, L. H. et al. Anticancer drugs cause release of exosomes with heat shock proteins from human hepatocellular carcinoma cells that elicit effective natural killer cell antitumor responses in vitro. *J. Biol. Chem.* **287**, 15874–15885 (2012).
83. Geng, W. et al. Inhibition of osteoclast formation and function by bicarbonate: role of soluble adenylyl cyclase. *J. Cell. Physiol.* **220**, 332–340 (2009).
84. Crescitelli, R. et al. Distinct RNA profiles in subpopulations of extracellular vesicles: apoptotic bodies, microvesicles and exosomes. *J. Extracell. Vesicles* **2**, https://doi.org/10.3402/jev.v2i0.20677 (2013).
85. Thery, C., Amigorena, S., Raposo, G. & Clayton, A. Isolation and characterization of exosomes from cell culture supernatants and biological fluids. *Curr. Protoc. Cell Biol.* **Chapter 3**, Unit 3 22 (2006).
86. Li, C. W. et al. Eradication of triple-negative breast cancer cells by targeting glycosylated PD-L1. *Cancer Cell* **33**, 187–201.e110 (2018).
87. Biesiadecki, B. J. & Jin, J. P. A high-throughput solid-phase microplate protein-binding assay to investigate interactions between myofilament proteins. *J. Biomed. Biotechnol.* **2011**, 421701 (2011).
88. Zengel, P. et al. mu-Slide chemotaxis: a new chamber for long-term chemotaxis studies. *BMC Cell Biol.* **12**, 21 (2011).
89. Reich, M. et al. GenePattern 2.0. *Nat. Genet.* **38**, 500–501 (2006).

Acknowledgements

This work was supported by NIH grants RO1CA173499, R01CA185650, and R01CA205067 (to K.W.). This study used various Core Facilities and Departmental Shared Equipment resources including Cellular Imaging Shared Resource, Biostatistics Shared Resource, Tumor Tissue and Pathology Shared Resource Cell and Viral Vector Core Laboratory and Cancer Genomics Shared Resource that are supported by the Comprehensive Cancer Center of Wake Forest University NCI, National Institutes of Health Grant (P30CA012197). We also thank Dr. Xandra O. Breakefield, Ph.D. (Harvard Medical School), and Dr. Joan Massagué, Ph.D. (Memorial Sloan Kettering Cancer Center) for kindly providing the materials used in this work. The Figs. 4f, j and 8 were created from images provided by Servier Medical art (http://servier.com/Powerpoint-image-bank). Servier Medical Art by Servier is licensed under a Creative Commons Attribution 3.0 Unported License.

Author contributions

Conception and design: K. Wu and K. Watabe. Development of methodology: K. Wu, J.F., F.X., S.S., K. Watabe. Acquisition of data (provided animals, acquired and managed patient specimens, provided facilities, etc.): K. Wu, J.F., F.L., R.S., F.X., S.S., Y.L., S.-Y.W, D.Z, X.P., M.G.R., H.T., S.T., T.K., Y.-y.M., Y.S., A.T., R.P.D., K. Watabe. Analysis and interpretation of data (e.g., statistical analysis, biostatistics, computational analysis): K. Wu, D.Z., K. Watabe. Writing, review, and/or revision of the manuscript: K. Wu, S.S., K. Watabe. Administrative, technical, or material support: K. Wu, Y.L., R.S., K. Watabe. Study supervision: K. Watabe.

Competing interests

The authors declare no competing interests.

Additional information

Supplementary information The online version contains supplementary material available at https://doi.org/10.1038/s41467-021-25473-y.

Correspondence and requests for materials should be addressed to K.W.

Peer review information *Nature Communications* thanks Jacqueline F. Bromberg and the other, anonymous, reviewer(s) for their contribution to the peer review of this work. Peer reviewer reports are available.

Biochemical Pharmacology 198 (2022) 114972

Contents lists available at ScienceDirect

Biochemical Pharmacology

journal homepage: www.elsevier.com/locate/biochempharm

Functional roles of neuromedin B and gastrin-releasing peptide in regulating itch and pain in the spinal cord of non-human primates

Norikazu Kiguchi[a,*,1], Huiping Ding[b,1], Sun H. Park[c], Kelsey M. Mabry[b], Shiroh Kishioka[d], Yusuke Shiozawa[c], E. Alfonso Romero-Sandoval[e], Christopher M. Peters[e], Mei-Chuan Ko[b,*]

[a] *Department of Physiological Sciences, School of Pharmaceutical Sciences, Wakayama Medical University, Wakayama City, Wakayama 640-8156, Japan*
[b] *Department of Physiology and Pharmacology, Wake Forest School of Medicine, Winston-Salem, NC 27157, USA*
[c] *Department of Cancer Biology and Wake Forest Baptist Comprehensive Cancer Center, Wake Forest School of Medicine, Winston-Salem, NC 27157, USA*
[d] *Faculty of Wakayama Health Care Sciences, Takarazuka University of Medical and Health Care, Wakayama City, Wakayama 640-8392, Japan*
[e] *Department of Anesthesiology, Wake Forest School of Medicine, Winston-Salem, NC 27157, USA*

ARTICLE INFO

Keywords:
Dorsal horn
Non-human primates
Pruritus
Rhesus macaque
Scratching

ABSTRACT

Despite accumulating evidence in rodents, the functional role of neuromedin B (NMB) in regulating somatosensory systems in primate spinal cord is unknown. We aimed to compare the expression patterns of NMB and its receptor (NMBR) and the behavioral effects of intrathecal (i.t.) NMB with gastrin-releasing peptide (GRP) on itch or pain in non-human primates (NHPs). We used six adult rhesus monkeys. The mRNA or protein expressions of NMB, GRP, and their receptors were evaluated by quantitative reverse transcription polymerase chain reaction, immunohistochemistry, or *in situ* hybridization. We determined the behavioral effects of NMB or GRP via acute thermal nociception, capsaicin-induced thermal allodynia, and itch scratching response assays. NMB expression levels were greater than those of GRP in the dorsal root ganglia and spinal dorsal horn. Conversely, NMBR expression was significantly lower than GRP receptor (GRPR). I.t. NMB elicited only mild scratching responses, whereas GRP caused robust scratching responses. GRP- and NMB-elicited scratching responses were attenuated by GRPR (RC-3095) and NMBR (PD168368) antagonists, respectively. Moreover, i.t. NMB and GRP did not induce thermal hypersensitivity and GRPR and NMBR antagonists did not affect peripherally elicited thermal allodynia. Consistently, NMBR expression was low in both itch- and pain-responsive neurons in the spinal dorsal horn. Spinal NMB-NMBR system plays a minimal functional role in the neurotransmission of itch and pain in primates. Unlike the functional significance of the GRP-GRPR system in itch, drugs targeting the spinal NMB-NMBR system may not effectively alleviate non-NMBR-mediated itch.

1. Introduction

Of all nociceptive somatosensory systems, acute itch/pruritus is an essential alert system that eliminates noxious components by scratching responses. However, intractable itch associated with several skin or systemic diseases (e.g., atopic dermatitis, dry skin, diabetes mellitus, and cholestatic liver disease) significantly affects the quality of life and causes huge economic losses globally [1,2]. Several lines of evidence reveal critical molecules that contribute to the transmission of itch from the periphery to the central nervous system [3–5]. The intrathecal (i.t.) administration of gastrin-releasing peptide (GRP), a mammalian bombesin-related peptide, elicits robust itch-related scratching behavior in rodents and primates [6,7]. Moreover, the ablation of GRP receptor (GRPR)$^+$ neurons in the spinal dorsal horn (SDH) markedly reduces scratching behavior induced by different types of pruritic stimuli, without affecting the pain threshold in rodents [8,9]. The enhancement of GRP-GRPR activity based on the upregulation of each molecule and the sensitization of GRPR$^+$ neurons may not only underlie acute but also chronic itch [10,11].

Neuromedin B (NMB) is a decapeptide that bears close homology with bombesin-related peptide, and it mediates several physiological functions such as smooth muscle contraction, hormone secretion, and cell growth [12,13]. In contrast to GRP, NMB may be involved in both itch and pain signaling. Initially, intracerebroventricular administration

---

* Corresponding authors.
E-mail addresses: kiguchi@wakayama-med.ac.jp (N. Kiguchi), mko@wakehealth.edu (M.-C. Ko).
[1] These authors contributed equally to this work.

https://doi.org/10.1016/j.bcp.2022.114972
Received 3 January 2022; Received in revised form 15 February 2022; Accepted 15 February 2022
Available online 18 February 2022

of NMB elicits itch-related scratching behavior [14], supported by other rodent studies using i.t. or an intracerebroventricular delivery route [15–17]. However, the degree of NMB-induced scratching is considerably less than that of GRP. Conversely, the intraplantar administration of NMB elicits nociceptive hypersensitivity and the ablation of NMB receptor (NMBR)$^+$ neurons results in thermal hypoalgesia [18]. NMBR and GRPR, which have close structural homology, are predominantly expressed in separate subpopulations of spinal neurons, and the NMB-NMBR system may function upstream of the GRP-GRPR system in rodents [15,19]. Despite accumulating evidence in rodents, there is no evidence regarding the functional role of spinal NMB-NMBR system for regulating itch and pain in primates.

A substantial neurochemical gap between rodents and primates [20–22] warrants confirming the functional significance of key molecules contributing to sensory processing in primates. The pharmacological effects of opioid peptides (i.e., μ-opioid peptides and nociceptin/orphanin FQ) on pain and itch-related behaviors in non-human primates (NHPs) differ from those in rodents [23–25]. The i.t. administration of μ-opioid receptor agonists, such as morphine, produces itch sensation in patients and elicits robust scratching behavior in NHPs [6,26]; however, the degree of scratching in rodents is much less than that in NHPs [16,27,28]. Unlike opioids, the behavioral effects of i.t. GRP in rodents are similar to those in NHPs [6,29], thereby indicating the functional significance of GRP-GRPR system in rodents can be translated to NHPs. NMBR is distributed in the central nervous system of primates [30], thus functional evidence for the NMB-NMBR system in NHPs is needed to understand the mechanisms in the spinal transmission of itch. We aimed to compare the expression patterns of NMB-NMBR and GRP-GRPR systems and the behavioral effects of i.t. NMB with GRP on itch or pain sensation in NHPs.

2. Materials and methods

2.1. Animals

We used six adult rhesus monkeys (*Macaca mulatta*), comprising four males and two females, with a body weight of 6–11 kg and aged 10–16 years. The animals were housed at an indoor facility accredited by the Association for Assessment and Accreditation of Laboratory Animal Care International (Frederick, MD, USA). They were individually placed in cages with a floor space of 6–12 square feet, 2.7–5.4-feet high ceiling, and an environmentally controlled room (21–25 °C, 40–60% relative humidity) with a 12-h light/dark cycle (lights on: 6:30–18:30). They were provided with water, monkey chow (LabDiet St. Louis, MO, USA), and fresh fruit *ad libitum*. We provided them with primate enrichment devices and treats daily. They were not subjected to any experiment 1 month before initiating the study. The animals were assigned to each experiment based on the tasks they were trained to perform. All experiments followed a within-subject design (i.e., each group of animals served as its own control and all dosing conditions were randomized by a counterbalanced design). All experiments were conducted during late mornings of weekdays until the completion of time courses or testing sessions. All animal care and experiments were conducted in accordance with the Guide for the Care and Use of Laboratory Animals by the US National Institutes of Health (Bethesda, MD, USA), and were approved by the Institutional Animal Care and Use Committee of Wake Forest University (Winston-Salem, NC, USA). The present study was reported in accordance with the Animal Research: Reporting of In Vivo Experiments [31].

2.2. Tissue collection

Researchers have previously described detailed procedures for tissue collection [32]. Briefly, the animals were deeply anesthetized with sodium pentobarbital (Sigma-Aldrich, St. Louis, MO, USA) and the vascular system was flushed with saline (Baxter, Deerfield, IL, USA). The spinal column was dissected to expose the spinal cord and the attached dorsal root ganglia (DRG). For reverse transcription-quantitative real-time polymerase chain reaction (RT-qPCR), the spinal dorsal horn (SDH) and DRG tissues from the lumbar segment 4 (L4) were flash frozen in dry ice. For *in situ* hybridization and immunohistochemistry, one block of L4 spinal cord tissue was fixed in 4% paraformaldehyde (Sigma-Aldrich), cryopreserved in 30% sucrose (Sigma-Aldrich) prepared in phosphate buffered saline (PBS) (Sigma-Aldrich), and embedded in an optimal cutting temperature compound (Sakura Finetek, Torrance, CA, USA). All tissues were stored at −80 °C until use.

2.3. RT-qPCR

We performed SDH and DRG tissue processing and the RT-qPCR protocol according to a previous study [32]. The mRNA expression levels of *NMB*, *GRP*, *NMBR*, and *GRPR* from five animals were quantified based on the comparative threshold cycle (C_T) method [33]. PCR amplification efficiency for each primer was determined by the slope of standard curve generated from tenfold serial dilutions (0.02–20 ng) of the cDNA mixture from subjects. The average C_T values were obtained from three replicates and normalized against that of β-actin (*ACTB*) using the following formula: $2^{-(C_T\ \text{target gene} - C_T\ \text{ACTB})}$ $(2^{-\Delta C_T})$.

2.4. Immunohistochemistry

Fixed frozen spinal cord tissues were sectioned at a thickness of 30 μm using a cryostat (Leica CM3050S; Leica Biosystems, Wetzlar, Germany) for free-floating immunostaining. The tissue sections were washed in PBS containing 0.3% Triton X-100 (Sigma-Aldrich) and treated with TrueBlack Lipofusin Autofluorescence Quencher (Biotium, Fremont, CA, USA) for 2 min. After washing with PBS, we blocked the tissues with PBS containing 3% normal donkey serum (Jackson ImmunoResearch Laboratories, West Grove, PA, USA) at room temperature for 1 h. The sections were incubated with a primary antibody against GRPR (rabbit polyclonal, 1:500 dilution; MC-831, MBL International, Woburn, MA, USA), NMBR (rabbit polyclonal, 1:500 dilution; ABR-004, Alomone Labs, Jerusalem, Israel), and NeuN (mouse monoclonal, 1:500 dilution; MAB377, MilliporeSigma, Burlington, MA, USA; markers for neuronal nuclei) at 4 °C overnight. The following day, we rinsed the sections in PBS before incubation with donkey anti-rabbit or anti-mouse IgG secondary antibody conjugated to AlexaFluor 594 or 488, respectively (1:500 dilution; Jackson ImmunoResearch Laboratories), at room temperature for 3 h. All antibodies were prepared in PBS containing 1% normal donkey serum. The tissue sections were rinsed in PBS, mounted on glass slides to air dry, and cover-slipped with Prolong Gold AntiFade mounting media (ThermoFisher Scientific, Waltham, MA, USA).

2.5. In situ hybridization

Fixed frozen spinal cord tissues were sectioned at a thickness of 10 μm using a cryostat (Leica) for detecting mRNA expression. We performed *in situ* hybridization according to the protocol of the RNAscope Multiplex Fluorescent v2 Assay (Advanced Cell Diagnostics, Newark, CA, USA). Briefly, the spinal cord sections were fixed in 4% paraformaldehyde, dehydrated in ethanol, and treated with H_2O_2, target retrieval reagent, and protease III. The tissues were hybridized with commercial probes for NMBR (# 821681, GRPR (# 821671), protein kinase C γ (PKCG; # 837971; marker for pain processing neurons), vesicular glutamate transporter 2 (VGLUT2; # 540961; marker for excitatory neurons), and vesicular GABA transporter (VGAT; # 428881; marker for inhibitory neurons). Moreover, we visualized the nuclei with the DAPI. The tissue sections were cover-slipped with Prolong Gold AntiFade mounting media, followed by the capture of confocal images using Olympus FV1200 confocal microscope (Olympus America, Center Valley, PA, USA). For quantifying the percentage of co-expression, we captured mosaic images with Z series by setting a fixed matrix that

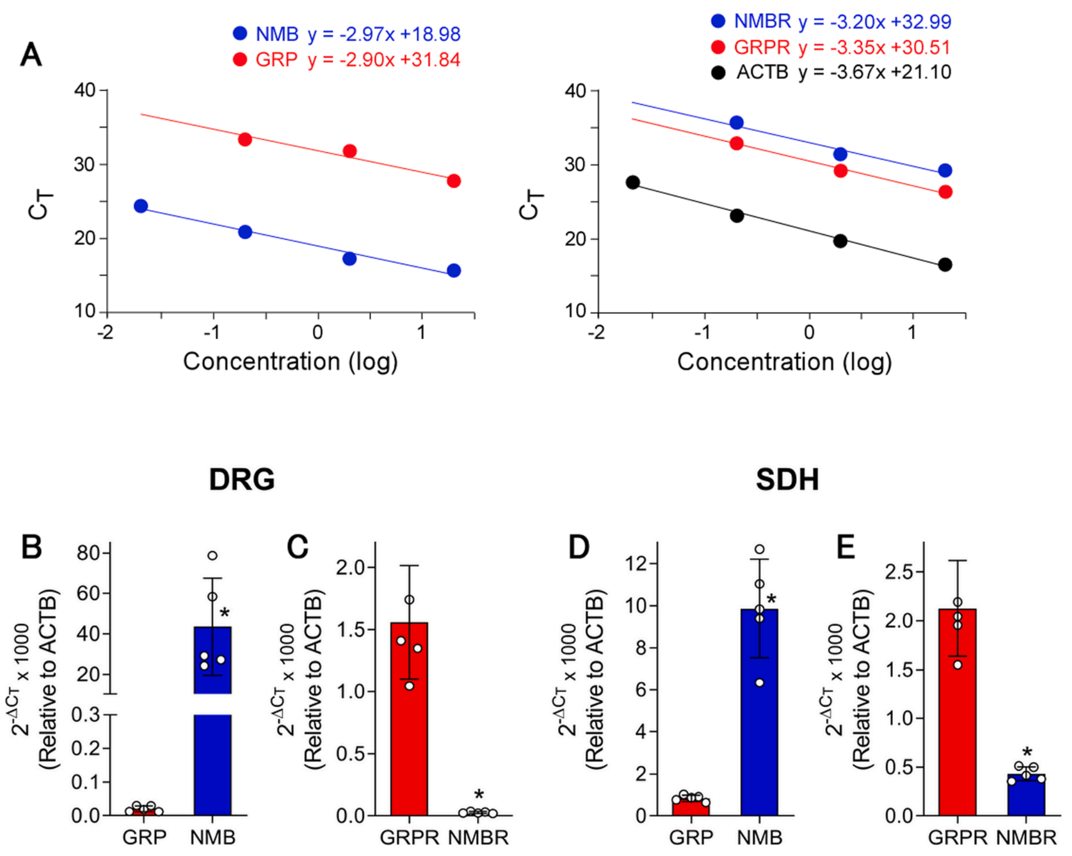

Fig. 1. A comparison of mRNA expression of *GRP* versus *NMB,* and *GRPR* versus *NMBR,* in the dorsal root ganglia and spinal dorsal horn of monkeys. mRNA levels were quantified using RT-qPCR and analyzed by the comparative C_T method. (A) PCR amplification efficiency for each primer (*NMB, GRP, NMBR, GRPR,* and *ACTB*) was determined by the slope of standard curve generated from tenfold serial dilutions (0.02–20 ng) of the cDNA mixture from subjects. (B-E) Relative mRNA expression levels in the dorsal root ganglia (B, C) and spinal dorsal horn (D, E). Data represent the mean ± SD (n = 5), with dots representing individual NHP. Data were analyzed by the paired *t*-test. $^*p < 0.05$, significantly different between *GRP* and *NMB* (B, D) or *GRPR* and *NMBR* (C, E).

contained the entire spinal dorsal horn. To quantify the distribution of $NMBR^+$ and $GRPR^+$ cells, we identified laminae I-III versus IV-V using standard lamination criteria [34]. Cells containing at least three dots of punctate staining were counted with the software Image J, developed by the National Institute of Health (NIH, Bethesda, MD, USA).

2.6. *Itch scratching responses*

We recorded the scratching responses of six animals in their home cages to assess the itching sensation caused by test compounds [35]. Each 15-min recording session followed the i.t. administration of NMB, GRP, or a mixture of NMB or GRP with different antagonists. The number of scratches was the primary outcome. A scratch was defined as one brief (<1 s) scraping on the skin surface of other body parts using the forepaw or hind paw. The total number of scratches for each 15-min period was calculated by experimenters blinded to the dosing conditions.

2.7. *Acute thermal nociception*

We performed the warm water tail-withdrawal assay to measure nociceptive responses of five animals to thermal stimuli and the effects of test compounds [36,37]. The animals were seated in primate restraint chairs, followed by the immersion of lower parts of their shaved tails (~15 cm) in water maintained at 42 °C, 46 °C, or 50 °C. We used water at 42 °C or 46 °C as a normally non-noxious stimulus (i.e., no tail-withdrawal expected), whereas that at 50 °C was used as an acute noxious stimulus (i.e., 2–3 s tail-withdrawal latency); however, it did not cause thermal injury. The tail-withdrawal latency was the primary outcome. The animals were randomly assigned to the dosing condition. Experimenters unaware of the dosing conditions measured the tail-withdrawal latencies at each temperature, randomly using a computerized timer. They recorded a maximum duration of 20 s (the cut-off) if the animal did not withdraw its tail within 20 s. Test sessions commenced with the baseline measurements at each temperature. Subsequently, the tail-withdrawal latencies were measured at 15 min, 30 min, 45 min, and 60 min following the i.t. administration of the test compound.

2.8. *Capsaicin-induced thermal allodynia*

We evaluated the antiallodynic effects of the test compound using a 1-h pretreatment regimen (i.e. 1 h before capsaicin administration) [38,39] in five animals. Capsaicin (1.2 mg/mL × 0.3 mL) was topically administered via a bandage attached to the terminal 3–5 cm of the tail for 15 min. The allodynic response was manifested as reduced tail-withdrawal latency from a maximum value of 20 s to approximately 2–3 s in 46 °C water. The aforementioned allodynic effect peaked at 15 min following the removal of the capsaicin bandage, during which we measured the tail withdrawal latency in 46 °C water (i.e., to determine the antiallodynic effects of the test compound).

2.9. *Drugs*

NMB (Sigma-Aldrich), RC-3095 (Sigma-Aldrich), GRP (Tocris Bioscience, Minneapolis, MN, USA), and DAMGO ([D-Ala^2,*N*-MePhe^4, Gly-ol^5]-enkephalin) (Cayman Chemical, Ann Arbor, MI, USA) were dissolved in sterile water. PD168368 (Tocris) stock solution was

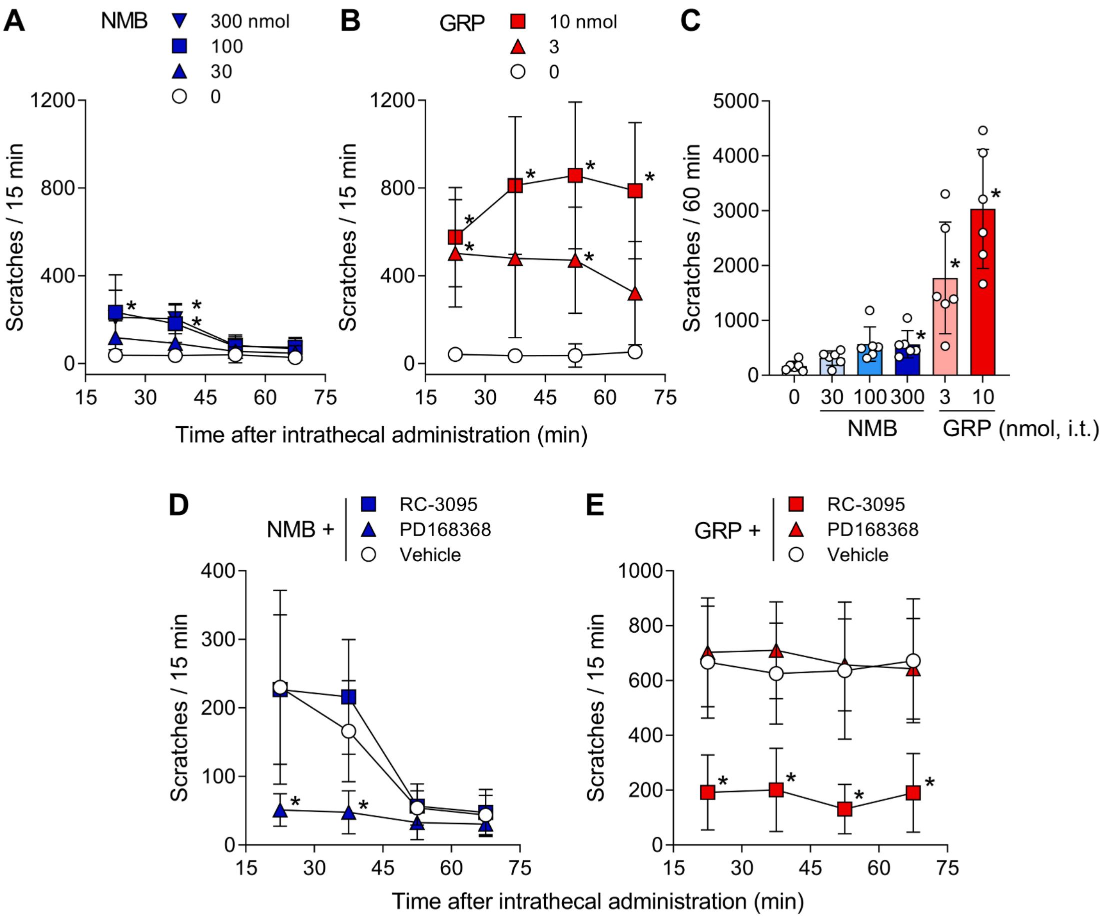

Fig. 2. Effects of intrathecal NMB and GRP on itch scratching responses in monkeys. (A, B) Time courses of itch scratching responses elicited by varying doses of NMB and GRP. (C) Total number of scratches summed from the four time points displayed in A and B. (D, E) Time courses of itch scratching responses elicited by NMB (100 nmol) or GRP (10 nmol), in combination with the GRPR antagonist RC-3095 (100 nmol) or NMBR antagonist PD168368 (300 nmol). Data represent the mean ± SD (n = 6), with dots representing individual NHP. Data were analyzed by the two- (A, B, D, and E) or one-way (C) repeated measures ANOVA, followed by Dunnett's multiple comparison test. $^*p < 0.05$, significantly different from the vehicle condition.

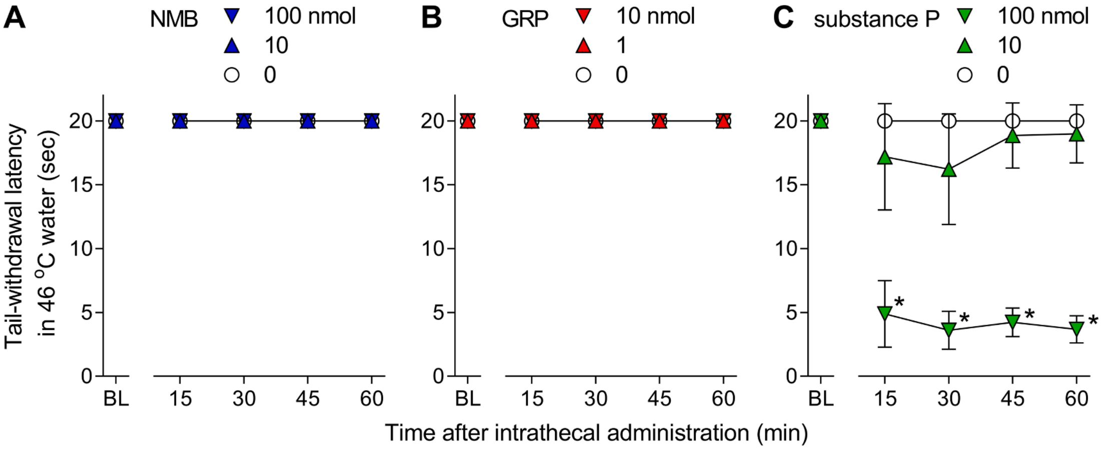

Fig. 3. Effects of intrathecal NMB and GRP on the thermal nociceptive threshold, compared with substance P in monkeys. (A-C) Time courses of tail-withdrawal latencies measured in 46 °C water following the intrathecal administration of varying doses of NMB (A), GRP (B), or substance P (C). Data represent the mean ± SD (n = 5), and were analyzed by the two-way repeated measures ANOVA, followed by Dunnett's multiple comparison test $^*p < 0.05$, significantly different from the vehicle condition.

prepared in a 1:1:8 ratio of dimethyl sulfoxide (ThermoFisher Scientific), Tween 80 (ThermoFisher Scientific) and sterile water, and diluted with sterile water to obtain the target working solution. The doses of these test ligands were based on previous NHP studies [6,35,40]. We administered the drugs intrathecally following a previously described drug delivery procedure [35]. Briefly, the animals were positioned in primate restraint chairs and anesthetized by intravenous propofol (2.5–4.0 mg/kg for bolus infusion and 0.3–0.4 mg/kg/min for

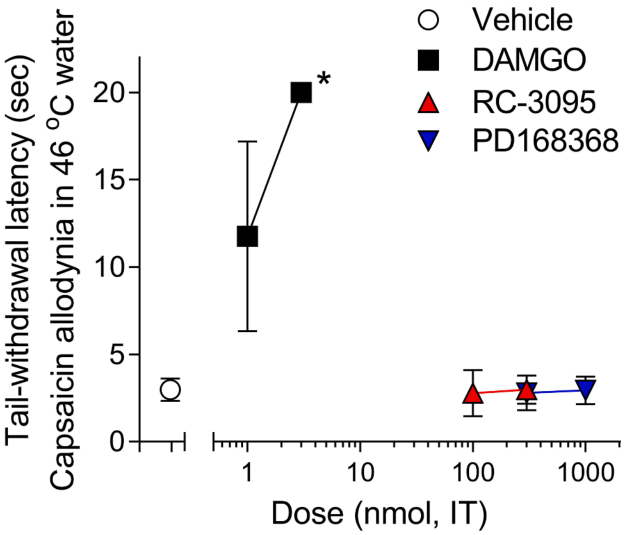

Fig. 4. Effects of intrathecal NMBR and GRPR antagonists on peripherally elicited pain, compared with DAMGO ([D-Ala^2,*N*-MePhe^4,Gly-ol^5]-enkephalin) in monkeys. Topical capsaicin-induced allodynia was evaluated by tail-withdrawal assays in 46 °C water following the intrathecal administration of μ-opioid receptor agonist DAMGO (1 and 3 nmol), GRPR antagonist RC-3095 (100 and 300 nmol), or NMBR antagonist PD168368 (300 and 1000 nmol). Data represent the mean ± SD (n = 5), and were analyzed via a one-way repeated measures ANOVA, followed by Dunnett's multiple comparison test. *$p < 0.05$, significantly different from the vehicle condition.

continuous infusion; AstraZeneca Pharmaceuticals LP, Wilmington, DE, USA). A spinal needle (22-gauge × 1.5; BD Biosciences, Franklin Lakes, NJ, USA) was inserted into the subarachnoid space between the L4/L5 lumbar vertebra. A 1-mL solution of compound was slowly infused through the spinal needle within 30 s. Animals recovered from anesthesia within 10 min after the termination of propofol infusion, and were returned to their home cages.

2.10. Statistical analyses

Data are presented as mean values ± SD. We performed comparisons for similar monkeys across all test sessions for one experiment. We conducted the paired *t*-test (Fig. 1) and two- or one-way repeated measures analysis of variance (ANOVA) (Figs. 2, 3, and 4) to compare the outcome measures (i.e., tail-withdrawal latency and the number of scratches). The criterion for significance was set at p-value < 0.05. We used GraphPad Prism version 9 software for statistical analyses. Behavioral data collection was performed under blinded conditions. No statistical power calculations were performed prior to the study. The sample size was based on our previous experience with this design [38,40].

3. Results

3.1. Expression of NMB, GRP, and their receptors in the DRG and SDH

First, we investigated the gene expression levels of *NMB*, *GRP*, and their receptors in the DRG and SDH of NHPs by RT-qPCR. The slopes of the standard curves for each gene were almost identical, which indicated that the PCR amplification efficiencies were similar among same categories of molecules (Fig. 1A). In both the DRG and SDH, mRNA expression levels of *NMB* (relative to *ACTB*) were substantially greater than those of *GRP* (Fig. 1B, D), whereas the levels of *NMBR* were significantly lower than those of *GRPR* (Fig. 1C, E).

3.2. Effects of i.t. NMB and GRP on itch sensation

We conducted behavioral analyses to evaluate the effects of spinally-delivered NMB and GRP on itch sensation in NHPs. The i.t. administration of NMB transiently elicited scratching behavior in a dose-dependent manner (Fig. 2A, C). In contrast, the i.t. administration of GRP caused robust and prolonged scratching behavior (Fig. 2B, C). NMB-induced scratching behavior was completely blocked by the NMBR antagonist (PD168368), but not the GRPR antagonist (RC-3095) (Fig. 2D). Conversely, GRP-induced scratching behavior was antagonized by RC-3095, but not PD168368 (Fig. 2E).

3.3. Effects of i.t. NMBR or GRPR ligands on pain sensation

Subsequently, we determined the impact of i.t. NMB and GRP on pain sensitivity in NHPs. Neither NMB nor GRP affected withdrawal latency to innoxious stimuli, whereas the i.t. administration of substance P reduced the latency to stimuli, thus displaying thermal allodynia (Fig. 3). Moreover, we assessed the anti-allodynic effects of PD168368 or RC-3095 on capsaicin-induced thermal allodynia. Unlike DAMGO, a μ-opioid receptor agonist with anti-allodynic effects, PD168368 and RC-3095 did not exert an effect on thermal allodynia over the behaviorally active dose range (Fig. 4).

3.4. Localization of NMBR in different subsets of neurons in the SDH

We characterized the distributions of NMBR and GRPR in the SDH. By immunohistochemistry with NeuN antibody that labels neuronal nuclei, protein expressions of NMBR and GRPR were located on the NeuN$^+$ neurons mainly in the superficial laminae and much less in the deeper area (Fig. 5 A, B). By *in situ* hybridization using RNAscope, close to 90% of the NMBR$^+$ neurons and GRPR$^+$ neurons were distributed in laminae I-III and only about 10% were in laminae IV-V (Fig. 6A, D). Less than 20% of the NMBR was colocalized with GRPR (Fig. 6 A, E), and the majority of NMBR and GRPR did not colocalize with PKCG, a marker of pain-responsive neurons (Fig. 6B, C, F). Approximately 60% and 70% of the NMBR$^+$ neurons and GRPR$^+$ neurons, respectively, were VGLUT2$^+$ excitatory neurons (Fig. 7A, B, E), whereas the minority of NMBR$^+$ and GRPR$^+$ neurons were VGAT$^+$ inhibitory neurons in the SDH (Fig. 7C, D, F).

4. Discussion

We provided three key findings to define the functional roles of the NMB-NMBR system in the SDH of NHPs. First, the i.t. administration of NMB elicited a milder scratching behavior with lower potency than GRP. Moreover, the activation of spinal NMB-NMBR or GRP-GRPR systems resulted in scratching responses via independent receptor mechanisms. Second, i.t. NMB and GRP did not induce thermal hypersensitivity. Neither did i.t. NMBR and GRPR antagonists modulate peripherally elicited thermal allodynia induced by capsaicin. Third, NMBR displayed lower expression in both itch- and pain-responsive neurons in the SDH, namely GRPR$^+$ and PKCγ^+, respectively. In other words, the spinal NMB-NMBR system plays a limited role in the neurotransmission of itch and pain in NHPs.

Exploring the functional roles of spinal NMB-NMBR and GRP-GRPR systems in regulating itch and pain in primates necessitates determining their expression patterns in the sensory neurons and SDH. Despite the functional significance of GRP in itch transmission [8,19,41,42], sources of GRP contributing to itch sensation are still controversial in rodents. GRP is produced in the interneurons located on the SDH [43–45], whereas a recent report demonstrated that functionally-important GRP is located on the sensory neurons, despite lower expression levels of GRP in the DRG than that in the SDH [46]. Nevertheless, expression patterns of GRP in NHPs are consistent with findings from rodent studies that GRP-expressing cells are principally located on the SDH, but not the

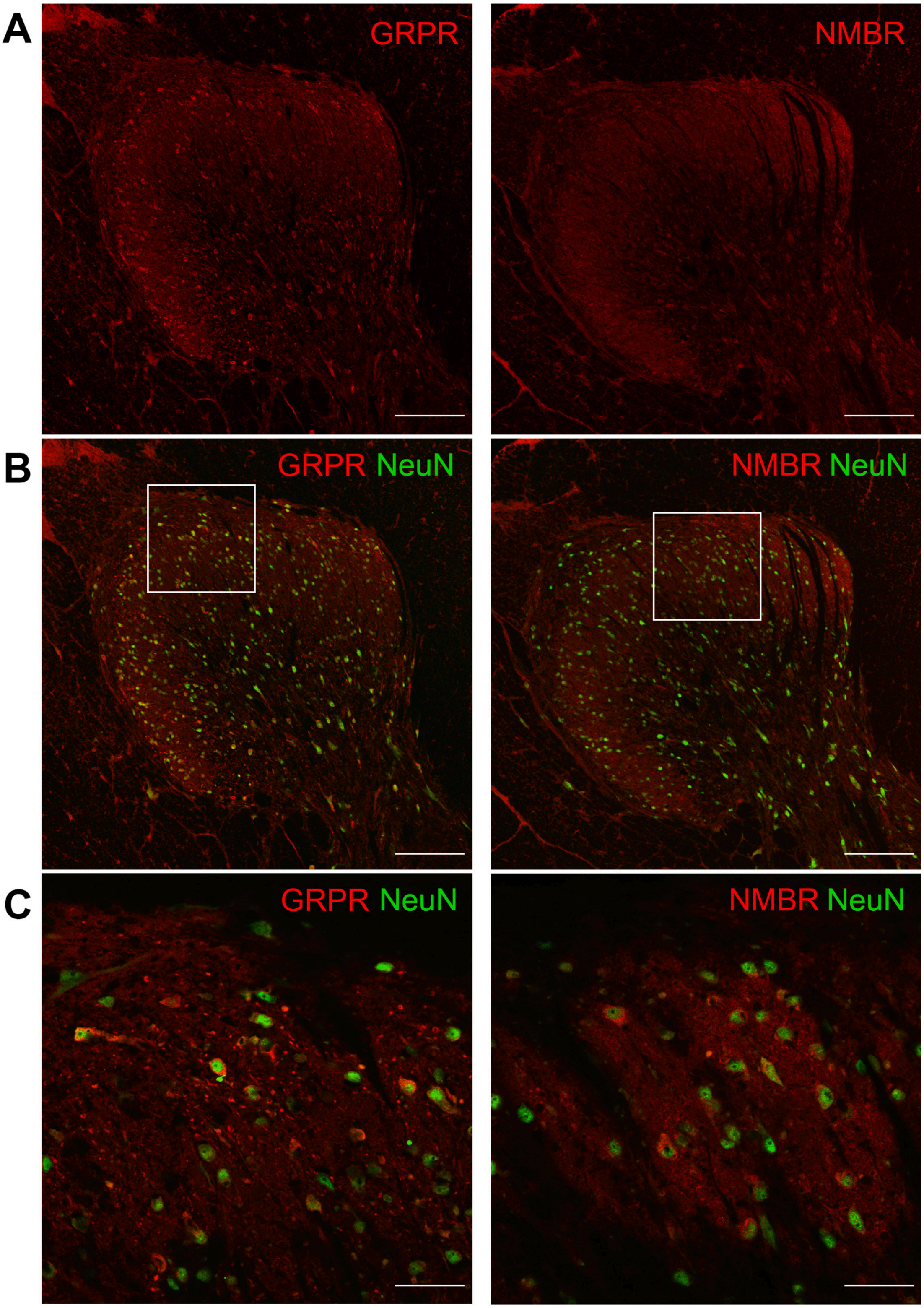

Fig. 5. Expression of NMBR and GRPR protein in the spinal dorsal horn of monkeys. (A, B) Representative images of immunohistochemistry depict the expression of GRPR (left column) and NMBR (right column) in NeuN$^+$ cells. (C) Higher magnification of the boxed areas in (B). Scale bar = 200 μm (A, B), and 50 μm (C).

DRG. However, NMB is produced by DRG neurons and contributes to nociceptive transmission in rodents [15,18,47]. The expression levels of NMB are greater than that of GRP in both the DRG and SDH of NHPs, thus suggesting NMB may modulate sensory processing, such as itch, in NHPs. Regardless of the exact neuroanatomical site releasing endogenous ligands, it is important to understand that NMB and GRP are released within the SDH, and subsequently mediate itch sensation. I.t. GRP elicited robust scratching behavior, whereas NMB caused mild scratching behavior. The expression patterns of NMB and NMBR in comparison with GRP and GRPR in NHPs are similar to a previous study performed in dogs [48]. Possibly, lower expression levels of NMBR relative to GRPR and shorter half-life of neuromedin peptides may

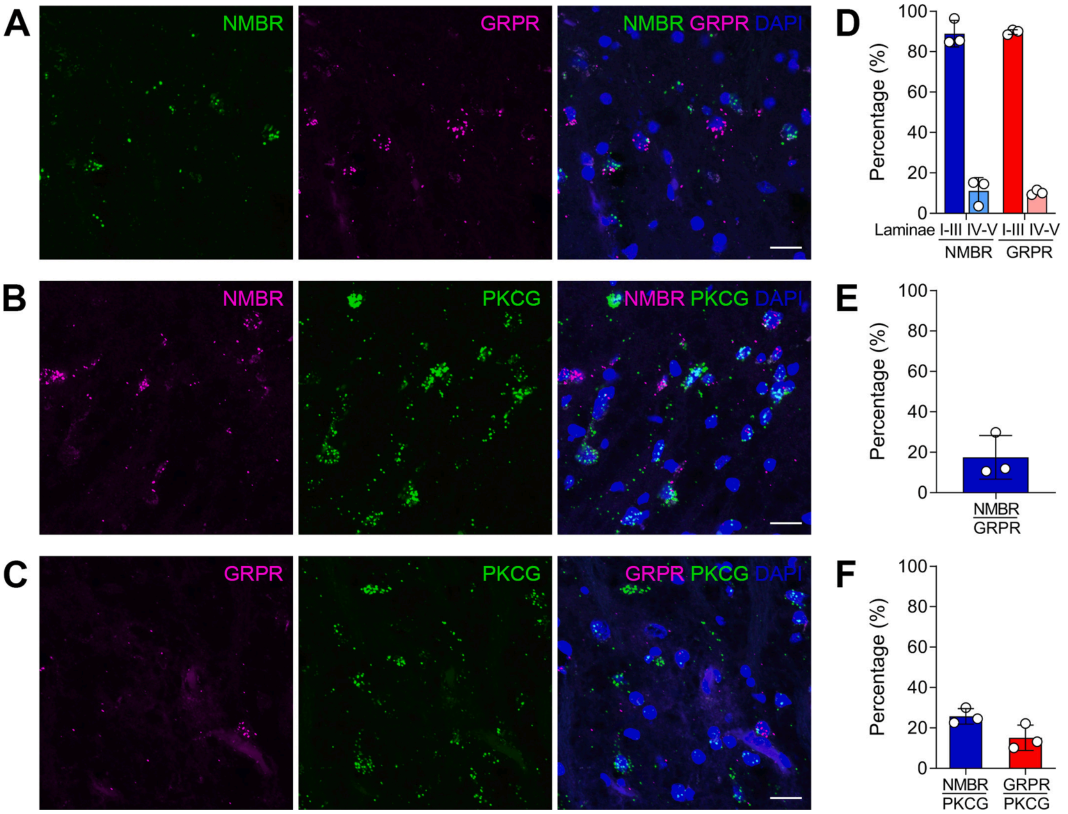

Fig. 6. Expression of NMBR and GRPR mRNA in the spinal dorsal horn of monkeys (A-C). Representative confocal images of *in situ* hybridization (RNAscope) depict the mRNA expression of NMBR in GRPR$^+$ (A) or PKCG$^+$ neurons (B) and the mRNA expression of GRPR in PKCG$^+$ neurons (C). (D) Quantification of the distribution of NMBR$^+$ and GRPR$^+$ neurons in laminae I-III and IV-V of the spinal dorsal horn. (E, F) Bar graphs depict the percentage of co-expression. Data represent the mean ± SD (n = 3), with dots representing individual NHP. Scale bar = 20 μm.

explain these behavioral differences in scratching [49]. Higher expression level of NMB in the peripheral tissues may indicate that this peptide is involved in other peripheral functions such as muscle contraction and endocrine secretion [12,13]. Moreover, the majority of NMBR and GRPR are distributed on different subpopulations, and rarely observed in PKCγ$^+$ pain-associated neurons. Therefore, NMB-NMBR and GRP-GRPR pairs in spinal cord may not significantly contribute to pain in primates.

Itch-associated functions of NMB have been determined in rodents, as the i.t. or intracerebroventricular administration of NMB increases scratching behavior. Although i.t.-administered agents could be distributed in the DRG [50], the likelihood of i.t. NMB acting on NMBR in the DRG seems low as NMBR is expressed in the DRG of NHPs at a minimal level compared to the SDH. This may indicate a species difference considering that i.t. NMB affected the NMBR-expressing DRG neurons in rodents [51]. Scratching responses by centrally administered NMB were considerably lower than those of GRP [14,16,17]. Nevertheless, another group demonstrated that NMB-induced scratching responses were significantly higher than those of GRP, based on a single dose in mice [15,19]. Different mouse strains or species may contribute to the aforementioned discrepancy. Herein, the full dose-response curve confirmed the mild scratching effects of NMB, compared with GRP in the same group of NHPs, consistent with previous rodent studies [14,16,17,52]. NMB and GRP bind to NMBR and GRPR, respectively; however, the cross-reactivity of NMB and GRP against other receptors (i.e., GRP to NMBR) constitute the cross-binding theory for itch regulation in rodents [15]. In primates, NMB-induced scratching responses were blocked by a NMBR antagonist, but not a GRPR antagonist, and *vice versa*, consistent with other rodent studies [16]. Therefore, each ligand (NMB and GRP) acts on its cognate receptor to elicit scratching. Unlike substance P, i.t. NMB and GRP did not affect pain sensitivity in NHPs, despite NMB-induced thermal hypersensitivity in rodents [18]. I.t. GRP did not exert anti-hypersensitive effects on carrageenan-induced thermal hyperalgesia in NHPs [6]. Furthermore, we tested if NMBR and GRPR antagonists affected thermal hypersensitivity. Normally, μ-opioid receptor agonists, such as DAMGO and morphine, induce significant antinociceptive and antiallodynic effects in rodents and primates [53]. Unlike DAMGO, neither NMBR nor GRPR antagonists attenuated capsaicin-induced allodynia. Therefore, the spinal NMB-NMBR system partially contributed to itch; however, it did not affect pain regulation in NHPs.

Behaviorally, NMB and GRP only acted on their cognate receptors for regulating itch in NHPs. Anatomically, NMB-saporin only ablated NMBR$^+$ neurons, but not GRPR$^+$ neurons, and *vice versa* in rodents [15,18]. In NHPs, the localization of NMBR and GRPR were restricted to the NeuN$^+$ neurons. Moreover, the aforementioned receptors were principally expressed in VGLUT2$^+$ excitatory interneurons, but not in VGAT$^+$ inhibitory neurons. Therefore, both NMB-NMBR and GRP-GRPR systems directly facilitated itch transmission in the SDH. The majority of NMBR did not colocalize with GRPR, a marker of itch-responsive neurons, in the SDH of both rodents and NHPs. Thus, NMB-NMBR and GRP-GRPR systems may activate the spinal transmission of itch via independent mechanisms. Particularly, the spinal NMB-NMBR system plays a functional role in regulating mild itch.

The pharmacological effects of ligand-receptor systems vary between rodents and primates [23,24]. Particularly, opioid ligands (i.e., μ-opioid receptor and nociceptin receptor agonists) often exert diverse effects in sensory processing between rodents and primates [54,55]. μ-opioid receptor agonists, such as morphine, produces itch sensation in humans and exerts robust scratching behavior in NHPs [36,56]. However, the degree of scratching behavior caused by μ-opioid receptor agonists in rodents is considerably less than that in NHPs [16,27], thereby indicating itch sensation elicited by μ-opioid receptor agonists in humans is

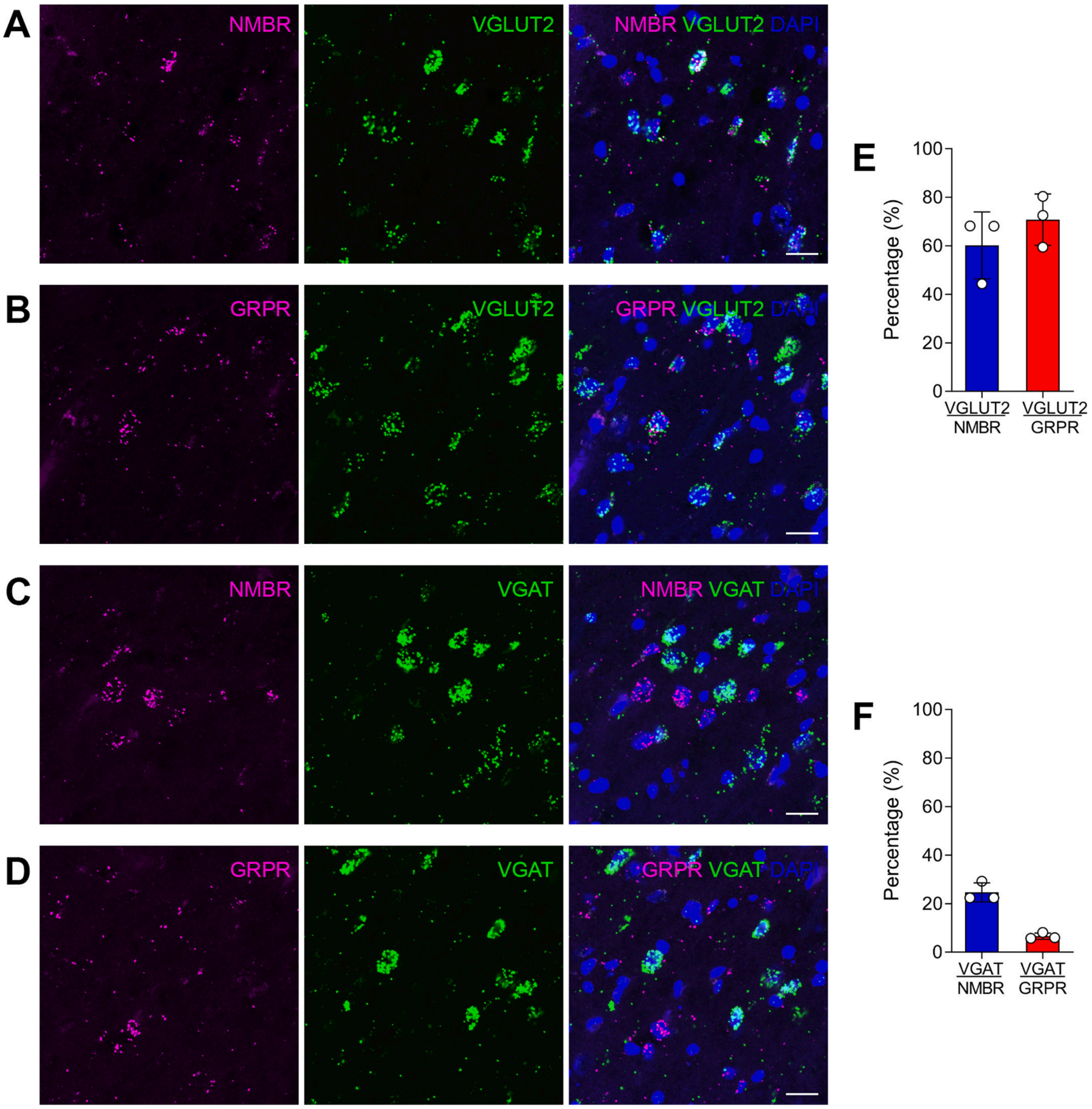

Fig. 7. Expression of VGLUT2 and VGAT mRNA in NMBR$^+$ and GRPR$^+$ neurons in the spinal dorsal horn of monkeys. (A-D) Representative confocal images of *in situ* hybridization (RNAscope) show the mRNA expression of VGLUT2 in NMBR$^+$ (A) or GRPR$^+$ (B) neurons and the mRNA expression of VGAT in NMBR$^+$ (C) or GRPR$^+$ (D) neurons. (E, F) Bar graphs show the percentage of co-expression. Data represent the mean ± SD (n = 3) with dots representing individual NHP. Scale bar = 20 μm.

modeled in NHPs, but not in rodents [23]. Moreover, nociceptin receptor agonists demonstrate differential effects between rodents and NHPs. The effects of an endogenous nociceptin receptor agonist, nociceptin/orphanin FQ, on pain regulation in rodents depends on the administration route or pain modality [24,55], whereas nociceptin/orphanin FQ exerts distinct antinociceptive effects in NHPs under varied experimental conditions [25,54]. Therefore, pharmacological and behavioral studies in NHPs are pivotal for the translational relevance in humans [23]. GRP-induced scratching behavior is robust in both rodents and primates; thus, it may be reasonable to emphasize the functional and translational significance of GRP and explore the neurobiological mechanisms of itch mediated by the GRP-GRPR system in rodents. In contrast, i.t. NMB caused mild scratching behavior in NHPs; however, the potency was $< 1/100$, compared with that of GRP. Moreover, intradermal NMB resulted in weak scratching behavior in NHPs [51]. Taken together, NMB is highly expressed in the DRG and SDH, but the NMB-NMBR pair plays a minimal “functional” role in regulating itch than the GRP-GRPR pair in primates. Both NMBR$^+$ and GRPR$^+$ neurons are mainly expressed in laminae I-III of SDH, which may not explain the observed differences between GRP and NMB in NHP behavioral tests. Further studies are warranted to elucidate the other functions of NMB in the peripheral tissues and central nervous system [12].

By focusing the translational relevance of the spinal NMB-NMBR system previously evaluated only in rodents, our study revealed the neuroanatomical and functional evidence for the NMB-NMBR system in primates. Spinal NMB-NMBR and GRP-GRPR systems can independently elicit scratching; nonetheless, both systems are insignificantly involved in pain regulation. In terms of the expression patterns of NMB and NMBR in the DRG and SDH, our findings for NHPs were consistent with previous studies in rodents. Despite the high expression of NMB in DRG and SDH, low expression of NMBR in the GRPR$^+$ neurons of the SDH may limit its function in regulating itch. Unlike the functional significance of spinal GRP-GRPR system in itch, drugs targeting the spinal NMB-NMBR system may not effectively alleviate non-NMBR-mediated itch. This warrants future neuropharmacological studies assessing translational properties from rodents to primates to validate the functional significance of these target molecules.

CRediT authorship contribution statement

Norikazu Kiguchi: Conceptualization, Methodology, Validation, Formal analysis, Investigation, Writing – original draft, Writing – review

& editing. **Huiping Ding:** Conceptualization, Methodology, Validation, Formal analysis, Investigation, Writing – original draft, Writing – review & editing. **Sun H. Park:** Validation, Investigation, Writing – review & editing. **Kelsey M. Mabry:** Validation, Investigation, Writing – review & editing. **Shiroh Kishioka:** Validation, Writing – review & editing. **Yusuke Shiozawa:** Validation, Writing – review & editing. **E. Alfonso Romero-Sandoval:** Validation, Writing – review & editing. **Christopher M. Peters:** Validation, Investigation, Writing – review & editing. **Mei-Chuan Ko:** Conceptualization, Methodology, Validation, Formal analysis, Writing – original draft, Writing – review & editing, Supervision, Project administration, Funding acquisition.

Declaration of Competing Interest

The authors declare that they have no known competing financial interests or personal relationships that could have appeared to influence the work reported in this paper.

Acknowledgements

This study was supported by the US-PHS grants AR064456 and AR069861. The content is the sole responsibility of the authors and does not necessarily represent the official views of the U.S. federal agencies. We thank Ms. Brittany Kelly for her technical assistance with animal training and data collection and the Animal Resources Program of Wake Forest School of Medicine for veterinary care.

References

[1] T. Hashimoto, G. Yosipovitch, Itching as a systemic disease, J. Allergy Clin. Immunol. 144 (2) (2019) 375–380.
[2] R.J. Hay, N.E. Johns, H.C. Williams, I.W. Bolliger, R.P. Dellavalle, D.J. Margolis, R. Marks, L. Naldi, M.A. Weinstock, S.K. Wulf, C. Michaud, J.L.M. Christopher, M. Naghavi, The global burden of skin disease in 2010: an analysis of the prevalence and impact of skin conditions, J. Invest. Dermatol. 134 (6) (2014) 1527–1534.
[3] E. Carstens, T. Follansbee, M. Carstens, The Challenge of Basic Itch Research, Acta Derm. Venereol. 100 (2) (2020) 3–9.
[4] G. Yosipovitch, T. Hashimoto, Itch: From mechanism to (novel) therapeutic approaches, J. Allergy Clin. Immunol. 142 (5) (2018) 1375–1390.
[5] X. Dong, X. Dong, Peripheral and Central Mechanisms of Itch, Neuron 98 (3) (2018) 482–494.
[6] H. Lee, M.C. Ko, Distinct functions of opioid-related peptides and gastrin-releasing peptide in regulating itch and pain in the spinal cord of primates, Sci. Rep. 5 (2015) 11676.
[7] Y.-G. Sun, Z.-F. Chen, A gastrin-releasing peptide receptor mediates the itch sensation in the spinal cord, Nature 448 (7154) (2007) 700–703.
[8] N. Kiguchi, D. Uta, H. Ding, H. Uchida, F. Saika, S. Matsuzaki, Y. Fukazawa, M. Abe, K. Sakimura, M.C. Ko, S. Kishioka, GRP receptor and AMPA receptor cooperatively regulate itch-responsive neurons in the spinal dorsal horn, Neuropharmacology 170 (2020), 108025.
[9] Y.-G. Sun, Z.-Q. Zhao, X.-L. Meng, J. Yin, X.-Y. Liu, Z.-F. Chen, Cellular basis of itch sensation, Science 325 (5947) (2009) 1531–1534.
[10] X. Liu, D.e. Wang, Y. Wen, L. Zeng, Y. Li, T. Tao, Z. Zhao, A. Tao, Spinal GRPR and NPRA Contribute to Chronic Itch in a Murine Model of Allergic Contact Dermatitis, J. Invest. Dermatol. 140 (9) (2020) 1856–1866.e7.
[11] K. Koga, R. Yamagata, K. Kohno, T. Yamane, M. Shiratori-Hayashi, Y. Kohro, H. Tozaki-Saitoh, M. Tsuda, Sensitization of spinal itch transmission neurons in a mouse model of chronic itch requires an astrocytic factor, J. Allergy Clin. Immunol. 145 (1) (2020) 183–191.e10.
[12] R.T. Jensen, J.F. Battey, E.R. Spindel, R.V. Benya, International Union of Pharmacology. LXVIII. Mammalian bombesin receptors: nomenclature, distribution, pharmacology, signaling, and functions in normal and disease states, Pharmacol. Rev. 60 (1) (2008) 1–42.
[13] H. Ohki-Hamazaki, Neuromedin B, Prog. Neurobiol. 62 (3) (2000) 297–312.
[14] A. Masui, N. Kato, T. Itoshima, K. Tsunashima, T. Nakajima, N. Yanaihara, Scratching behavior induced by bombesin-related peptides. Comparison of bombesin, gastrin-releasing peptide and phyllolitorins, Eur. J. Pharmacol. 238 (2-3) (1993) 297–301.
[15] Z.-Q. Zhao, L. Wan, X.-Y. Liu, F.-Q. Huo, H. Li, D.M. Barry, S. Krieger, S. Kim, Z.-C. Liu, J. Xu, B.E. Rogers, Y.-Q. Li, Z.-F. Chen, Cross-inhibition of NMBR and GRPR signaling maintains normal histaminergic itch transmission, J. Neurosci. 34 (37) (2014) 12402–12414.
[16] D.D. Sukhtankar, M.C. Ko, Physiological function of gastrin-releasing peptide and neuromedin B receptors in regulating itch scratching behavior in the spinal cord of mice, PLoS One 8 (6) (2013) e67422.
[17] P.-Y. Su, M.-C. Ko, The role of central gastrin-releasing peptide and neuromedin B receptors in the modulation of scratching behavior in rats, J. Pharmacol. Exp. Ther. 337 (3) (2011) 822–829.
[18] S.K. Mishra, S. Holzman, M.A. Hoon, A nociceptive signaling role for neuromedin B, J. Neurosci. 32 (25) (2012) 8686–8695.
[19] L. Wan, H. Jin, X.Y. Liu, J. Jeffry, D.M. Barry, K.F. Shen, J.H. Peng, X.T. Liu, J. H. Jin, Y. Sun, R. Kim, Q.T. Meng, P. Mo, J. Yin, A. Tao, R. Bardoni, Z.F. Chen, Distinct roles of NMB and GRP in itch transmission, Sci. Rep. 7 (1) (2017) 15466.
[20] B.A. Strange, M.P. Witter, E.S. Lein, E.I. Moser, Functional organization of the hippocampal longitudinal axis, Nat. Rev. Neurosci. 15 (10) (2014) 655–669.
[21] J. Seok, H.S. Warren, A.G. Cuenca, M.N. Mindrinos, H.V. Baker, W. Xu, D. R. Richards, G.P. McDonald-Smith, H. Gao, L. Hennessy, C.C. Finnerty, C.M. Lopez, S. Honari, E.E. Moore, J.P. Minei, J. Cuschieri, P.E. Bankey, J.L. Johnson, J. Sperry, A.B. Nathens, T.R. Billiar, M.A. West, M.G. Jeschke, M.B. Klein, R.L. Gamelli, N. S. Gibran, B.H. Brownstein, C. Miller-Graziano, S.E. Calvano, P.H. Mason, J. P. Cobb, L.G. Rahme, S.F. Lowry, R.V. Maier, L.L. Moldawer, D.N. Herndon, R. W. Davis, W. Xiao, R.G. Tompkins, L.S.C.R.P. Inflammation, Host Response to Injury, Genomic responses in mouse models poorly mimic human inflammatory diseases, Proc. Natl. Acad. Sci. USA 110 (9) (2013) 3507–3512.
[22] S. Shiers, R.M. Klein, T.J. Price, Quantitative differences in neuronal subpopulations between mouse and human dorsal root ganglia demonstrated with RNAscope in situ hybridization, Pain 161 (10) (2020) 2410–2424.
[23] H. Ding, M.C. Ko, Translational value of non-human primates in opioid research, Exp. Neurol. 338 (2021), 113602.
[24] N. Kiguchi, H. Ding, M.C. Ko, Central N/OFQ-NOP Receptor System in Pain Modulation, Adv. Pharmacol. 75 (2016) 217–243.
[25] N. Kiguchi, M.C. Ko, Effects of NOP-Related Ligands in Nonhuman Primates, Handb. Exp. Pharmacol. 254 (2019) 323–343.
[26] N. Kiguchi, H. Ding, G. Cami-Kobeci, D.D. Sukhtankar, P.W. Czoty, H.B. DeLoid, F. C. Hsu, L. Toll, S.M. Husbands, M.C. Ko, BU10038 as a safe opioid analgesic with fewer side-effects after systemic and intrathecal administration in primates, Br. J. Anaesth. 122 (6) (2019) e146–e156.
[27] X.Y. Liu, Z.C. Liu, Y.G. Sun, M. Ross, S. Kim, F.F. Tsai, Q.F. Li, J. Jeffry, J.Y. Kim, H. H. Loh, Z.F. Chen, Unidirectional cross-activation of GRPR by MOR1D uncouples itch and analgesia induced by opioids, Cell 147 (2) (2011) 447–458.
[28] E. Nguyen, G. Lim, H. Ding, J. Hachisuka, M.C. Ko, S.E. Ross, Morphine acts on spinal dynorphin neurons to cause itch through disinhibition, Sci. Transl. Med. 13 (579) (2021).
[29] N. Kiguchi, D.D. Sukhtankar, H. Ding, K. Tanaka, S. Kishioka, C.M. Peters, M.C. Ko, Spinal Functions of B-Type Natriuretic Peptide, Gastrin-Releasing Peptide, and Their Cognate Receptors for Regulating Itch in Mice, J. Pharmacol. Exp. Ther. 356 (3) (2016) 596–603.
[30] H. Sano, S.D. Feighner, D.L. Hreniuk, H. Iwaasa, A.W. Sailer, J. Pan, M.L. Reitman, A. Kanatani, A.D. Howard, C.P. Tan, Characterization of the bombesin-like peptide receptor family in primates, Genomics 84 (1) (2004) 139–146.
[31] C. Kilkenny, W. Browne, I.C. Cuthill, M. Emerson, D.G. Altman, N.C.R.R.G. W. Group, Animal research: reporting in vivo experiments: the ARRIVE guidelines, Br. J. Pharmacol. 160 (7) (2010) 1577–1579.
[32] N. Kiguchi, H. Ding, C.M. Peters, N.D. Kock, S. Kishioka, J.M. Cline, J.D. Wagner, M.C. Ko, Altered expression of glial markers, chemokines, and opioid receptors in the spinal cord of type 2 diabetic monkeys, Biochim. Biophys. Acta, Mol. Basis Dis. 1863 (1) (2017) 274–283.
[33] T.D. Schmittgen, K.J. Livak, Analyzing real-time PCR data by the comparative C(T) method, Nat. Protoc. 3 (6) (2008) 1101–1108.
[34] G. Sengul, C. Watson, I. Tanaka, G. Paxinos, Atlas of the Spinal Cord: Mouse, Rat, Rhesus, Marmoset, and Human, Academic Press, 2012.
[35] M.C. Ko, M.S. Song, T. Edwards, H. Lee, N.N. Naughton, The role of central mu opioid receptors in opioid-induced itch in primates, J. Pharmacol. Exp. Ther. 310 (1) (2004) 169–176.
[36] H. Ding, N. Kiguchi, D.A. Perrey, T. Nguyen, P.W. Czoty, F.C. Hsu, Y. Zhang, M. C. Ko, Antinociceptive, reinforcing, and pruritic effects of the G-protein signalling-biased mu opioid receptor agonist PZM21 in non-human primates, Br. J. Anaesth. 125 (4) (2020) 596–604.
[37] M.C. Ko, M.D. Johnson, E.R. Butelman, K.J. Willmont, H.I. Mosberg, J.H. Woods, Intracisternal nor-binaltorphimine distinguishes central and peripheral kappa-opioid antinociception in rhesus monkeys, J. Pharmacol. Exp. Ther. 291 (3) (1999) 1113–1120.
[38] H. Ding, N. Kiguchi, D. Yasuda, P.R. Daga, W.E. Polgar, J.J. Lu, P.W. Czoty, S. Kishioka, N.T. Zaveri, M.C. Ko, A bifunctional nociceptin and mu opioid receptor agonist is analgesic without opioid side effects in nonhuman primates, Sci. Transl. Med. 10 (456) (2018).
[39] M.C. Ko, E.R. Butelman, J.H. Woods, Activation of peripheral kappa opioid receptors inhibits capsaicin-induced thermal nociception in rhesus monkeys, J. Pharmacol. Exp. Ther. 289 (1) (1999) 378–385.
[40] H. Ding, K. Hayashida, T. Suto, D.D. Sukhtankar, M. Kimura, V. Mendenhall, M. C. Ko, Supraspinal actions of nociceptin/orphanin FQ, morphine and substance P in regulating pain and itch in non-human primates, Br. J. Pharmacol. 172 (13) (2015) 3302–3312.
[41] M. Pagani, G.W. Albisetti, N. Sivakumar, H. Wildner, M. Santello, H.C. Johannssen, H.U. Zeilhofer, How Gastrin-Releasing Peptide Opens the Spinal Gate for Itch, Neuron 103 (1) (2019) 102e5–117e5.
[42] T. Akiyama, M. Tominaga, K. Takamori, M.I. Carstens, E. Carstens, Roles of glutamate, substance P, and gastrin-releasing peptide as spinal neurotransmitters of histaminergic and nonhistaminergic itch, Pain 155 (1) (2014) 80–92.
[43] N. Kiguchi, Y. Fukazawa, A. Saika, D. Uta, F. Saika, T.Y. Nakamura, M.C. Ko, S. Kishioka, Chemogenetic activation of central gastrin-releasing peptide-

expressing neurons elicits itch-related scratching behavior in male and female mice, Pharmacol. Res. Perspect. 9 (3) (2021), e00790.

[44] M. Haring, A. Zeisel, H. Hochgerner, P. Rinwa, J.E.T. Jakobsson, P. Lonnerberg, G. La Manno, N. Sharma, L. Borgius, O. Kiehn, M.C. Lagerstrom, S. Linnarsson, P. Ernfors, Neuronal atlas of the dorsal horn defines its architecture and links sensory input to transcriptional cell types, Nat. Neurosci. 21 (6) (2018) 869–880.

[45] M. Gutierrez-Mecinas, M. Watanabe, A.J. Todd, Expression of gastrin-releasing peptide by excitatory interneurons in the mouse superficial dorsal horn, Mol. Pain 10 (2014) 79.

[46] D.M. Barry, X.T. Liu, B. Liu, X.Y. Liu, F. Gao, X. Zeng, J. Liu, Q. Yang, S. Wilhelm, J. Yin, A. Tao, Z.F. Chen, Exploration of sensory and spinal neurons expressing gastrin-releasing peptide in itch and pain related behaviors, Nat. Commun. 11 (1) (2020) 1397.

[47] M.S. Fleming, D. Ramos, S.B. Han, J. Zhao, Y.J. Son, W. Luo, The majority of dorsal spinal cord gastrin releasing peptide is synthesized locally whereas neuromedin B is highly expressed in pain- and itch-sensing somatosensory neurons, Mol. Pain 8 (2012) 52.

[48] J.J. Wheeler, B.D. Lascelles, T. Olivry, S.K. Mishra, Itch-associated Neuropeptides and Their Receptor Expression in Dog Dorsal Root Ganglia and Spinal Cord, Acta Derm. Venereol. 99 (12) (2019) 1131–1135.

[49] B. Gevaert, E. Wynendaele, S. Stalmans, N. Bracke, M. D'Hondt, I. Smolders, A. van Eeckhaut, B. De Spiegeleer, Blood-brain barrier transport kinetics of the neuromedin peptides NMU, NMN, NMB and NT, Neuropharmacology 107 (2016) 460–470.

[50] Y. Kawasaki, Z.Z. Xu, X. Wang, J.Y. Park, Z.Y. Zhuang, P.H. Tan, Y.J. Gao, K. Roy, G. Corfas, E.H. Lo, R.R. Ji, Distinct roles of matrix metalloproteases in the early- and late-phase development of neuropathic pain, Nat. Med. 14 (3) (2008) 331–336.

[51] S. Ehling, T. Fukuyama, M.C. Ko, T. Olivry, W. Baumer, Neuromedin B Induces Acute Itch in Mice via the Activation of Peripheral Sensory Neurons, Acta Derm. Venereol. 99 (6) (2019) 587–893.

[52] J.F. Bishop, T.W. Moody, T.L. O'Donohue, Peptide transmitters of primary sensory neurons: similar actions of tachykinins and bombesin-like peptides, Peptides 7 (5) (1986) 835–842.

[53] Z. Wang, C. Jiang, Q. He, M. Matsuda, Q. Han, K. Wang, S. Bang, H. Ding, M.C. Ko, R.R. Ji, Anti-PD-1 treatment impairs opioid antinociception in rodents and nonhuman primates, Sci. Transl. Med. 12 (531) (2020).

[54] N. Kiguchi, H. Ding, M.C. Ko, Therapeutic potentials of NOP and MOP receptor coactivation for the treatment of pain and opioid abuse, J. Neurosci. Res. 100 (1) (2022) 191–202.

[55] W. Schroder, D.G. Lambert, M.C. Ko, T. Koch, Functional plasticity of the N/OFQ-NOP receptor system determines analgesic properties of NOP receptor agonists, Br. J. Pharmacol. 171 (16) (2014) 3777–3800.

[56] H. Ding, C. Trapella, N. Kiguchi, F.C. Hsu, G. Calo, M.C. Ko, Functional Profile of Systemic and Intrathecal Cebranopadol in Nonhuman Primates, Anesthesiology 135 (3) (2021) 482–493.

European Journal of Nuclear Medicine and Molecular Imaging (2021) 48:3408–3421
https://doi.org/10.1007/s00259-021-05315-1

ORIGINAL ARTICLE

Preclinical evaluation of [^{225}Ac]Ac-DOTA-TATE for treatment of lung neuroendocrine neoplasms

Narges K. Tafreshi[1] · Darpan N. Pandya[2] · Christopher J. Tichacek[3,4,5] · Mikalai M. Budzevich[6] · Zhen Wang[7] · Jordan N. Reff[1] · Robert W. Engelman[8] · David C. Boulware[9] · Alberto A. Chiappori[10] · Jonathan R. Strosberg[11] · Haitao Ji[7] · Thaddeus J. Wadas[2] · Ghassan El-Haddad[12] · David L. Morse[1,4,5,6]

Received: 5 January 2021 / Accepted: 10 March 2021 / Published online: 26 March 2021

Abstract

Purpose There is significant interest in the development of targeted alpha-particle therapies (TATs) for treatment of solid tumors. The metal chelator-peptide conjugate, DOTA-TATE, loaded with the β-particle emitting radionuclide ^{177}Lu ([^{177}Lu]Lu-DOTA-TATE) is now standard care for neuroendocrine tumors that express the somatostatin receptor 2 (SSTR2) target. A recent clinical study demonstrated efficacy of the corresponding [^{225}Ac]Ac-DOTA-TATE in patients that were refractory to [^{177}Lu]Lu-DOTA-TATE. Herein, we report the radiosynthesis, toxicity, biodistribution (BD), radiation dosimetry (RD), and efficacy of [^{225}Ac]Ac-DOTA-TATE in small animal models of lung neuroendocrine neoplasms (NENs).

Methods [^{225}Ac]Ac-DOTA-TATE was synthesized and characterized for radiochemical yield, purity and stability. Non-tumor–bearing BALB/c mice were tested for toxicity and BD. Efficacy was determined by single intravenous injection of [^{225}Ac]Ac-DOTA-TATE into SCID mice–bearing human SSTR2 positive H727 and H69 lung NENs. RD was calculated using the BD data.

Results [^{225}Ac]Ac-DOTA-TATE was synthesized with 98% yield, 99.8% purity, and displayed 97% stability after 2 days incubation in human serum at 37 °C. All animals in the toxicity study appeared healthy 5 months post injection with no indications of toxicity, except that animals that received $\geq$111 kBq of [^{225}Ac]Ac-DOTA-TATE had chronic progressive nephropathy. BD studies revealed that the primary route of elimination is by the renal route. RD calculations determined pharmacokinetics parameters and absorbed α-emission dosages from ^{225}Ac and its daughters. For both tumor models, a significant tumor growth delay and time to experimental endpoint were observed following a single administration of [^{225}Ac]Ac-DOTA-TATE relative to controls.

Conclusions These results suggest significant potential for the clinical translation of [^{225}Ac]Ac-DOTA-TATE for lung NENs.

Keywords ^{225}Ac targeted alpha therapy · [^{225}Ac]Ac-DOTA-TATE · Lung neuroendocrine neoplasms

This article is part of the Topical Collection on Translational research.

✉ Ghassan El-Haddad
Ghassan.ElHaddad@moffitt.org

✉ David L. Morse
David.Morse@moffitt.org

Jordan N. Reff
jordan.reff@yahoo.com

[1] Department of Cancer Physiology, H. Lee Moffitt Cancer Center & Research Institute, Tampa, FL, USA
[2] Department of Radiology, University of Iowa Health Care, Iowa City, IA, USA
[3] Department of Radiation Oncology, H. Lee Moffitt Cancer Center & Research Institute, Tampa, FL, USA
[4] Department of Physics and Oncologic Sciences, University of South Florida, Tampa, FL, USA
[5] Oncologic Sciences, University of South Florida, Tampa, FL, USA
[6] Small Animal Imaging Laboratory Shared Resource, Tampa, FL, USA
[7] Department of Drug Discovery, H. Lee Moffitt Cancer Center & Research Institute, Tampa, FL, USA
[8] Department of Pediatrics, Pathology & Cell Biology, University of South Florida, Tampa, FL, USA
[9] Biostatistics and Bioinformatics Shared Resource, H. Lee Moffitt Cancer Center & Research Institute, Tampa, FL, USA
[10] Department of Thoracic Oncology, H. Lee Moffitt Cancer Center & Research Institute, Tampa, FL, USA
[11] Gastrointestinal Oncology, H. Lee Moffitt Cancer Center & Research Institute, Tampa, FL, USA
[12] Diagnostic Imaging and Interventional Radiology, H. Lee Moffitt Cancer Center & Research Institute, Tampa, FL, USA

Introduction

Neuroendocrine tumors (NETs) arise from the neuroendocrine system in the lung, gastrointestinal tract, and pancreas, among other organs [1]. A large fraction (25%) of well-differentiated NETs are of bronchopulmonary origin. Well-differentiated and moderately differentiated lung NETs are referred to as lung carcinoids and are divided into typical and atypical classifications. Poorly differentiated lung neuroendocrine carcinomas are divided into large cell neuroendocrine carcinoma and small cell lung cancer (SCLC) [2, 3]. Few trials have investigated systemic treatments for patients with lung NETs [4–8]. The only medication approved by the US Food and Drug Administration (FDA) for progressive lung NETs is everolimus, an oral inhibitor of the mechanistic target of rapamycin (mTOR) [9].

Overexpression of somatostatin receptors in patients with neuroendocrine neoplasms (NEN) is utilized for both diagnosis and treatment. Somatostatin receptor 2 (SSTR2) is widely expressed in pulmonary NENs, including typical carcinoids, atypical carcinoids, large cell neuroendocrine carcinoma, and SCLC [10]. Therefore, somatostatin analogues (SSAs) with high affinity to SSTR2 can be used for targeting these types of tumors [10]. Peptide receptor radionuclide therapy (PRRT) with the [^{177}Lu]Lu-DOTA chelate conjugated to the octreotate SSA ([^{177}Lu]Lu-DOTA-TATE) has proved to be an effective therapy option for NETs [6, 7, 11].

The limitations of [^{177}Lu]Lu-DOTA-TATE therapy are that only 26–55% of patients achieve stable disease, 18–32% are treatment refractory, and half progress within 2 to 3 years after starting treatment [12–14].

^{177}Lu is a β-particle emitting radionuclide and there is evidence that a superior therapeutic index could be achieved using targeted α-particle therapy (TAT) as an alternative [15–20]. Compared to β particles, α particles have a 200–400× greater linear energy transfer and a shorter range in solid tissue, <100 μm for α-emissions relative to a few mm for β-emissions. Hence, α-particle emissions are more likely to deposit energy within the boundaries of a tumor or metastasis relative to β-emissions, which can cause toxicity in surrounding normal tissues, and greater energy deposition leads to greater cell killing. Unlike β-emissions, it is hypothesized that α-emissions do not rely solely on generation of free radicals to generate DNA damage. Instead, the energy deposited is sufficient to directly cause DNA double-strand breaks [21]. This enables TATs to potentially evade a common mechanism of radiation resistance, i.e., free radical scavenging. To demonstrate these advantages, [^{225}Ac]Ac-DOTA-TOC was compared to [^{177}Lu]Lu-DOTA-TOC in the treatment of rat pancreatic exocrine tumor xenografts in immunocompromised mice and TAT demonstrated greater efficacy and lower toxicity relative to the TBT [16]. In recently published case studies, significant efficacy of [^{225}Ac]Ac-DOTA-TATE was demonstrated in patients' refractory to [^{177}Lu]Lu-DOTA-TATE [22]. Furthermore, [^{177}Lu]Lu-DOTA-TATE has been compared with [^{177}Lu]Lu-DOTATOC in patients and a greater tumor residence time was observed for [^{177}Lu]Lu-DOTA-TATE, indicating that DOTA-TATE may be a superior targeting ligand for delivery of radiotherapy [23].

^{225}Ac is an α-particle emitting isotope that has demonstrated significant utility in TAT and decays with a 10-day half-life via a complex decay scheme, emitting four α particles and depositing significantly higher energy levels in local tissue, 28 MeV, compared to single α-particle emitters, e.g., 7.8 MeV for ^{212}Bi (or ^{212}Pb), or 384 keV for the β-emitter ^{177}Lu [24, 25]. Hence, ^{225}Ac has been described as an in vivo α-particle generator [26]. The main method for generating ^{225}Ac for clinical studies is through the decay of ^{229}Th which originates from ^{233}U. There are three main sources of ^{229}Th in the world: Oak Ridge National Laboratory (USA), The Institute of Physics and Power Engineering (Russia), and The Institute for Transuranium Elements (Germany). In addition, it has been shown that large-scale quantities can be produced through the decay of ^{232}Th [27, 28]. To address the shortage of the clinical need of ^{225}Ac, the US Department of Energy formed a Tri-lab collaboration of Los Alamos (LANL), Brookhaven (BNL), and Oak Ridge (ORNL) National Laboratories with the goal of developing an alternative route for production of ^{225}Ac by use of a linear accelerator [29]. Due to the long half-life, ^{225}Ac-based TATs can be produced at regional radiopharmaceutical facilities and distributed for use by Nuclear Medicine Departments within 1 to 3 days post-production.

Herein, we investigate the toxicity, biodistribution (BD), radiation dosimetry (RD) in mice, and efficacy of [^{225}Ac]Ac-DOTA-TATE in xenograft tumor models of pulmonary NENs. These preclinical studies are needed to support the clinical translation of [^{225}Ac]Ac-DOTA-TATE.

Materials and methods

Cell culture

NCI-H69 human SCLC, NCI-H727 human lung carcinoid, and HEK293 cells were purchased from American Type Culture Collection, expanded for 2 passages and cryopreserved. NCI-H69 and NCI-H727 cells were grown in RPMI-1640 Medium, (Life Technologies), 10% FBS (Life Technologies), 100 units/mL penicillin, 100 mg/mL streptomycin in 5% CO_2 at 37 °C. HEK293 cells were grown in DMEM/F12 medium (Life Technology). Cells were authenticated using short tandem repeat (STR) DNA typing according to ATCC's guidelines [30], monitored by microscopy to assure maintenance of their original morphology, tested for mycoplasma contamination using the MycoAlert kit (Lonza) and experiments used cells of passage numbers <25.

SSTR2 transfection of HEK293 cells

HEK293 cells were transfected with 2 μg of SSTR2 (NM_001050) Human Tagged ORF Clone in pCMV6 vector with Neomycin selection marker (Origene) using the FuGENE HD Transfection Reagent (Promega) as described before [31]. SSTR2 expression was determined by quantitative real-time RT-PCR (qRT-PCR) using the primers described below. The HEK293/SSTR2 clone with the highest expression was maintained in medium containing 400 μg/mL of G418.

Chelation of lanthanum and europium

DOTA-(Tyr3)-octreotate (DOTA-TATE), ≥98% purity, was purchased (Bachem). DOTA-TATE was loaded with lanthanum (La^{3+}) by addition of $LaCl_3 \cdot 7H_2O$ (3.9 mg, 10.5 μmol) to DOTA-TATE (5.0 mg, 3.5 μmol) in 1 mL of 0.1 M AcONa buffer (pH 6.0) and europium (Eu^{3+}), by addition of $EuCl_3 \cdot 6H_2O$ (1.6 mg, 4.2 μmol) to DOTA-TATE (2 mg, 1.4 μmol) in 5 mL H_2O and 0.1 mL DMSO, and stirring 12 h at room temperature (RT). For both chelates, reaction completion was determined by HPLC (Agilent 1260 Infinity II HPLC system with a quaternary pump, a vial sampler, and a DAD detector) and a C18 column yielded the final product (~3.3 mg and 1.9 mg, respectively). A Phenomenex C18 column (Luna 5 μL C18(2) 100 Å, 4.6 × 250 mm) was used. The DAD detector was set to 214 nm. Phase A: 0.1% TEA/AcOH (TEAA) in water (pH 6.0) and Phase B: 90% acetonitrile in Phase A (pH adjusted to 6.0 with AcOH) using the following: 10–45% Phase B in Phase A in 50 min. Mass and purity were determined by HRMS (ESI) and HPLC, respectively.

Binding assay

The receptor number of HEK293/SSTR2 cells was determined using time-resolved fluorescence (TRF) saturation binding assay. Different concentrations of Eu^{3+}-DOTA-TATE (0–2500 nM) were used as the test ligand and 5 μM of La^{3+}-DOTA-TATE was used as the blocking ligand. Briefly, black 96-well plates (clear bottom, Corning, #3603) were coated with 0.25 mg/ml of PDL (Poly-D Lysine, Sigma). Hek293/SSTR2 cells were plated in the coated plates, at a density of 30,000 cells/well. On the day of the experiment (1 day after seeding the cells), the medium was aspirated and for the top half of the plate (total binding) 50 μL of the Eu^{3+}-DOTA-TATE (2.5–2500 nM) test ligand was added to each well in a series of decreasing concentrations, followed by 50 μL of binding medium (DMEM, 1 mM 1,10-phenanthroline, 200 mg/L bacitracin, 0.5 mg/L leupeptin, 0.3% BSA). The bottom half of the plate (non-specific binding), was prepared as the top half, except that 5 μM of blocking La^{3+}-DOTA-TATE ligand was added instead of binding medium. Cells were incubated with the ligands for 1 h at 37 °C in a cell culture incubator, followed by two washes with PBS. After washing, the cells were incubated with 50 μl of 2.0 M HCl for 2 h at 37 °C followed by neutralization with 55 μl of 2.0 M NaOH. Then, 115 μL of enhancement solution (PerkinElmer) was added to each well and cells were incubated for an additional 30 min at 37 °C prior to reading. The plates were read on a PerkinElmer VICTORx4 2030 multilabel reader using the standard Eu^{3+} time-resolved fluorescence (TRF) measurement (340-nm excitation, 400-μs delay, and emission collection for 400 μs at 615 nm). The standard curve was used to determine the amount of ligand present at the B_{max} obtained in the saturation binding assay. The average number of cells per well at the end of the assay was calculated. To determine the receptor number, the following equation was used: (Eu^{3+} amount for B_{max} (moles)/average cell number per well) × 6.023 × 10^{23} =mreceptor number per cell. This B_{max} value was then used to calculate ligand association and binding kinetics for each cell using the following equation: $B = B_0 + (B_{max}\text{-}B_0)/(1\text{-}e^{-kt})$, where B corresponds to a receptor saturation parameter, an analog of ligand-receptor complex formation [RL], with values between initial saturation B_0 and the maximum saturation B_{max}; k is the reaction rate constant, and t is time. NCI-H69 receptor number was determined as above except that ligand incubation step was reduced to 30 min with only × 1 PBS wash.

La^{3+}-DOTA-TATE binding affinity was determined using a TRF competitive binding assay as previously [32], using HEK293/SSTR2 cells and 50 nM Eu^{3+}-DOTA-TATE used as the competing ligand. Data points were acquired in quadruplicate and each assay was repeated 3 times.

Radiochemical synthesis and characterization

The $^{225}Ac(NO_3)_3$ (5.80 × 10^4 Ci/g; carrier free; >10 mCi/ml concentration) was purchased from Oak Ridge National Laboratory (TN, USA). Complexation was achieved by reacting DOTA-TATE (5–10 μg in 5–10 μL water from 1.0 mg/mL solution) with $^{225}Ac(NO_3)_3$ (3.4 MBq) that was diluted in 100 μL of water containing 10 μL of 20% L-ascorbic acid. The pH was adjusted to 5.8 using 1 M Tris buffer (10–12 μL), and then incubated at 75 °C for 1 h (Scheme 1). Reaction progress and radiochemical purity of [^{225}Ac]Ac-DOTA-TATE were measured without further purification 24 h after collection (to ensure secular equilibrium among ^{225}Ac and its daughters) using ITLC with γ counting, radio-TLC, and γ counting of radio-HPLC fractions. Stability was determined by adding 50 μL of [^{225}Ac]Ac-DOTA-TATE (1702 kBq) to 1 mL of human serum (n = 4), 37 °C incubation

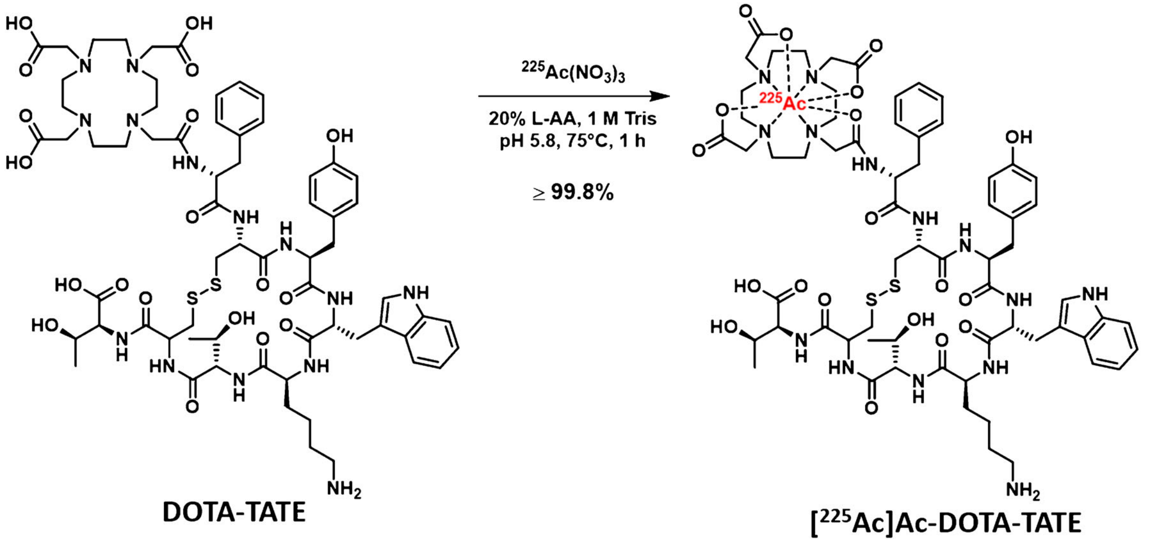

Scheme 1 Radiochemical synthesis of [^{225}Ac]Ac-DOTA-TATE

for 10 days, and TLC scanner (Bioscan) and γ-counter (PerkinElmer) quantification at time points [33].

Animal studies

Protocols were approved: University of South Florida IACUC protocol IS00006466. Animals were purchased from Charles River (Wilmington, MA). An equal number of males and females were used for each cohort.

Injected activity measurement

Syringes were prefilled with ±10% of [^{225}Ac]Ac-DOTA-TATE activity. Activities were measured using the Atomlab 500 Dose Calibrator (Biodex) as described before [34].

Toxicity

Cohorts ($n = 6$) of non-tumor-bearing BALB/c mice (6–8 weeks old) were given a single intravenous injection by tail-vein catheter of 200 µl of 55.5, 111 or 185 kBq of [^{225}Ac]Ac-DOTA-TATE activity in 0.9% sterile saline (Cardinal Pharmaceuticals) in the syringe (45.8 ± 14.8, 94.7 ± 4.8, and 163.9 ± 9.6 mean injected activity), or 0.9% sterile saline alone as a control. These administration activities were selected based on results from a previous preclinical study using an ^{225}Ac-based peptidic TAT [34]. Injected activity is determined for each animal by subtracting the amount of activity remaining in the syringe and catheter from the pre-injection amount of activity in the syringe. Mice were monitored for distressed behavior and weighed twice per week for 5 months, followed by euthanasia and tissue collection. Blood urea nitrogen (BUN), creatinine, alkaline phosphatase (ALKP), alanine aminotransferase (ALT), and aspartate aminotransferase (AST) in serum were analyzed using an automated biochemical analyzer (CLIP, Catalyst DX, IDEXX). Bone, bone marrow, brain, cecum, duodenum, kidney, liver, lymph nodes, muscle, pancreas, salivary gland, small intestine, and spleen were harvested and fixed in 10% formalin. Bone was decalcified in 14% ethylene diaminetetraacetic acid (EDTA) solution after fixation. Tissues were embedded in paraffin, sectioned (4–6 µm thickness), stained with hematoxylin and eosin (H&E), and examined blind by the veterinary pathologist (R.E.).

Biodistribution

Non-tumor-bearing BALB/c mice (6–8 weeks old) were administered by tail-vein catheter 200 µl of 74 kBq of [^{225}Ac]Ac-DOTA-TATE activity in 0.9% sterile saline in the syringe (66.6 ± 2.9 kBq mean injected activity), euthanized at 24, 48, and 96 h p.i., $n = 4$ mice per cohort. This administration activity was selected based on results from a previous preclinical BD study using an ^{225}Ac-based peptidic TAT [34]. Tissues were removed, weighed, and the percent injected activity per gram (%IA/g) calculated as before [34].

Radiation dosimetry

Dosimetry calculations were performed using BD data as previously described [34].

qRT-PCR and immunocytochemistry

SSTR2 expression was verified by qRT-PCR and ICC performed to determine protein. NCI-H69 and NCI-H727 RNA was extracted (RNeasy, Qiagen). Two sets of human SSTR2 primers were designed (Gene Runner for Windows 3.05): set

1: forward, 5’-AACCAGACAGAGCCGTACTA-3′ and reverse, 5′- GCATAGCGGAGGATGACA-3′; and set 2: forward, 5’-GCTGGCTTCCCTTCTACATATT-3′ and reverse, 5’-GAGGACCACCACAAAGTCAA-3′. B-actin was used for normalization as previously [35]. NCI-H69 and NCI-H727 ICC was performed using 30 μg/mL anti-SSTR2 antibody (Sigma, HPA007264) as before [34], except that H69 were grown on coverslips coated with 0.25 mg/ml poly-D-lysine (Sigma).

Anti-tumor efficacy

NCI-H69 and NCI-H727 subcutaneous xenograft tumor–bearing SCID mice (6–8 weeks old, $n = 10$/cohort) were injected by tail-vein catheter with 200 μl of 185 kBq [^{225}Ac]Ac-DOTA-TATE activity in 0.9% sterile saline in the syringe (148.0 ± 17.8 and 144.3 ± 18.8 kBq mean injected activity), or 0.9% sterile saline alone as a control. This administration activity was selected based on preliminary results from the toxicity study herein. The efficacy study was initiated 4–1/2 months after initiation of the toxicity study and no toxicities were detected at this activity at that time. Animals underwent euthanasia after reaching 2000 mm^3 tumor volume or if clinical endpoints were observed, e.g., 20% weight loss, tumor ulceration, hunched back, lack of grooming, and lethargy.

Histology and immunohistochemistry

Following euthanasia, organs (toxicity) and tumors (efficacy) were excised, formalin fixed, paraffin embedded, sectioned (5 μm), and stained with H&E (tumors and organs) and IHC (tumors) using rabbit SSTR2 polyclonal antibody (1:200 dilution, GTX70735, GeneTex) and a Discovery XT automated system (Ventana Medical Systems). Slides were scanned using a ScanScope XT digital slide scanner (Aperio, CA). To quantify SSTR2 expression in tumors, images from serial H&E and IHC central sections were analyzed using Visiopharm 2017.7 as before [34].

SSTR2 expression was evaluated in using gray-level co-occurrence texture analysis in three main steps: (1) tumor segmentation, (2) target expression extraction, and (3) texture analysis. The tumor region was segmented to limit the analysis to cells within the tumor. For target expression, a binary mask was created from the positive and negative stained cells with each pixel representing a cell with the value of 1 if unstained or 2 if stained. A co-occurrence texture analysis was applied to the binary mask to calculate the heterogeneity score for target expression. Specifically, the diagonal values in the gray-level co-occurrence matrix measure the closeness of the distribution of all gray levels. Therefore, heterogeneity is calculated from diagonal entries that are related, i.e., with target expression. The heterogeneity score ranges from 0 to 1, where 0 is completely homogeneous and 1 is completely heterogeneous.

Statistics

Cohort size was determined by power analyses. Analysis of variance (ANOVA) was used to assess differences in toxicity by activity and Dunnett’s test to determine differences among activities and saline control. Prior to ANOVA, the Anderson Darling test assessed whether a transformation was required. The unpaired *t*-test compared the ICC or IHC expression level of SSTR2 in NCI-H69 and NCI-H727 cells and tumors. Two-way ANOVA was used to compare tumor volume among treatment and saline groups and Kaplan-Meier analyses (GraphPad Prism 7 software) determined significance among the cohorts.

Results

Binding affinity of La^{3+}-DOTA-TATE

There are no non-radioactive isotopes of actinium and lanthanum is a useful surrogate for Ac since both are trivalent ions in solution [36]. The HRMS (ESI) calculated mass for the prepared La^{3+}-DOTA-TATE, $C_{65}H_{87}LaN_{14}O_{19}S_2$ $(M + H)^+$, 1571.4855 MW, was 1571.4867 with 100% purity, $t_R =$ 22.15 min (**Supplemental Fig. 1**). La^{3+}-DOTA-TATE bound SSTR2 expressing HEK293/SSTR2 cells with high, 19.00 ± 9.2 nM K_i (Fig. 1).

The HRMS (ESI) calculated mass for the Eu^{3+}-DOTA-TATE chelate, $C_{65}H_{87}EuN_{14}O_{19}S_2$ $(M + H)^+$, 1585.5004 MW, was 1585.5031 with 100% purity, $t_R =$ 22.14 min (**Supplemental Fig. 2**). Eu^{3+}-DOTA-TATE binding affinity for SSTR2 was 22.12 nM K_d, and HEK293/

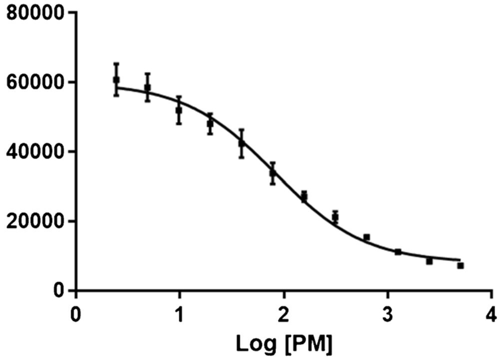

Fig. 1 Whole-cell competitive binding assay of La^{3+}-DOTA-TATE. The binding affinity of La^{3+}-DOTA-TATE was calculated to be 19.00 ± 9.2 nM K_i ($n = 3$ repeats). In this whole-cell lanthanide time-resolved fluorescence assay, HEK293/SSTR2 cells were used and 50 nM of Eu^{3+}-DOTA-TATE was used as the competing ligand

Table 1 In vitro serum stability of [^{225}Ac]Ac-DOTA-TATE

Day	% Intact TLC scanner
0	100
1	100.44±0.88
3	99.27±0.29
5	96.74±2.06
7	93.19±1.50
10	90.29±4.00

SSTR2 cells were shown to express 1.87 × 10^6 SSTR2 receptors on the cell-surface per cell (**Supplemental Fig. 3A).**

Radiosynthesis and characterization of [^{225}Ac]Ac-DOTA-TATE

Radiosynthesis (Scheme 1) provided >98% yield with high radiochemical purity (≥99.8%) (**Supplemental Fig. 4**). Also, [^{225}Ac]Ac-DOTA-TATE had an excellent in vitro stability, with 97% integrity remaining after 2 days in human serum at 37 °C (Table 1).

Toxicity

Weight gain was observed in all animals at 5 months post injection (p.i.), albeit less weight was gained by animals at the highest dose level relative to the lowest (Fig. 2a). Significant differences in weight change were observed among saline and 111 kBq and 185 kBq treatments ($p < 0.01$ and $p < 0.001$, respectively), but not 55.5 kBq ($p = 0.50$) (**Supplemental Table 1**). Blood BUN and creatinine were all in the normal range (Fig. 2b and c**),** p values = 0.12 and 0.33, respectively (**Supplemental Table 2 and 3**). No significant differences in ALT, AST, or ALKP liver enzymes were observed among the cohorts (Fig. 2d–f **and Supplemental Table 4–6**).

No pathologic findings were observed for 55.5 and 111 kBq cohorts. In contrast, animals in cohorts receiving ≥111 kBq in the syringe (≥94.8 kBq actual injected activity) began to lose weight at ~100 days p.i. (**Supplemental Fig. 5**), and at necropsy chronic progressive nephropathy was observed (Fig. 3). No other organ (bone, bone marrow, brain, cecum, duodenum, liver, lymph nodes, muscle, pancreas, salivary gland, small intestine, and spleen) showed pathologic changes related to the treatment. Glycogen accumulation was observed in the livers of some animals (including the saline control group), but this was considered an incidental finding.

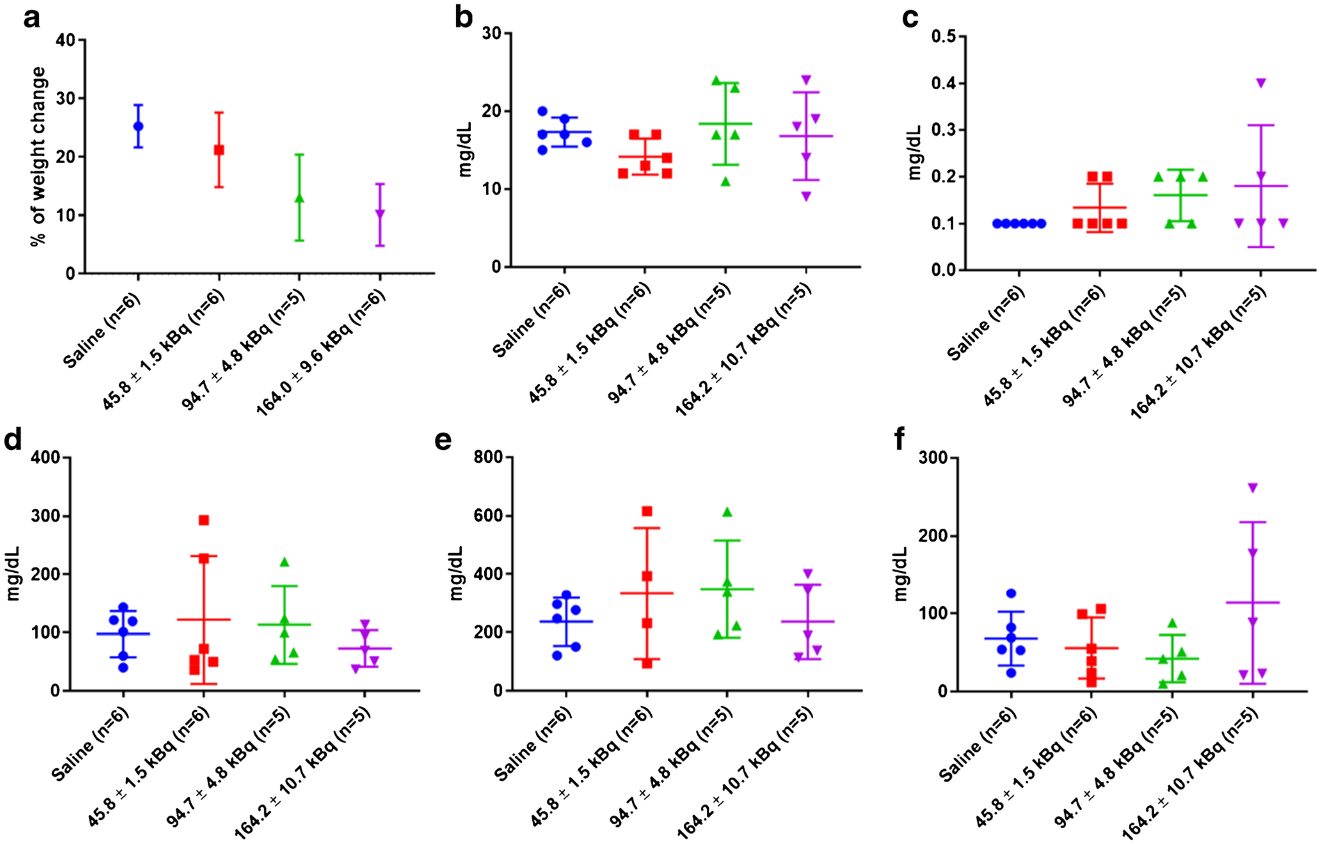

Fig. 2 Toxicity of [^{225}Ac]Ac-DOTA-TATE in BALB/c mice. **a** Percent weight gain, **b** BUN (reference range: 18–29 mg/dl), **c** blood creatinine (reference range: 0.2–0.8 mg/dL), **d** ALT (reference range: 28–132 U/L), **e** AST (reference range: 59–247 U/L), and **f** ALKP (reference range: 62–209 U/L)

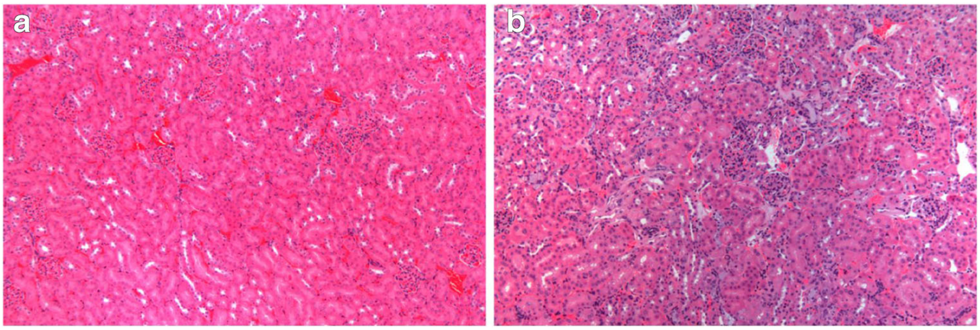

Fig. 3 Histological appearance of kidney from a mouse administered **a** saline or **b** 179.0 kBq. (a) Kidney histology of a saline administered mouse, without significant abnormalities, where glomeruli are normocellular, with open capillary loops, and tubular epithelium is uniformly cuboidal, with round nuclei, and a prominent brush border. (b) Kidney histology of a 179.0-kBq administered mouse, with chronic progressive nephropathy. Extensive tubular cell regeneration, diffuse fibrosis, mild mononuclear inflammatory cell infiltrates, and thickened, hypercellular glomerular tufts are evident

Biodistribution

BALB/c mice ($n = 4$ per cohort) were injected intravenously with 74 kBq of [^{225}Ac]Ac-DOTA-TATE α activity in the syringe. The activities from ^{225}Ac and daughters ^{221}Fr and ^{213}Bi in equilibrium were determined for each organ and time point using γ spectroscopy (Fig. 4a–c **and Supplementary Fig. 6**). [34, 37] At 24 h p.i., the kidneys, liver, and stomach had 1.63 ± 0.72, 0.147 ± 0.07, and 0.31 ± 0.08 %IA/g, respectively, while only negligible activity was observed in the other

Fig. 4 Biodistribution of **a** ^{225}Ac, **b** ^{221}Fr, and **c** ^{213}Bi after intravenous injection of [^{225}Ac]Ac-DOTA-TATE in BALB/c mice

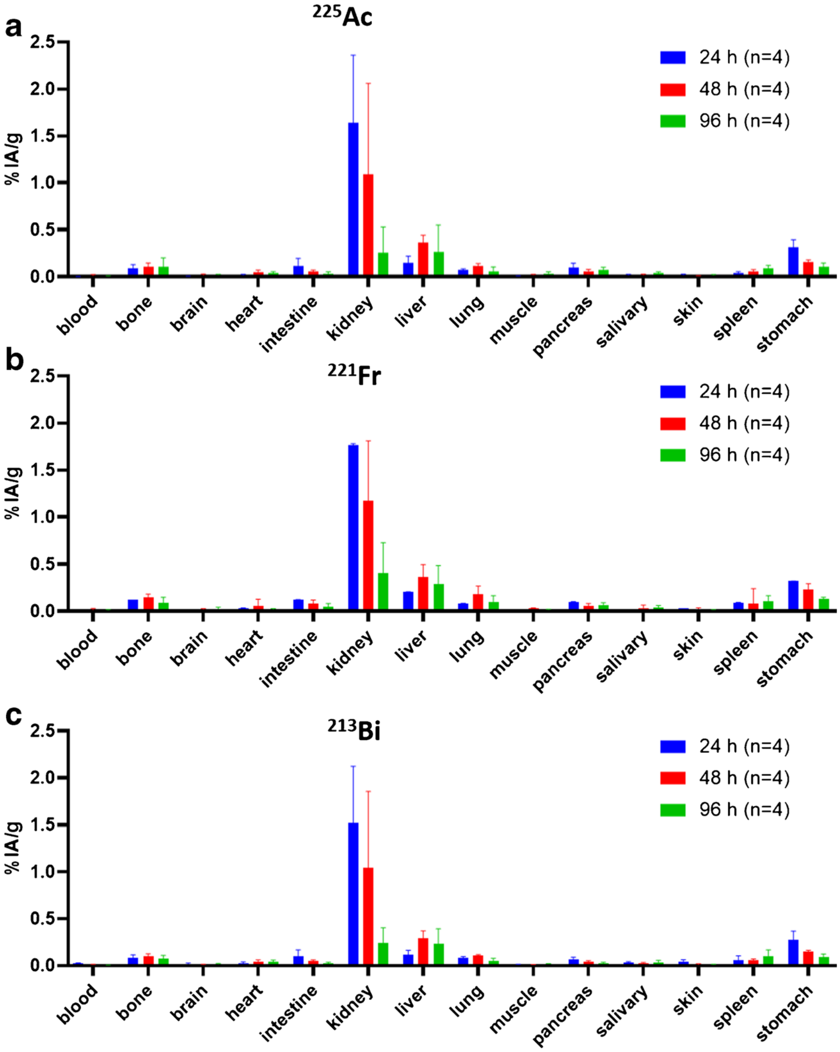

Table 2 Radiation dosimetry and clearance kinetics parameters for [^{225}Ac]Ac-DOTA-TATE in BALB/c mice

Parameter	Blood	Bone	Brain	Heart	Intestine	Kidney	Liver	Lung	Muscle	Pancreas	Salivary	Skin	Spleen	Stomach
^{225}Ac														
Initial activity/organ, $A_{\circ}$ (kBq)	0.0003	0.0131	0.0019	0.0033	0.1527	0.3862	0.1200	0.0227	0.0024	0.0171	0.0028	0.0023	0.0039	0.0859
Decay rate constant, λ_{eff}(h^{-1})	0.0206	0.0030	−0.0103	−0.0004	0.0200	0.0250	−0.0053	0.0130	−0.0049	0.0060	−0.0077	−0.0092	0.0062	0.0190
Decay half-life, T_{eff} (days)	1.4020	9.6270	2.8040	72.2028	1.4441	1.1552	5.4493	2.2216	5.8941	4.8135	3.7508	3.1393	4.6582	1.5201
Accumulated activity/organ,$\widetilde{A}$ (kBq × h)	0.0080	1.4274	0.8190	0.4871	4.4589	8.2462	29.4458	1.0829	0.5613	1.4271	0.8906	0.8656	0.3228	2.6801
Absorbed dose/injected activity (Gy/kBq)	0.0000	0.0004	0.0001	0.0001	0.0001	0.0012	0.0012	0.0001	0.0001	0.0003	0.0002	0.0001	0.0001	0.0004
^{221}Fr														
Initial activity/organ, $A_{\circ}$ (kBq)	0.0019	0.0170	0.0036	0.0067	0.01532	0.4011	0.1612	0.0251	0.0052	0.0169	0.0037	0.0039	0.0097	0.0852
Decay rate constant, λ_{eff} (h^{-1})	−0.0071	0.0100	−0.0044	0.0190	0.0130	0.0190	−0.0033	0.0080	0.0170	0.0080	−0.0028	−0.0015	0.0030	0.0170
Decay half-life, T_{eff} (days)	4.0678	2.8881	6.5639	1.5201	2.2216	1.5201	8.7519	3.6101	1.6989	3.6101	10.3147	19.2541	9.6270	1.6989
Accumulated activity/organ, $\widetilde{A}$ (kBq × h)	0.5594	1.0195	0.7934	0.2102	7.2991	12.5136	32.1637	1.7734	0.1848	1.1933	0.7036	0.6489	1.0604	3.0452
Absorbed dose/injected activity (Gy/kBq)	0.0001	0.0003	0.0001	0.0000	0.0002	0.0019	0.0014	0.0003	0.0000	0.0003	0.0002	0.0001	0.0004	0.0004
^{217}At														
Initial activity/organ, $A_{\circ}$ (kBq)	0.0019	0.0170	0.0036	0.0067	0.1532	0.4011	0.1612	0.251	0.0052	0.0169	0.0037	0.0039	0.0097	0.852
Decay rate constant, λ_{eff} (h^{-1})	−0071	0.0100	−0.0044	0.0190	0.0130	0.0190	−0.0033	0.0080	0.0170	0.0080	−0.0028	−0.0015	0.0030	0.0170
Decay half-life, T_{eff} (days)	4.0678	2.8881	6.5639	1.5201	2.2216	1.5201	8.7519	3.6101	1.6989	3.6101	10.3147	19.2541	9.6270	1.6989
Accumulated activity/organ, $\widetilde{A}$ (kBq × h)	0.5594	1.0195	0.7934	0.2102	7.2991	12.5136	32.1637	1.7734	0.1848	1.1933	0.7036	0.6489	1.0604	3.0452
Absorbed dose/injected activity (Gy/kBq)	0.001	0.0003	0.0001	0.00001	0.0002	0.0021	0.0016	0.00003	0.00000	0.0003	0.0002	0.0001	0.0004	0.0005
^{213}Bi														
Initial activity/organ, $A_{\circ}$ (kBq)	0.0042	0.0125	0.0066	0.0053	0.1340	0.3639	0.0948	0.0270	0.0034	0.0119	0.0056	0.0056	0.0068	0.0777
Decay rate constant, λ_{eff} (h^{-1})	0.01100	0.0070	0.0080	0.0030	0.0210	0.0250	−0.0073	0.0170	0.0050	0.0140	0.0030	0.0040	−0.0024	0.0190
Decay half-life, T_{eff} (days)	2.6256	4.1259	3.6101	9.6270	1.3753	1.1552	3.9563	1.6989	5.7762	2.0629	9.6270	7.2203	12.0338	1.5201
Accumulated activity/organ, $\widetilde{A}$ (kBq × h)	0.2345	0.9591	0.4653	0.5789	3.6681	7.7700	28.7854	0.9636	0.3058	0.5253	0.6047	0.5575	1.2470	2.4230
Absorbed dose/injected activity (Gy/kBq)	0.0000	0.0000	0.0000	0.0000	0.0000	0.0000	0.0000	0.0000	0.0000	0.0000	0.000	0.000	0.0000	0.0000
^{213}Po														
Initial activity/organ, $A_{\circ}$ (kBq)	0.0042	0.0125	0.0066	0.0053	0.1340	0.3639	0.0948	0.0270	0.0034	0.0119	0.0056	0.0056	0.0068	0.0777
Decay rate constant, λ_{eff} (h^{-1})	0.0110	0.0070	0.0080	0.0030	0.0210	0.0250	−0.0073	0.0170	0.0050	0.0140	0.0030	0.0040	−0.0024	0.0190
Decay half-life, T_{eff} (days)	2.6256	4.1259	3.6101	9.6270	1.3753	1.1152	3.9563	1.6989	5.7762	2.0629	9.6270	7.2203	12.0338	1.5201
Accumulated activity/organ, $\widetilde{A}$ (kBq × h)	0.2345	0.9591	0.4653	0.5789	3.6681	7.7700	28.7854	0.9636	0.3058	0.5253	0.6047	0.5575	1.2470	2.4230
Absorbed dose/injected activity (Gy/kBq)	0.0000	0.0004	0.0001	0.0002	0.0001	0.0015	0.0016	0.0002	0.0001	0.0002	0.0002	0.0001	0.0006	0.0005
Total absorbed dose/injected activity (Gy/kBq)	0.0002	0.0014	0.0004	0.0004	0.0007	0.0068	0.0059	0.0009	0.0003	0.0011	0.0008	0.0004	0.0016	0.0017

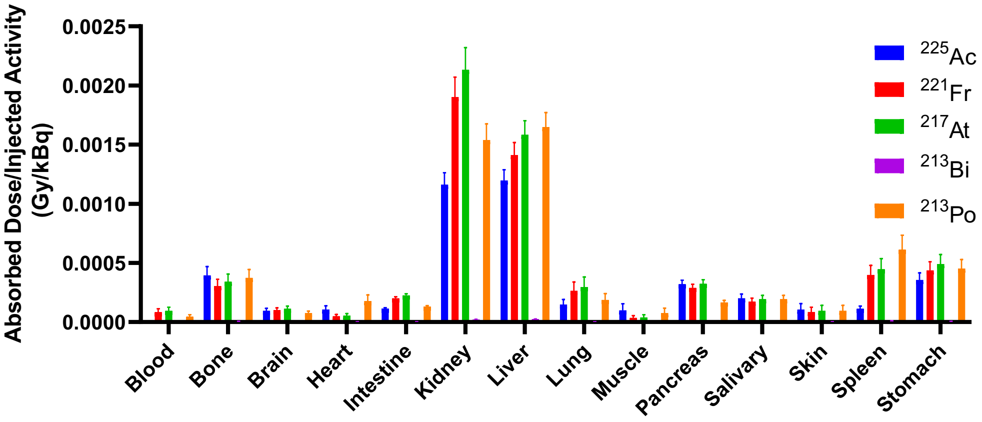

Fig. 5 Radiation dosimetry of ^{225}Ac and daughters following administration of [^{225}Ac]Ac-DOTA-TATE in BALB/c mice

tissues measured. Activity had largely cleared from the tissues by 96 h p.i. Since at the time of the BD measurement, ^{225}Ac was in equilibrium with its daughters, whereas the actual distributed daughters had been decayed, ^{221}Fr and ^{213}Bi only represent the biodistribution of ^{225}Ac.

Radiation Dosimetry

Radiation dosimetry (RD) calculations were based on the data obtained from the BD studies at 24, 48 and 96 h p.i. The α-particle dose from ^{225}Ac and each of its α-emitting daughters was calculated (**Supplementary Fig. 6**). The decay of ^{221}Fr to ^{217}At was assumed to take place in the same location as ^{221}Fr. Similarly, the decay of ^{213}Po was assumed to take place at the same location as ^{213}Bi, while accounting for its 98% branching ratio.

BD data for the different tissues were fitted using an exponential decay nonlinear regression, allowing the estimation of the initial activity due to uptake (A_o), the decay rate constant (λ_{eff}), decay half-life (T_{eff}), accumulated activity ($\widetilde{A}$), and absorbed dose/injected activity (Gy/kBq) for each radionuclide in each tissue (Table 2). The total absorbed dose is the summation of the values for the five α-emitting radionuclides.

The calculated total absorbed dose for [^{225}Ac]Ac-DOTA-TATE was minimal in all tissues except kidney and liver, with 0.0068 and 0.0059 Gy/kBq, respectively. Figure 5 represents graphs of the absorbed dose from each radionuclide per tissue.

The effective decay half-lives (T_{eff}) calculated for ^{225}Ac in tissues that had significant uptake were shorter than the radioactive decay half-life of ^{225}Ac (10 days), indicating biological clearance. For example, the calculated T_{eff} in kidney and liver were 1.16 and 5.45 days, respectively (Table 2). Hence, T_{eff} is a composite of radioactive decay and active biological clearance. The T_{eff} was only calculated to be longer in tissues with minimal uptake where instrument background likely interfered with the accuracy of measurement. It is notable that the kidneys had the highest initial activity, 0.39 kBq, relative to liver, 0.12 kBq, but the kidneys had a nearly 5-fold lower effective half-life compared to liver, leading to faster kidney clearance relative to liver and a higher but comparable total absorbed dose.

SSTR2 expression in NEN cells

NCI-H69 cells have significantly higher SSTR2 mRNA ($p < 0.001$) and protein expression ($p < 0.05$) relative to NCI-

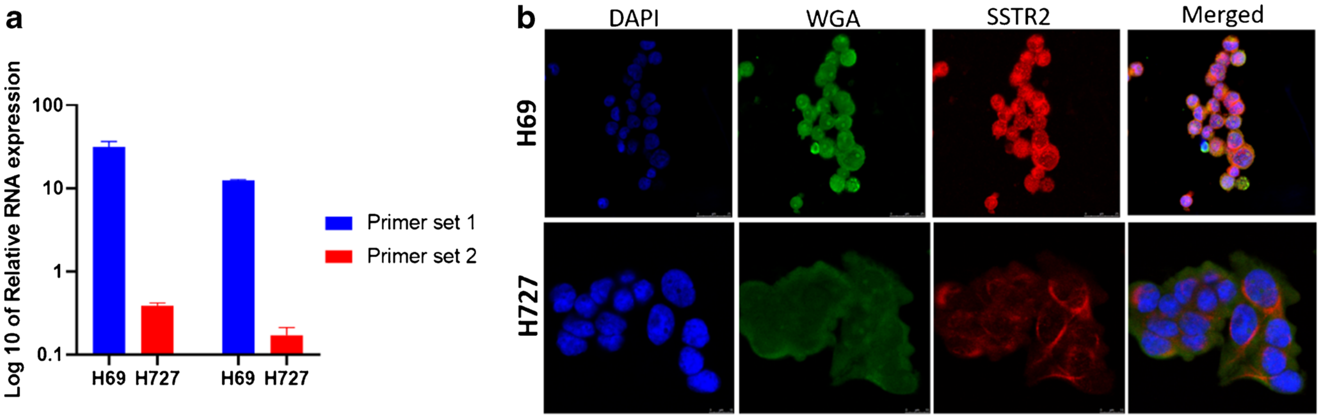

Fig. 6 SSTR2 expression on NCI-H69 and NCI-H727 cells. **a** qRT-PCR. Note the Log10 scale for the expression level. **b** ICC using DAPI (blue), WGA (green), and anti-SSTR2 antibody (red)

H727 (Fig. 6). The SSTR2 cell-surface receptor number per NCI-H69 cell was 1.60×10^6 (**Supplemental Fig. 3b**). SSTR2 expression in NCI-H727 cells was not high enough to accurately calculate the receptor number.

Anti-tumor efficacy

Eight days after tumor cell xenoengraftment, mice ($n = 10$ per cohort) were intravenously injected with a single bolus of 148.7 kBq or 144.3 kBq mean ^{225}Ac activity for H69 and H727 cohorts, respectively, or saline solution. Figure 7a and b show representative images at 25 days p.i. Tumor volumes decreased significantly after treatment relative to saline controls ($p < 0.001$) prior to eventual regrowth (Fig. 7c and d). Saline control mice had significantly greater tumor volumes at the 25 d p.i. time point ($p < 0.0001$) compared to mice treated with [^{225}Ac]Ac-DOTA-TATE. Fig. 7e and f show Kaplan-Meier analyses. Animals treated with [^{225}Ac]Ac-DOTA-TATE had a significantly delayed time to experimental endpoint ($p < 0.0001$ for H69 and $p = 0.0009$ for H727) relative to the saline controls. The median time to endpoint was 93.6 ± 10.1 and 62.7 ± 6.7 days for the H69-treated and saline cohorts, respectively, and the median time to experimental endpoint was 62.7 ± 7.9 days and 51.4 ± 4.4 for the H727-treated and saline cohorts, respectively.

IHC staining determined SSTR2 expression in tumors with and without treatment after reaching the experimental endpoint of 2000 mm^3 tumor volume (Fig. 7 g–j). As seen in the in vitro ICC results, saline treated H69 tumors had significantly greater SSTR2 expression relative to saline treated H727, $p < 0.0001$ (Fig. 7i). Heterogeneity of SSTR2 expression was quantified and saline treated H727 tumors had significantly greater heterogeneity scores relative to saline treated H69 tumors, $p < 0.0001$ (Fig. 7j). Following a single administration of [^{225}Ac]Ac-DOTA-TATE, SSTR2 expression significantly decreased by 10%, $p < 0.01$, in H69-treated tumors relative to saline treated tumors, with no significant difference observed in H727 tumors (Fig. 7i). Similarly, H69 tumors demonstrated increased heterogeneity by 22%, $p < 0.05$, following treatment, with no significant difference observed for H727 tumors (Fig. 7j). Hence, the decrease in expression in H69 tumors likely represents a population of cells with decreased SSTR2 expression rather than a general decrease in every cell within the tumor.

Discussion

Ballal, et al. recently presented the first clinical experience and early results on the efficacy and safety of [^{225}Ac]Ac-DOTA-TATE in 32 patients with SSTR expressing metastatic GEP-NETs who were [^{177}Lu]Lu-DOTA-TATE refractory [22]. For these case studies, systemic TAT using [^{225}Ac]Ac-DOTA-TATE was performed in all the patients with [^{225}Ac]Ac-DOTA-TATE (100 kBq/kg body weight) at an interval of 8 weeks, to a cumulative dose of 55,500 kBq [22]. This pilot study was reported at an early stage, too soon to calculate overall and event-free survival. However, the short-term clinical results with a median follow-up duration of 8 months suggests that treatment with [^{225}Ac]Ac-DOTA-TATE can overcome resistance to [^{177}Lu]Lu-DOTA-TATE and that [^{225}Ac]Ac-DOTA-TATE can be used as a promising treatment option.

Despite this early clinical experience, preclinical animal studies are needed to better understand the biodistribution and radiation dosimetry of [^{225}Ac]Ac-DOTA-TATE, and to support the development of novel methods of determining radiation dosimetry in patients. Furthermore, preclinical studies are required to support an investigational new drug (IND) application to the United States Food and Drug Administration (US FDA) to enable clinical trials in the USA and to enable development of advanced radiation dosimetry methods for clinical use. In addition, the method for synthesis and quality assurance of [^{225}Ac]Ac-DOTA-TATE were not presented in the Ballal study.

Herein, we report the first preclinical study for [^{225}Ac]Ac-DOTA-TATE. We have synthesized [^{225}Ac]Ac-DOTA-TATE with high radiochemical yield and purity, and performed stability, BD, RD, toxicity, and efficacy studies in preclinical models of somatostatin receptor 2 (SSTR2) positive lung tumors. DOTA-TATE was chosen because [^{177}Lu]Lu-DOTA-TATE has been compared with [^{177}Lu]Lu-DOTA-TOC in patients and a greater tumor residence time was observed for [^{177}Lu]Lu-DOTA-TATE, indicating that DOTA-TATE may be a superior targeting ligand for delivery of radiotherapy [23].

Previous somatostatin receptor-targeted PRRT studies have shown that nephrotoxicity is a dose-limiting factor since reabsorption of radio-labeled SSAs by cells in the proximal tubule of the nephron occurs [38, 39]. A preclinical study on PRRT with [^{225}Ac]Ac-DOTA-TOC conducted in nude mice bearing AR42J rat pancreatic NET xenograft tumors demonstrated significant kidney tubular necrosis at activities higher

Fig. 7 Efficacy of [^{225}Ac]Ac-DOTA-TATE in SCID mice–bearing H69 ▶ and H727 tumors. The treated animals were intravenously injected with a single bolus of 148.7 kBq and 144.3 kBq mean ^{225}Ac activity for H69 and H727 cohorts, respectively, or saline solution at 8 days after tumor cells inoculation. Representative images of mice-bearing **a** H69 and **b** H727 tumors (outlined), 25 days p.i. Tumor growth volumes of **c** H69 and **d** H727 tumors relative to saline controls (arrow indicates the day of injection). Kaplan-Meier plots of **e** % H69 and **f** H727 tumor–bearing mice that have reached the experimental endpoint. (g) Representative SSTR2 IHC images of treated and control **g** H69 tumors and **h** H727 tumors at experimental endpoint. **i** Quantified SSTR2 IHC expression **j** and quantified heterogeneity in treated and control H69 tumors and H727 tumors

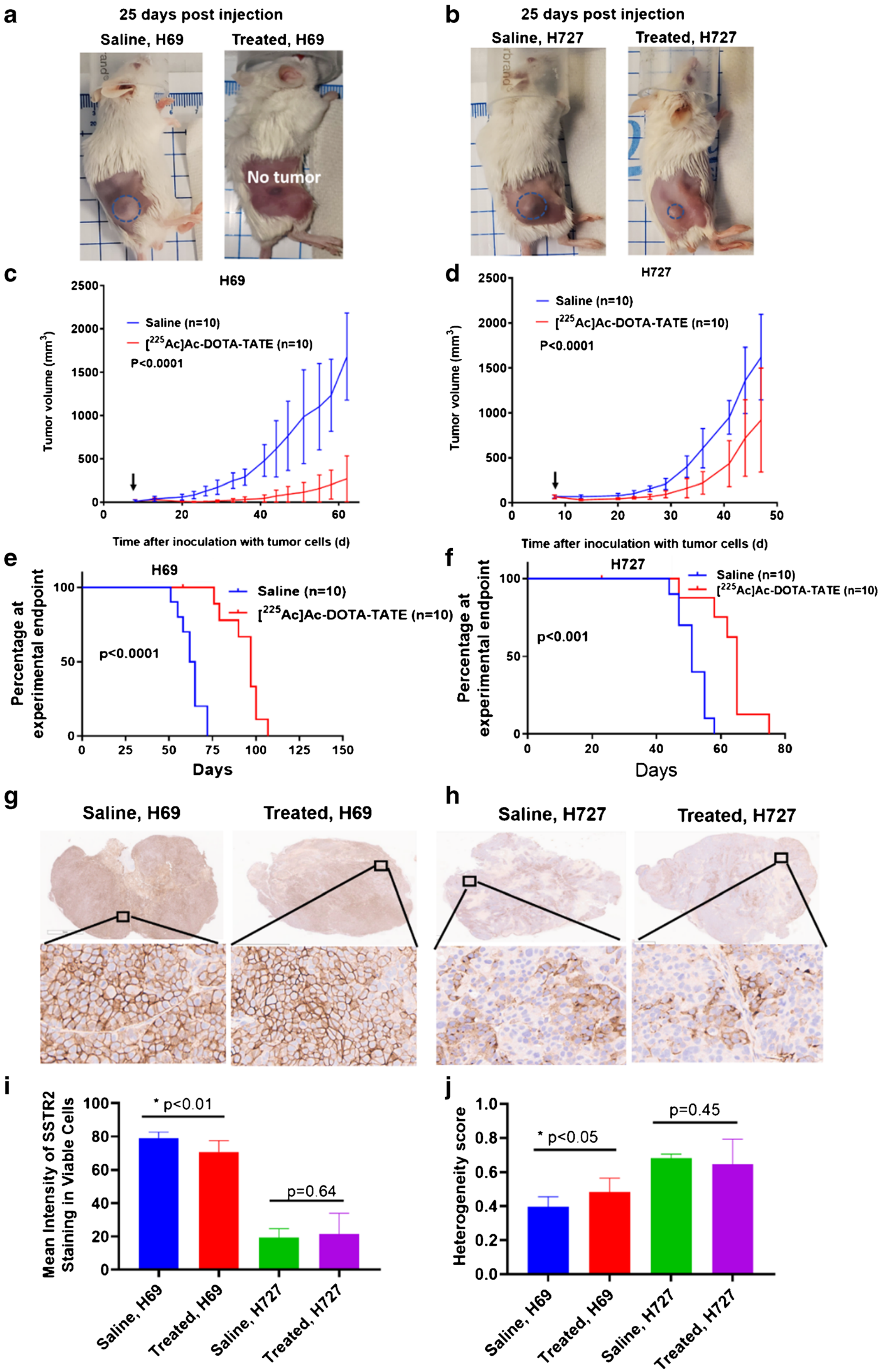
a
25 days post injection
Saline, H69
Treated, H69
No tumor
b
25 days post injection
Saline, H727
Treated, H727
c
H69
Tumor volume (mm³)
Saline (n=10)
[225Ac]Ac-DOTA-TATE (n=10)
P<0.0001
2500
2000
1500
1000
500
0
0
20
40
60
Time after inoculation with tumor cells (d)
d
H727
Tumor volume (mm³)
Saline (n=10)
[225Ac]Ac-DOTA-TATE (n=10)
P<0.0001
2500
2000
1500
1000
500
0
0
10
20
30
40
50
Time after inoculation with tumor cells (d)
e
H69
Percentage at experimental endpoint
Saline (n=10)
[225Ac]Ac-DOTA-TATE (n=10)
p<0.0001
100
50
0
0
25
50
75
100
125
150
Days
f
H727
Percentage at experimental endpoint
Saline (n=10)
[225Ac]Ac-DOTA-TATE (n=10)
p<0.001
100
50
0
0
20
40
60
80
Days
g
Saline, H69
Treated, H69
h
Saline, H727
Treated, H727
i
Mean Intensity of SSTR2 Staining in Viable Cells
* p<0.01
p=0.64
100
80
60
40
20
0
Saline, H69
Treated, H69
Saline, H727
Treated, H727
j
Heterogeneity score
* p<0.05
p=0.45
1.0
0.8
0.6
0.4
0.2
0.0
Saline, H69
Treated, H69
Saline, H727
Treated, H727

than 30 kBq [16]. Our BD results demonstrated that [^{225}Ac]Ac-DOTA-TATE is primarily cleared by the renal route, with some hepatic clearance. Clearance kinetics parameters and RD were calculated, and the highest accumulated doses were observed in the kidneys and liver, with the highest uptake (initial accumulation, A_o) and fastest clearance (T_{eff}) in the kidney relative to the liver.

In the toxicity study, all animals survived to 5 months p.i., and there was no acute kidney damage observed by pathology at any dose level. BUN and creatinine levels were in the normal range for all animals in the study. However, chronic progressive nephropathy was observed in animals injected with ≥2.56 μCi (94.72 kBq) and, despite overall weight gain, animals that were injected with the highest activities, averaging 4.43 μCi (164 kBq) began losing weight at ~100 days p.i. It is notable that for clinical administrations, SSA PRRTs are co-infused with amino acids for renal protection by blocking peptide reabsorption in the proximal tubules, which significantly diminishes the radiation dose to the kidneys [6, 40]. Liver enzymes were normal and there was no treatment related damage observed in the liver or other tissues by pathology.

We confirmed a high and moderate endogenous expression of SSTR2 in H69 and H727 human lung cancer cells, respectively. Following a *single* treatment of [^{225}Ac]Ac-DOTA-TATE, the in vivo efficacy study demonstrated significantly decreased tumor volume, increased tumor growth delay, and a prolonged time to experimental endpoint for animals bearing both tumor types. The responses were greater in H69 tumor–bearing animals compared to H727, which is likely due to the relatively higher and more homogeneous SSTR2 expression in H69 tumors. It is notable that H69 tumors that regrew following treatment had 10% lower SSTR2 expression and 22% increased heterogeneity of SSTR2 expression relative to controls, and these differences were significant, but the H727 tumors regrew with unaltered expression. Tumor regrowth with retained target expression suggests the potential for multiple dosing regimens to prolong survival. However, the loss of some expression in regrowth suggests the potential for development of treatment resistance over time.

In conclusion, our overall results suggest significant potential for the clinical translation of [^{225}Ac]Ac-DOTA-TATE as a novel therapy for lung neuroendocrine neoplasms. Nephrotoxicity results suggest that renal protective measures will be needed, such as the co-injection of amino acid that is currently done during clinical administration of [^{177}Lu]Lu-DOTA-TATE [6, 40]. Furthermore, since it is not practical to directly image ^{225}Ac in patients, personalized methods for determining radiation dosimetry need to be developed using companion imaging agents, e.g., [^{68}Ga]Ga-DOTA-TATE positron emission tomography and image voxel-based Monte Carlo simulations.

Supplementary Information The online version contains supplementary material available at https://doi.org/10.1007/s00259-021-05315-1.

Acknowledgements Animal studies were conducted in the Moffitt Vivarium administered by the University of South Florida. The Analytic Microscopy, Bioinformatics and Biostatistics, Small Animal Imaging Laboratory and Tissue Core Facilities at the H. Lee Moffitt Cancer Center & Research Institute provided support. Actinium-225 was supplied by the United States Department of Energy Office of Science Isotope Program in the Office of Nuclear Physics.

Authors' contributions Drs. Morse and El-Haddad are the corresponding authors and principal investigators that initiated and led the coordination, planning, and execution of the multi-institutional and multi-disciplinary studies reported herein. Dr. Wadas planned, led, and conducted the radiochemistry at University of Iowa. Dr. Tafreshi contributed to the planning and coordination of the biological studies conducted at Moffitt. Dr. Tafreshi also prepared the first draft of the manuscript. Dr. Pandya performed the radiochemistry at University of Iowa. Drs. Tichacek and Budzevich participated in activity measurements, biodistribution data analyses, and radiation dosimetry calculations. Jordan Reff contributed to the animal studies at Moffitt. Dr. Engelman performed the pathology analyses for the toxicity studies at Moffitt. Drs. Ji and Wang performed the lanthanum and europium chelations. David Boulware performed statistical analyses. Drs. Chiappori and Dr. Strosberg advised regarding the clinical perspective and clinical aspects of this work.

Funding Funding was provided by the Neuroendocrine Tumor Research Foundation (Morse, El-Haddad), the Moffitt Radiology Pilot Award (El-Haddad, Morse), and the Moffitt NET Research Fund (El Haddad, Strosberg). The Analytic Microscopy, Bioinformatics and Biostatistics, Small Animal Imaging Laboratory and Tissue Core Facilities at the H. Lee Moffitt Cancer Center & Research Institute an NCI designated Comprehensive Cancer Center (P30-CA076292) provided support.

Declarations

Conflict of interest Drs. Morse and Wadas are co-inventors on a provisional patent application. No other potential conflicts of interest relevant to this article exist.

References

1. Oronsky B, Ma PC, Morgensztern D, Carter CA. Nothing But NET: A review of neuroendocrine tumors and carcinomas. Neoplasia. 2017;19(12):991–1002. https://doi.org/10.1016/j.neo.2017.09.002.
2. Hendifar AE, Marchevsky AM, Tuli R. Neuroendocrine tumors of the lung: current challenges and advances in the diagnosis and management of well-differentiated disease. J Thorac Oncol. 2017;12(3):425–36. https://doi.org/10.1016/j.jtho.2016.11.2222.
3. Rekhtman N. Neuroendocrine tumors of the lung: an update. Arch Pathol Lab Med. 2010;134(11):1628–38. https://doi.org/10.1043/2009-0583-RAR.1.
4. Delavault P, Caplin ME, Liyange N, Blumberg J, UK, Society INTSENT. The CLARINET study: assessing the effect of lanreotide autogel on tumor progression-free survival in patients with nonfunctioning gastroenteropancreatic neuroendocrine tumors. Journal of Clinical Oncology. 2012;30(15_suppl):TPS4153–TPS. https://doi.org/10.1200/jco.2012.30.15_suppl.tps4153.

5. Rinke A, Muller HH, Schade-Brittinger C, Klose KJ, Barth P, Wied M, et al. Placebo-controlled, double-blind, prospective, randomized study on the effect of octreotide LAR in the control of tumor growth in patients with metastatic neuroendocrine midgut tumors: a report from the PROMID Study Group. J Clin Oncol. 2009;27(28):4656–63. https://doi.org/10.1200/JCO.2009.22.8510.
6. Strosberg J, El-Haddad G, Wolin E, Hendifar A, Yao J, Chasen B, et al. Phase 3 trial of (177)Lu-Dotatate for midgut neuroendocrine tumors. N Engl J Med. 2017;376(2):125–35. https://doi.org/10.1056/NEJMoa1607427.
7. Strosberg J, Wolin E, Chasen B, Kulke M, Bushnell D, Caplin M, et al. Health-related quality of life in patients with progressive midgut neuroendocrine tumors treated with (177)Lu-Dotatate in the phase III NETTER-1 trial. J Clin Oncol. 2018;36(25):2578–84. https://doi.org/10.1200/JCO.2018.78.5865.
8. Yao JC, Fazio N, Singh S, Buzzoni R, Carnaghi C, Wolin E, et al. Everolimus for the treatment of advanced, non-functional neuroendocrine tumours of the lung or gastrointestinal tract (RADIANT-4): a randomised, placebo-controlled, phase 3 study. Lancet. 2016;387(10022):968–77. https://doi.org/10.1016/S0140-6736(15)00817-X.
9. Lamberti G, Brighi N, Maggio I, Manuzzi L, Peterle C, Ambrosini V, et al. The role of mTOR in neuroendocrine tumors: future cornerstone of a winning strategy? Int J Mol Sci. 2018;19(3). https://doi.org/10.3390/ijms19030747.
10. Lo Russo G, Pusceddu S, Prinzi N, Imbimbo M, Proto C, Signorelli D, et al. Peptide receptor radionuclide therapy: focus on bronchial neuroendocrine tumors. Tumour Biol. 2016;37(10):12991–3003. https://doi.org/10.1007/s13277-016-5258-9.
11. Mittra ES. Neuroendocrine tumor therapy: (177)Lu-DOTATATE. AJR Am J Roentgenol. 2018;211(2):278–85. https://doi.org/10.2214/AJR.18.19953.
12. Ballal S, Yadav MP, Damle NA, Sahoo RK, Bal C. Concomitant 177Lu-DOTATATE and capecitabine therapy in patients with advanced neuroendocrine tumors: a long-term-outcome, toxicity, survival, and quality-of-life study. Clin Nucl Med. 2017;42(11):e457–e66. https://doi.org/10.1097/RLU.0000000000001816.
13. Bodei L, Cremonesi M, Grana CM, Fazio N, Iodice S, Baio SM, et al. Peptide receptor radionuclide therapy with (1)(7)(7)Lu-DOTATATE: the IEO phase I-II study. Eur J Nucl Med Mol Imaging. 2011;38(12):2125–35. https://doi.org/10.1007/s00259-011-1902-1.
14. Navalkissoor S, Grossman A. Targeted alpha particle therapy for neuroendocrine tumours: the next generation of peptide receptor radionuclide therapy. Neuroendocrinology. 2019;108(3):256–64. https://doi.org/10.1159/000494760.
15. Andersson H, Palm S, Lindegren S, Back T, Jacobsson L, Leser G, et al. Comparison of the therapeutic efficacy of 211At- and 131I-labelled monoclonal antibody MOv18 in nude mice with intraperitoneal growth of human ovarian cancer. Anticancer Res. 2001;21(1A):409–12.
16. Miederer M, Henriksen G, Alke A, Mossbrugger I, Quintanilla-Martinez L, Senekowitsch-Schmidtke R, et al. Preclinical evaluation of the alpha-particle generator nuclide 225Ac for somatostatin receptor radiotherapy of neuroendocrine tumors. Clin Cancer Res. 2008;14(11):3555–61. https://doi.org/10.1158/1078-0432.CCR-07-4647.
17. Milenic D, Garmestani K, Dadachova E, Chappell L, Albert P, Hill D, et al. Radioimmunotherapy of human colon carcinoma xenografts using a 213Bi-labeled domain-deleted humanized monoclonal antibody. Cancer Biother Radiopharm. 2004;19(2):135–47. https://doi.org/10.1089/108497804323071904.
18. Song H, Hobbs RF, Vajravelu R, Huso DL, Esaias C, Apostolidis C, et al. Radioimmunotherapy of breast cancer metastases with alpha-particle emitter 225Ac: comparing efficacy with 213Bi and 90Y. Cancer Res. 2009;69(23):8941–8. https://doi.org/10.1158/0008-5472.CAN-09-1828.
19. Wild D, Frischknecht M, Zhang H, Morgenstern A, Bruchertseifer F, Boisclair J, et al. Alpha- versus beta-particle radiopeptide therapy in a human prostate cancer model (213Bi-DOTA-PESIN and 213Bi-AMBA versus 177Lu-DOTA-PESIN). Cancer Res. 2011;71(3):1009–18. https://doi.org/10.1158/0008-5472.CAN-10-1186.
20. Tafreshi NK, Doligalski ML, Tichacek CJ, Pandya DN, Budzevich MM, El-Haddad G, et al. Development of targeted alpha particle therapy for solid tumors. Molecules. 2019;24(23). https://doi.org/10.3390/molecules24234314.
21. Nonnekens J, Chatalic KL, Molkenboer-Kuenen JD, Beerens CE, Bruchertseifer F, Morgenstern A, et al. (213)Bi-labeled prostate-specific membrane antigen-targeting agents induce DNA double-Strand breaks in prostate cancer xenografts. Cancer Biother Radiopharm. 2017;32(2):67–73. https://doi.org/10.1089/cbr.2016.2155.
22. Ballal S, Yadav MP, Bal C, Sahoo RK, Tripathi M. Broadening horizons with (225)Ac-DOTATATE targeted alpha therapy for gastroenteropancreatic neuroendocrine tumour patients stable or refractory to (177)Lu-DOTATATE PRRT: first clinical experience on the efficacy and safety. Eur J Nucl Med Mol Imaging. 2020;47(4):934–46. https://doi.org/10.1007/s00259-019-04567-2.
23. Esser JP, Krenning EP, Teunissen JJ, Kooij PP, van Gameren AL, Bakker WH, et al. Comparison of [(177)Lu-DOTA(0),Tyr(3)]octreotate and [(177)Lu-DOTA(0),Tyr(3)]octreotide: which peptide is preferable for PRRT? Eur J Nucl Med Mol Imaging. 2006;33(11):1346–51. https://doi.org/10.1007/s00259-006-0172-9.
24. Ma D, McDevitt MR, Finn RD, Scheinberg DA. Breakthrough of 225Ac and its radionuclide daughters from an 225Ac/213Bi generator: development of new methods, quantitative characterization, and implications for clinical use. Appl Radiat Isot. 2001;55(5):667–78. https://doi.org/10.1016/s0969-8043(01)00062-8.
25. Yong K, Brechbiel M. Application of (212)Pb for targeted alpha-particle therapy (TAT): pre-clinical and mechanistic understanding through to clinical translation. AIMS Med Sci. 2015;2(3):228–45. https://doi.org/10.3934/medsci.2015.3.228.
26. Borchardt PE, Yuan RR, Miederer M, McDevitt MR, Scheinberg DA. Targeted actinium-225 in vivo generators for therapy of ovarian cancer. Cancer Res. 2003;63(16):5084–90.
27. Zhuikov BL, Kalmykov SN, Ermolaev RA, Aliev VM, Kokhanyuk VL, Matushko IG, et al. Production of 225Ac and 223Ra by irradiation of Th with accelerated protons. Radiochemistry. 2011;53(1):77–80.
28. Griswold JR, Medvedev DG, Engle JW, Copping R, Fitzsimmons JM, Radchenko V, et al. Large scale accelerator production of (225)Ac: effective cross sections for 78-192MeV protons incident on (232)Th targets. Appl Radiat Isot. 2016;118:366–74. https://doi.org/10.1016/j.apradiso.2016.09.026.
29. John K, editor. Targeted Alpha Therapy: The US DOE Tri-Lab (ORNL, BNL, LANL) Research Effort to Provide Accelerator-Produced 225Ac for Radiotherapy. American Physical Society Annual Meeting; 2017 January 2017; New Orleans, LA USA.
30. Reid Y, Storts D, Riss T, Minor L. Authentication of human cell lines by STR DNA profiling analysis. In: Sittampalam GS, Coussens NP, Brimacombe K, Grossman A, Arkin M, Auld D et al., editors. Assay Guidance Manual. Bethesda (MD)2004.
31. Tafreshi NK, Enkemann SA, Bui MM, Lloyd MC, Abrahams D, Huynh AS, et al. A mammaglobin-a targeting agent for noninvasive detection of breast cancer metastasis in lymph nodes. Cancer Res. 2011;71(3):1050–9. https://doi.org/10.1158/0008-5472.CAN-10-3091.
32. Barkey NM, Tafreshi NK, Josan JS, De Silva CR, Sill KN, Hruby VJ, et al. Development of melanoma-targeted polymer micelles by

conjugation of a melanocortin 1 receptor (MC1R) specific ligand. J Med Chem. 2011;54(23):8078–84. https://doi.org/10.1021/jm201226w.

33. Pandya DN, Hantgan R, Budzevich MM, Kock ND, Morse DL, Batista I, et al. Preliminary therapy evaluation of (225)Ac-DOTA-c(RGDyK) demonstrates that Cerenkov radiation derived from (225)Ac daughter decay can be detected by optical imaging for in vivo tumor visualization. Theranostics. 2016;6(5):698–709. https://doi.org/10.7150/thno.14338.
34. Tafreshi NK, Tichacek CJ, Pandya DN, Doligalski ML, Budzevich MM, Kil H, et al. Melanocortin 1 receptor-targeted alpha-particle therapy for metastatic uveal melanoma. J Nucl Med. 2019;60(8):1124–33. https://doi.org/10.2967/jnumed.118.217240.
35. Morse DL, Carroll D, Weberg L, Borgstrom MC, Ranger-Moore J, Gillies RJ. Determining suitable internal standards for mRNA quantification of increasing cancer progression in human breast cells by real-time reverse transcriptase polymerase chain reaction. Anal Biochem. 2005;342(1):69–77. https://doi.org/10.1016/j.ab.2005.03.034.
36. Morss LR, Edelstein N, Fuger J, Katz JJ. The chemistry of the actinide and transactinide elements, Volumes 1–6. In: Morss LR, Edelstein, N., Fuger, J., Katz, J.J., editor. 4th ed: Springer Science and Business Media; 2011.
37. Tichacek CJ, Budzevich MM, Wadas TJ, Morse DL, Moros EG. A Monte Carlo method for determining the response relationship between two commonly used detectors to indirectly measure alpha particle radiation activity. Molecules. 2019;24(18). doi:https://doi.org/10.3390/molecules24183397.
38. Lambert B, Cybulla M, Weiner SM, Van De Wiele C, Ham H, Dierckx RA, et al. Renal toxicity after radionuclide therapy. Radiat Res. 2004;161(5):607–11. https://doi.org/10.1667/rr3105.
39. Vegt E, de Jong M, Wetzels JF, Masereeuw R, Melis M, Oyen WJ, et al. Renal toxicity of radiolabeled peptides and antibody fragments: mechanisms, impact on radionuclide therapy, and strategies for prevention. J Nucl Med. 2010;51(7):1049–58. https://doi.org/10.2967/jnumed.110.075101.
40. Rolleman EJ, Valkema R, de Jong M, Kooij PP, Krenning EP. Safe and effective inhibition of renal uptake of radiolabelled octreotide by a combination of lysine and arginine. Eur J Nucl Med Mol Imaging. 2003;30(1):9–15. https://doi.org/10.1007/s00259-002-0982-3.

ACS Pharmacology & Translational Science

pubs.acs.org/ptsci

Article

Lipophilicity Determines Routes of Uptake and Clearance, and Toxicity of an Alpha-Particle-Emitting Peptide Receptor Radiotherapy

Narges K. Tafreshi, HyunJoo Kil, Darpan N. Pandya, Christopher J. Tichacek, Michael L. Doligalski, Mikalai M. Budzevich, Nella C. Delva, Michael L. Langsen, John A. Vallas, David C. Boulware, Robert W. Engelman, Kenneth L. Gage, Eduardo G. Moros, Thaddeus J Wadas, Mark L. McLaughlin, and David L. Morse*

Cite This: *ACS Pharmacol. Transl. Sci.* 2021, 4, 953−965

Read Online

ACCESS | Metrics & More | Article Recommendations | Supporting Information

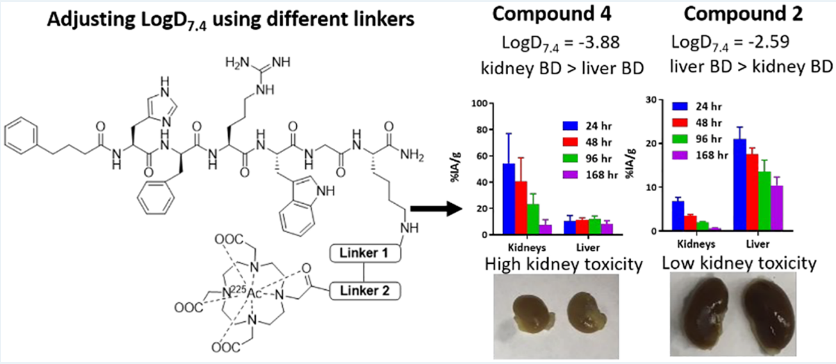

ABSTRACT: Lipophilicity is explored in the biodistribution (BD), pharmacokinetics (PK), radiation dosimetry (RD), and toxicity of an internally administered targeted alpha-particle therapy (TAT) under development for the treatment of metastatic melanoma. The TAT conjugate is comprised of the chelator DOTA (1,4,7,10-tetraazacyclododecane-1,4,7,10-tetraacetate), conjugated to melanocortin receptor 1 specific peptidic ligand (MC1RL) using a linker moiety and chelation of the ^{225}Ac radiometal. A set of conjugates were prepared with a range of lipophilicities (log $D_{7.4}$ values) by varying the chemical properties of the linker. Reported are the observations that higher log $D_{7.4}$ values are associated with decreased kidney uptake, decreased absorbed radiation dose, and decreased kidney toxicity of the TAT, and the inverse is observed for lower log $D_{7.4}$ values. Animals administered TATs with lower lipophilicities exhibited acute nephropathy and death, whereas animals administered the highest activity TATs with higher lipophilicities lived for the duration of the 7 month study and exhibited chronic progressive nephropathy. Changes in TAT lipophilicity were not associated with changes in liver uptake, dose, or toxicity. Significant observations include that lipophilicity correlates with kidney BD, the kidney-to-liver BD ratio, and weight loss and that blood urea nitrogen (BUN) levels correlated with kidney uptake. Furthermore, BUN was identified as having higher sensitivity and specificity of detection of kidney pathology, and the liver enzyme alkaline phosphatase (ALKP) had high sensitivity and specificity for detection of liver damage associated with the TAT. These findings suggest that tuning radiopharmaceutical lipophilicity can effectively modulate the level of kidney uptake to reduce morbidity and improve both safety and efficacy.

KEYWORDS: *Biodistribution, Melanocortin receptor 1, Actinium-225, Lipophilicity, Radiotherapy, α-Particle emmiter*

Drug discovery and development is a complex, labor-intensive, and lengthy process. This long road includes determining a clinical need, identification and validation of clinically relevant target(s), discovery of targeting moieties, preclinical testing of the drug candidates, and documentation of the efficacy and safety of the drug candidate in the clinical trial phase.[1−3] On average, this process can take 12−15 years with a cost of hundreds of millions of dollars.[4,5] Furthermore, roughly 10% of compounds that are selected for further clinical

Received: January 22, 2021
Published: March 12, 2021

https://dx.doi.org/10.1021/acsptsci.1c00035

study make it to the marketplace as safe and effective drugs, demonstrating that the overall drug development process is formidable.[6]

The success of a new drug candidate is determined not only by its efficacy but also by proper pharmacokinetic behavior. Many promising drug candidates with appreciable activity *in vitro* fail to become marketable products, most often due to inappropriate pharmacokinetic behavior. Physicochemical properties can be used in the optimization of pharmacokinetics and the early prediction of absorption, distribution, metabolism, and excretion (ADME) can save time and money.[7,8]

Lipophilicity, which is the affinity of a molecule or a moiety for a lipophilic environment, is a key physicochemical property that plays a crucial role in ADME characteristics of drugs.[9,10] It is one of the factors included in the rule of five formulated by Lipinski in 1997, a tool for medicinal chemists that is used for quick assessment of compounds during drug discovery.[11] It also has considerable impact on solubility and membrane permeability,[12,13] potency,[14] selectivity,[15] and promiscuity[15] of drugs, therefore affecting their biodistribution (e.g., hepatic elimination vs renal excretion), pharmacodynamics, and toxicological profile.[9,10,16] Lipophilicity is commonly described by the processes of partition between two phases, a nonpolar (organic phase) and a polar (mostly aqueous phase), and expressed as the logarithm of the *n*-octanol partition coefficient (log P or log D).[17]

Peptide−ligand drug conjugates can have high binding affinity and specificity for targets that are highly expressed on cancer cells but have low or nonexpression on normal cells of concern for toxicity. These properties have created significant interest in the use of peptide ligands in pharmaceutical research and development (R&D),[18] as there are currently ∼140 therapeutics with peptide targeting ligands in clinical trials.[2] The systemic clearance route of peptide-drug conjugates can be a significant factor in terms of dose-limiting toxicity (i.e., renal vs hepatic). Although several studies have correlated the route of clearance with the physicochemical properties of small molecules,[9,19−21] to the best of our knowledge, these correlations are largely unexplored for peptide conjugates.

Because of the high linear energy transfer (LET) and short-range of α particles in tissue, there is significant interest in the development of targeted alpha-particle therapy (TAT) for the treatment of solid tumors (reviewed recently by our group).[22] We recently published studies demonstrating the conjugation of a peptide based ligand (MC1RL) with high affinity and selectivity for the melanocortin 1 receptor (MC1R)[23] to a metal chelator (dodecane tetraacetic acid, DOTA) using an aminohexanoic acid (Ahx) linker (DOTA-Ahx-MC1RL). This conjugate was radiolabeled with the α-particle-emitting radionuclide, ^{225}Ac, for use as TAT for treatment of metastatic uveal melanoma.[22] The melanocortin 1 receptor (MC1R) is expressed in 94% of uveal melanoma metastases.

Our preclinical studies demonstrated low toxicity, significantly prolonged survival, and decreased metastasis burden following treatment with ^{225}Ac-DOTA-Ahx-MC1RL.[22] We also observed that ^{225}Ac-DOTA-Ahx-MC1RL was cleared more via the hepatic route, which differed from our previously reported near-infrared fluorescent dye conjugate (MC1RL-800) that has predominant renal clearance.[24,25] We observed that the log $D_{7.4}$ value of ^{225}Ac-DOTA-Ahx-MC1RL was significantly higher than the value of MC1RL-800 and hypothesized that lipophilicity may have a role in determining the clearance route of these two conjugates. To test this hypothesis, we designed and synthesized a library of DOTA-linker-MC1RL compounds with diverse linkers and a predicted range of log $D_{7.4}$ values. Herein, we report the synthesis and characterization of lipophilicity, biodistribution, clearance route, radiation dosimetry, and toxicity profile of this new library of compounds.

■ MATERIALS AND METHODS

Synthesis of DOTA-linker-MC1RL Compound Library. MC1RL compounds[23] with different linkers were synthesized on Rink Amide resin (initial loading: 0.568 mmol/g) using N$^{\alpha}$-Fmoc-protecting amino acids and a HCTU/DIEA strategy. After the resin was swollen in DCM for 30 min, the Fmoc protecting group was removed with 2% DBU in DMF (2 × 5 min). The resin was washed with NMP and DCM three times each, and the first amino acid was coupled using HCTU and DIEA in NMP (4 equiv of N$^{\alpha}$-Fmoc amino acid, 4 equiv of HCTU, and 8 equiv of DIEA). The double coupling was performed at all steps under the same coupling conditions due to the sequence deletion and the slower coupling rate in longer sequences. After coupling, the resin was washed with NMP (×3) and DCM (×3), and any unreacted free amine groups on the resin were treated using 50% acetic anhydride in pyridine for 5 min. After the resin was washed with NMP (×3) and DCM (×3), the same procedure was repeated for the next amino acid coupling until every residue in the sequence was coupled.

The Alloc protecting group of the C-terminal Lys was deprotected with piperidine (5−10 drops) and Pd(PPh$_3$)$_4$ (0.2 equiv) in anhydrous chloroform. Under nitrogen gas, the reaction mixture was stirred for 15 min and then repeated. After the resin was washed with chloroform, NMP, and DCM; DOTA (no-linker), aminohexanoic acid−DOTA, D-Lys-D-Lys−DOTA, or D-Lys-D-Glu−DOTA, were coupled to the free amine via HCTU coupling as described above.

The peptide and every protecting group was cleaved using cleavage cocktail (88% TFA, 5% water, 5% phenol, and 2% triethylsilane) for 4 h. The crude peptide was isolated from the resin by filtration, and the filtrate was concentrated. The peptide was precipitated in ice cold diethyl ether, dissolved in water, and lyophilized. The off-white crude powder was purified by reverse-phase chromatography.

Complexation of the peptides with lanthanum (La^{3+}) was accomplished by incubation (25 °C) of the purified peptide in 0.1 M of sodium acetate, pH 6 buffer solution with 3 equiv of lanthanum chloride heptahydrate. The complexation reaction was assayed for completion by monitoring the retention time shift of the ligands on a linear gradient of analytical RP-HPLC. After 16 h of incubation, the reaction was complete, and peptide ligand solutions were separated from the excess metal and buffer by semiprep RP-HPLC. Eu-DTPA-MC1RL was synthesized as described before.[22]

Cell Culture. HEK293/MC1R (HEK293 cells engineered to express MC1R)[26] were grown in DMEM/F12 (Life Technologies) containing 10% FBS, 100 units/mL penicillin, and 100 mg/mL streptomycin in 5% CO$_2$ at 37 °C. All experiments were performed with cells of passage number less than 25. Cells were authenticated using short tandem repeat (STR) DNA typing according to ATCC's guidelines by the Molecular Genomics Core Facility at Moffitt[27] and monitored by microscopy to ensure maintenance of their original morphology. Cells were tested for mycoplasma contamination using the MycoAlert kit (Lonza).

Binding Assay. HEK293/MC1R cells[28] were used to assess ligand binding in a lanthanide-based time-resolved fluorescence competitive binding assay as described previously.[23] Briefly, the cells were plated on SigmaScreen poly-D-lysine coated plates (Sigma-Aldrich) at a density of 30 000 cells/well 1 day before the experiment. On the day of the experiment, the medium was aspirated, and 50 μL of nonlabeled competing ligand was added to each well in a series of decreasing concentrations (ranging from ~1 μM to 0.1 nM), followed by 50 μL of Eu-DTPA-MC1RL at 10 nM. All ligands were diluted in binding medium (DMEM, 1 mM 1,10-phenanthroline, 200 mg/L bacitracin, 0.5 mg/L leupeptin, and 0.3% BSA). Cells were incubated with ligands for 30 min at 37 °C. Following incubation, cells were washed two times with PBS, and 100 μL of enhancement solution (PerkinElmer) was added to each well. Cells were incubated for an additional 30 min at 37 °C prior to reading. The plates were read on a PerkinElmer VICTORx4 2030 multilabel reader using the standard Eu time-resolved fluorescence (TRF) measurement (340 nm excitation, 400 μs delay, and emission collection for 400 μs at 615 nm). Competitive binding curves were analyzed with GraphPad Prism software using the sigmoidal dose—response (variable slope) classical equation for nonlinear regression analysis.

Lipophilicity. The lipophilicities of the unmetalated and La^{3+}-chelated DOTA-linker-MC1RL compounds were determined by a miniaturized shake-flask method similar to a previous report.[24] Stock solutions of the compounds (200 μM) in 10 mM, pH 7.4, phosphate buffer were prepared. Aliquots of the stock solutions were vortexed with three different ratios of *n*-octanol. The resulting emulsions were centrifugated and the PBS and *n*-octanol layers separated. Unknown compound concentrations in the aqueous and organic layers were measured by HPLC-triple quadrupole MRM mass spectroscopy. Triplicate measurements of compound concentration were used to calculate the log of partition between the lipid and aqueous phases at pH 7.4 (log $D_{7.4}$).

Radiochemical Synthesis and Quality Control for ^{225}Ac-DOTA-linker-MC1RL Compounds. Actinium-225 (^{225}Ac: $t_{1/2}$ = 10 days; $E_{\alpha\max}$ = 6−8 MeV) was purchased from Oak Ridge National Laboratories. The complexation of ^{225}Ac was achieved for DOTA-Ahx-MC1RL as previously described[29] and by reacting DOTA-MC1RL (no linker), DOTA-DLDL-MC1RL (D-Lys-D-Lys linker), or DOTA-DLDG-MC1RL (D-Lys-D-Glu linker) (5−10 μg in 5−10 μL water from 1.0 mg/mL solution) with $^{225}Ac(NO_3)_3$ (3.4 MBq) that was diluted in 100 μL of water containing 10 μL of 20% L-ascorbic acid. The pH of the resulting solution was adjusted to 5.5−6 using 1 M Tris buffer (10−12 μL) and then incubated at 60 °C for 1 h. Reaction progress and radiochemical purity were measured without further purification using ITLC with gamma counting, radio-TLC, and gamma counting of radio-HPLC fractions. Specific activity was calculated using a standard method.[30] Analysis was performed 24 h after sample collection to ensure secular equilibrium was achieved between ^{225}Ac and its daughter products. The proportion of chelated ^{225}Ac in this preparation relative to the proportion of chelated La^{3+} is described in Supplemental Experimental Methods.

Animal Studies. All protocols were approved as University of South Florida IACUC protocol IS00004454.

Injected Activity Measurement. Syringes were prefilled with ^{225}Ac radiopharmaceutical activity, and since α-particles from ^{225}Ac cannot be directly measured in tissue due to the range,[31] the activity was measured using the isomeric gamma spectra by the 4π well-type Atomlab 500 Wipe Test Gamma Counter (BioDex) and converted to ^{225}Ac alpha activity using factors for γ ray abundance per alpha decay as described previously.[22] The spectra were acquired using a full energy window to include gamma counts from ^{225}Ac, with peak at 99.8 keV (abundance 1%), and its two γ-emitting daughters, ^{221}Fr (4.9 min $T_{1/2}$) with peak at 218.1 keV (abundance 11.4%) and ^{213}Bi (46 min $T_{1/2}$) with peak at 440.5 keV (abundance 25.9%).[32] The alpha activity in 1 μCi of each radionuclide was determined by fitting each peak with a multi-Gaussian fit and integrating to determine the net number of counts while incorporating the acquisition time. The activity was injected into each mouse via tail-vein catheter. Activity remaining in the syringe and catheter postinjection were calculated and subtracted to determine net administered activity. Spectra were acquired at ≥24 h post-radiosynthesis or tissue rendering ensuring that ^{225}Ac and daughters were in secular equilibrium.[33]

Biodistribution (BD). Male and female BALB/c mice (10−12 weeks, 18−22 g, Charles River) were used for the BD studies. Tail vein catheters were used for agent administration to mice. All mice were intravenously administered 148 kBq ± 10% of ^{225}Ac alpha activity in the syringe. The animals were euthanized at multiple time-points between 24 h and 1 week post-injection (p.i.) (n = 5 mice per time point), and tissues were removed and weighed. The isomeric gamma spectra were measured for each tissue sample as described above. Using the net administered activity for ^{225}Ac, ^{221}Fr, and ^{213}Bi, the percent injected activity per gram (%IA/g) were then calculated and compared to a weighed, counted standard for all groups.

In-house-designed Matlab (MathWorks) code was used to calculate the pharmacokinetics (PK) rates of uptake and clearance for each compound. Data were fit using the nonlinear least-squares approach and the logarithmic equation for uptake and two-exponential decay equation for clearance to find relevant parameters (e.g., rates of uptake and clearance).[34] The following equation was used for uptake:

$$y = A \times \log(x) + \lambda$$

where y [%IA/g] is the percentage of measured radioactivity per gram of tissue, A [%IA/g] is the peak percentage of radioactivity per gram of tissue, and λ [%IA/g/h] is the rate of uptake.

A two-compartment model was used where rapid clearance of radiopharmaceutical circulating in the blood and a slower clearance of radiopharmaceutical from tissues are observed. Hence, the following two-exponential equation was used for clearance:

$$y = A_1 \times e^{(-\lambda_1 x)} + A_2 \times e^{(-\lambda_2 x)}$$

where y [%IA/g] is the percentage of measured radioactivity per gram of tissue, A_1 [%IA/g] and A_2 [%IA/g] are the initial percentages of radioactivity per gram of tissue at two different phases of clearance, and λ_1 [%IAg/h] and λ_2 [%IAg/h] are the rates of clearance for two different phases.

Radiation Dosimetry (RD). Dosimetry calculations were performed as previously described.[29] As described above for BD studies, isomeric γ-emission spectra of ^{225}Ac and the two

Scheme 1. Synthetic Route of DOTA-Linker-MC1RL Compounds

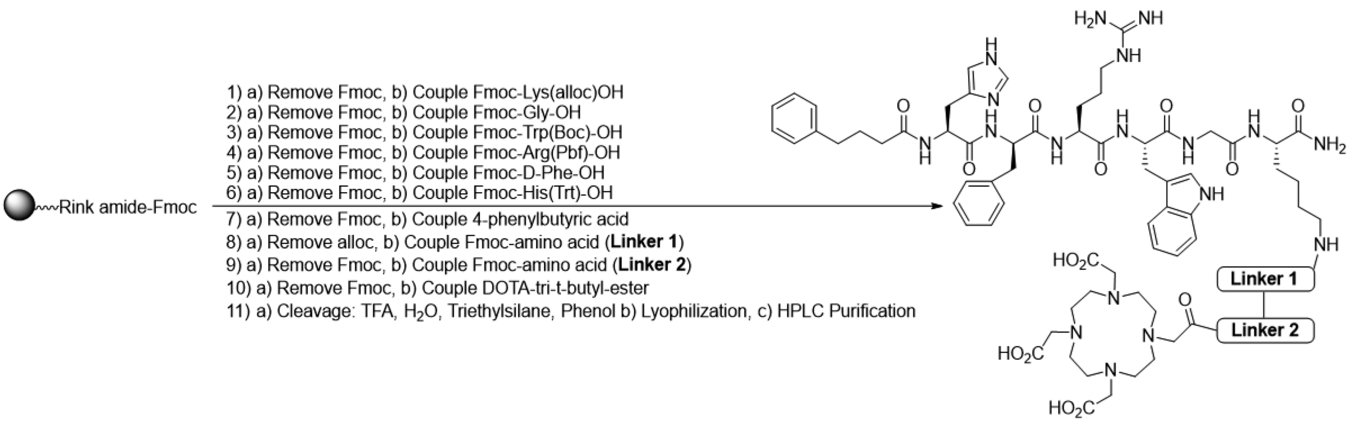

Compounds	MW	Linker Residue 1	Linker Residue 2
1	1361	-	-
2	1474	Ahx	-
3	1586	D-Lys	D-Lys
4	1618	D-Lys	D-Glu

radionuclides in the decay chain with detectable emissions, ^{221}Fr and ^{213}Bi, were acquired in tissues rendered at different p.i. time points and used for these calculations. Because of their short half-lives, ^{217}At (32.2 ms) and ^{213}Po (4.2 μs) were assumed to decay at the site of their parent radionuclides, ^{221}Fr and ^{213}Bi, respectively. The β decay branching ratio for ^{217}At to ^{217}Rn is only 0.01%; therefore, it was assumed that all decays of ^{217}At progressed by α emission to ^{213}Bi. The branching ratios for decay of ^{213}Bi are 98% to ^{213}Po and 2% to ^{209}Tl and were accounted for in the calculation. Due to the relatively low LET and the small dimensions of the target tissues, the β emissions from ^{217}At, ^{213}Bi, ^{209}Tl, and ^{209}Pb were assumed to be negligible and are not included in the calculations.[35]

Organ and tumor absorbed doses from ^{225}Ac, ^{221}Fr, ^{217}At, ^{213}Bi, and ^{213}Po were determined using acquired BD data. Dosimetry calculations were performed using the generalized internal dosimetry schema of the MIRD Committee for α-particle emitters.[35,36] According to MIRD #21, the absorbed radiation dose due to particle type x, $D_x(r_T, T_D)$, is the mean energy imparted to target tissue r_T per unit tissue mass, defined by eq 1:

$$D_x(r_T, T_D) = k\,\tilde{A}(r_S, T_D)\frac{\sum_i \Delta_i^x \varphi(r_T \leftarrow r_S; E_i^x)}{M(r_T)} \quad (1)$$

where $\tilde{A}(r_S, T_D)$ is the total number of nuclear transitions in the target region (accumulated activity), Δ_i^x is the mean energy emitted per nuclear transition, $\varphi(r_T \leftarrow r_S; E_i^x)$ is the fraction of energy emitted per nuclear transition in the source region that is absorbed in the target region by the ith emission that is emitted with initial energy E, k is a conversion factor, and $M(r_T)$ is the mass of the target tissue. Time−activity curves were generated for each organ and fit with an exponential decay nonlinear regression. Accumulated activity in each organ/tumor was determined by analytically integrating the resulting equation of fit. Several assumptions were made in the calculation of absorbed dose. It was assumed that the α-particle activity was uniformly distributed in each organ/tumor volume, and as a result of its short-range in tissue, no α particles escaped from its source organ/tumor. Electron and photon contributions were assumed to be negligible compared to α-particle energy deposition.[37] After these assumptions, eq 1 simplifies to

$$D_\alpha(r, T_D) = \frac{k\tilde{A}(r, T_D)\Delta^\alpha}{M(r)} \quad (2)$$

It was assumed that α particles from ^{221}Fr (4.9 min $T_{1/2}$), ^{217}At (32.2 ms $T_{1/2}$), ^{213}Bi (46 min $T_{1/2}$), and ^{213}Po (4.2 μs $T_{1/2}$) were deposited in the same location as ^{225}Ac (10 day $T_{1/2}$) due to the relatively shorter half-lives of these daughter isotopes. Although ^{217}At and ^{213}Po do not have detectable γ emissions, under the assumption that the decay chain had reached secular equilibrium, the accumulated activity of these two daughters would equal that of ^{221}Fr and ^{213}Bi, respectively. The total absorbed α-particle dose was calculated from the summation of doses from ^{225}Ac, ^{221}Fr, ^{217}At, ^{213}Bi, and ^{213}Po.

Toxicity. Toxicity studies were conducted using cohorts of normal BALB/c mice. After a single intravenous injection of each ^{225}Ac conjugate ranging from 3 to 314 kBq ^{225}Ac activity or saline, cohorts (n = 6 mice/cohort) were weighed 2 times per week and monitored for 7 months for signs of distressed behavior. At the end of that period, animals were euthanized, and serum was collected by centrifugation at 1500 × g. Blood urea nitrogen (BUN), creatinine, alkaline phosphatase (ALKP), alanine aminotransferase (ALT), and aspartate aminotransferase (AST) content in serum were analyzed using the Catalyst DX automated chemistry analyzer and CLIP (IDEXX, ME). Liver, kidney, spleen, pancreas, cecum, small intestine, lymph nodes, bone marrow, muscle, salivary gland, and bone were harvested and fixed in 10% formalin. Bone was decalcified in 14% ethylene diaminetetraacetic acid (EDTA) solution after fixation in formalin. All tissues were embedded in

https://dx.doi.org/10.1021/acsptsci.1c00035
ACS Pharmacol. Transl. Sci. 2021, 4, 953−965

paraffin, sectioned (4−6 μm thickness), and stained with hematoxylin and eosin. The slides were scanned in the Moffitt Analytical Microscopy Core Facility using a ScanScope XT digital slide scanner (Aperio, CA) and examined by the veterinary pathologist (R.E.), in a blind manner.

Statistical Analysis. Analysis of variance (ANOVA) was used to assess the relationship of BD (%IA/g) with the log D value, with log D and time as the independent variables. These analyses were modeled on liver BD, kidney BD, and the kidney/liver BD ratio (i.e., three separate models). An interaction effect with time and BD (either kidney or liver or the ratio) was included too.

Logistic regression analyses were used to assess the toxicities for each compound and injected activity group using standard reference ranges (adjusted for control levels if necessary) based on the injected activity. Weight change for each compound and activity was evaluated relative to the control group's weight change. A predicted probability of toxicity was then generated across the range of injected activity levels to generate curves for each of compound group.

Using the Spearman's correlation coefficient, the correlation of log D values with uptake values for both kidney and liver were estimated for each radiopharmaceutical. Also, for each derived toxicity measure for either kidney or liver, we calculated the sensitivity and specificity of toxicity using pathology as the standard.

■ RESULTS

Synthesis and Characterization of DOTA-linker-MC1RL Compounds. The library of DOTA-linker-MC1RL compounds were synthesized using the synthetic route shown in Scheme 1. Synthesis of the DOTA-Ahx-MC1RL version was previously described.[29] Each compound was chelated with La^{3+} to facilitate *in vitro* characterizations. La^{3+} has been reported as a useful surrogate for compounds being developed with Ac, since both exist as trivalent ions in solution.[28] See Figures S1−S8 for HPLC chromatograms and MALDI-TOF spectra of each compound, with and without La^{3+} chelation.

Via competitive binding assay, we determined that all of the La^{3+}-DOTA-linker-MC1RL compounds have high binding affinity for MC1R (i.e., 0.08, 0.20, 0.06, and 0.23 nM K_i) for versions with the following linkers: no linker, Ahx, DLDL, and DLDG, respectively (Figure 1).

Log $D_{7.4}$, which can influence the tissue distribution of a compound and is an indicator of lipophilicity or solubility, was determined for the unmetalated and La^{3+}-chelated compounds (Table S1). Complexation with La^{3+} reduced the log $D_{7.4}$ for each compound. These values suggest that the compounds are soluble in aqueous buffer, but with variable lipophilicities (ranging from −1.79 to −2.75 for the unmetalated compounds and from −2.14 to −3.88 for the compounds chelated with La^{3+}).

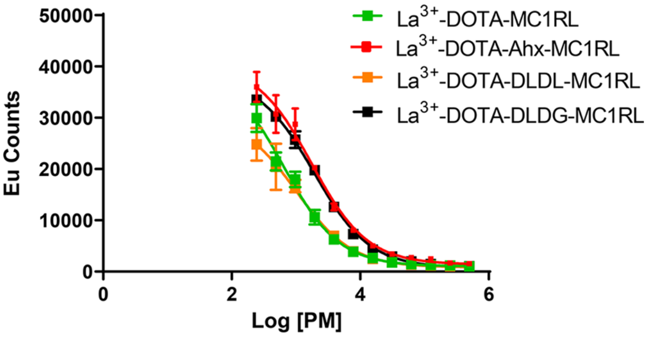

Figure 1. Competitive binding assay for La^{3+}-DOTA-linker-MC1RL compounds.

Radiosynthesis and Characterization of ^{225}Ac-DOTA-linker-MC1RL Radiopharmaceuticals. Radiosynthesis (Scheme 2) for all ^{225}Ac-DOTA-linker-MC1RL radiopharmaceuticals provided a greater than 95% yield with high radiochemical purity (≥99.0%) as determined by radio-TLC and radio-HPLC (Figures S9−S12).

Biodistribution and Pharmacokinetics. Tissue BD of the ^{225}Ac-DOTA-linker-MC1RL radiopharmaceuticals were determined in BALB/c mice. Following intravenous injection, ^{225}Ac activity was observed primarily in clearance tissues (i.e., liver, kidneys, and intestine), and clearance occurred over a period of weeks (Figure 2). Using the BD data, the pharmacokinetics of kidney and liver uptake and clearance rates, and blood clearance rates were calculated for each radiopharmaceutical (Table 1). The uptake data were best fit using the logarithmic uptake equation. A two-compartment model for clearance was assumed, and clearance data were fitted using the two-exponential clearance equation.

Radiation Dosimetry. Radiation dosimetry (RD) calculations were based on the data obtained from the BD studies. RD for targeted radiotherapy is the determination of the absorbed energy deposited per unit mass by ionizing radiation in the different tissue compartments within the body. As described in the Materials and Methods, the α-particle dose from ^{225}Ac and each of its α-emitting daughters was calculated using γ spectroscopy of ^{225}Ac, ^{221}Fr, and ^{213}Bi (Figure S13).

BD data for the different tissues were fitted using an exponential decay nonlinear regression, allowing the estimation of clearance kinetics, tissue biological half-life, accumulated activity, and absorbed dose/injected activity (Gy/kBq) for each radionuclide in each tissue. See Table S2A−C for ^{225}Ac-DOTA-MC1RL, ^{225}Ac-DOTA-DLDL-MC1RL, and ^{225}Ac-DOTA-DLDG-MC1RL. RD for ^{225}Ac-DOTA-Ahx-MC1RL was previously reported.[29] The total absorbed dose is the summation of the values for the five α-emitting radionuclides. The calculated total absorbed dose for each of the ^{225}Ac-labeled compounds was minimal in all tissues except clearance organs (kidneys and liver). The total absorbed dose of ^{225}Ac and daughters was greater in the liver relative to the kidneys for ^{225}Ac-DOTA-MC1RL (no linker) and ^{225}Ac-DOTA-Ahx-MC1RL with 0.56 and 0.24 Gy/kBq for kidneys and 0.79 and 0.70 Gy/kBq for liver, respectively. The total absorbed dose of ^{225}Ac and daughters was greater in the kidneys (1.59 and 0.92 Gy/kBq) relative to the liver (1.36 and 0.45 Gy/kBq) for ^{225}Ac-DOTA-DLDL-MC1RL and ^{225}Ac-DOTA-DLDG-MC1RL, respectively. Figure 3 presents graphs of the absorbed dose from each radionuclide per tissue for all four radiopharmaceuticals.

It is noted that in tissues with significant uptake, the effective decay half-lives (T_{eff}) calculated for ^{225}Ac were shorter than the radiodecay half-life of ^{225}Ac (10 days) for all the compounds, indicating biological clearance. For example, the calculated T_{eff} in kidneys and liver for ^{225}Ac−no linker was 4.8 and 5.7 days, respectively (Table S2A). Hence, T_{eff} is a composite of radiodecay and active biological clearance. The T_{eff} was only calculated to be longer in some tissues with minimal uptake where instrument background likely interfered with the accuracy of measurement.

Scheme 2. Radiochemical Synthesis of ^{225}Ac-DOTA-linker-MC1RL Compounds

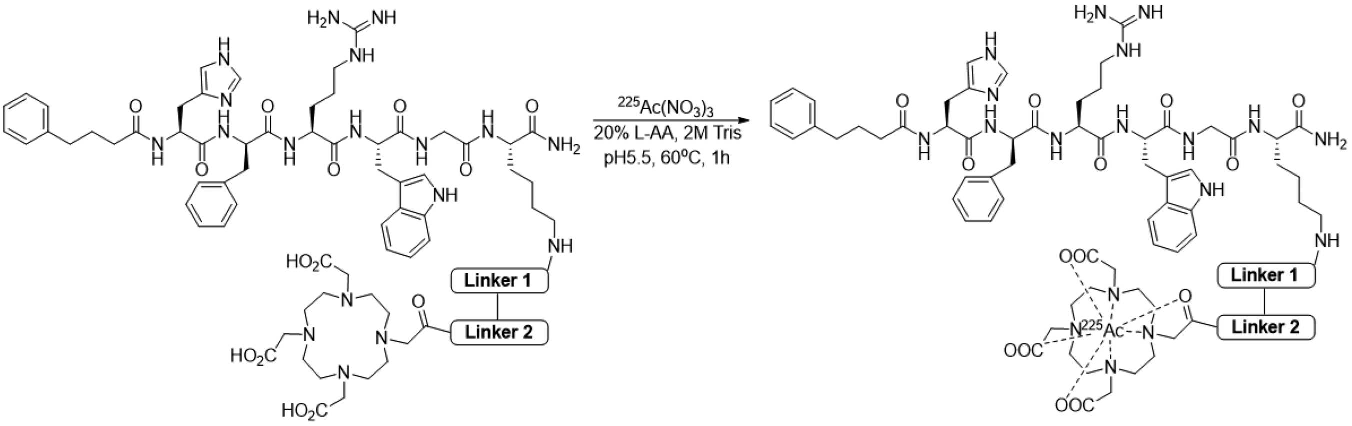

Compounds	Linker Residue 1	Linker Residue 2
1	-	-
2	Ahx	-
3	D-Lys	D-Lys
4	D-Lys	D-Glu

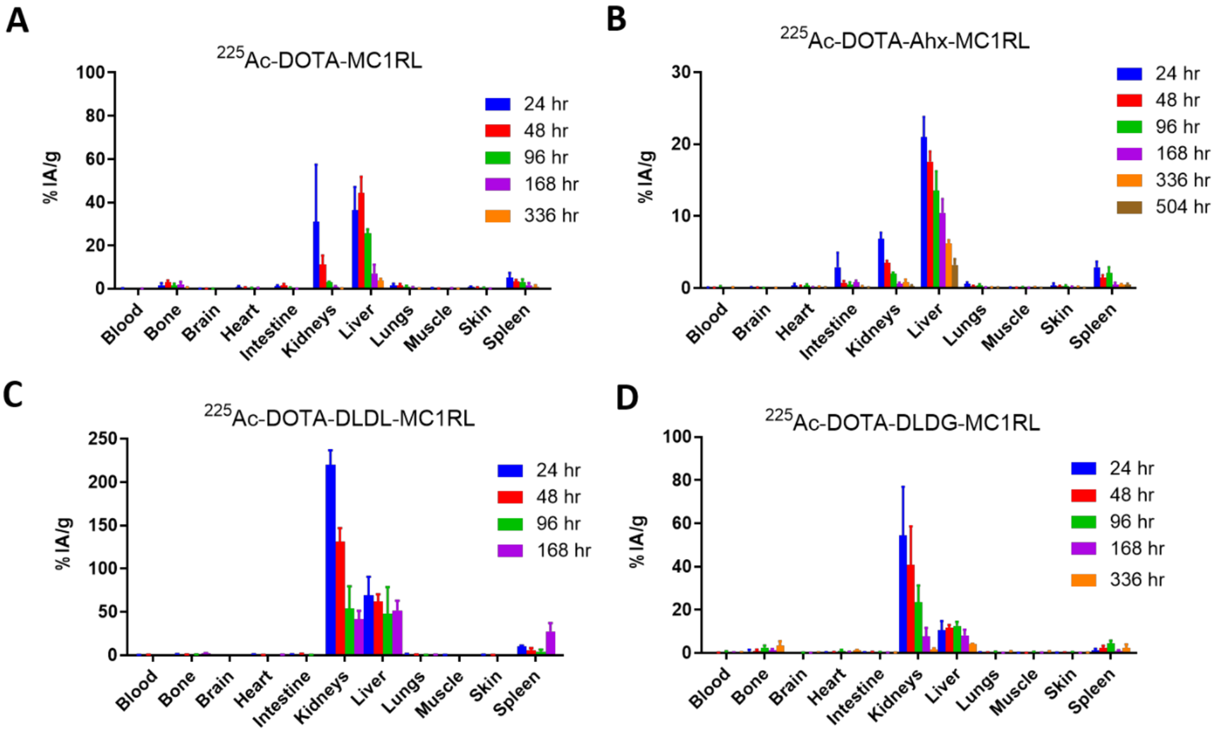

Figure 2. BD results for (A) ^{225}Ac-DOTA-MC1RL, (B) ^{225}Ac-DOTA-Ahx-MC1RL, (C) ^{225}Ac-DOTA-DLDL-MC1RL, and (D) ^{225}Ac-DOTA-DLDG-MC1RL. Activities were calculated for tissues rendered from BALB/c mice (*n* = 6 per time point). The time courses vary among the different compounds due to differences in animal survival and liver clearance.

Toxicity. Cohorts of mice received a single intravenous injection of a range of ^{225}Ac activities from 3 to 314 kBq of each radiopharmaceutical. Animals were weighed twice per week and monitored for 7 months for signs of discomfort or declining condition. At the completion of the study, serum was collected for renal and hepatic toxicity assays, and tissues were collected for histological staining and pathology examination. See Table S3 for the histopathology scoring of all tissues in the study.

Death due to acute renal failure was observed in some cohorts. There were no deaths observed in mice administered ^{225}Ac-DOTA-MC1RL (no linker) or ^{225}Ac-DOTA-Ahx-MC1RL at any injected activity. All mice treated with ≥77.6 kBq of ^{225}Ac-DOTA-DLDL-MC1RL and a single mouse

Table 1. Pharmacokinetics of Uptake and Clearance Rate Constants for Each Compound

compound	organ	uptake rate constant, λ (%IA/g/h)	fast clearance rate constant, λ_1 (%IA/g/h)	slow clearance rate constant, λ_2 (%IA/g/h)
^{225}Ac-DOTA-MC1RL	blood		0.00756	1.89
	kidney	3.98	0.0361	0.0275
	liver	30.1	63.8	0.00737
^{225}Ac-DOTA-Ahx-MC1RL	blood		0.507	0.0125
	kidney	5.63	0.0605	0.00514
	liver	17.3	0.0662	0.00319
^{225}Ac-DOTA-DLDL-MC1RL	blood		1.87	0.00577
	kidney	179	0.0229	−0.0109
	liver	55.9	0.00511	−0.0323
^{225}Ac-DOTA-DGDL-MC1RL	blood		0.0198	2.00
	kidney	44.1	0.0117	−0.0118
	liver	8.97	0.0412	0.00360

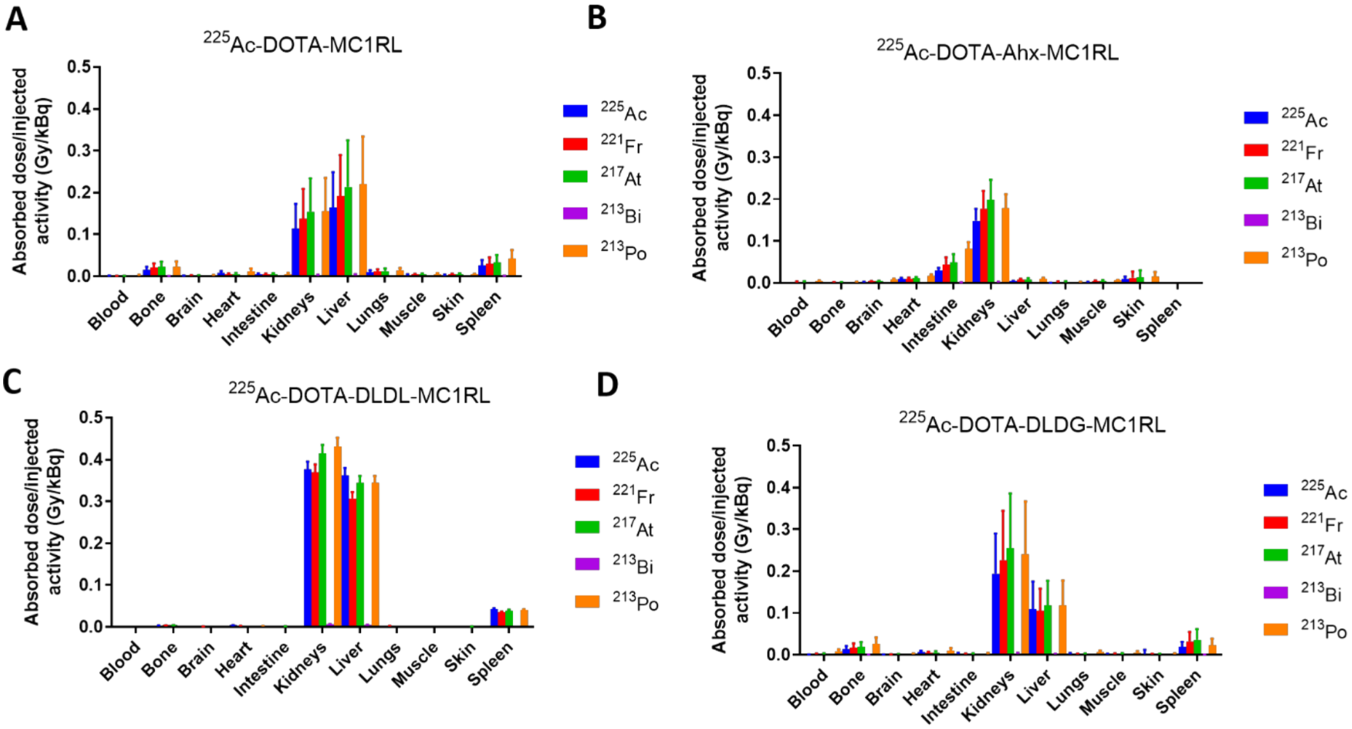

Figure 3. Radiation dosimetry of ^{225}Ac and daughters following administration of (A) ^{225}Ac-DOTA-MC1RL (no linker), (B) ^{225}Ac-DOTA-Ahx-MC1RL, (C) ^{225}Ac-DOTA-DLDL-MC1RL, and (D) ^{225}Ac-DOTA-DLDG-MC1RLin BALB/c mice.

injected with 44.0 kBq of ^{225}Ac-DOTA-DLDG-MC1RL died within 1−2 weeks p.i., and at necropsy, kidneys appeared grossly pale, pitted, small, and irregular in shape (Figure 4A). Histologically, tubular cell necrosis was characterized by intense cytoplasmic eosinophilia with pyknotic nuclei, while other tubules appeared regenerative with cytoplasmic basophilia and nuclear crowding (Figure 4C).

By the end of the study, mice injected with ^{225}Ac-DOTA-MC1RL, ^{225}Ac-DOTA-Ahx-MC1RL, ^{225}Ac-DOTA-DLDL-MC1RL, and ^{225}Ac-DOTA-DLDG-MC1RL at ≥268.9, 181.5, 11.5, and 50.2 kBq of ^{225}Ac activity, respectively, had chronic progressive nephropathy. Histologically, this pathophysiological entity was characterized by little normal renal parenchyma remains due to extensive tubular cell necrosis, epithelial sloughing and cast formation, extensive tubular cell regeneration, diffuse interstitial edema and fibrosis with mild mononuclear inflammatory cell infiltrates, and hypercellular glomerular tufts (Figure 4D,E). Animals injected with less than the above activities survived without abnormal kidney pathology.

None of the animals injected with ^{225}Ac-DOTA-MC1RL or ^{225}Ac-DOTA-DGDL-MC1RL had histopathological liver damage. By the end of the study, mice injected with greater than >317.8 kBq of ^{225}Ac-DOTA-Ahx-MC1RL had treatment-related liver damage such as bile duct hyperplasia and hepatocyte apoptosis (Figure 4G), and mice injected with >27.0 kBq of ^{225}Ac-DOTA-DLDL-MC1RL had treatment related hepatocyte granular degeneration, apoptosis, and necrosis (Figure 4H,I). Incidental hepatocyte glycogen accumulation and mild, focal, hepatocellular fatty changes were observed in the livers of some treated and untreated control mice.

The spleen of some animals injected with >125.8 kBq of ^{225}Ac-DOTA-DLDL-MC1RL had moderate lymphoid depletion. A mild multifocal lymphoplasmacytic infiltration of salivary glands was observed in some treated mice.

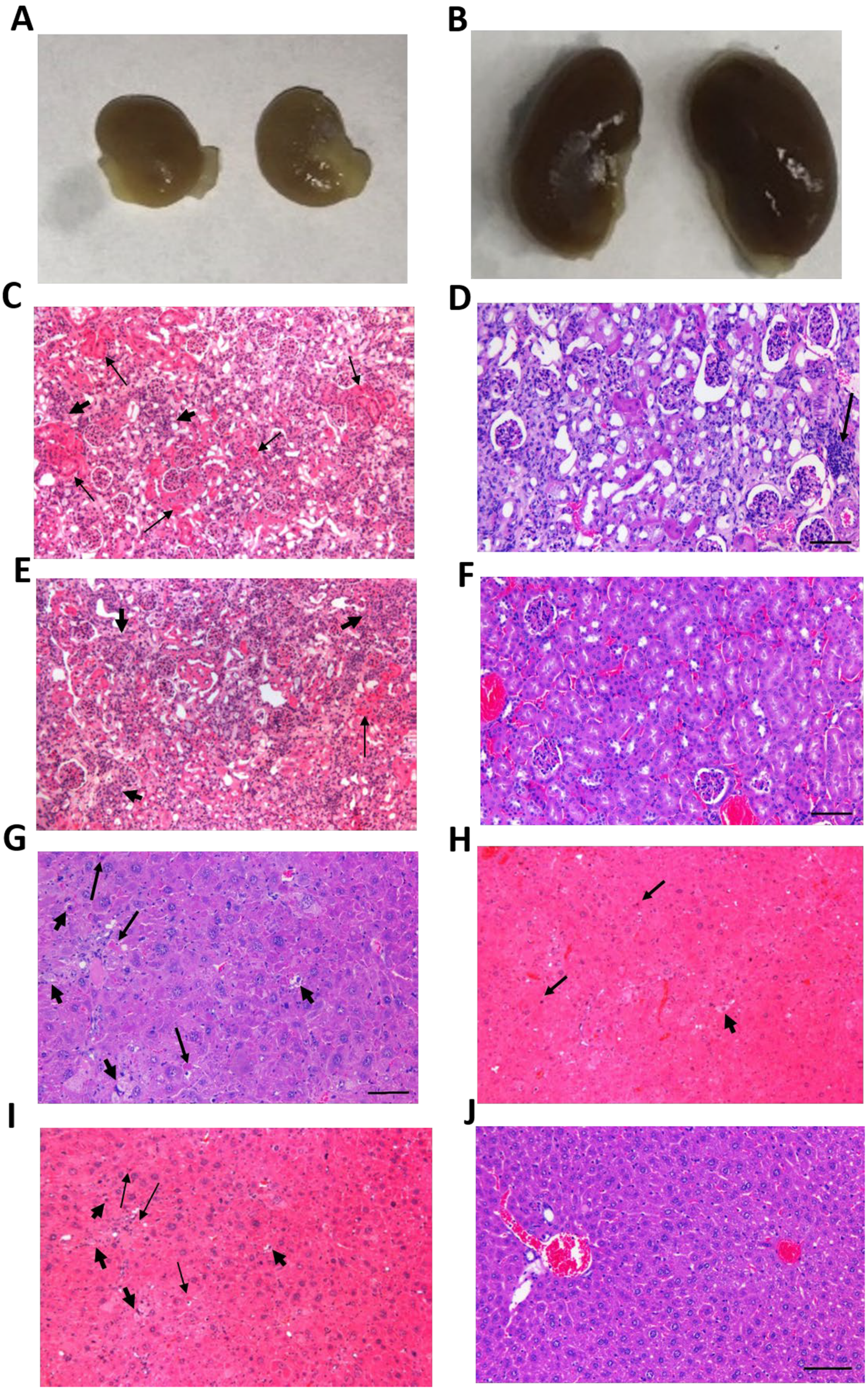

Figure 4. Gross appearance of kidneys (A, B) and histological appearance of kidney (C–F) and liver (G–J) from mice treated with different peptides in the toxicity study. (A, B) Gross appearance of kidneys from mice injected with 79.4 kBq of ^{225}Ac-DOTA-DLDL-MC1RL and 305.4 kBq ^{225}Ac-DOTA-MC1RL. (C) Kidney histology of a 135.4 kBq of ^{225}Ac-DOTA-DLDL-MC1RL administered mouse, with acute tubular necrosis resulting in death at 11 days after administration. At necropsy, kidneys appeared grossly pale, pitted, small, and irregular in shape. Histologically, tubular cell necrosis was characterized by intense cytoplasmic eosinophilia with pyknotic nuclei (arrows), while other tubules appeared regenerative with cytoplasmic basophilia and nuclear crowding (arrowheads). (D) Kidney of a 293.4 kBq of the ^{225}Ac–No linker administered mouse with nephropathy comprised of tubular epithelial cell degeneration with cytoplasmic vacuolization, necrosis, and regeneration with cytoplasmic

Figure 4. continued

basophilia and nuclear crowding, hypercellularity of glomerular tufts, and focal infiltration of mononuclear cells (arrow). (E) Kidney histology of a 84.2 kBq of ^{225}Ac-DOTA-DLDG-MC1RL administered mouse euthanized 7 months after administration, with chronic progressive nephropathy. Little normal renal parenchyma remains due to extensive tubular cell necrosis (arrow), epithelial sloughing and cast formation, extensive tubular cell regeneration (arrowheads), diffuse interstitial edema and fibrosis with mild mononuclear inflammatory cell infiltrates, and hypercellular glomerular tufts. (F) Kidney of saline-treated mouse with normal eosinophilic cuboidal tubular epithelium, and normal glomeruli. (G) Liver of 292.2 kBq of the ^{225}Ac-DOTA-Ahx-MC1RL administered mouse with hepatocellular eosinophillic cytoplasmic swelling, single hepatocellular apoptosis (arrows) with hypereosinophillic cytoplasm and pyknotic nuclei, and single hepatocellular necrosis (arrowheads) with pale eosinophilic cytoplasm and karyolysis. (H) Liver histology of a 135.4 kBq of ^{225}Ac-DOTA-DLDL-MC1RL administered mouse, with focal hepatocellular eosinophillic cytoplasmic swelling, single hepatocellular apoptosis (arrows) with hypereosinophillic cytoplasm and pyknotic nuclei, and single hepatocellular necrosis (arrowhead) with pale eosinophilic cytoplasm and karyolysis. (I) Liver histology of a 36.0 kBq of ^{225}Ac-DOTA-DLDL-MC1RL administered mouse, with hepatocellular eosinophillic cytoplasmic swelling, hepatocellular apoptosis (arrows), and hepatocellular necrosis (arrowhead). (J) Liver of saline administered mouse with normal, well-delineated hepatic cords and sinusoids, a portal triad (left), and a central vein (right).

The animal weights for each radiopharmaceutical and administered activity are plotted in Figures S14−S17. By the end of the study, mice injected with ^{225}Ac-DOTA-MC1RL, ^{225}Ac-DOTA-DLDL-MC1RL, and ^{225}Ac-DOTA-DGDL-MC1RL at ≥268.9, 25.5, and 44.4 kBq of ^{225}Ac activity, respectively, decreased in weight over the course of the study. Mice injected with ≥192.9 kBq of ^{225}Ac-DOTA-Ahx-MC1RL lost weight, but three mice injected with 200, 212, and 315 kBq of activity gained weight. Mice administered lower activities gained weight over the course of the study.

Serum specimens were tested for BUN and creatinine levels as indicators of renal toxicity, and ALKP, ALT, and AST levels as indicators of hepatic toxicity (Table S4).[38] Elevated BUN levels were observed in some mice injected with ^{225}Ac-DOTA-MC1RL, ^{225}Ac-DOTA-Ahx-MC1RL, ^{225}Ac-DOTA-DLDL-MC1RL, and ^{225}Ac-DOTA-DLDG-MC1RL at ≥193.6, 200.1, 11.5, and 19.36 kBq of ^{225}Ac activity, respectively.

Since histopathology is considered the gold standard of determining toxicity of exposure to ionizing radiation and since weight loss and serum biomarkers are indirect indicators of damage due to toxicity, the sensitivity and specificity of these indirect measures were evaluated relative to pathology (Table 2). Weight loss was shown to have high sensitivity and specificity for tissue damage to either kidney or liver. BUN levels had high sensitivity and specificity for kidney damage, and ALKP levels had high sensitivity and specificity for liver damage. The probabilities of kidney or liver damage by pathology, elevated BUN or ALKP levels, or weight loss per injected activity for each radiopharmaceutical are shown in Figure 5A−E.

Table 2. Determination of Sensitivity and Specificity of the Indirect Indicators of Toxicity Incomparison to Pathology

parameter	% sensitivity	% specificity
	Kidney Pathology	
weight loss	87	95
BUN	74	97
	Liver Pathology	
weight loss	85	74
AST	14	90
ALKP	85	86
ALT	28	95

Relationship of BD, PK, RD, and Toxicity with Compound Lipophilicity. Using the BD data for all four compounds, a significant relationship was determined between log $D_{7.4}$ and kidney BD, $p < 0.05$, and between log $D_{7.4}$ and the kidney-to-liver BD ratio, $p < 0.001$ (Table S5). It is noted that no relationship was observed between log $D_{7.4}$ and liver BD. Since BD is a composite of agent uptake and clearance, the correlations among log $D_{7.4}$ and kidney and liver uptake, and clearance rates and toxicity indicators (weight loss, pathology, BUN and ALKP levels) were examined (Table S6). The statistical analysis showed that log $D_{7.4}$ is significantly associated with weight loss, $p < 0.0001$, and that both log $D_{7.4}$ and weight loss are significantly associated with kidney clearance rates, $p < 0.0001$. Furthermore, BUN levels are significantly associated with kidney uptake rates, $p < 0.0001$, and liver clearance rates, $p < 0.0001$.

■ DISCUSSION

Lipophilicity is a major determinant of route of clearance of small molecule drugs due to the dependence of renal clearance on membrane permeability.[39] However, this observation has not been fully substantiated for peptide conjugates.[40] Mass can influence the route of clearance (i.e., molecules <50 kDa are removed from circulation via renal glomeruli, while larger macromolecules clear via the splenic and hepatic routes).[40] With the goal of characterizing the relationship between lipophilicity and clearance route, we designed and synthesized a set of peptide-conjugate based radiopharmaceuticals for TAT with a range of lipophilicities (log $D_{7.4}$ values) and comparable mass values ranging from 1361 to 1618 MW without metal chelation. Also, unnatural amino acids are incorporated into the peptidic component of these compounds, and high radiochemical stability has been previously demonstrated for the ^{225}Ac-DOTA-Ahx-MC1RL radiopharmaceutical.[29] Hence, peptide metabolism is likely a minor factor in determining the route of clearance. Herein, we report characterization of the BD, PK, RD, and toxicity of these compounds in mice and the relationships of log $D_{7.4}$ values with the route and PK of uptake and clearance of the administered TAT.

Since the lipophilicities of the compounds were adjusted by inserting linkers that have different structures and chemical properties between the peptide targeting moiety and the metal chelator, quality control characterizations were also performed. As a nonradioactive surrogate of ^{225}Ac, La^{3+} chelates were used for these assays. The high binding affinity (low nM K_i) of the MC1RL peptide for the MC1R receptor and log $D_{7.4}$ values were confirmed for each compound.

For BD, PK, and RD determinations, each compound was labeled with ^{225}Ac with high radiochemical yield and purity. When evaluating the BD, PK, and RD data, general observations can be made that the metalated compounds

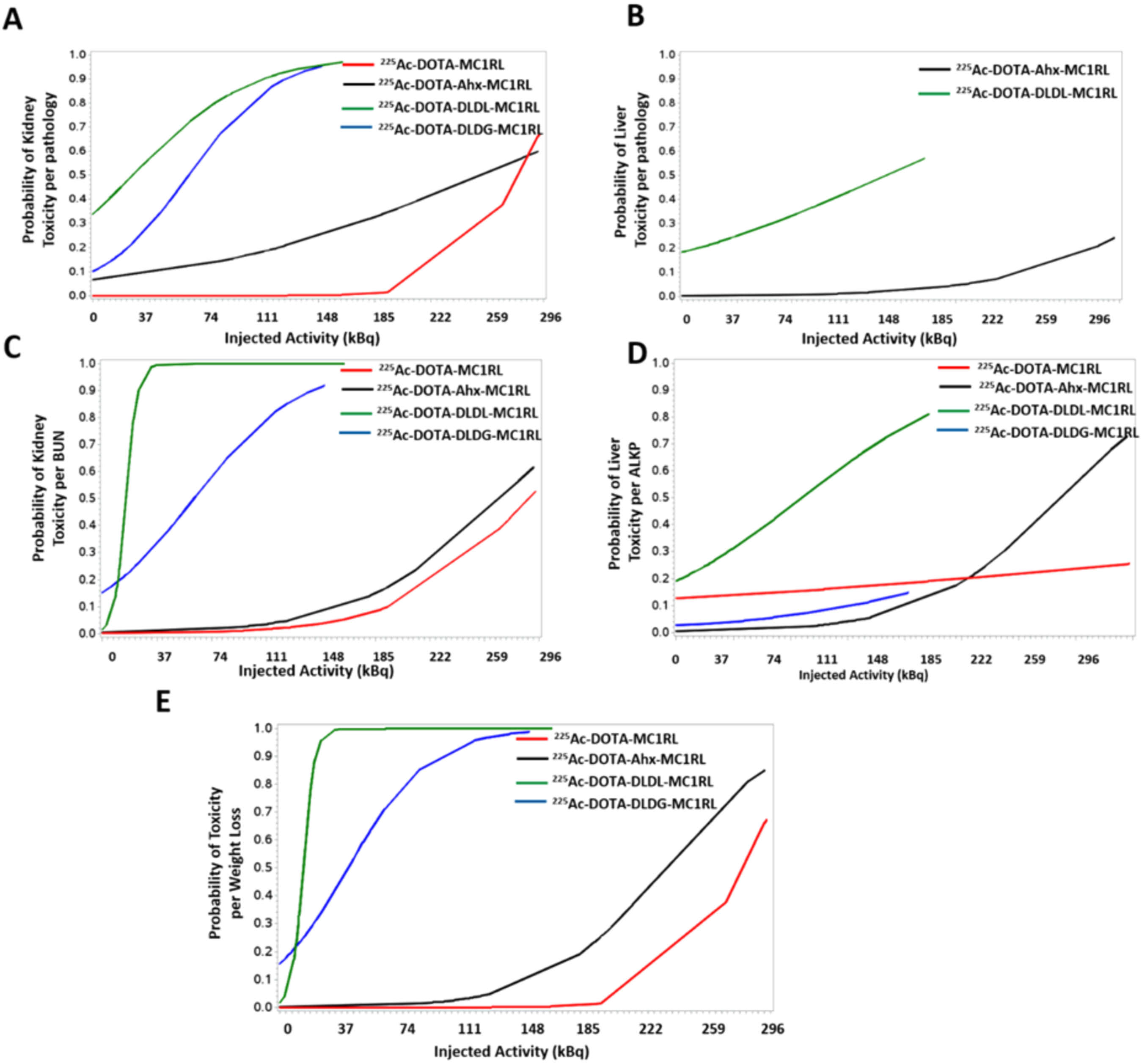

Figure 5. Toxicity probability curves per injected activity for each radiopharmaceutical per (A) kidney pathology, (B) liver pathology [no toxicities were observed for the other two radiopharmaceuticals], (C) BUN, (D) ALKP, and (E) weight loss.

with log $D_{7.4}$ values above −2.6 have lower kidney uptake rates, are cleared more by the hepatic route than renal, and have a lower radiation dose to the kidney when compared to the compounds with log $D_{7.4}$ values below −3.4, which are cleared more by the renal route, have higher kidney uptake rates, and have a higher radiation dose to the kidney. This negative correlation of decreased kidney uptake and decreased radiation dose with increasing lipophilicity can be explained as a result of an increase in passive reabsorption in the kidney tubule, leading to less renal uptake.[21,39]

Radiation-induced renal toxicity is a major concern in the therapeutic application of peptides labeled with radiometals.[41] In this study, we observed two distinct pathological features: acute kidney damage and chronic kidney damage. Acute kidney failure was observed in animals that were administered compounds with log $D_{7.4}$ values below −3.4 and was grossly characterized by pale, pitted, small, and irregular shaped kidneys at necropsy and by acute nephropathy via pathology examination. Acute kidney damage resulted in a rapid loss of kidney function and death within the week following treatment. Animals administered compounds with log $D_{7.4}$ values above −2.6 lived for the duration of the 7 month study and exhibited chronic pathologies of the kidney and liver at high administered activities. The relative probabilities of pathology in the kidney and liver by administered activity were calculated for all cohorts. Weight loss and serum biomarkers of kidney and liver toxicity were also quantified, and weight loss was shown to have high sensitivity and specificity for detection of both kidney and liver pathology. While creatinine and BUN levels are typically used as biomarkers of kidney damage,[42] BUN was identified in our study as having higher sensitivity and specificity of detection of

Table 3. Relationship of log $D_{7.4}$ with Kidney Uptake, Radiation Doses, and Toxicity

		kidney[b]				
				probability of toxicity at 148 kBq injected activity		
linker	log $D_{7.4}$[a]	uptake rate constant, λ (%IA/g/h)	total absorbed dose (Gy/kBq)	pathology	BUN	weight loss
no linker	−2.41 ± 0.26	3.985	0.5628	0.00	0.04	0.01
Ahx	−2.59 ± 0.20	5.625	0.1366	0.23	0.10	0.10
DLDL	−3.49 ± 0.27	178.5	1.5980	0.95	1.00	1.00
DGDL	−3.88 ± 0.17	44.08	0.9200	0.95	0.94	0.99

[a] Determined using the La^{3+} chelate. [b] Determined using the ^{225}Ac chelate.

kidney pathology. Of all liver enzymes tested, ALKP levels had both high sensitivity and high specificity for detection of liver damage. Statistical analyses identified significant relationships between log $D_{7.4}$ and kidney BD, the kidney-to-liver BD ratio, weight loss, and kidney clearance rates. Weight loss also significantly correlated with kidney clearance rates. BUN levels were significantly correlated with kidney uptake and liver clearance rates.

Table 3 was prepared to highlight the relevant relationships among the log $D_{7.4}$ values of the La^{3+}-chelated compounds and the kidney uptake, kidney total absorbed dose, and kidney toxicity values of the corresponding ^{225}Ac-chelated compounds. It is notable that the compounds with log $D_{7.4}$ values above −2.6 have kidney uptake rates, total absorbed doses, and probabilities of toxicity that range from 3- to 100-fold lower than the compounds with log $D_{7.4}$ values below −3.4.

The arginine side chain in the MC1R targeting ligand is likely to be positively charged in all of the peptide conjugates at pH 7.4. This likely gives an overall plus one charge to the metalated no-linker, Ahx linker, and DLDG analogs and no overall charge for those same unmetalated analogs. The +3 metals, La and ^{225}Ac, are balanced by the three carboxylates giving no overall charge for the DOTA-metal-chelated portion of the conjugates. The free DOTA-MC1RL species have three negative charges from the DOTA carboxylates and two positive charges from the protonation of two of the four tertiary amines in the 1,4,7,10-tetrazadodecane ring system. The metalated and unmetalated DLDL MC1RL analogs are expected to have overall +3 or +4 charge, respectively, but they are less polar than the relevant DLDG MC1RL analogs, which suggests significantly reduced basicity for the Lys side chains at physiological pH due to the overall charge density of DLDL analogs.

All of the linkers used for conjugation are expected to be stable to metabolic changes and all of the conjugates have epsilon lysine-amide linkages which are unlikely to be substrates of proteolytic enzymes. D-Amino acids were used in the polar linkers to inhibit possible proteolytic cleavage between the first and second amino acids in the linkers themselves.

In conclusion, by using different linker chemistry to increase the lipophilicity of a TAT radiopharmaceutical, we demonstrated that the kidney uptake rate can be significantly decreased, which also decreases the total absorbed dose and probability of toxicity to the kidney. Liver uptake, dose, and toxicity were not significantly influenced by the increase in lipophilicity. Hence, there is significant potential to decrease the kidney toxicity of radiopharmaceuticals via medicinal chemistry approaches that adjust lipophilicity.

■ ASSOCIATED CONTENT

Supporting Information

The Supporting Information is available free of charge at https://pubs.acs.org/doi/10.1021/acsptsci.1c00035.

Lipophilicty (log $D_{7.4}$) for unmetalated and La^{3+} chelated compounds, radiation dosimetry and clearance kinetics parameters in BALB/c mice; relationship between log D and kidney, liver and kidney/liver biodistrbution (BD): statistical analysis, correlation of log $D_{7.4}$, and kidney and liver uptake and clearance with indicators of toxicity (weight change, pathology, BUN and ALKP); analytical HPLC chromatograms and MALDI-TOF spectra; radiochemical purities of ^{225}Ac-DOTA-MC1RL, ^{225}Ac-DOTA-Ahx-MC1RL, ^{225}Ac-DOTA-DLDL-MC1RL, and ^{225}Ac-MC1RL-DLDG-DOTA; isomeric gamma spectrum of mouse kidneys for ^{225}Ac-DOTA-MC1RL (no linker) at 24 h post-injection; weights over time of the animals in this study injected with different activities of radiopharmaceutical or saline (PDF)

Histopathology scoring for all tissues in the study (XLSX)

Toxicity indicators: weight change, pathology and serum markers (XLSX)

■ AUTHOR INFORMATION

Corresponding Author

David L. Morse − *Department of Cancer Physiology and Small Animal Imaging Laboratory, H. Lee Moffitt Cancer Center & Research Institute, Tampa, Florida 33612, United States; Department of Physics and Department of Oncologic Sciences, University of South Florida, Tampa, Florida 33612, United States*; Email: David.Morse@moffitt.org

Authors

Narges K. Tafreshi − *Department of Cancer Physiology, H. Lee Moffitt Cancer Center & Research Institute, Tampa, Florida 33612, United States*; orcid.org/0000-0002-2680-319X

HyunJoo Kil − *Department of Pharmaceutical Sciences, West Virginia University, Health Sciences Center, Morgantown, West Virginia 26506, United States; Modulation Therapeutics, Inc., Morgantown, West Virginia 26506, United States*

Darpan N. Pandya − *Department of Radiology, University of Iowa Health Care, Iowa City, Iowa 52242, United States*

Christopher J. Tichacek − *Departments of Radiation Oncology, Tampa, Florida 33612, United States; Department of Physics, University of South Florida, Tampa,* *Florida 33612, United States;* orcid.org/0000-0003-4238-9512

Michael L. Doligalski − *Department of Cancer Physiology, H. Lee Moffitt Cancer Center & Research Institute, Tampa, Florida 33612, United States;* orcid.org/0000-0003-1920-7485

Mikalai M. Budzevich − *Small Animal Imaging Laboratory, H. Lee Moffitt Cancer Center & Research Institute, Tampa, Florida 33612, United States*

Nella C. Delva − *Department of Cancer Physiology, H. Lee Moffitt Cancer Center & Research Institute, Tampa, Florida 33612, United States*

Michael L. Langsen − *Department of Cancer Physiology, H. Lee Moffitt Cancer Center & Research Institute, Tampa, Florida 33612, United States;* orcid.org/0000-0002-1145-3262

John A. Vallas − *Department of Cancer Physiology, H. Lee Moffitt Cancer Center & Research Institute, Tampa, Florida 33612, United States*

David C. Boulware − *Biostatistics and Bioinformatics Core, H. Lee Moffitt Cancer Center & Research Institute, Tampa, Florida 33612, United States*

Robert W. Engelman − *Departments of Pediatrics, Pathology & Cell Biology, University of South Florida, Tampa, Florida 33612, United States*

Kenneth L. Gage − *Radiology, Tampa, Florida 33612, United States*

Eduardo G. Moros − *Department of Cancer Physiology and Departments of Radiation Oncology, H. Lee Moffitt Cancer Center & Research Institute, Tampa, Florida 33612, United States; Department of Physics and Department of Oncologic Sciences, University of South Florida, Tampa, Florida 33612, United States*

Thaddeus J Wadas − *Department of Radiology, University of Iowa Health Care, Iowa City, Iowa 52242, United States;* orcid.org/0000-0002-9913-0336

Mark L. McLaughlin − *Department of Pharmaceutical Sciences, West Virginia University, Health Sciences Center, Morgantown, West Virginia 26506, United States; Modulation Therapeutics, Inc., Morgantown, West Virginia 26506, United States*

Complete contact information is available at:
https://pubs.acs.org/10.1021/acsptsci.1c00035

Notes

The authors declare the following competing financial interest(s): D.L.M. and N.K.T. are co-inventors of an awarded patent. D.L.M., T.J.W., M.L.M., H.K., and N.K.T. are co-inventors on a pending patent application. Modulation Therapeutics, Inc., has licensed related intellectual property, and M.L.M. is a co-founder of that company.

■ ACKNOWLEDGMENTS

Animal studies were conducted in the Moffitt Vivarium administered by the University of South Florida Comparative Medicine Department. The actinium-225 isotope used in this research was supplied by the U.S. Department of Energy Office of Science by the Isotope Program in the Office of Nuclear Physics. Funding was provided by an NIH/NCI SBIR Phase 1 Contract to Modulation Therapeutics, Inc. (PI: N.K.T.), a Melanoma Research Alliance Team Science Award (PI: D.L.M.), and a Moffitt Radiology Pilot Award (K.L.G.). This work was supported by the Analytic Microscopy, Bioinformatics and Biostatistics, and Tissue and Small Animal Imaging Laboratory cores at the H. Lee Moffitt Cancer Center & Research Institute, an NCI-designated Comprehensive Cancer Center (P30-CA076292).

■ ABBREVIATIONS

MC1RL, Melanocortin receptor 1 ligand; Ahx, 6-Aminohexanoic acid linker; BD, Biodistribution; BUN, Blood urea nitrogen; Fmoc, Fluorenylmethyloxycarbonyl; HCTU, *O*-(1*H*-6-Chlorobenzotriazole-1-yl)-1,1,3,3-tetramethyluronium hexafluorophosphate; DIEA, Diisopropylethylamine; DCM, Dichloromethane; DBU, 1,8-Diazabicyclo(5.4.0)undec-7-ene; DMF, Dimethylformamide; NMP, *N*-methyl-2-pyrrolidone; Alloc, allyloxycarbonyl; $Pd(PPh_3)_4$, Tetrakis(triphenylphosphine)palladium(0); DOTA, 1,4,7,10-Tetraazacyclododecane-1,4,7-tris-*tert*-butyl acetate-10-acetic acid; D-Glu, Fmoc-D-glutamic acid; D-Lys, Fmoc-D-lysine; TFA, Trifluoroacetic acid; RT-HPLC, Reverse-phase high-performance liquid chromatography; Ahx, Aminohexanoic acid; DLDL, D-Lys-D-Lys; DLDG, D-Lys-D-Glu

■ REFERENCES

(1) Campbell, I. B., Macdonald, S. J. F., and Procopiou, P. A. (2018) Medicinal chemistry in drug discovery in big pharma: past, present and future. *Drug Discovery Today 23* (2), 219−234.

(2) Fosgerau, K., and Hoffmann, T. (2015) Peptide therapeutics: current status and future directions. *Drug Discovery Today 20* (1), 122−8.

(3) Speck-Planche, A., and Cordeiro, M. N. (2015) Multitasking models for quantitative structure-biological effect relationships: current status and future perspectives to speed up drug discovery. *Expert Opin. Drug Discovery 10* (3), 245−56.

(4) DiMasi, J. A., Grabowski, H. G., and Hansen, R. W. (2016) Innovation in the pharmaceutical industry: New estimates of R&D costs. *J. Health Econ 47*, 20−33.

(5) Prasad, V., and Mailankody, S. (2017) Research and Development Spending to Bring a Single Cancer Drug to Market and Revenues After Approval. *JAMA Intern Med. 177* (11), 1569−1575.

(6) Paul, S. M., Mytelka, D. S., Dunwiddie, C. T., Persinger, C. C., Munos, B. H., Lindborg, S. R., and Schacht, A. L. (2010) How to improve R&D productivity: the pharmaceutical industry's grand challenge. *Nat. Rev. Drug Discovery 9* (3), 203−14.

(7) Kola, I., and Landis, J. (2004) Can the pharmaceutical industry reduce attrition rates? *Nat. Rev. Drug Discovery 3* (8), 711−5.

(8) Zhivkova, Z. D. (2017) Quantitative Structure - Pharmacokinetic Relationships for Plasma Clearance of Basic Drugs with Consideration of the Major Elimination Pathway. *J. Pharm. Pharm. Sci. 20* (0), 135−147.

(9) Arnott, J. A., and Planey, S. L. (2012) The influence of lipophilicity in drug discovery and design. *Expert Opin. Drug Discovery 7* (10), 863−75.

(10) Rutkowska, E., Pajak, K., and Jozwiak, K. (2013) Lipophilicity–methods of determination and its role in medicinal chemistry. *Acta Polym. Pharm. 70* (1), 3−18.

(11) Lipinski, C. A., Lombardo, F., Dominy, B. W., and Feeney, P. J. (2001) Experimental and computational approaches to estimate solubility and permeability in drug discovery and development settings. *Adv. Drug Delivery Rev. 46* (1−3), 3−26.

(12) Liu, X., Testa, B., and Fahr, A. (2011) Lipophilicity and its relationship with passive drug permeation. *Pharm. Res. 28* (5), 962−77.

(13) Waring, M. J. (2009) Defining optimum lipophilicity and molecular weight ranges for drug candidates-Molecular weight dependent lower log *D* limits based on permeability. *Bioorg. Med. Chem. Lett. 19* (10), 2844−51.

(14) Gleeson, M. P., Hersey, A., Montanari, D., and Overington, J. (2011) Probing the links between in vitro potency, ADMET and physicochemical parameters. *Nat. Rev. Drug Discovery 10* (3), 197−208.

(15) Leeson, P. D., and Springthorpe, B. (2007) The influence of drug-like concepts on decision-making in medicinal chemistry. *Nat. Rev. Drug Discovery 6* (11), 881−90.

(16) Hughes, J. D., Blagg, J., Price, D. A., Bailey, S., Decrescenzo, G. A., Devraj, R. V., Ellsworth, E., Fobian, Y. M., Gibbs, M. E., Gilles, R. W., Greene, N., Huang, E., Krieger-Burke, T., Loesel, J., Wager, T., Whiteley, L., and Zhang, Y. (2008) Physiochemical drug properties associated with in vivo toxicological outcomes. *Bioorg. Med. Chem. Lett. 18* (17), 4872−5.

(17) Kwon, Y. (2001) *Handbook of Essential Pharmacokinetics, Pharmacodynamics, and Drug Metabolism for Industrial Scientists*, p xix, Kluwer Academic/Plenum Publishers, New York.

(18) Aina, O. H., Sroka, T. C., Chen, M. L., and Lam, K. S. (2002) Therapeutic cancer targeting peptides. *Biopolymers 66* (3), 184−99.

(19) Gleeson, M. P. (2008) Generation of a set of simple, interpretable ADMET rules of thumb. *J. Med. Chem. 51* (4), 817−34.

(20) Obach, R. S., Lombardo, F., and Waters, N. J. (2008) Trend analysis of a database of intravenous pharmacokinetic parameters in humans for 670 drug compounds. *Drug Metab. Dispos. 36* (7), 1385−405.

(21) Varma, M. V., Feng, B., Obach, R. S., Troutman, M. D., Chupka, J., Miller, H. R., and El-Kattan, A. (2009) Physicochemical determinants of human renal clearance. *J. Med. Chem. 52* (15), 4844−52.

(22) Tafreshi, N. K., Doligalski, M. L., Tichacek, C. J., Pandya, D. N., Budzevich, M. M., El-Haddad, G., Khushalani, N. I., Moros, E. G., McLaughlin, M. L., Wadas, T. J., and Morse, D. L. (2019) Development of Targeted Alpha Particle Therapy for Solid Tumors. *Molecules 24* (23), 4314.

(23) Barkey, N. M., Tafreshi, N. K., Josan, J. S., De Silva, C. R., Sill, K. N., Hruby, V. J., Gillies, R. J., Morse, D. L., and Vagner, J. (2011) Development of melanoma-targeted polymer micelles by conjugation of a melanocortin 1 receptor (MC1R) specific ligand. *J. Med. Chem. 54* (23), 8078−84.

(24) Tafreshi, N. K., Huang, X., Moberg, V. E., Barkey, N. M., Sondak, V. K., Tian, H., Morse, D. L., and Vagner, J. (2012) Synthesis and characterization of a melanoma-targeted fluorescence imaging probe by conjugation of a melanocortin 1 receptor (MC1R) specific ligand. *Bioconjugate Chem. 23* (12), 2451−9.

(25) Tafreshi, N. K., Silva, A., Estrella, V. C., McCardle, T. W., Chen, T., Jeune-Smith, Y., Lloyd, M. C., Enkemann, S. A., Smalley, K. S., Sondak, V. K., Vagner, J., and Morse, D. L. (2013) In vivo and in silico pharmacokinetics and biodistribution of a melanocortin receptor 1 targeted agent in preclinical models of melanoma. *Mol. Pharmaceutics 10* (8), 3175−85.

(26) Handl, H. L., Vagner, J., Yamamura, H. I., Hruby, V. J., and Gillies, R. J. (2004) Lanthanide-based time-resolved fluorescence of in cyto ligand-receptor interactions. *Anal. Biochem. 330* (2), 242−50.

(27) Reid, Y., Storts, D., Riss, T., and Minor, L. (2004) Authentication of Human Cell Lines by STR DNA Profiling Analysis, in *Assay Guidance Manual* (Sittampalam, G. S., Coussens, N. P., Brimacombe, K., Grossman, A., Arkin, M., Auld, D., Austin, C., Baell, J., Bejcek, B., and Chung, T. D. Y., et al., Eds.), Eli Lilly & Company and the National Center for Advancing Translational Sciences, Bethesda, MD.

(28) Morss, L. R., Edelstein, N., Fuger, J., and Katz, J. J. (2011) *The Chemistry of the Actinide and Transactinide Elements* (Morss, L. R., Edelstein, N., Fuger, J., and Katz, J. J., Eds.) 4th ed., Vol. *1−6*, Springer Science and Business Media.

(29) Tafreshi, N. K., Tichacek, C. J., Pandya, D. N., Doligalski, M. L., Budzevich, M. M., Kil, H., Bhatt, N. B., Kock, N. D., Messina, J. L., Ruiz, E. E., Delva, N. C., Weaver, A., Gibbons, W. R., Boulware, D. C., Khushalani, N. I., El-Haddad, G., Triozzi, P. L., Moros, E. G., McLaughlin, M. L., Wadas, T. J., and Morse, D. L. (2019) Melanocortin 1 Receptor-Targeted alpha-Particle Therapy for Metastatic Uveal Melanoma. *J. Nucl. Med. 60* (8), 1124−1133.

(30) Bonardi, M. L., and de Goeij, J. J. M. (2005) How do we ascertain specific activities in no-carrier-added radionuclide preparations? *J. Radioanal. Nucl. Chem. 263* (1), 87−92.

(31) Ma, D., McDevitt, M. R., Finn, R. D., and Scheinberg, D. A. (2001) Breakthrough of 225Ac and its radionuclide daughters from an 225Ac/213 Bi generator: development of new methods, quantitative characterization, and implications for clinical use. *Appl. Radiat. Isot. 55* (5), 667−78.

(32) Apostolidis, C., Molinet, R., Rasmussen, G., and Morgenstern, A. (2005) Production of Ac-225 from Th-229 for targeted alpha therapy. *Anal. Chem. 77* (19), 6288−91.

(33) Robertson, A. K. H., Ramogida, C. F., Rodriguez-Rodriguez, C., Blinder, S., Kunz, P., Sossi, V., and Schaffer, P. (2017) Multi-isotope SPECT imaging of the (225)Ac decay chain: feasibility studies. *Phys. Med. Biol. 62* (11), 4406−4420.

(34) Dennis, J. E. (1977) Nonlinear least-squares, in *State of the Art in Numerical Analysis* (Jacobs, D., Ed.), pp 269−312, Academic Press.

(35) Bolch, W. E., Eckerman, K. F., Sgouros, G., and Thomas, S. R. (2009) MIRD pamphlet No. 21: a generalized schema for radiopharmaceutical dosimetry–standardization of nomenclature. *J. Nucl. Med. 50* (3), 477−84.

(36) Song, H., Hobbs, R. F., Vajravelu, R., Huso, D. L., Esaias, C., Apostolidis, C., Morgenstern, A., and Sgouros, G. (2009) Radioimmunotherapy of breast cancer metastases with alpha-particle emitter 225Ac: comparing efficacy with 213 Bi and 90Y. *Cancer Res. 69* (23), 8941−8.

(37) Kratochwil, C., Bruchertseifer, F., Rathke, H., Bronzel, M., Apostolidis, C., Weichert, W., Haberkorn, U., Giesel, F. L., and Morgenstern, A. (2017) Targeted Alpha Therapy of mCRPC with 225Actinium-PSMA-617: Dosimetry estimate and empirical dose finding. *J. Nucl. Med. 58*, 1624−1631.

(38) Choi, S. I., Kim, J. E., Hwang, I. S., Lee, H. R., Lee, Y. J., Kwak, M. H., Son, H. J., Lee, H. S., Lee, J. S., Kang, B. C., and Hwang, D. Y. (2012) Toxicity of red Liriope platyphylla manufactured by steaming process on liver and kidney organs of ICR mice. *Lab Anim Res. 28* (4), 229−38.

(39) van De Waterbeemd, H., Smith, D. A., Beaumont, K., and Walker, D. K. (2001) Property-based design: optimization of drug absorption and pharmacokinetics. *J. Med. Chem. 44* (9), 1313−33.

(40) Datta-Mannan, A. (2019) Mechanisms Influencing the Pharmacokinetics and Disposition of Monoclonal Antibodies and Peptides. *Drug Metab. Dispos. 47* (10), 1100−1110.

(41) Behr, T. M., Sharkey, R. M., Sgouros, G., Blumenthal, R. D., Dunn, R. M., Kolbert, K., Griffiths, G. L., Siegel, J. A., Becker, W. S., and Goldenberg, D. M. (1997) Overcoming the nephrotoxicity of radiometal-labeled immunoconjugates: improved cancer therapy administered to a nude mouse model in relation to the internal radiation dosimetry. *Cancer 80*, 2591−610.

(42) Bonventre, J. V., Vaidya, V. S., Schmouder, R., Feig, P., and Dieterle, F. (2010) Next-generation biomarkers for detecting kidney toxicity. *Nat. Biotechnol. 28* (5), 436−40.

Biochemical Pharmacology 197 (2022) 114916

Contents lists available at ScienceDirect

Biochemical Pharmacology

journal homepage: www.elsevier.com/locate/biochempharm

Review

The gut microbiota can be a potential regulator and treatment target of bone metastasis

Kelly F. Contino [a], Hariom Yadav [b], Yusuke Shiozawa [a,*]

[a] Department of Cancer Biology and Comprehensive Cancer Center, Wake Forest University Health Sciences, Winston-Salem, NC 27157, USA
[b] Department of Neurosurgery and Brain Repair and Institute for Microbiome, University of South Florida, Tampa, FL 33612, USA

ARTICLE INFO

Keywords:
Gut Microbiota
Bone Metastasis
Gastrointestinal Cancer
Bone Remodeling
Gut Dysbiosis
Immunotherapy

ABSTRACT

The gut microbiota, an often forgotten organ, have a tremendous impact on human health. It has long been known that the gut microbiota are implicated in cancer development, and more recently, the gut microbiota have been shown to influence cancer metastasis to distant organs. Although one of the most common sites of distant metastasis is the bone, and the skeletal system has been shown to be a subject of interactions with the gut microbiota to regulate bone homeostasis, little research has been done regarding how the gut microbiota control the development of bone metastasis. This review will discuss the mechanisms through which the gut microbiota and derived microbial compounds (i) regulate gastrointestinal cancer disease progression and metastasis, (ii) influence skeletal remodeling and potentially modulate bone metastasis, and (iii) affect and potentially enhance immunotherapeutic treatments for bone metastasis.

1. Introduction

In the human body, it is estimated that there are ten times as many microorganisms as nucleated host cells [1]. The genome of these microorganisms, known as the human microbiome, is found to contain approximately 100 times the number of genes present in the human genome [2]. Microorganisms, established in the human body *in utero*, begin to multiply and diversify immediately after birth until stabilization occurs at three years of age [3,4]. One of the major sites where microorganisms exist in the human body is the gut [5]. The collection of microorganisms that exists in the gut is labeled as the gut microbiota, as microorganisms that live in a specific environment are coined the microbiota. The gut microbiota consists of a vast number of bacteria, viruses, fungi, archaea, and protists, and can have a tremendous impact on human health [6,7]. Especially, with all components working in conjunction, the gut microbiota plays a fundamental role in human digestion, as it is capable of breaking down nutrients that the host would be incapable of digesting on its own [8]. For example, a single gene locus in *Bacteroides ovatus* is responsible for the digestion of xyloglucans, a sugar from plants that would otherwise be indigestible for the human host [9]. Similarly, there are specific microbiota that regulate the uptake of vitamins and minerals [10]. Additionally, *Prevotella corpi* and *Lactobacillus plantarum* are just two of the gut microorganisms believed to be necessary for vitamin B2 synthesis [11]. Through these functions, the gut microbiota contribute to maintaining host health.

Another important role of the gut microbiota in the host environment is to equilibrate and maintain the interaction between the gut and host microorganisms. In a healthy individual, this equilibrated state is

---

Abbreviations: **GI**, gastrointestinal; **CRC**, colorectal cancer; **H. pylori**, Helicobacter pylori; **B. fragilis**, Bacteroides fragilis; **E. coli**, Escherichia coli; **CagA**, cytotoxin-associated gene A; **AKT**, protein kinase B; **PI3K**, phosphoinositide 3-kinase; **ERK**, extracellular signal-regulated kinase; **GRB2**, growth factor receptor bound protein 2; **MEK**, mitogen-activated protein kinase; **WNT**, wingless/integrated; **IL**, interleukin; **NF-κB**, nuclear factor kappa light chain enhancer of activated B cells; **ROS**, reactive oxygen species; **BM-MSC**, bone marrow-derived mesenchymal stem cell; **SCFA**, short chain fatty acid; **GPR**, G protein-coupled receptor; **iNOS**, inducible nitric oxide synthase; **COX**, cyclooxygenase; **LPS**, lipopolysaccharide; **TLR4**, toll-like receptor 4; **TNF**, tumor necrosis factor; **VEGF**, vascular endothelial growth factor; **TGF-β**, transforming growth factor β; **DTC**, disseminated tumor cell; **PTHrP**, parathyroid hormone-related protein; **RANKL**, receptor activator of NF-κB ligand; **TNFR-1**, tumor necrosis factor receptor 1; **NFATc1**, nuclear factor of activated T cells c1; **EP4**, prostaglandin E receptor 4; **LCA**, lithocholic acid; **HSC**, hematopoietic stem cell; **IGF-1**, insulin-like growth factor 1; **ADT**, androgen-deprivation therapy; **FMT**, fecal microbiota transplantation; $^{223}\mathbf{RaCl_2}$, radium-223 dichloride; **PD-1**, programmed cell death-1; **PD-L1**, programmed death-ligand 1; **CTLA-4**, cytotoxic T lymphocyte antigen 4; **ICI**, immune checkpoint inhibitor; $\mathbf{T_h17}$, T helper 17; **Tregs**, regulatory T cells; $\mathbf{T_h1}$, T helper 1; **CEA**, carcinoembryonic antigen; **VEGFR**, VEGF Receptor.

* Corresponding author at: Wake Forest School of Medicine, Medical Center Blvd, Winston-Salem, NC 27157-1082, USA.
E-mail address: yshiozaw@wakehealth.edu (Y. Shiozawa).

https://doi.org/10.1016/j.bcp.2022.114916
Received 15 November 2021; Received in revised form 10 January 2022; Accepted 10 January 2022
Available online 15 January 2022

achieved by crosstalk and cross-regulation between the gut microbiota and their human host, which serves to create a stable balance in the gastrointestinal (GI) tract [12]. The primary functions of the healthy GI tract are to regulate nutrient and water absorption in addition to preventing toxins from entering circulation, and the design of the gut barrier is indicative of these roles [13]. The gut barrier is comprised of three layers (i) a mucus layer that serves as protection for epithelial cells from gut microbiota, (ii) a single layer of epithelial cells that comprise the majority of the physical intestinal wall, and (iii) a series of junctional complexes that regulate the transport of molecules and maintain the intestinal barrier [14–16]. Typically, gut microbiota can reside within the gut without problem due to this barrier system; however, problems arise when the gut microenvironment is thrown into a state of dysbiosis, the state in which equilibrium between the gut microbiota and their human host is disrupted [17,18]. Dysbiosis is brought on by a variety of causes primarily related to environmental contaminants, excess alcohol consumption, and unhealthy eating [19]. The physical, biochemical, and immune barriers that serve to protect the host become compromised during dysbiosis resulting in systemic inflammation [20–23]. When dysbiosis is induced, this can lead to permeability within the gut barrier, essentially impairing the protective responses and normal function within the gut, creating what is known as a “leaky gut”. When the gut barrier becomes compromised, the bacteria that in some cases initially created the leaky gut, along with toxins and food particles, can leak out into the blood stream stimulating a proinflammatory response and secreting cytokines [24–27]. A chronic state of gut dysbiosis is known to be linked to irritable bowel syndrome, osteoarthritis, obesity, diabetes, cancer, and many other diseases [28–30].

Chronic inflammation has long been known to be associated with cancer development [31]. Innate immune cells are capable of detecting infection or injury in a tissue through pattern recognition receptors in the cytoplasm [32]. When damage is detected, innate immune cells move into the damaged, precancerous tissue and induce an inflammatory response; this leads to angiogenesis, tissue remodeling, and cytokine and chemokine presence, creating an ideal environment for tumorigenesis [33]. Recent evidence has come to suggest that environmental factors that induce inflammation can cause the composition of the gut microbiota to fluctuate, which can then influence different types of cancer, namely colorectal cancer (CRC), through gut microbiota-related mechanisms [34]. As previously stated, one of these environmental agents is infection, and several types of bacteria are known to be linked to cancer. *Helicobacter pylori* (*H. pylori*) infection, for example, has a known association with GI cancer development [35]. *Streptococcus bovis* was the first bacterium to be associated with CRC, and since then several other bacteria including *Bacteroides fragilis (B. fragilis)*, *Enterococcus faecalis*, *Fusobacterium nucleatum*, and *Escherichia coli (E. coli)* have all been implicated in colorectal carcinogenesis [36]. These findings corroborate the idea that the gut microbiota play a role in tumorigenesis.

Although there are clear examples of the gut microbiota’s involvement primarily in GI cancer, research regarding gut dysbiosis and cancer outside of the gut remains elusive. In this review, we will discuss the effects of the gut microbiota and gut dysbiosis on cancer development and metastasis, specifically as it pertains to bone metastasis, and potential therapeutic strategy for bone metastatic disease using probiotics.

2. The mechanisms whereby gut microbiota induce GI cancer tumorigenesis

H. pylori was linked to stomach inflammation, and ultimately gastric cancer, in what some would consider a reckless, albeit dedicated demonstration of scientific commitment that later won two researchers the Nobel Prize. Subject to much scrutiny, Dr. Barry Marshall intentionally infected himself with *H. pylori* and underwent a stomach biopsy in order to prove that the bacterium was linked to gastric disease [37,38]. While this was the first known class I oncogenic bacterium with a carcinogenic effect, this discovery was a gateway for further exploration into bacteria that induce cancer and the mechanisms through which this induction occurs [39]. When exploration of bacteria as carcinogenic agents first began, it was learned that bacteria induce cancer by both creating a chronic state of inflammation and generating metabolites that are known to be carcinogenic [40]. Since this discovery in the late 1900s, the knowledge of these mechanisms has expanded.

It is currently known that bacteria are capable of promoting carcinogenesis through several different mechanisms, and one of the primary courses of action for which the gut microbiota induce GI carcinogenesis is through chronic inflammation caused by bacterial infection. When bacteria such as *H. pylori* breach the gut epithelium, this bacterium induces chronic inflammation by invading the gastric cells where it can reside, potentially asymptomatic, for years, all while releasing the oncoprotein, cytotoxin-associated gene A (CagA) [41,42]. CagA ultimately effects gastric epithelial cells in multiple ways. Inducing cell proliferation of gastric epithelial cells is one of the known functions of CagA, and this occurs through (i) the activation of the protein kinase B (AKT) pathway through phosphoinositide 3-kinase (PI3K), (ii) the activation of the extracellular signal-regulated kinase (ERK) pathway through growth factor receptor bound protein 2 (GRB2) and mitogen-activated protein kinase (MEK), and (iii) β-catenin activation of the wingless/integrated (WNT) pathway [43–47]. CagA has also been found to induce an inflammatory response through its contribution to interleukin (IL)-8 expression in gastric epithelial cells; by acting on the Ras pathway, CagA helps stimulate IL-8 induction which triggers an inflammatory response through nuclear factor kappa light chain enhancer of activated B cells (NF-κB) signaling [48]. Additionally, CagA stimulates reactive oxygen species (ROS) in infected gastric epithelial cells. When ROS production occurs in excess, DNA damage and carcinogenesis can occur in gastric epithelial cells [49]. These findings suggest that *H. pylori* infection contributes to carcinogenesis in the gut through the induction of inflammation and DNA damage.

In recent years, there has been some success in treating *H. pylori* infection, which has led to the finding that this bacterium is primarily responsible for non-cardia gastric cancer (cardia gastric cancer is located near the esophageal-gastric junction, while non-cardia gastric cancer is located in the distal section of the stomach [50]), whose rates have been declining with lower *H. pylori* infection rates [51]. Subsequently, cardia gastric cancer rates have been seen to increase seven-fold [52]. While *H. pylori* infection increases the risk of gastric cancer, it is also thought to play a protective role in esophageal cancer by reducing acid secretion in this area [50]. There is some evidence to suggest that by eradicating *H. pylori* in the developing world, the incidence of the cardia subtype has increased, because the quantity of acid in this area has decreased [52,53]. Regardless of gastric subtype, it is through mechanisms that induce inflammation and DNA damage that *H. pylori* infection, or lack thereof, contributes to carcinogenesis in the gut.

Other bacteria also utilize similar mechanisms to induce DNA damage and ultimately cancer. When *B. fragilis* breach the gut epithelium and release *B. fragilis* toxin, an inflammatory immune response, one of the hallmarks of cancer, occurs in the body [54]. This bacterium induces an inflammatory response through (i) the activation of β-catenin and the WNT pathway and (ii) the induction of IL-8 secretion [55–58]. *Helicobacter hepaticus* and *E. coli* are examples of gut bacteria that act to promote carcinogenesis through mechanisms that induce an inflammatory response. These two bacteria produce DNA double-strand breaks in epithelial cells by inducing cytolethal distending toxin, which causes cancer proliferation in conjunction with inflammation [59,60]

An alternative mechanism through which gut bacterial carcinogenesis occurs is the mediation of bile acid metabolism by the gut microbiota [61]. In a healthy microenvironment, bile acids are expelled into bile where they are then digested by the gut microbiota for reuptake into the blood stream [62]. Problems can occur however, when bile acids are present at high levels, because bile acids are cholesterol derivatives whose detergent properties act to disrupt bacterial and host cell membranes, denature proteins, and cause oxidative DNA damage [63,64]. When these acids are highly concentrated, a process that can be facilitated by bacteria such as *Salmonella typhi*, they quickly induce inflammatory reactions in the body's attempt to repair the damaged tissue [41,65,66]. In the process of tissue repair, an accumulation of bone marrow-derived mesenchymal stem cells (BM-MSCs) is seen in the mucosal layer of the gut barrier, contributing to the now precancerous state of the gut [67,68]. In addition to generating this precancerous state, bile acids are also known to stimulate ROS, which disrupts the base excision repair pathway, contributing to DNA damage which leads to carcinogenesis through gene mutation [66,69]. When exposure to excess bile acids occurs chronically, this causes degradation of p53, a tumor suppressor, leading to a decrease in the apoptosis of cancer cells [65]. This degradation further impairs the process of DNA repair as the cell cycle will not arrest in response to DNA damage and apoptosis will not be induced [65,70]. This evidence implicates bile acids in the induction and progression of the cancer disease state, primarily in gastric cancer and CRC.

While contributing heavily to gut carcinogenesis, the gut microbiota can also play anti-tumorigenic roles in the gut. Gut bacteria, in the process of digesting carbohydrates and fibers that the body would otherwise be unable to digest, generate short chain fatty acids (SCFAs) which interact with cancer cells [71]. It was recently discovered that the concentration of SCFAs – and SCFA producing bacteria – is reduced in patients with CRC, as compared to a control group [72]. One specific SCFA, butyrate, can act as a ligand to G protein-coupled receptor (GPR) 109A, a cell surface receptor of macrophages and adipocytes that was shown to correlate with CRC development when expression of butyrate is decreased [73]. Butyrate, in conjunction with GPR109A, can downregulate the activity of NF-κB and decrease the expression of inducible nitric oxide synthase (iNOS) and cyclooxygenase (COX)-2, known to be involved in tumorigenesis [74–76].

3. The mechanisms whereby gut microbiota control GI cancer metastasis

While primary tumorigenesis remains a problem, metastasis is considered to be the predominant cause of poor prognosis in patients with GI cancer [77]. In patients diagnosed with CRC, approximately 60% develop metastases to secondary sites within five years, and when CRC metastasizes, patients are faced with poor prognosis [78]. The five-year survival rates for patients with distant metastasis from CRC are just 14% (colon cancer) and 16% (rectal cancer), while those for patients without metastasis are 91% and 89%, respectively [79]; this accounts for 9.4% of all the patient deaths attributed to cancer in 2020, second only to lung cancer [80,81]. One of the GI cancer counterparts, stomach cancer has an average five year survival rate of just 31% across all disease states, largely because this cancer has already metastasized upon diagnosis [52], thus making gastric cancer the third leading cause of cancer related death globally [82]. When cancer metastasizes from the GI system, the most common secondary sites include liver, peritoneum, lung, and bone [83]. Although not as thoroughly studied as its role in primary GI carcinogenesis, the gut microbiota has also been found to heavily influence metastasis of GI cancers.

Bacteria are known carcinogens, functioning to promote carcinogenesis and metastasis, in part, through the release of toxins, primarily lipopolysaccharide (LPS), which interfere with immune and inflammatory cell signaling pathways in a healthy individual [84,85]. LPS is a glycolipid on the outer membrane of gram-negative bacteria [86], many of which safely reside in the gut microenvironment [87]. LPS can be released from the bacterial cell wall through bacterial lysis or shedding [88–90], and is known to interact with immune cells through ligand/receptor binding [91,92]. In a healthy gut microenvironment, LPS will not breach through the gut wall; however, the leaky gut status caused by dysbiosis enables toxins from bacteria, including LPS, to leak through the intestinal epithelium via a defective tight junction barrier [93–95]. Thereafter, lipid A on LPS interacts with macrophages through the activation of toll-like receptor 4 (TLR4) [96]. This activation of TLR4 activates NF-κB to induce the release of inflammatory cytokines, associated with metastatic progression, such as tumor necrosis factor (TNF)-α, IL-1, and IL-6 [97,98], as well as vascular endothelial growth factor (VEGF) [99] and transforming growth factor β (TGF-β) [100]. This LPS-induced VEGF promotes CRC metastasis by (i) enhancing angiogenesis [101,102] and lymphangiogenesis [103–105]; (ii) inducing epithelial-mesenchymal transition of CRC cells; and (iii) stimulating the mobile ability of CRC cells by upregulating the transcription of protein coding gene, CNTN-1 [106] and the protein moesin through the RhoA/ROCK-2 pathway [107].

While it is evident that the gut microbiota directly influence GI cancer metastasis, recent evidence exists to implicate the gut microbiota as a contributor to the development of the pre-metastatic niche. In order for a primary tumor to metastasize, the local microenvironment in the secondary site must be favorable for metastatic tumor cells, or disseminated tumor cells (DTCs), to grow within this new environment [108]. This is the premise of Paget's 1889 "seed and soil" hypothesis; just like a seed needs to land on nutrient rich soil to grow, DTCs (seeds) need a fertile environment in the metastatic site (soil) in order to take hold [109]. Indeed, a recent study of CRC showed that *E. coli* from the primary tumor site in the colon penetrated through the gut barrier and migrated to the liver, where they enhanced pre-metastatic niche formation, leading to DTC recruitment and eventually full-blown liver metastasis [110].

In addition to gut bacteria being found in secondary tumor sites, evidence supports the idea that the gut microbiota communicate and interact with other cell types to facilitate cancer metastasis [111,112]. Gut microbiota also provide another pathway for GI cancers to metastasize by communicating with BM-MSCs. It is known that BM-MSCs have an affinity for tumor or cancer cells, and that once recruited, these cancer-associated BM-MSCs can differentiate into fibroblasts and macrophages to influence progression of tumors [113]. However, recent evidence has begun to suggest that BM-MSCs are also recruited to metastatic sites, and then serve as the metastatic niche to promote metastatic progression [114–118]. For example, a study of lymph node metastasis from gastric cancer demonstrated the ability of these gastric cancer cells to educate BM-MSCs via secretory exosomes to create the metastatic niche in the lymph nodes, resulting in enhancement of the dissemination of gastric cancer into lymph node, as well as enhancement of lymphangiogenesis which promotes further dissemination [119]. These findings suggest that the gut microbiota also facilitate GI cancer metastasis by influencing the microenvironment in the metastatic site in either a direct or indirect manner.

4. The potential mechanisms whereby gut microbiota regulate bone metastatic process of solid tumors

While little evidence exists to support the idea that the gut microbiota influence GI cancer metastasis, there are a number of parallels between the mechanisms regulating metastasis of solid tumors out of gut and the mechanisms through which the gut microbiota act on the metastatic microenvironment "soil". Bone is one of the most common metastatic sites of solid tumors. While how gut microbiota control the bone dissemination process of solid tumors outside of the gut has not been thoroughly explored, there is a growing body of evidence that exists to support the gut microbiota as a regulator of the bone microenvironment and skeletal health. For example, the gut microbiota has been implicated as a modulator of other bone diseases, such as osteoarthritis and osteoporosis, through the brain-gut-bone axis [120,121]. The brain-gut-bone axis - sometimes referred to as the gut-bone axis - is a term used to reference the communicative interactions between the brain/nervous system, the gut microbiota, and the skeletal system through which bone health is affected [122,123]. Enhanced osteoclast activity found in osteoarthritis and osteoporosis likely contributes to bone metastasis, creating space for tumor cells to infiltrate the bone microenvironment. It was shown that arthritic mice have higher incidence of bone metastasis from breast cancer cells than their non-arthritic counterparts [124]. Further, while osteoporosis was not deemed to be a risk factor for bone metastasis, it was found that bone metastasis is accelerated in breast cancer patients with untreated osteoporosis [125]. Together, these findings suggest that the gut microbiota may play a crucial role in both the development of bone metastasis and an environment suitable for bone metastatic diseases.

Bone homeostasis is a result of the balance of bone formation mediated by osteoblasts and bone resorption induced by osteoclasts [126]. When cancer cells disseminate to the bone, they disrupt this homeostatic process [127]. Bone metastases are derived into three primary categories: osteolytic, osteoblastic, and mixed; which types of bone metastasis develop appears to be associated with how DTCs interfere with the balance between osteoclastogensis and osteoblastogenesis [128]. As is the case in osteolytic bone metastases, the tumor cells present in the bone upregulate the cytokines IL-1, IL-6, and TNF-α, all of which promote osteoclast formation from macrophages [129] and induce osteoblast apoptosis [130]. In addition to these proinflammatory cytokines, the parathyroid hormone-related protein (PTHrP), derived from bone metastatic cancer cells, also contributes to osteoclastogenesis. The cancer-derived PTHrP is known to induce bone resorption by activating a G-protein coupled receptor PTHrP receptor that is highly expressed on the osteoblasts and osteocytes [131,132]. Upon binding, PTHrP enhances the production of receptor activator of NF-κB ligand (RANKL) by osteoblasts and osteocytes, which binds to its receptor RANK on osteoclasts and their precursors acting to stimulate bone resorption and osteoclast differentiation, respectively [133,134]. This induced osteoclastogenesis contributes to significant bone destruction, creating space for tumor cells to proliferate in the bone [135].

Osteoclastogenesis can also be influenced by the gut microbiota. The relationship between the gut microbiota and bone homeostasis, especially osteoclastogenesis, was exemplified in a study comparing skeletal development of germ-free mice with that of conventionally raised mice. In this study, significantly higher trabecular bone volume and reduced osteoclast cell counts were observed in the bones of germ-free mice, compared to those of the conventionally raised mice. When germ free mice were treated with gut microbiota from conventionally raised donor mice, trabecular bone volume and osteoclast numbers became comparable with those of the conventionally raised mice [136]. As stated earlier, LPS derived from the gut microbiota enters circulation when dysbiosis occurs. LPS in circulation stimulates the osteoclast differentiation of monocytes and macrophages and promotes the maturation and survival of the resulting osteoclasts [137,138]. High levels of systemically circulating LPS also induce the release of the proinflammatory cytokine TNF-α from macrophages, known to control osteoclast activities by binding with the TNF-α tumor necrosis factor receptor 1 (TNFR-1) [137,139–143]. Indeed, LPS-induced TNF-α can induce bone resorption by driving osteoclastogenesis of a murine macrophage cell line RAW 264.7 cells without going through the RANK/RANKL pathway [143]. One proposed mechanism of LPS-associated osteoclastogenesis is that LPS induces the upregulation of a transcription factor nuclear factor of activated T cells c1 (NFATc1), essential for the differentiation of osteoclast cells, in the nucleus of osteoclast precursors [144,145]. Along with these notions, LPS treatments stimulate the reduction of bone density in two rodent models of chronic inflammation and one rodent model of prostaglandin E receptor 4 (EP4) deficient mice, which lack a receptor on osteoblasts (EP4) that regulates osteoclast formation [146–148]. Further, the LPS-TLR4 axis has also been implicated in enhancing the severity of osteoporosis and osteoarthritis [146,149–151]. In addition to circulating LPS, the gut microbiota can also regulate osteoclastogenesis through bile acid metabolism. Bile acid mediated osteoclastogenesis is facilitated primarily by lithocholic acid (LCA), a secondary bile acid converted through the 7alpha-dehydroxylation of chenodeoxycholic acid, a process heavily influenced by bacterial hydrolases located on the cell walls of gut bacteria [152,153]. Once converted, LCA serves as a ligand for the vitamin D receptor. Traditionally, the vitamin D receptor, which binds with vitamin D, is known for its role in calcium absorption, and high levels of vitamin D are positively correlated with bone mineral density [154,155]. However, when LCA binds to the vitamin D receptor on osteoblasts, it inhibits bone formation [156]. Furthermore, LCA directly damages osteoblasts, resulting in bone loss [157,158]. These studies suggest that osteoclastogenesis is regulated in part by gut microbiota-derived systemic LPS and LCA.

While osteoclastogenesis proves to be essential for creating space for bone metastatic tumor cells to grow, the osteoblasts also play a vital role in the bone metastatic progression. Osteoblasts, located at the endosteum of bone [159], support self-renewal, multi-potency, homing and migration of hematopoietic stem cells (HSCs) [160,161]. Therefore, osteoblasts are known as the specific microenvironment for HSCs, or the osteoblastic HSC “niche”. Importantly, the osteoblastic HSC niche is not only involved in the HSC maintenance, but also implicated in early colonization of bone DTCs. Prostate cancer cells compete directly with HSCs to gain space in the osteoblastic HSC niche when they disseminate to the bone [162]. Furthermore, bone metastatic breast cancer cells first colonized the osteoblastic niche through cell–cell adherens junctions [163]. Thereafter, these DTCs within the osteoblastic niche can remain in a dormant state for years before being reactivated to form full blown bone metastases [164,165]. These findings suggest that osteoblasts are crucial for the early onset of cancer colonization and its survival within the bone.

The gut microbiota can also be involved in the establishment of early colonization of bone metastatic cancer cells, as they also induce bone formation by activating osteoblasts. As discussed above, the gut microbiota are capable of breaking down nutrients that the host would be incapable of digesting on its own through anaerobic fermentation [8] and often, SCFAs are the product of this biochemical reaction [166]. These gut microbiota-inducing SCFAs are known to up-regulate skeletal formation. Indeed, treatments with probiotics, which are fermented into SCFAs by the gut microbiota, improved skeletal health in various animal models [167,168]. Moreover, SCFAs enhanced bone formation by stimulating the production of insulin-like growth factor 1 (IGF-1), a growth factor known to enhance skeletal formation, from the intestinal epithelial cells [169–172]. An additional mechanism by which the gut microbiota influence bone formation is through the regulation of the sex hormone androgen. Androgens are known to promote the growth of normal and cancerous prostate cells, and often androgen-deprivation therapy (ADT) is the first-line treatment for prostate cancer. The gut microbiota *Clostridium scindens* is known to convert glucocorticoids into androgens through enzymatic processes [173]. Further, a transplantation of gut microbiota from male mice into the female intestines resulted in an increase in systemic testosterone, from which androgen is derived. It is proposed that gut microbiota-derived sex steroids moderate bone remodeling [174] through (i) androgens stimulating longitudinal bone growth due, in part, to the upregulation of IGF-1 [175] and (ii) androgens activating androgen receptors on the osteoblasts which in turn inhibit bone resorption and osteolytic activity; this androgen activity has been shown to preserve cortical thickness, predominately in aging [176]. The importance of androgens in bone regulation is also supported by a *meta*-analysis evaluating studies of the efficacy of androgen-deprivation therapies (ADT) and/or androgen receptor inhibitors on prostate cancer patients, which revealed that non-metastatic castration-resistant prostate cancer patients presented with increased bone fragility and decreased bone mineral density following these anti-androgen treatments [177]. Moreover, a recent work demonstrated that ADT enhanced the commensal microbiota that contribute to castration resistance, and when resistance to ADT developed, the gut microbiota that enhance androgen formation were increased [178]. These suggest that gut derived androgens contribute to ADT resistance in prostate cancer patients [179], a disease state which is often accompanied by bone metastasis, since androgen signaling likely contributes to and accelerates this metastatic process [180,181]. Furthermore, antibiotic treatments and fecal microbiota transplantations (FMT) were both found to prolong the time to castration resistance and control tumor growth [178]. Together, these findings suggest that the gut microbiota serve as an extraneous source of androgen in the presence of ADT and may contribute to bone metastasis.

Although evidence does not exist specifically implicating the gut microbiota as a causative factor in bone metastasis, the gut microbiota have been seen to affect the metastatic process of breast cancer that commonly disseminates to bone. In a mouse model of hormone receptor positive breast cancer, gut dysbiosis can promote breast cancer metastasis through increased tumor cell dissemination into the blood and secondary sites, as well as the activation of macrophages and the release of proinflammatory cytokines [182]. Additionally, treatments of an antioxidant and -inflammatory agent muscadine grape extract reduced metastases of triple negative breast cancer by inducing microbial richness *in vivo* [31,183].

Taken together, although further studies are clearly warranted, these findings on the roles of the gut microbiota in both bone remodeling and metastases of solid tumors that commonly metastasizes to bone suggest that the gut microbiota may affect bone metastatic development (Fig. 1).

5. The potential roles of gut microbiota in enhancing the efficacy of treatments for bone metastasis

When compared with treatment strategies for other metastatic sites, approaches for treating bone metastasis are fairly unique. In typical cancer disease treatment, primary and metastatic tumors are subject to similar therapeutic approaches focused on either targeting the tumors themselves or stimulating the immune system around the area encompassing the tumor. However, treatment strategies for bone metastasis engage a different target. Bone metastasis therapies usually aim to target the function of the bone, an organ that couples osteoclast and osteoblast activity to continuously remodel [184]. It has been suggested that bone metastatic cancer cells are capable of interacting with the osteoclasts, osteoblasts, osteocytes, and other cells involved in the bone remodeling process. This crosstalk between bone metastatic cancer cells and cells involved in bone remodeling induces what is known as “the vicious cycle of bone metastasis” in which bone metastatic progression hastens [185]. The involvement of the bone organ in metastatic progression makes it logical to target bone remodeling in order to treat bone metastasis. Two current bone metastasis treatment options are bisphosphonates and the human monoclonal anti-RANKL antibody denosumab, both of which function to decrease osteolytic activity [186,187]. While these treatments provide necessary palliative relief for patients with bone metastasis, they ultimately fail to improve survival outcomes [186,187]. Recent clinical trials, however, show some promise for a new therapeutic agent that has been shown to improve survival outcomes for patients with bone metastasis, albeit only slightly. Radium-223 dichloride ($^{223}RaCl_2$), an alpha particle-emitting radiopharmaceutical that targets hydroxyapatite or osteoblastic bone metastatic lesions has been shown to improve survival for a few months (mean = 3 months) in patients with bone metastases from prostate cancer [188]. While the overall survival of patients with bone metastasis can also be enhanced for a few months through treatment with complementary systemic therapies (eg. hormone therapies, chemotherapies), $^{223}RaCl_2$ is the only bone-targeted therapy that is capable of improving survival outcomes for patients with bone metastases [189]. Since at current moment treatment options that target bone remodeling have had only moderate success, elucidating treatment options that function through mechanisms other than targeting bone remodeling is essential in order to eradicate bone metastasis in patients.

In recent years, immune checkpoint inhibition, a type of

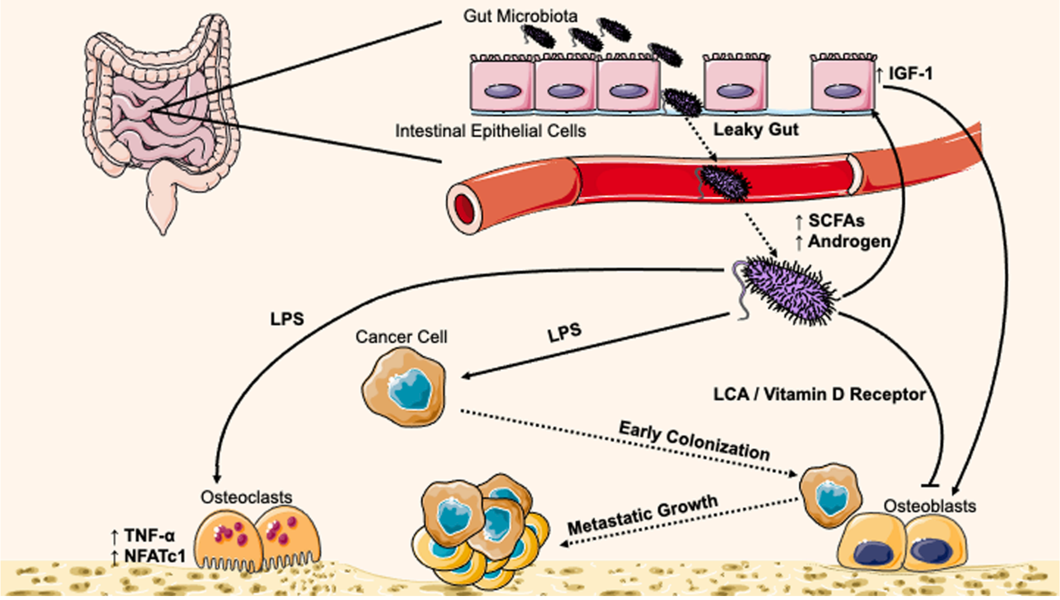

Fig. 1. Potential mechanisms whereby gut microbiota induce bone metastatic progression. The intestines are comprised of a single layer of epithelial cells that allow for absorption of nutrients into circulation. However, when dysbiosis occurs, the tight junctions in the gut become loose, creating what is known as a leaky gut epithelium. This status allows the gut microbiota to escape from the intestines and enter circulation. Once in circulation, the gut microbiota stimulate cancer cells through lipopolysaccharide (LPS) to acquire mobile ability. These cancer cells have disseminated from the primary tumor cite to the bone through systemic circulation. The gut microbiota also directly interact with osteoclasts and osteoblasts. To induce bone resorption, gut microbiota-derived LPS enhances osteoclast activities by upregulating tumor necrosis factor (TNF)-α and the transcription factor nuclear factor of activated T cells c1 (NFATc1) in osteoclasts. Further, lithocholic acid (LCA), which is converted from bile acid by the gut microbiota, inhibits osteoblast activities by binding with the vitamin D receptor on osteoblasts. To induce bone formation, gut microbiota-mediated increased short chain fatty acids (SCFAs) and upregulated androgen stimulate osteoblastogensis by inducing insulin-like growth factor (IGF)-1 secretion from intestinal epithelial cells. Since osteoclasts are also creating space for bone metastatic tumor cells and osteoblasts are a key microenvironment for the early colonization of bone metastatic cancer cells, this suggests that the gut microbiota modulate both cancer cells and the bone microenvironment to create an environment favorable for bone metastasis. Graphics adapted from Smart Servier Medical Art (https://smart.servier.com/).

immunotherapy, has emerged as a novel cancer treatment. The immune checkpoint programmed cell death-1 (PD-1) is expressed on several immune cells, including T cells, B cells, monocytes, natural killer T cells, and dendritic cells, with high quantities on cancer antigen-specific T cells [190]. Its ligand programmed death-ligand 1 (PD-L1) is generally expressed by macrophages, however, in the case of cancer, cancer cells express PD-L1 as a pro-tumor response to repress T cell activity [191,192]. Similarly, the immune checkpoint cytotoxic T lymphocyte antigen 4 (CTLA-4), expressed by activated effector T cells, functions as a pro-tumorigenic agent through T cell suppression [193]. When the immune checkpoints PD-1 or CTLA-4, located on T cells, are activated, they function to restrain T cell functions; however, when PD-1 and/or CTLA-4 are inhibited, as is the case in immune checkpoint inhibitor (ICI) therapy, previously restrained T cells are unrestricted and are capable of targeting cancer cells [194]. PD-1 has become a primary immunotherapeutic target as blocking its activation by PD-L1 has shown high efficacy and low toxicity clinically in its aim to normalize the immune system, rather than boost the immune cells effect on cancer specifically [195]. A *meta*-analysis performed to evaluate the efficacy and toxicity of anti-PD-1/PD-L1 inhibitors in patients with advanced stage and metastatic cancers (lung cancer, head-and-neck cancer, gastric cancer, renal-cell carcinoma, multiple myeloma, urothelial carcinoma, breast cancer, and CRC) revealed that enhanced survival outcomes and overall patient safety are the result of ICI treatment [196].

While ICIs have shown to be somewhat effective in controlling metastasis in general, the treatment efficacy of ICIs on bone metastasis has not been superior to conventional therapies for bone metastatic disease, listed above. In a recent phase III clinical trial investigating the efficacy of an anti-CTLA-4 antibody ipilimumab in advanced stage metastatic castration-resistant prostate cancer patients, including bone metastatic patients, ipilimumab failed to enhance patients' overall survival, although it positively influenced progression free survival (4.0 months, 95% confidence interval (CI): 3.6–4.3 vs. 3.1 months, CI 95%: 2.9–3.4) [197]. A phase II trial of an anti-PD-1 antibody pembrolizumab was conducted in three cohorts of metastatic castration-resistant prostate cancer patients (tumor with measurable PD-L1 positive, tumor with measurable PD-L1 unknown, and bone predominant disease). It revealed that in patients treated with docetaxel and at least one targeted endocrine therapy, pembrolizumab treatment did slightly increase progression free survival (2.1 months, 2.1 months, and 3.7 months) though it did not reach statistical significance; however, interestingly, it appeared to be most effective in patients with bone-predominant metastases (estimated 12 month survival: 41%, 35%, and 62%) [198]. Additionally, non-small cell lung cancer patients with bone metastases treated with an anti-PD-1 monoclonal antibody nivolumab had significantly shorter survival outcomes than those treated with docetaxel alone (patient deaths: 26/86 nivolumab treated, 11/75 docetaxel treated, $p = 0.019$) [199]. Moreover, in bone metastatic animal models using PD-1 knockout mice or wild type mice treated with nivolumab, anti-PD-1 effects could only prevent fractures of tumor-bearing bones and diminish cancer-induced bone pain, but not improve their survival [200]. Together, these findings suggest that ICI therapies themselves generally cannot reverse the negative survival outcomes of cancer patients with bone metastases.

It has been proposed that ICI therapy is not successful in patients with bone metastasis due to the immune regulatory nature of the bone metastatic environment. Once in the bone, bone metastatic cancer cells interact with osteocytes to induce their release of TGF-β, which in turn activates cancer cells to produce osteolytic factors, including PTHrP, IL-6, and IL-11 [201]. Importantly, the abundant TGF-β within the marrow is known to act as an immunosuppressant. When TGF-β is rampant in the bone microenvironment, TGF-β drives polarization of immune suppressor T cells, T helper 17 (T_h17) cells and regulatory T cells (Tregs) from naïve $CD4^+$ T cells, whereas it prevents the differentiation into immune effector T cell, T helper 1 (T_h1) cell [202,203]. Indeed, in a bone metastatic mouse model, the high levels of TGF-β created during the bone metastatic process prevented T_h1 cell development in the marrow, resulting in reducing the optimal function of ICI therapy and eventually the development of resistance to it [204]. In addition, in a syngeneic breast cancer model, when the levels of TGF-β were reduced using either an oncolytic adenovirus expressing a soluble form of the TGF-β receptor 2, sTGF-βRII-Fc, that can directly target TGF-β, or pan-TGF-β neutralizing antibody 1D11, $CD8^+$ T cell tumor-infiltration and the cytotoxic factors they release (e.g. perforin and granzymes) were increased in the breast tumors [205,206].

Interestingly, recent studies demonstrated that alteration of the gut microbiota can enhance the efficacy of ICI therapy for several cancer types, including GI cancer, melanoma, non-small cell lung cancer, and renal cell carcinoma through two mechanisms: (i) antigen-specific mechanisms in which the gut microbiota share epitopes with tumor antigens to reduce anti-tumor responses and (ii) antigen-independent mechanisms involving innate immune cells such as effector T cells and myeloid cells, both of which can be found in the gut mucosa [207–211]. For example, a study conducted an analysis on renal cell carcinoma and non-small cell lung cancer patient stool samples treated with ICIs, and identified that *Akkermansia muciniphila* (*A. muciniphila*) was positively correlated with progression free survival and patients' response to PD-1 inhibition [212]. Based on this finding, mouse intestines were colonized with *A. muciniphila* alone or in combination with *E. hirae*, and then these mice were injected orthotopically with either murine Ret melanoma cells or Lewis lung carcinoma cells. As expected, colonization with these two gut microbiota in the gut of the tumor-bearing mice enhanced PD-1 blockade efficacy. Furthermore, treatment using anti-PD-1 antibody with *A. muciniphila* and *E. hirae* induced accumulation of memory $CD4^+$ T cells in the mouse tumors and increased the levels of IL-12, a cytokine that induces T_h1 differentiation, in the circulation [212]. More interestingly, recent case reports demonstrated that cytotoxic T cell-based immunotherapy completely attenuated bone metastases in a chemotherapy–resistant gastric cancer patient [213], and that pembrolizumab induced complete response in lung cancer patients with bone metastases [214,215]. In the case of the patient with bone metastases from chemotherapy-resistant gastric cancer, complete attenuation was obtained through treatment with dendritic cell-cytotoxic T lymphocytes specific to carcinoembryonic antigen (CEA) and VEGF receptor (VEGFR)-2 (the two most commonly expressed antigens in gastric cancer) with adjunct low dose cyclophosphamide (an immune suppressor which in low doses depletes Treg cells, increasing T cell activity) [213]. In the three patients with lung cancer, systemic treatment with pembrolizumab, an anti-PD-1 antibody, in addition to palliative treatment of the bone metastases showed success in driving patients into remission [214,215]. These findings suggest that ICI therapy can be effective in treating bone metastasis when immune effector T cell activities are enhanced by manipulating the gut microbiota. To do so, probiotics, which enhance immune effector T cell activities, as well as reduce immune suppressor T cell activities, can be combined with ICI therapy for bone metastasis. Indeed, increased T_h1 cell number and decrease in T_h17 cell number were observed in peripheral blood mononuclear cells of atopic dermatitis mice treated with the probiotic Duolac ATP (which contains *Lactobacillus casei*, *L. plantarum*, *lactobacillus rhamnosus*, and *B. lactis*) [216]. Additionally, *Lactobacillus casei* and Bio-Three (a combination of *Bacillus mesentericus*, *Clostridium butyricum*, and *Enterococcus faecalis*) are known to promote T_h1 cell differentiation [217,218]. Since the modulation of immune compartment mediated by the gut microbiota depends on the bacteria contained in each respective probiotic cocktail, selecting the right probiotics specific to enhancing T_h1 cell lineage may be a key to improve the efficacy of ICI therapy in patients with bone metastasis. Moreover, FMT - often thought of as a super probiotic - may also prove useful in the enhancement of ICI therapy for patients with bone metastasis. FMT was first used in patients with recurrent *Clostridium difficile* infection [219,220], and involves taking stool from a healthy donor and delivering it via colonoscopy, nasoenteric tube, or ingestible capsules to the dysbiotic GI tract of a recipient with the goal of repopulating the microbiota to restore normal gut function [221,222]. FMT has already been used to successfully treat patients with complications from cancer or cancer treatments, such as ICI colitis and *Clostridium difficile* infection [223,224]. A recent clinical trial demonstrated that FMT, using stool samples from long-term responders to PD-1 treatment, can be used in conjunction with anti-PD-1 ICI therapy in advanced melanoma patients with PD-1 resistance in order to re-colonize the gut and re-educate the tumor microenvironment to respond to anti-PD1 treatment [225]. Further studies in this area are clearly needed to strengthen ICI efficacy for bone metastatic disease.

While FMT has not been studied in prostate cancer patients, FMT from patients with castration-resistant prostate cancer exasperated castration-resistant prostate cancer in mice, whereas FMT from ADT-sensitive prostate cancer patients suppressed tumor growth in mice with castration-resistant prostate cancer [178]. The significance of this data warrants studies into FMT as a therapeutic agent for advanced prostate cancer patients with bone metastases, which do not successfully respond to most current treatments, including ADT and ICI. ADT is known to induce osteolytic activity in prostate cancer patients, resulting in a decrease in bone mineral density and an increase in associated risks, including fracture [226]. Currently, bisphosphonates and denosumab have both shown to enhance bone mineral density in prostate cancer patients without bone metastases receiving ADT [227,228]; however, these treatment strategies are not widely implemented in patients without bone metastasis, since they do not improve survival outcomes and have associated side effects (e.g. osteonecrosis of the jaw). Recent studies conducted in osteoarthritis patients suggest that FMT or probiotic treatment may prove useful in improving bone health in prostate cancer patients receiving ADT. For example, treatment with *Lactobacillus casei Shirota* was found to reduce both pain and levels of the inflammatory marker high-sensitivity C-reactive protein - associated with enhanced risk of fractures - in osteoarthritis patients [229,230]. Therefore, if FMT or probiotic treatment can be geared towards repopulating the gut with bacteria that re-educate the bone microenvironment to enhance osteoblastic activity, this may prolong the length of time for which patients can endure ADT treatments and mitigate the risk of skeletal related events. Further research is needed, however, these findings, combined with the evidence supporting FMT enhancing ICI, suggests that the manipulation of gut microbiota by probiotics and/or FMT may be a useful tool to treat advanced cancer patients with bone metastasis. The concept of re-colonizing the gut microbiota and re-educating the tumor microenvironment using probiotics and/or FMT to respond to treatment and suppress tumor growth in untreatable patients is clinically novel, and further research into this field - exploring the ability of both probiotics and/or FMT to mitigate the effects of the dysbiotic gut on the bone microenvironment - may yield key insight into successful treatments of bone metastasis (Fig. 2).

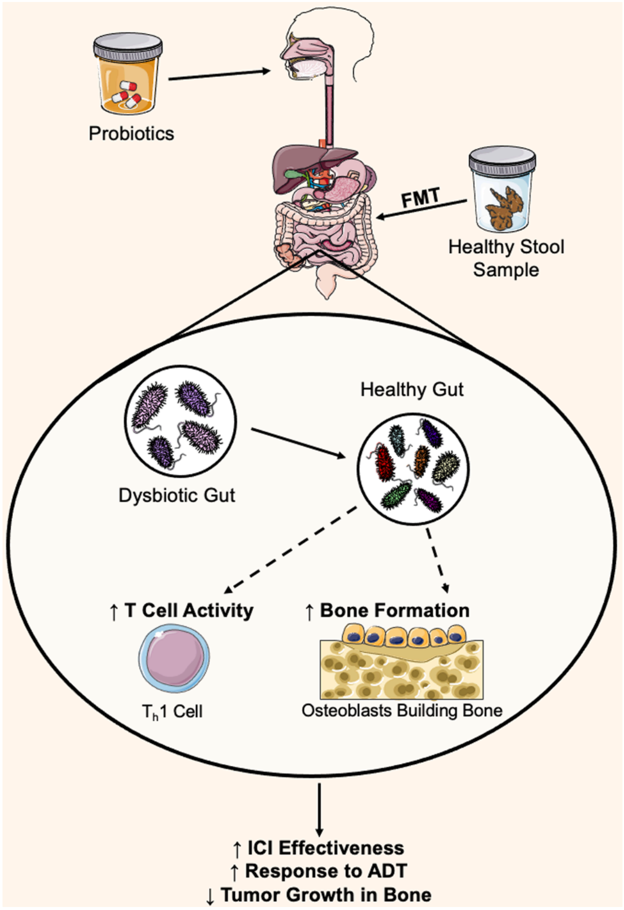

Fig. 2. Proposed treatment strategies for bone metastasis by manipulation of gut microbiota. Probiotics, ingested orally, provide the gastrointestinal system with a new supply of beneficial bacteria and yeasts that help maintain or restore gut health. Similarly, fecal microbiota transplantations (FMT), which involves inserting stool from a healthy donor into a recipient with a dysbiotic gut, can be used to repopulate the gut with healthy bacteria. When the dysbiotic gut microbiota are repopulated with healthy bacteria, both T cell activity and bone formation are increased. If this recolonization is performed specifically with bacteria that enhance T_h1 cell activity, this helps increase the effectiveness of immune checkpoint inhibitor (ICI) treatment. This technique may be useful to enhance ICI efficacy in patients with bone metastasis, where ICI treatment is generally ineffective. Further, repopulating the gut with healthy bacteria, specifically from prostate cancer patients who are responsive to androgen-deprivation therapy (ADT), has been shown to re-educate the tumor microenvironment to respond to ADT in patients who have resistance to this treatment. This concept of re-educating the tumor microenvironment, using bacteria that favor bone formation and a balanced gut, has the potential to decrease tumor growth in the bone by making the bone microenvironment unfavorable for tumor growth and enhancing the effectiveness of common cancer therapies. Graphics adapted from Smart Servier Medical Art (https://smart.servier.com/).

6. Discussion/Conclusion

In this article, we have detailed the apparent involvement of the gut microbiota in tumorigenesis, cancer metastasis, and skeletal health. In the human body, the gut microbiota interact with the host to maintain homeostasis. However, when microbial dysbiosis is induced, changes in these gut microbiota/host interactions enhance pro-tumor and metastatic activities [231] and alter the bone remodeling process [174]. Although little is known regarding the mechanisms through which the gut microbiota influence bone metastasis, evidence we discussed here suggest that the gut microbiota, by stimulating both bone metastatic cancer cells and the bone microenvironment, contributes to the development of bone metastasis. However, the following outstanding questions remain to be answered:

1. Which specific gut microbiota are implicated in bone metastatic progression?
2. Does gut microbiota composition differ among different bone metastatic phenotypes (e.g. osteolytic, osteoblastic, mixed)?
3. Do changes in gut microbiota directly influence the process of cancer dissemination to the bone?
4. Can FMT be used to enhance the effectiveness of treatments for bone metastasis, by repopulating the gut?
5. Can probiotics really enhance ICI efficacy for bone metastasis? If so, what types of probiotics?
6. Can prebiotics, which induce the growth of beneficial bacteria in the gut, further enhance the effect of probiotics on ICI efficacy?
7. Does preventing and/or blocking gut dysbiosis prevent bone metastasis or increase progression free survival?

Clinically, when cancer cells disseminate to the bone, patient survival outcomes diminish significantly. Unfortunately, treatments for bone metastasis at this point are generally palliative and have been shown to provide minimal curative effect [232]. Therefore, there is an apparent need for further studies elucidating the mechanisms through which bone metastasis occurs in order to identify novel treatment options for patients. These mechanisms are elusive; however, recently the gut microbiota have emerged as a likely contributor to bone metastasis, and their manipulation may enhance the efficacy of immunotherapies which are currently known to be ineffective on bone metastasis. Part of the mystery that needs to be uncovered is how bacteria from "the outside world (e.g. gut mucosal tissues)" can influence and educate the non-mucosal organ system that is the bone, to create an environment favorable for metastatic disease. While further clinical evaluation is warranted, current data suggest that ICI therapy plus probiotics, including FMT, alone or in concert with current standard treatments for bone metastasis may lead to much-needed improvements in the clinical management of cancer bone metastasis.

Author Contributions

K.F.C., H.Y., and Y.S. wrote the manuscript. All authors reviewed and approved the final manuscript.

Declaration of Competing Interest

The authors declare that they have no known competing financial interests or personal relationships that could have appeared to influence the work reported in this paper.

Acknowledgements

This work is directly supported by the National Cancer Institute (R01-CA238888, Y.S.; R44-CA203184, Y.S.), Department of Defense (W81XWH-17-1-0541, Y.S.; W81XWH-19-1-0045, Y.S.), METAvivor (METAvivor Research Award, Y.S.), and the Wake Forest Baptist Comprehensive Cancer Center Internal Pilot Funding (Y.S.). This work is also supported by the National Cancer Institute's Cancer Center Support Grant award number P30-CA012197 issued to the Wake Forest Baptist Comprehensive Cancer Center. The content is solely the responsibility of the authors and does not necessarily represent the official views of the National Cancer Institute and Department of Defense. Graphics adapted from Smart Servier Medical Art (https://smart.servier.com/).

References

[1] R. Sender, S. Fuchs, R. Milo, Revised Estimates for the Number of Human and Bacteria Cells in the Body, PLoS Biol 14 (8) (2016), e1002533.
[2] S. Altves, H.K. Yildiz, H.C. Vural, Interaction of the microbiota with the human body in health and diseases, Biosci Microbiota Food Health 39 (2) (2020) 23–32.
[3] E.Z. Gomaa, Human gut microbiota/microbiome in health and diseases: a review, Antonie Van Leeuwenhoek 113 (12) (2020) 2019–2040.
[4] A.L. Byrd, Y. Belkaid, J.A. Segre, The human skin microbiome, Nat Rev Microbiol 16 (3) (2018) 143–155.
[5] Y. Vazquez-Baeza, C. Callewaert, J. Debelius, E. Hyde, C. Marotz, J.T. Morton, A. Swafford, A. Vrbanac, P.C. Dorrestein, R. Knight, Impacts of the Human Gut Microbiome on Therapeutics, Annu Rev Pharmacol Toxicol 58 (2018) 253–270.
[6] W.V. Ingman, The Gut Microbiome: A New Player in Breast Cancer Metastasis, Cancer Res 79 (14) (2019) 3539–3541.
[7] G. Berg, D. Rybakova, D. Fischer, T. Cernava, M.C. Verges, T. Charles, X. Chen, L. Cocolin, K. Eversole, G.H. Corral, et al., Microbiome definition re-visited: old concepts and new challenges, Microbiome 8 (1) (2020) 103.
[8] A.B. Shreiner, J.Y. Kao, V.B. Young, The gut microbiome in health and in disease, Curr Opin Gastroenterol 31 (1) (2015) 69–75.
[9] J. Larsbrink, T.E. Rogers, G.R. Hemsworth, L.S. McKee, A.S. Tauzin, O. Spadiut, S. Klinter, N.A. Pudlo, K. Urs, N.M. Koropatkin, et al., A discrete genetic locus confers xyloglucan metabolism in select human gut Bacteroidetes, Nature 506 (7489) (2014) 498–502.
[10] M. Das, O. Cronin, D.M. Keohane, E.M. Cormac, H. Nugent, M. Nugent, C. Molloy, P.W. O'Toole, F. Shanahan, M.G. Molloy, et al., Gut microbiota alterations associated with reduced bone mineral density in older adults, Rheumatology (Oxford) 58 (12) (2019) 2295–2304.
[11] K. Yoshii, K. Hosomi, K. Sawane, J. Kunisawa, Metabolism of Dietary and Microbial Vitamin B Family in the Regulation of Host Immunity, Front Nutr 6 (2019) 48.
[12] A.K. DeGruttola, D. Low, A. Mizoguchi, E. Mizoguchi, Current Understanding of Dysbiosis in Disease in Human and Animal Models, Inflamm Bowel Dis 22 (5) (2016) 1137–1150.
[13] A. Farhadi, A. Banan, J. Fields, A. Keshavarzian, Intestinal barrier: an interface between health and disease, J Gastroenterol Hepatol 18 (5) (2003) 479–497.
[14] M. Vancamelbeke, S. Vermeire, The intestinal barrier: a fundamental role in health and disease, Expert Rev Gastroenterol Hepatol 11 (9) (2017) 821–834.
[15] K.R. Groschwitz, S.P. Hogan, **Intestinal barrier function: molecular regulation and disease pathogenesis**. *J Allergy Clin Immunol* **124**(1) (2009) 3-20; quiz 21-22.
[16] J.R. Turner, Intestinal mucosal barrier function in health and disease, Nat Rev Immunol 9 (11) (2009) 799–809.
[17] P. Katongole, O.J. Sande, M. Joloba, S.J. Reynolds, N. Niyonzima, The human microbiome and its link in prostate cancer risk and pathogenesis, Infect Agent Cancer 15 (2020) 53.
[18] J.R. Marchesi, J. Ravel, The vocabulary of microbiome research: a proposal, Microbiome 3 (2015) 31.
[19] T.C. Schmidt, M. Schirmer, H. Weiss, S.B. Haderlein, Microbial degradation of methyl tert-butyl ether and tert-butyl alcohol in the subsurface, J Contam Hydrol 70 (3–4) (2004) 173–203.
[20] L.M. Coussens, Z. Werb, Inflammation and cancer, Nature 420 (6917) (2002) 860–867.
[21] G.M. Birchenough, M.E. Johansson, J.K. Gustafsson, J.H. Bergstrom, G. C. Hansson, New developments in goblet cell mucus secretion and function, Mucosal Immunol 8 (4) (2015) 712–719.
[22] O.D. Cooney, P.R. Nagareddy, A.J. Murphy, M.K.S. Lee, Healthy Gut, Healthy Bones: Targeting the Gut Microbiome to Promote Bone Health, Front Endocrinol (Lausanne) 11 (2020), 620466.
[23] K. Nishiyama, M. Sugiyama, T. Mukai, Adhesion Properties of Lactic Acid Bacteria on Intestinal Mucin, Microorganisms 4 (3) (2016).
[24] M. Camilleri, Leaky gut: mechanisms, measurement and clinical implications in humans, Gut 68 (8) (2019) 1516–1526.
[25] L. Ibanez, M. Rouleau, A. Wakkach, C. Blin-Wakkach, Gut microbiome and bone, Joint Bone Spine 86 (1) (2019) 43–47.
[26] J.Y. Li, B. Chassaing, A.M. Tyagi, C. Vaccaro, T. Luo, J. Adams, T.M. Darby, M. N. Weitzmann, J.G. Mulle, A.T. Gewirtz, et al., Sex steroid deficiency-associated bone loss is microbiota dependent and prevented by probiotics, J Clin Invest 126 (6) (2016) 2049–2063.
[27] W. Guo, X. Zhou, X. Li, Q. Zhu, J. Peng, B. Zhu, X. Zheng, Y. Lu, D. Yang, B. Wang, et al., Depletion of Gut Microbiota Impairs Gut Barrier Function and Antiviral Immune Defense in the Liver, Front Immunol 12 (2021), 636803.
[28] J.E. Belizario, J. Faintuch, **Microbiome and Gut Dysbiosis**. *Exp Suppl* 109 (2018) 459–476.
[29] E. Patterson, P.M. Ryan, J.F. Cryan, T.G. Dinan, R.P. Ross, G.F. Fitzgerald, C. Stanton, Gut microbiota, obesity and diabetes, Postgrad Med J 92 (1087) (2016) 286–300.
[30] Z. Guan, J. Jia, C. Zhang, T. Sun, W. Zhang, W. Yuan, H. Leng, C. Song, Gut microbiome dysbiosis alleviates the progression of osteoarthritis in mice, Clin Sci (Lond) 134 (23) (2020) 3159–3174.
[31] M. Collard, N. Austin, A. Tallant, P. Gallagher, **Muscadine Grape Extract Reduces Lung and Liver Metastasis in Mice with Triple Negative Breast Cancer in Association with Changes in the Gut Microbiome**, Current Developments in Nutrition 3 (2019).
[32] K. Newton, V.M. Dixit, Signaling in innate immunity and inflammation, Cold Spring Harb Perspect Biol 4 (3) (2012).
[33] A. Mantovani, Cancer: inflammation by remote control, Nature 435 (7043) (2005) 752–753.
[34] M. Song, A.T. Chan, Environmental Factors, Gut Microbiota, and Colorectal Cancer Prevention, Clin Gastroenterol Hepatol 17 (2) (2019) 275–289.
[35] A. Mantovani, P. Allavena, A. Sica, F. Balkwill, Cancer-related inflammation, Nature 454 (7203) (2008) 436–444.
[36] J. Gagniere, J. Raisch, J. Veziant, N. Barnich, R. Bonnet, E. Buc, M.A. Bringer, D. Pezet, M. Bonnet, Gut microbiota imbalance and colorectal cancer, World J Gastroenterol 22 (2) (2016) 501–518.
[37] N. Ahmed, 23 years of the discovery of Helicobacter pylori: is the debate over? Ann Clin Microbiol Antimicrob 4 (2005) 17.
[38] E. Dolgin, Fighting cancer with microbes, Nature 577 (7792) (2020) S16–S18.
[39] S.F. Moss, The Clinical Evidence Linking Helicobacter pylori to Gastric Cancer, Cell Mol Gastroenterol Hepatol 3 (2) (2017) 183–191.
[40] J. Parsonnet, Bacterial infection as a cause of cancer, Environ Health Perspect 103 (Suppl 8) (1995) 263–268.
[41] S.A. Sheweita, A.S. Alsamghan, Molecular Mechanisms Contributing Bacterial Infections to the Incidence of Various Types of Cancer, Mediators Inflamm 2020 (2020) 4070419.
[42] M. Amieva, R.M. Peek Jr., Pathobiology of Helicobacter pylori-Induced Gastric Cancer, Gastroenterology 150 (1) (2016) 64–78.
[43] A.T. Franco, D.A. Israel, M.K. Washington, U. Krishna, J.G. Fox, A.B. Rogers, A. S. Neish, L. Collier-Hyams, G.I. Perez-Perez, M. Hatakeyama, et al., Activation of beta-catenin by carcinogenic Helicobacter pylori, Proc Natl Acad Sci U S A 102 (30) (2005) 10646–10651.
[44] S. Keates, A.C. Keates, M. Warny, R.M. Peek Jr., P.G. Murray, C.P. Kelly, Differential activation of mitogen-activated protein kinases in AGS gastric

epithelial cells by cag+ and cag- Helicobacter pylori, J Immunol 163 (10) (1999) 5552–5559.

[45] H. Mimuro, T. Suzuki, J. Tanaka, M. Asahi, R. Haas, C. Sasakawa, Grb2 is a key mediator of helicobacter pylori CagA protein activities, Mol Cell 10 (4) (2002) 745–755.

[46] T.A. Nagy, M.R. Frey, F. Yan, D.A. Israel, D.B. Polk, R.M. Peek Jr., Helicobacter pylori regulates cellular migration and apoptosis by activation of phosphatidylinositol 3-kinase signaling, J Infect Dis 199 (5) (2009) 641–651.

[47] J.T. Neal, T.S. Peterson, M.L. Kent, K.H. Guillemin, pylori virulence factor CagA increases intestinal cell proliferation by Wnt pathway activation in a transgenic zebrafish model, Dis Model Mech 6 (3) (2013) 802–810.

[48] S. Brandt, T. Kwok, R. Hartig, W. Konig, S. Backert, NF-kappaB activation and potentiation of proinflammatory responses by the Helicobacter pylori CagA protein, Proc Natl Acad Sci U S A 102 (26) (2005) 9300–9305.

[49] O. Handa, Y. Naito, T. Yoshikawa, CagA protein of Helicobacter pylori: a hijacker of gastric epithelial cell signaling, Biochem Pharmacol 73 (11) (2007) 1697–1702.

[50] K. Mukaisho, T. Nakayama, T. Hagiwara, T. Hattori, H. Sugihara, Two distinct etiologies of gastric cardia adenocarcinoma: interactions among pH, Helicobacter pylori, and bile acids, Front Microbiol 6 (2015) 412.

[51] M. Balakrishnan, R. George, A. Sharma, D.Y. Graham, Changing Trends in Stomach Cancer Throughout the World, Curr Gastroenterol Rep 19 (8) (2017) 36.

[52] P. Rawla, A. Barsouk, Epidemiology of gastric cancer: global trends, risk factors and prevention, Prz Gastroenterol 14 (1) (2019) 26–38.

[53] D.Y. Graham, Helicobacter pylori update: gastric cancer, reliable therapy, and possible benefits, Gastroenterology 148 (4) (2015) 719–731 e713.

[54] C.L. Sears, A.L. Geis, F. Housseau, Bacteroides fragilis subverts mucosal biology: from symbiont to colon carcinogenesis, J Clin Invest 124 (10) (2014) 4166–4172.

[55] S. Zamani, R. Taslimi, A. Sarabi, S. Jasemi, L.A. Sechi, M.M. Feizabadi, Enterotoxigenic Bacteroides fragilis: A Possible Etiological Candidate for Bacterially-Induced Colorectal Precancerous and Cancerous Lesions, Front Cell Infect Microbiol 9 (2019) 449.

[56] S.A. Shiryaev, A.E. Aleshin, N. Muranaka, M. Kukreja, D.A. Routenberg, A. G. Remacle, R.C. Liddington, P. Cieplak, I.A. Kozlov, A.Y. Strongin, Structural and functional diversity of metalloproteinases encoded by the Bacteroides fragilis pathogenicity island, FEBS J 281 (11) (2014) 2487–2502.

[57] S. Wu, K.C. Lim, J. Huang, R.F. Saidi, C.L. Sears, Bacteroides fragilis enterotoxin cleaves the zonula adherens protein, E-cadherin, Proc Natl Acad Sci U S A 95 (25) (1998) 14979–14984.

[58] T. Zhan, N. Rindtorff, M. Boutros, Wnt signaling in cancer, Oncogene 36 (11) (2017) 1461–1473.

[59] G. Cuevas-Ramos, C.R. Petit, I. Marcq, M. Boury, E. Oswald, J.P. Nougayrede, Escherichia coli induces DNA damage in vivo and triggers genomic instability in mammalian cells, Proc Natl Acad Sci U S A 107 (25) (2010) 11537–11542.

[60] Z. Ge, Y. Feng, L. Ge, N. Parry, S. Muthupalani, J.G. Fox, Helicobacter hepaticus cytolethal distending toxin promotes intestinal carcinogenesis in 129Rag2-deficient mice, Cell Microbiol 19 (7) (2017).

[61] A. Dart, Gut microbiota bile acid metabolism controls cancer immunosurveillance, Nat Rev Microbiol 16 (8) (2018) 453.

[62] C.D. Klaassen, J.Y. Cui, Review: Mechanisms of How the Intestinal Microbiota Alters the Effects of Drugs and Bile Acids, Drug Metab Dispos 43 (10) (2015) 1505–1521.

[63] C.M. Payne, C. Bernstein, K. Dvorak, H. Bernstein, Hydrophobic bile acids, genomic instability, Darwinian selection, and colon carcinogenesis, Clin Exp Gastroenterol 1 (2008) 19–47.

[64] R. Prete, S.L. Long, A.L. Gallardo, C.G. Gahan, A. Corsetti, S.A. Joyce, Beneficial bile acid metabolism from Lactobacillus plantarum of food origin, Sci Rep 10 (1) (2020) 1165.

[65] T.T. Nguyen, T.T. Ung, N.H. Kim, Y.D. Jung, Role of bile acids in colon carcinogenesis, World J Clin Cases 6 (13) (2018) 577–588.

[66] H. Ajouz, D. Mukherji, A. Shamseddine, Secondary bile acids: an underrecognized cause of colon cancer, World J Surg Oncol 12 (2014) 164.

[67] T. Ochsenkuhn, E. Bayerdorffer, A. Meining, M. Schinkel, C. Thiede, V. Nussler, M. Sackmann, R. Hatz, A. Neubauer, G. Paumgartner, Colonic mucosal proliferation is related to serum deoxycholic acid levels, Cancer 85 (8) (1999) 1664–1669.

[68] C. Varon, P. Dubus, F. Mazurier, C. Asencio, L. Chambonnier, J. Ferrand, A. Giese, N. Senant-Dugot, M. Carlotti, F. Megraud, Helicobacter pylori infection recruits bone marrow-derived cells that participate in gastric preneoplasia in mice, Gastroenterology 142 (2) (2012) 281–291.

[69] H. Bernstein, C. Bernstein, C.M. Payne, K. Dvorakova, H. Garewal, Bile acids as carcinogens in human gastrointestinal cancers, Mutat Res 589 (1) (2005) 47–65.

[70] H.B. Lieberman, S.K. Panigrahi, K.M. Hopkins, L. Wang, C.G. Broustas, p53 and RAD9, the DNA Damage Response, and Regulation of Transcription Networks, Radiat Res 187 (4) (2017) 424–432.

[71] J. Yan, A. Takakura, K. Zandi-Nejad, J.F. Charles, Mechanisms of gut microbiota-mediated bone remodeling, Gut Microbes 9 (1) (2018) 84–92.

[72] F. Yusuf, S. Adewiah, F. Fatchiyah, The Level Short Chain Fatty Acids and HSP 70 in Colorectal Cancer and Non-Colorectal Cancer, Acta Inform Med 26 (3) (2018) 160–163.

[73] M. Thangaraju, G.A. Cresci, K. Liu, S. Ananth, J.P. Gnanaprakasam, D. D. Browning, J.D. Mellinger, S.B. Smith, G.J. Digby, N.A. Lambert, et al., GPR109A is a G-protein-coupled receptor for the bacterial fermentation product butyrate and functions as a tumor suppressor in colon, Cancer Res 69 (7) (2009) 2826–2832.

[74] G. Chen, X. Ran, B. Li, Y. Li, D. He, B. Huang, S. Fu, J. Liu, W. Wang, Sodium Butyrate Inhibits Inflammation and Maintains Epithelium Barrier Integrity in a TNBS-induced Inflammatory Bowel Disease Mice Model, EBioMedicine 30 (2018) 317–325.

[75] W. Feng, Y. Wu, G. Chen, S. Fu, B. Li, B. Huang, D. Wang, W. Wang, J. Liu, Sodium Butyrate Attenuates Diarrhea in Weaned Piglets and Promotes Tight Junction Protein Expression in Colon in a GPR109A-Dependent Manner, Cell Physiol Biochem 47 (4) (2018) 1617–1629.

[76] S.P. Fu, S.N. Li, J.F. Wang, Y. Li, S.S. Xie, W.J. Xue, H.M. Liu, B.X. Huang, Q.K. Lv, L.C. Lei, et al., BHBA suppresses LPS-induced inflammation in BV-2 cells by inhibiting NF-kappaB activation, Mediators Inflamm 2014 (2014), 983401.

[77] J.L. Chen, R.R. Gurski, K. Takahashi, R. Andersson, Gastrointestinal cancer metastasis. Gastroenterol Res Pract 2012 (2012), 415498.

[78] E. Pretzsch, F. Bosch, J. Neumann, P. Ganschow, A. Bazhin, M. Guba, J. Werner, M. Angele, Mechanisms of Metastasis in Colorectal Cancer and Metastatic Organotropism: Hematogenous versus Peritoneal Spread, J Oncol 2019 (2019) 7407190.

[79] **Survival Rates for Colorectal Cancer** [https://www.cancer.org/cancer/colon-rectal-cancer/detection-diagnosis-staging/survival-rates.html#references].

[80] H. Sung, J. Ferlay, R.L. Siegel, M. Laversanne, I. Soerjomataram, A. Jemal, F. Bray, Global Cancer Statistics 2020: GLOBOCAN Estimates of Incidence and Mortality Worldwide for 36 Cancers in 185 Countries, CA Cancer J Clin 71 (3) (2021) 209–249.

[81] J. Wang, S. Li, Y. Liu, C. Zhang, H. Li, B. Lai, Metastatic patterns and survival outcomes in patients with stage IV colon cancer: A population-based analysis, Cancer Med 9 (1) (2020) 361–373.

[82] F. Bray, J. Ferlay, I. Soerjomataram, R.L. Siegel, L.A. Torre, A. Jemal, Global cancer statistics 2018: GLOBOCAN estimates of incidence and mortality worldwide for 36 cancers in 185 countries, CA Cancer J Clin 68 (6) (2018) 394–424.

[83] M. Riihimaki, A. Hemminki, K. Sundquist, J. Sundquist, K. Hemminki, Metastatic spread in patients with gastric cancer, Oncotarget 7 (32) (2016) 52307–52316.

[84] A.J. Lax, Opinion: Bacterial toxins and cancer–a case to answer? Nat Rev Microbiol 3 (4) (2005) 343–349.

[85] S. Song, M.S. Vuai, M. Zhong, The role of bacteria in cancer therapy - enemies in the past, but allies at present, Infect Agent Cancer 13 (2018) 9.

[86] R.F. Maldonado, I. Sa-Correia, M.A. Valvano, Lipopolysaccharide modification in Gram-negative bacteria during chronic infection, FEMS Microbiol Rev 40 (4) (2016) 480–493.

[87] R.K. Singh, H.W. Chang, D. Yan, K.M. Lee, D. Ucmak, K. Wong, M. Abrouk, B. Farahnik, M. Nakamura, T.H. Zhu, et al., Influence of diet on the gut microbiome and implications for human health, J Transl Med 15 (1) (2017) 73.

[88] J.C. Hurley, Endotoxemia: methods of detection and clinical correlates, Clin Microbiol Rev 8 (2) (1995) 268–292.

[89] A.S. Andreasen, K.S. Krabbe, R. Krogh-Madsen, S. Taudorf, B.K. Pedersen, K. Moller, Human endotoxemia as a model of systemic inflammation, Curr Med Chem 15 (17) (2008) 1697–1705.

[90] J.C. Marshall, P.M. Walker, D.M. Foster, D. Harris, M. Ribeiro, J. Paice, A. D. Romaschin, A.N. Derzko, Measurement of endotoxin activity in critically ill patients using whole blood neutrophil dependent chemiluminescence, Crit Care 6 (4) (2002) 342–348.

[91] T. Rossi, D. Vergara, F. Fanini, M. Maffia, S. Bravaccini, F. Pirini, Microbiota-Derived Metabolites in Tumor Progression and Metastasis, Int J Mol Sci 21 (16) (2020).

[92] T. Kawasaki, T. Kawai, Toll-like receptor signaling pathways, *Front Immunol* 5 (2014) 461.

[93] R. Benoit, S. Rowe, S.C. Watkins, P. Boyle, M. Garrett, S. Alber, J. Wiener, M. I. Rowe, H.R. Ford, Pure endotoxin does not pass across the intestinal epithelium in vitro, Shock 10 (1) (1998) 43–48.

[94] Y. Ge, R.M. Ezzell, H.S. Warren, Localization of endotoxin in the rat intestinal epithelium, J Infect Dis 182 (3) (2000) 873–881.

[95] S. Guo, R. Al-Sadi, H.M. Said, T.Y. Ma, Lipopolysaccharide causes an increase in intestinal tight junction permeability in vitro and in vivo by inducing enterocyte membrane expression and localization of TLR-4 and CD14, Am J Pathol 182 (2) (2013) 375–387.

[96] C.R. Raetz, C. Whitfield, Lipopolysaccharide endotoxins, Annu Rev Biochem 71 (2002) 635–700.

[97] B.S. Park, J.O. Lee, Recognition of lipopolysaccharide pattern by TLR4 complexes, Exp Mol Med 45 (2013), e66.

[98] G. Zhu, Q. Huang, Y. Huang, W. Zheng, J. Hua, S. Yang, J. Zhuang, J. Wang, J. Ye, Lipopolysaccharide increases the release of VEGF-C that enhances cell motility and promotes lymphangiogenesis and lymphatic metastasis through the TLR4-NF-kappaB/JNK pathways in colorectal cancer, Oncotarget 7 (45) (2016) 73711–73724.

[99] Y. Sun, C. Wu, J. Ma, Y. Yang, X. Man, H. Wu, S. Li, Toll-like receptor 4 promotes angiogenesis in pancreatic cancer via PI3K/AKT signaling, Exp Cell Res 347 (2) (2016) 274–282.

[100] L. Zhao, R. Yang, L. Cheng, M. Wang, Y. Jiang, S. Wang, LPS-induced epithelial-mesenchymal transition of intrahepatic biliary epithelial cells, J Surg Res 171 (2) (2011) 819–825.

[101] B.R. Zetter, Angiogenesis and tumor metastasis, Annu Rev Med 49 (1998) 407–424.

[102] D. Hanahan, R.A. Weinberg, Hallmarks of cancer: the next generation, Cell 144 (5) (2011) 646–674.

[103] D. Zhong, Y. Li, Q. Peng, J. Zhou, Q. Zhou, R. Zhang, H. Liang, Expression of Tiam1 and VEGF-C correlates with lymphangiogenesis in human colorectal carcinoma, Cancer Biol Ther 8 (8) (2009) 689–695.

[104] S.F. Martins, E.A. Garcia, M.A. Luz, F. Pardal, M. Rodrigues, A.L. Filho, Clinicopathological correlation and prognostic significance of VEGF-A, VEGF-C, VEGFR-2 and VEGFR-3 expression in colorectal cancer, Cancer Genomics Proteomics 10 (2) (2013) 55–67.

[105] N. Khromova, P. Kopnin, V. Rybko, B.P. Kopnin, Downregulation of VEGF-C expression in lung and colon cancer cells decelerates tumor growth and inhibits metastasis via multiple mechanisms, Oncogene 31 (11) (2012) 1389–1397.

[106] P. Liu, J. Zhou, H. Zhu, L. Xie, F. Wang, B. Liu, W. Shen, W. Ye, B. Xiang, X. Zhu, et al., VEGF-C promotes the development of esophageal cancer via regulating CNTN-1 expression, Cytokine 55 (1) (2011) 8–17.

[107] M. He, Y. Cheng, W. Li, Q. Liu, J. Liu, J. Huang, X. Fu, Vascular endothelial growth factor C promotes cervical cancer metastasis via up-regulation and activation of RhoA/ROCK-2/moesin cascade, BMC Cancer 10 (2010) 170.

[108] Q. Liu, H. Zhang, X. Jiang, C. Qian, Z. Liu, D. Luo, Factors involved in cancer metastasis: a better understanding to “seed and soil” hypothesis, Mol Cancer 16 (1) (2017) 176.

[109] S. Paget, The distribution of secondary growths in cancer of the breast, The Lancet 133 (3421) (1889) 571–573.

[110] A. Bertocchi, S. Carloni, P.S. Ravenda, G. Bertalot, I. Spadoni, A. Lo Cascio, S. Gandini, M. Lizier, D. Braga, F. Asnicar, et al., Gut vascular barrier impairment leads to intestinal bacteria dissemination and colorectal cancer metastasis to liver, Cancer Cell 39 (5) (2021) 708–724 e711.

[111] J. Xing, Y. Ying, C. Mao, Y. Liu, T. Wang, Q. Zhao, X. Zhang, F. Yan, H. Zhang, Hypoxia induces senescence of bone marrow mesenchymal stem cells via altered gut microbiota, Nat Commun 9 (1) (2018) 2020.

[112] E. Xiao, L. He, Q. Wu, J. Li, Y. He, L. Zhao, S. Chen, J. An, Y. Liu, C. Chen, et al., Microbiota regulates bone marrow mesenchymal stem cell lineage differentiation and immunomodulation, Stem Cell Res Ther 8 (1) (2017) 213.

[113] P. Barcellos-de-Souza, V. Gori, F. Bambi, P. Chiarugi, Tumor microenvironment: bone marrow-mesenchymal stem cells as key players, Biochim Biophys Acta 1836 (2) (2013) 321–335.

[114] S.M. Ridge, F.J. Sullivan, S.A. Glynn, Mesenchymal stem cells: key players in cancer progression, Mol Cancer 16 (1) (2017) 31.

[115] Y. Shi, L. Du, L. Lin, Y. Wang, Tumour-associated mesenchymal stem/stromal cells: emerging therapeutic targets, Nat Rev Drug Discov 16 (1) (2017) 35–52.

[116] U. Blache, E.R. Horton, T. Xia, E.M. Schoof, L.H. Blicher, A. Schonenberger, J. G. Snedeker, I. Martin, J.T. Erler, M. Ehrbar, Mesenchymal stromal cell activation by breast cancer secretomes in bioengineered 3D microenvironments, Life Sci Alliance 2 (3) (2019).

[117] K.J. Meade, F. Sanchez, A. Aguayo, N. Nadales, S.G. Hamalian, T.L. Uhlendorf, L. R. Banner, J.A. Kelber, Secretomes from metastatic breast cancer cells, enriched for a prognostically unfavorable LCN2 axis, induce anti-inflammatory MSC actions and a tumor-supportive premetastatic lung, Oncotarget 10 (32) (2019) 3027–3039.

[118] S.M. Ridge, D. Bhattacharyya, E. Dervan, S.D. Naicker, A.J. Burke, J.M. Murphy, K. O’Leary, J. Greene, A.E. Ryan, F.J. Sullivan, et al., Secreted factors from metastatic prostate cancer cells stimulate mesenchymal stem cell transition to a pro-tumourigenic ’activated’ state that enhances prostate cancer cell migration, Int J Cancer 142 (10) (2018) 2056–2067.

[119] M. Wang, X. Zhao, R. Qiu, Z. Gong, F. Huang, W. Yu, B. Shen, X. Sha, H. Dong, J. Huang, et al., Lymph node metastasis-derived gastric cancer cells educate bone marrow-derived mesenchymal stem cells via YAP signaling activation by exosomal Wnt5a, Oncogene 40 (12) (2021) 2296–2308.

[120] M.M. Zaiss, R.M. Jones, G. Schett, R. Pacifici, The gut-bone axis: how bacterial metabolites bridge the distance, J Clin Invest 129 (8) (2019) 3018–3028.

[121] K.D. Seely, C.A. Kotelko, H. Douglas, B. Bealer, A.E. Brooks, The Human Gut Microbiota: A Key Mediator of Osteoporosis and Osteogenesis, Int J Mol Sci 22 (17) (2021).

[122] M.M. Santisteban, S. Kim, C.J. Pepine, M.K. Raizada, Brain-Gut-Bone Marrow Axis: Implications for Hypertension and Related Therapeutics, Circ Res 118 (8) (2016) 1327–1336.

[123] X. Jia, R. Yang, J. Li, L. Zhao, X. Zhou, X. Xu, Gut-Bone Axis: A Non-Negligible Contributor to Periodontitis, Front Cell Infect Microbiol 11 (2021), 752708.

[124] L. Das Roy, J.M. Curry, M. Sahraei, D.M. Besmer, A. Kidiyoor, H.E. Gruber, P. Mukherjee, Arthritis augments breast cancer metastasis: role of mast cells and SCF/c-Kit signaling, Breast Cancer Res 15 (2) (2013) R32.

[125] H.M. Chen, F.P. Chen, K.C. Yang, S.S. Yuan, Association of Bone Metastasis With Early-Stage Breast Cancer in Women With and Without Precancer Osteoporosis According to Osteoporosis Therapy Status, JAMA Netw Open 2 (3) (2019), e190429.

[126] G.A. Rodan, Bone homeostasis, Proc Natl Acad Sci U S A 95 (23) (1998) 13361–13362.

[127] M.A. Riquelme, E.R. Cardenas, J.X. Jiang, Osteocytes and Bone Metastasis, *Front Endocrinol (Lausanne)* 11 (2020), 567844.

[128] F. Macedo, K. Ladeira, F. Pinho, N. Saraiva, N. Bonito, L. Pinto, F. Goncalves, Bone Metastases: An Overview, *Oncol Rev* 11 (1) (2017) 321.

[129] S.L. Teitelbaum, Bone resorption by osteoclasts, Science 289 (5484) (2000) 1504–1508.

[130] M. Tsuboi, A. Kawakami, T. Nakashima, N. Matsuoka, S. Urayama, Y. Kawabe, K. Fujiyama, T. Kiriyama, T. Aoyagi, K. Maeda, et al., Tumor necrosis factor-alpha and interleukin-1beta increase the Fas-mediated apoptosis of human osteoblasts, J Lab Clin Med 134 (3) (1999) 222–231.

[131] F.N. Soki, S.I. Park, L.K. McCauley, The multifaceted actions of PTHrP in skeletal metastasis, Future Oncol 8 (7) (2012) 803–817.

[132] W.F. Powell Jr., K.J. Barry, I. Tulum, T. Kobayashi, S.E. Harris, F.R. Bringhurst, P. D. Pajevic, Targeted ablation of the PTH/PTHrP receptor in osteocytes impairs bone structure and homeostatic calcemic responses, J Endocrinol 209 (1) (2011) 21–32.

[133] F. Boabaid, J.E. Berry, A.J. Koh, M.J. Somerman, L.K. McCcauley, The role of parathyroid hormone-related protein in the regulation of osteoclastogenesis by cementoblasts, J Periodontol 75 (9) (2004) 1247–1254.

[134] M.D. Ryser, Y. Qu, S.V. Komarova, Osteoprotegerin in bone metastases: mathematical solution to the puzzle, PLoS Comput Biol 8 (10) (2012), e1002703.

[135] A. Maurizi, N. Rucci, The Osteoclast in Bone Metastasis: Player and Target, Cancers (Basel) 10 (7) (2018).

[136] K. Sjogren, C. Engdahl, P. Henning, U.H. Lerner, V. Tremaroli, M.K. Lagerquist, F. Backhed, C. Ohlsson, The gut microbiota regulates bone mass in mice, J Bone Miner Res 27 (6) (2012) 1357–1367.

[137] H. Wu, B. Hu, X. Zhou, C. Zhou, J. Meng, Y. Yang, X. Zhao, Z. Shi, S. Yan, Artemether attenuates LPS-induced inflammatory bone loss by inhibiting osteoclastogenesis and bone resorption via suppression of MAPK signaling pathway, Cell Death Dis 9 (5) (2018) 498.

[138] H. Hotokezaka, E. Sakai, N. Ohara, Y. Hotokezaka, C. Gonzales, K. Matsuo, Y. Fujimura, N. Yoshida, K. Nakayama, Molecular analysis of RANKL-independent cell fusion of osteoclast-like cells induced by TNF-alpha, lipopolysaccharide, or peptidoglycan, J Cell Biochem 101 (1) (2007) 122–134.

[139] M. Manco, L. Putignani, G.F. Bottazzo, Gut microbiota, lipopolysaccharides, and innate immunity in the pathogenesis of obesity and cardiovascular risk, Endocr Rev 31 (6) (2010) 817–844.

[140] A. Hussain Mian, H. Saito, N. Alles, H. Shimokawa, K. Aoki, K. Ohya, Lipopolysaccharide-induced bone resorption is increased in TNF type 2 receptor-deficient mice in vivo, J Bone Miner Metab 26 (5) (2008) 469–477.

[141] M. Baer, A. Dillner, R.C. Schwartz, C. Sedon, S. Nedospasov, P.F. Johnson, Tumor necrosis factor alpha transcription in macrophages is attenuated by an autocrine factor that preferentially induces NF-kappaB p50, Mol Cell Biol 18 (10) (1998) 5678–5689.

[142] T. van der Bruggen, S. Nijenhuis, E. van Raaij, J. Verhoef, B.S. van Asbeck, Lipopolysaccharide-induced tumor necrosis factor alpha production by human monocytes involves the raf-1/MEK1-MEK2/ERK1-ERK2 pathway, Infect Immun 67 (8) (1999) 3824–3829.

[143] M.S. AlQranei, L.T. Senbanjo, H. Aljohani, T. Hamza, M.A. Chellaiah, Lipopolysaccharide- TLR-4 Axis regulates Osteoclastogenesis independent of RANKL/RANK signaling, BMC Immunol 22 (1) (2021) 23.

[144] X.Z. Zeng, Y.Y. Zhang, Q. Yang, S. Wang, B.H. Zou, Y.H. Tan, M. Zou, S.W. Liu, X. J. Li, Artesunate attenuates LPS-induced osteoclastogenesis by suppressing TLR4/TRAF6 and PLCgamma1-Ca(2+)-NFATc1 signaling pathway, Acta Pharmacol Sin 41 (2) (2020) 229–236.

[145] J.H. Kim, N. Kim, Regulation of NFATc1 in Osteoclast Differentiation, J Bone Metab 21 (4) (2014) 233–241.

[146] P. Chongwatpol, E. Rendina-Ruedy, B.J. Stoecker, S.L. Clarke, E.A. Lucas, B. J. Smith, Implications of compromised zinc status on bone loss associated with chronic inflammation in C57BL/6 mice, J Inflamm Res 8 (2015) 117–128.

[147] B.J. Smith, M.R. Lerner, S.Y. Bu, E.A. Lucas, J.S. Hanas, S.A. Lightfoot, R. G. Postier, M.S. Bronze, D.J. Brackett, Systemic bone loss and induction of coronary vessel disease in a rat model of chronic inflammation, Bone 38 (3) (2006) 378–386.

[148] Y. Sakuma, K. Tanaka, M. Suda, Y. Komatsu, A. Yasoda, M. Miura, A. Ozasa, S. Narumiya, Y. Sugimoto, A. Ichikawa, et al., Impaired bone resorption by lipopolysaccharide in vivo in mice deficient in the prostaglandin E receptor EP4 subtype, Infect Immun 68 (12) (2000) 6819–6825.

[149] L. Li, Y.R. Park, S.K. Shrestha, H.K. Cho, Y. Soh, Suppression of Inflammation, Osteoclastogenesis and Bone Loss by PZRAS Extract, J Microbiol Biotechnol 30 (10) (2020) 1543–1551.

[150] Z.Y. Huang, T. Stabler, F.X. Pei, V.B. Kraus, Both systemic and local lipopolysaccharide (LPS) burden are associated with knee OA severity and inflammation, Osteoarthritis Cartilage 24 (10) (2016) 1769–1775.

[151] M.E. Mendez, A. Sebastian, D.K. Murugesh, N.R. Hum, J.L. McCool, A.W. Hsia, B. A. Christiansen, G.G. Loots, LPS-Induced Inflammation Prior to Injury Exacerbates the Development of Post-Traumatic Osteoarthritis in Mice, J Bone Miner Res 35 (11) (2020) 2229–2241.

[152] T.M. Sarenac, M. Mikov, Bile Acid Synthesis: From Nature to the Chemical Modification and Synthesis and Their Applications as Drugs and Nutrients, Front Pharmacol 9 (2018) 939.

[153] J.M. Ridlon, D.J. Kang, P.B. Hylemon, J.S. Bajaj, Bile acids and the gut microbiome, Curr Opin Gastroenterol 30 (3) (2014) 332–338.

[154] R. Adachi, Y. Honma, H. Masuno, K. Kawana, I. Shimomura, S. Yamada, M. Makishima, Selective activation of vitamin D receptor by lithocholic acid acetate, a bile acid derivative, J Lipid Res 46 (1) (2005) 46–57.

[155] E. Laird, M. Ward, E. McSorley, J.J. Strain, J. Wallace, Vitamin D and bone health: potential mechanisms, Nutrients 2 (7) (2010) 693–724.

[156] J.A. Nehring, C. Zierold, H.F. DeLuca, Lithocholic acid can carry out in vivo functions of vitamin D, Proc Natl Acad Sci U S A 104 (24) (2007) 10006–10009.

[157] S. Ruiz-Gaspa, N. Guanabens, S. Jurado, M. Dubreuil, A. Combalia, P. Peris, A. Monegal, A. Pares, Bile acids and bilirubin effects on osteoblastic gene profile. Implications in the pathogenesis of osteoporosis in liver diseases, Gene 725 (144167) (2020).

[158] S. Ceryak, B. Bouscarel, M. Malavolti, H. Fromm, Extrahepatic deposition and cytotoxicity of lithocholic acid: studies in two hamster models of hepatic failure and in cultured human fibroblasts, Hepatology 27 (2) (1998) 546–556.

[159] P. Bianco, Bone and the hematopoietic niche: a tale of two stem cells, Blood 117 (20) (2011) 5281–5288.

[160] J. Seita, I.L. Weissman, Hematopoietic stem cell: self-renewal versus differentiation, Wiley Interdiscip Rev Syst Biol Med 2 (6) (2010) 640–653.

[161] P.M. Le, M. Andreeff, V.L. Battula, Osteogenic niche in the regulation of normal hematopoiesis and leukemogenesis, Haematologica 103 (12) (2018) 1945–1955.

[162] Y. Shiozawa, E.A. Pedersen, A.M. Havens, Y. Jung, A. Mishra, J. Joseph, J.K. Kim, L.R. Patel, C. Ying, A.M. Ziegler, et al., Human prostate cancer metastases target the hematopoietic stem cell niche to establish footholds in mouse bone marrow, J Clin Invest 121 (4) (2011) 1298–1312.

[163] H. Wang, C. Yu, X. Gao, T. Welte, A.M. Muscarella, L. Tian, H. Zhao, Z. Zhao, S. Du, J. Tao, et al., The osteogenic niche promotes early-stage bone colonization of disseminated breast cancer cells, Cancer Cell 27 (2) (2015) 193–210.

[164] J.A. Aguirre-Ghiso, Models, mechanisms and clinical evidence for cancer dormancy, Nat Rev Cancer 7 (11) (2007) 834–846.

[165] R.E. Hurst, A. Bastian, L. Bailey-Downs, M.A. Ihnat, Targeting dormant micrometastases: rationale, evidence to date and clinical implications, Ther Adv Med Oncol 8 (2) (2016) 126–137.

[166] D. Rios-Covian, P. Ruas-Madiedo, A. Margolles, M. Gueimonde, C.G. de Los Reyes-Gavilan, N. Salazar, Intestinal Short Chain Fatty Acids and their Link with Diet and Human Health, Front Microbiol 7 (2016) 185.

[167] J. Yan, J.F. Charles, Gut Microbiota and IGF-1, Calcif Tissue Int 102 (4) (2018) 406–414.

[168] L. McCabe, R.A. Britton, N. Parameswaran, Prebiotic and Probiotic Regulation of Bone Health: Role of the Intestine and its Microbiome, Curr Osteoporos Rep 13 (6) (2015) 363–371.

[169] J. Cheng, S. Feng, P. Kuimanda, G. Lee, Bone Density in Microgravity Conditions Cured by IGF-1, BioTreks (2019).

[170] J. Yan, J.W. Herzog, K. Tsang, C.A. Brennan, M.A. Bower, W.S. Garrett, B. R. Sartor, A.O. Aliprantis, J.F. Charles, Gut microbiota induce IGF-1 and promote bone formation and growth, Proc Natl Acad Sci U S A 113 (47) (2016) E7554–E7563.

[171] V. Locatelli, V.E. Bianchi, Effect of GH/IGF-1 on Bone Metabolism and Osteoporsosis, Int J Endocrinol 2014 (2014), 235060.

[172] A. Nishimura, M. Fujimoto, S. Oguchi, R.D. Fusunyan, R.P. MacDermott, I. R. Sanderson, Short-chain fatty acids regulate IGF-binding protein secretion by intestinal epithelial cells, Am J Physiol 275 (1) (1998) E55–E63.

[173] J.M. Ridlon, S. Ikegawa, J.M. Alves, B. Zhou, A. Kobayashi, T. Iida, K. Mitamura, G. Tanabe, M. Serrano, A. De Guzman, et al., Clostridium scindens: a human gut microbe with a high potential to convert glucocorticoids into androgens, J Lipid Res 54 (9) (2013) 2437–2449.

[174] C. Li, G. Pi, F. Li, The Role of Intestinal Flora in the Regulation of Bone Homeostasis, Front Cell Infect Microbiol 11 (2021), 579323.

[175] B.L. Clarke, S. Khosla, Androgens and bone, Steroids 74 (3) (2009) 296–305.

[176] F. Jardi, N. Kim, M.R. Laurent, R. Khalil, L. Deboel, D. Schollaert, G.H. van Lenthe, B. Decallonne, G. Carmeliet, F. Claessens, et al., Androgen Receptor in Neurons Slows Age-Related Cortical Thinning in Male Mice, J Bone Miner Res 34 (3) (2019) 508–519.

[177] A. Hussain, A. Tripathi, C. Pieczonka, D. Cope, A. McNatty, C. Logothetis, T. Guise, Bone health effects of androgen-deprivation therapy and androgen receptor inhibitors in patients with nonmetastatic castration-resistant prostate cancer, Prostate Cancer Prostatic Dis 24 (2) (2021) 290–300.

[178] N. Pernigoni, E. Zagato, A. Calcinotto, M. Troiani, R.P. Mestre, B. Cali, G. Attanasio, J. Troisi, M. Minini, S. Mosole, et al., Commensal bacteria promote endocrine resistance in prostate cancer through androgen biosynthesis, Science 374 (6564) (2021) 216–224.

[179] Y. Liu, H. Jiang, Compositional differences of gut microbiome in matched hormone-sensitive and castration-resistant prostate cancer, Transl Androl Urol 9 (5) (2020) 1937–1944.

[180] X. Zhang, Interactions between cancer cells and bone microenvironment promote bone metastasis in prostate cancer, Cancer Commun (Lond) 39 (1) (2019) 76.

[181] C. Dai, H. Heemers, N. Sharifi, Androgen Signaling in Prostate Cancer, Cold Spring Harb Perspect Med 7 (9) (2017).

[182] C. Buchta Rosean, R.R. Bostic, J.C.M. Ferey, T.Y. Feng, F.N. Azar, K.S. Tung, M. G. Dozmorov, E. Smirnova, P.D. Bos, M.R. Rutkowski, Preexisting Commensal Dysbiosis Is a Host-Intrinsic Regulator of Tissue Inflammation and Tumor Cell Dissemination in Hormone Receptor-Positive Breast Cancer, Cancer Res 79 (14) (2019) 3662–3675.

[183] M. Collard, P.E. Gallagher, E.A. Tallant, A Polyphenol-Rich Extract From Muscadine Grapes Inhibits Triple-Negative Breast Tumor Growth. *Integr Cancer Ther*(2020) 19:1534735420917444.

[184] D.J. Hadjidakis, I.I. Androulakis, Bone remodeling, Ann N Y Acad Sci 1092 (2006) 385–396.

[185] T.A. Guise, The vicious cycle of bone metastases, J Musculoskelet Neuronal Interact 2 (6) (2002) 570–572.

[186] A.T. Stopeck, A. Lipton, J.J. Body, G.G. Steger, K. Tonkin, R.H. de Boer, M. Lichinitser, Y. Fujiwara, D.A. Yardley, M. Viniegra, et al., Denosumab compared with zoledronic acid for the treatment of bone metastases in patients with advanced breast cancer: a randomized, double-blind study, J Clin Oncol 28 (35) (2010) 5132–5139.

[187] K. Fizazi, M. Carducci, M. Smith, R. Damiao, J. Brown, L. Karsh, P. Milecki, N. Shore, M. Rader, H. Wang, et al., Denosumab versus zoledronic acid for treatment of bone metastases in men with castration-resistant prostate cancer: a randomised, double-blind study, Lancet 377 (9768) (2011) 813–822.

[188] C. Parker, S. Nilsson, D. Heinrich, S.I. Helle, J.M. O'Sullivan, S.D. Fossa, A. Chodacki, P. Wiechno, J. Logue, M. Seke, et al., Alpha emitter radium-223 and survival in metastatic prostate cancer, N Engl J Med 369 (3) (2013) 213–223.

[189] J, McCain, Drugs that offer a survival advantage for men with bone metastases resulting from castration-resistant prostate cancer: new and emerging treatment options. *P T* 39(2) (2014)130-143.

[190] K.C. Ohaegbulam, A. Assal, E. Lazar-Molnar, Y. Yao, X. Zang, Human cancer immunotherapy with antibodies to the PD-1 and PD-L1 pathway, Trends Mol Med 21 (1) (2015) 24–33.

[191] Y. Han, D. Liu, L. Li, PD-1/PD-L1 pathway: current researches in cancer, Am J Cancer Res 10 (3) (2020) 727–742.

[192] M. Ahmadzadeh, L.A. Johnson, B. Heemskerk, J.R. Wunderlich, M.E. Dudley, D. E. White, S.A. Rosenberg, Tumor antigen-specific CD8 T cells infiltrating the tumor express high levels of PD-1 and are functionally impaired, Blood 114 (8) (2009) 1537–1544.

[193] Y. Zhao, W. Yang, Y. Huang, R. Cui, X. Li, B. Li, Evolving Roles for Targeting CTLA-4 in Cancer Immunotherapy, Cell Physiol Biochem 47 (2) (2018) 721–734.

[194] H.G. Ljunggren, R. Jonsson, P. Hoglund, Seminal immunologic discoveries with direct clinical implications: The 2018 Nobel Prize in Physiology or Medicine honours discoveries in cancer immunotherapy, Scand J Immunol 88 (6) (2018), e12731.

[195] Y. Jiang, M. Chen, H. Nie, Y. Yuan, PD-1 and PD-L1 in cancer immunotherapy: clinical implications and future considerations, Hum Vaccin Immunother 15 (5) (2019) 1111–1122.

[196] L. Sun, L. Zhang, J. Yu, Y. Zhang, X. Pang, C. Ma, M. Shen, S. Ruan, H.S. Wasan, S. Qiu, Clinical efficacy and safety of anti-PD-1/PD-L1 inhibitors for the treatment of advanced or metastatic cancer: a systematic review and meta-analysis, Sci Rep 10 (1) (2020) 2083.

[197] E.D. Kwon, C.G. Drake, H.I. Scher, K. Fizazi, A. Bossi, A.J. van den Eertwegh, M. Krainer, N. Houede, R. Santos, H. Mahammedi, et al., Ipilimumab versus placebo after radiotherapy in patients with metastatic castration-resistant prostate cancer that had progressed after docetaxel chemotherapy (CA184-043): a multicentre, randomised, double-blind, phase 3 trial, Lancet Oncol 15 (7) (2014) 700–712.

[198] E.S. Antonarakis, J.M. Piulats, M. Gross-Goupil, J. Goh, K. Ojamaa, C.J. Hoimes, U. Vaishampayan, R. Berger, A. Sezer, T. Alanko, et al., Pembrolizumab for Treatment-Refractory Metastatic Castration-Resistant Prostate Cancer: Multicohort, Open-Label Phase II KEYNOTE-199 Study, J Clin Oncol 38 (5) (2020) 395–405.

[199] L. Landi, F. D'Inca, A. Gelibter, R. Chiari, F. Grossi, A. Delmonte, A. Passaro, D. Signorelli, F. Gelsomino, D. Galetta, et al., Bone metastases and immunotherapy in patients with advanced non-small-cell lung cancer, J Immunother Cancer 7 (1) (2019) 316.

[200] K. Wang, Y. Gu, Y. Liao, S. Bang, C.R. Donnelly, O. Chen, X. Tao, A.J. Mirando, M. J. Hilton, R.R. Ji, PD-1 blockade inhibits osteoclast formation and murine bone cancer pain, J Clin Invest 130 (7) (2020) 3603–3620.

[201] J.T. Buijs, K.R. Stayrook, T.A. Guise, The role of TGF-beta in bone metastasis: novel therapeutic perspectives, Bonekey Rep 1 (2012) 96.

[202] G.J. Prud'homme, Pathobiology of transforming growth factor beta in cancer, fibrosis and immunologic disease, and therapeutic considerations, Lab Invest 87 (11) (2007) 1077–1091.

[203] E. Batlle, J. Massague, Transforming Growth Factor-beta Signaling in Immunity and Cancer, Immunity 50 (4) (2019) 924–940.

[204] S. Jiao, S.K. Subudhi, A. Aparicio, Z. Ge, B. Guan, Y. Miura, P. Sharma, Differences in Tumor Microenvironment Dictate T Helper Lineage Polarization and Response to Immune Checkpoint Therapy, Cell 179 (5) (2019) 1177–1190 e1113.

[205] V. Mendoza-Reinoso, L.K. McCauley, P.G.J. Fournier, Contribution of Macrophages and T Cells in Skeletal Metastasis, Cancers (Basel) 12 (4) (2020).

[206] Z. Hu, J. Gupta, Z. Zhang, H. Gerseny, A. Berg, Y.J. Chen, Z. Zhang, H. Du, C. B. Brendler, X. Xiao, et al., Systemic delivery of oncolytic adenoviruses targeting transforming growth factor-beta inhibits established bone metastasis in a prostate cancer mouse model, Hum Gene Ther 23 (8) (2012) 871–882.

[207] Z. Peng, S. Cheng, Y. Kou, Z. Wang, R. Jin, H. Hu, X. Zhang, J.F. Gong, J. Li, M. Lu, et al., The Gut Microbiome Is Associated with Clinical Response to Anti-PD-1/PD-L1 Immunotherapy in Gastrointestinal Cancer, Cancer Immunol Res 8 (10) (2020) 1251–1261.

[208] K.M. Hargadon, C.E. Johnson, C.J. Williams, Immune checkpoint blockade therapy for cancer: An overview of FDA-approved immune checkpoint inhibitors, Int Immunopharmacol 62 (2018) 29–39.

[209] E. Hayase, R.R. Jenq, Role of the intestinal microbiome and microbial-derived metabolites in immune checkpoint blockade immunotherapy of cancer, Genome Med 13 (1) (2021) 107.

[210] F. van Wijk, H. Cheroutre, Mucosal T cells in gut homeostasis and inflammation, Expert Rev Clin Immunol 6 (4) (2010) 559–566.

[211] C.M. Neophytou, C. Pierides, M.I. Christodoulou, P. Costeas, T.C. Kyriakou, P. Papageorgis, The Role of Tumor-Associated Myeloid Cells in Modulating Cancer Therapy, Front Oncol 10 (2020) 899.

[212] B. Routy, E. Le Chatelier, L. Derosa, C.P.M. Duong, M.T. Alou, R. Daillere, A. Fluckiger, M. Messaoudene, C. Rauber, M.P. Roberti, et al., Gut microbiome influences efficacy of PD-1-based immunotherapy against epithelial tumors, Science 359 (6371) (2018) 91–97.

[213] J. Du, J. Wei, Y. Yang, S. Su, J. Shao, F. Chen, F. Meng, Z. Zou, B. Liu, Disappearance of bone metastases in chemotherapy-resistant gastric cancer

treated with antigen peptide-pulsed dendritic cell-activated cytotoxic T lymphocyte immunotherapy: A case report, Oncol Lett 16 (1) (2018) 875–881.

[214] Y. Asano, N. Yamamoto, K. Hayashi, A. Takeuchi, S. Miwa, K. Igarashi, H. Yonezawa, Y. Araki, S. Morinaga, K. Kasahara, et al., Complete Response of Bone Metastasis in Non-small Cell Lung Cancer With Pembrolizumab: Two Case Reports, Anticancer Res 41 (3) (2021) 1693–1699.

[215] G. Sidhu, E. Tam, Complete resolution of bone metastases with pembrolizumab, Jpn J Clin Oncol 49 (7) (2019) 691–692.

[216] H.W. Kim, R. Hong, E.Y. Choi, K. Yu, N. Kim, J.Y. Hyeon, K.K. Cho, I.S. Choi, C. H. Yun, A Probiotic Mixture Regulates T Cell Balance and Reduces Atopic Dermatitis Symptoms in Mice, Front Microbiol 9 (2018) 2414.

[217] Y. Chiba, K. Shida, S. Nagata, M. Wada, L. Bian, C. Wang, T. Shimizu, Y. Yamashiro, J. Kiyoshima-Shibata, M. Nanno, et al., Well-controlled proinflammatory cytokine responses of Peyer's patch cells to probiotic Lactobacillus casei, Immunology 130 (3) (2010) 352–362.

[218] M.C. Hua, T.Y. Lin, M.W. Lai, M.S. Kong, H.J. Chang, C.C. Chen, Probiotic Bio-Three induces Th1 and anti-inflammatory effects in PBMC and dendritic cells, World J Gastroenterol 16 (28) (2010) 3529–3540.

[219] X. Tan, S. Johnson, Fecal microbiota transplantation (FMT) for C. difficile infection, just say 'No', Anaerobe 60 (102092) (2019).

[220] F. Rohlke, N. Stollman, Fecal microbiota transplantation in relapsing Clostridium difficile infection, Therap Adv Gastroenterol 5 (6) (2012) 403–420.

[221] K.O. Kim, M. Gluck, Fecal Microbiota Transplantation: An Update on Clinical Practice, Clin Endosc 52 (2) (2019) 137–143.

[222] A. Khoruts, Targeting the microbiome: from probiotics to fecal microbiota transplantation, Genome Med 10 (1) (2018) 80.

[223] M.K. Fasanello, K.T. Robillard, P.M. Boland, A.J. Bain, K. Kanehira, Use of Fecal Microbial Transplantation for Immune Checkpoint Inhibitor Colitis, ACG Case Rep J 7 (4) (2020), e00360.

[224] D. Chen, J. Wu, D. Jin, B. Wang, H. Cao, Fecal microbiota transplantation in cancer management: Current status and perspectives, Int J Cancer 145 (8) (2019) 2021–2031.

[225] D. Davar, A.K. Dzutsev, J.A. McCulloch, R.R. Rodrigues, J.M. Chauvin, R. M. Morrison, R.N. Deblasio, C. Menna, Q. Ding, O. Pagliano, et al., Fecal microbiota transplant overcomes resistance to anti-PD-1 therapy in melanoma patients, Science 371 (6529) (2021) 595–602.

[226] M. Bienz, F. Saad, Androgen-deprivation therapy and bone loss in prostate cancer patients: a clinical review, Bonekey Rep 4 (2015) 716.

[227] S.M.H. Alibhai, K. Zukotynski, C. Walker-Dilks, U. Emmenegger, A. Finelli, S. C. Morgan, S.J. Hotte, G.A. Tomlinson, E. Winquist, Bone Health and Bone-Targeted Therapies for Nonmetastatic Prostate Cancer: A Systematic Review and Meta-analysis, Ann Intern Med 167 (5) (2017) 341–350.

[228] A. Wang, N. Karunasinghe, L. Plank, S. Zhu, S. Osborne, K. Bishop, C. Brown, T. Schwass, J. Masters, M. Holmes, et al., Effect of Androgen Deprivation Therapy on Bone Mineral Density in a Prostate Cancer Cohort in New Zealand: A Pilot Study, Clin Med Insights Oncol 11 (2017), 1179554917733449.

[229] M. Lei, C. Guo, D. Wang, C. Zhang, L. Hua, The effect of probiotic Lactobacillus casei Shirota on knee osteoarthritis: a randomised double-blind, placebo-controlled clinical trial, Benef Microbes 8 (5) (2017) 697–703.

[230] S. Ishii, J.A. Cauley, G.A. Greendale, C.J. Crandall, M.E. Danielson, Y. Ouchi, A. S. Karlamangla, C-reactive protein, bone strength, and nine-year fracture risk: data from the Study of Women's Health Across the Nation (SWAN), J Bone Miner Res 28 (7) (2013) 1688–1698.

[231] A. Biragyn, L. Ferrucci, Gut dysbiosis: a potential link between increased cancer risk in ageing and inflammaging, Lancet Oncol 19 (6) (2018) e295–e304.

[232] A.N. Guerrieri, M. Montesi, S. Sprio, R. Laranga, L. Mercatali, A. Tampieri, D. M. Donati, E. Lucarelli, Innovative Options for Bone Metastasis Treatment: An Extensive Analysis on Biomaterials-Based Strategies for Orthopedic Surgeons, Front Bioeng Biotechnol 8 (2020), 589964.